



UNIVERSITAT
POLITÈCNICA
DE VALÈNCIA

A finite element-based approach for the analysis and design of 3D reinforced concrete elements and its application to D-regions

Author: Carlos Méendez Gimeno

Advisors: Dr. Pedro F. Miguel Sosa
Dr. Luis Pallarés Rubio

Valencia, June 2017

This document will be downloadable from the institutional repository of Universitat Politècnica de València (<https://riunet.upv.es/>)

The finite element tool presented in this document has been entirely developed in MATLAB (2014). Figures in this document showing finite element analysis results have been generated using typical plotting functions of the program.

Figures marked with the symbol  on top are interactive to permit a better visualisation. The reader can rotate and scale them in the 3D space by left clicking on them. Viewers Adobe Acrobat Reader (freely available at <https://get.adobe.com/reader/>) or Adobe Acrobat Pro are recommended. To return to the original image, right click on the image and select “Deactive content”.

Acknowledgements

Completing a PhD is a long journey with uncertain results. I am thankful to the Ministry of Education of the Spanish Government for the FPU grant (reference FPU12/01459), which permitted me to focus on this investigation for four years.

Completing a PhD is challenging work. Being able to delve deeper into a topic that interests you is really important. Numerical modelling, and in particular finite element modelling of structures, had always attracted my attention during my civil engineering studies. I must thank my advisor Dr. Pedro Miguel Sosa and Dr. Luis Pallarés Rubio for trusting me and giving me the opportunity to start this work back in 2012 as part of the research project BIA2009-11369 (financed by the Ministry of Science and Innovation of the Spanish Government). I am also grateful to the Instituto de Ciencia y Tecnología del Hormigón (ICITECH) and Universitat Politècnica de València for facilitating this work.

Completing a PhD is a good opportunity to get to know other outstanding foreign institutions and meet experts in the field. I was fortunate enough to undertake a research stay for seven months at the University of Surrey (United Kingdom) under the supervision of Dr. Juan Sagaseta. I am thankful to him for this opportunity and for his guidance, time and interest in my work.

Completing a PhD is sometimes a lonely journey which can only be finished if you are accompanied by good friends. I am thankful to my flatmates who kept me away from (concrete) cracking after office hours. I am also grateful to my colleagues at ICITECH, especially those who I worked closely with. Special thanks to Dr. Jaime Mata Falcón for his comments and encouragement. I cannot forget my friends from Teruel, los preciosos: despite being spread around the country, we always manage to get together from time to time.

Completing a PhD is a long-distance race that starts well before the beginning of university studies. Estoy especialmente agradecido a mis padres, Pilar y Vicente, por su cariño, por todas las oportunidades que me han dado y por su ejemplo de sacrificio. Gracias por las tortillas de patata que han alegrado los lunes después de un fin de semana en casa. Gracias por fomentar mi curiosidad (aunque las visitas a los museos se hicieran interminables). Gracias también a mi hermana Marta y a Javi, por visitarme allá donde haya estado. Espero que pronto podamos disfrutar de muchos más viajes con Álvaro.

Completing a PhD is a time absorbing machine and a patience test. I am thankful to my girlfriend Jenny, who accompanied me along the whole path (and suffered reading some of the following chapters to correct my English). Thank you for showing me what distance (and a PhD) cannot separate.

Abstract

The finite element method is a powerful analysis tool which has facilitated a better understanding of the behaviour of reinforced concrete structures. Its use in the research field is widespread and complements experimental tests and the development of new analytical models. Its application in practice engineering has permitted the analysis of complex elements and the proposal of more consistent designs. However, the general structural engineer is still reluctant to consider finite element modelling for his work as he finds most of these models excessively sophisticated for his needs and knowledge. Of special concern is the use of finite element tools by some of them even when they do not understand the fundamentals on which these models are based, which can represent a risk to the structural safety of the design. In order to bring closer finite element modelling to the practising engineer it is necessary to acknowledge that his needs are different to those of the researcher and, therefore, tools and models need to be adapted. In particular, complexity of many finite element tools usually derives from the adoption of advanced concrete constitutive models. Implementation of more simple models based on engineering practice could facilitate its use by less experienced finite element users.

In structural engineering practice finite element analysis can be of great usefulness to deal with those more problematic elements and/or where the application of traditional analysis methods presents limitations. This includes the so-called D-regions with a 3D behaviour, characterised by complex stress fields caused by abrupt changes in the geometry of the structure and/or concentrated loads. The strut-and-tie method and the stress field method are consistent and rational tools for the analysis and design of D-regions, but while their application to 2D elements is well covered in literature, its extension to 3D is problematic. This generally explains why excessively conservative assumptions are still common in the design of these elements. Refinement of current analytical and design approaches or the use of finite element analysis could lead to more rational solutions which in turn will reduce material requirements and costs.

A 3D nonlinear finite element-based tool was developed in this thesis oriented towards the analysis and design of 3D D-regions by less experienced finite element users. Regarding material modelling, an orthotropic concrete model was adopted to permit the use of uniaxial stress-strain relationships. Only one single parameter, the uniaxial compressive strength of concrete, needs to be

defined. Initially the tensile strength of concrete was neglected in the analyses following the hypotheses of the strut-and-tie method and the stress field method. A more advanced, but still simple, constitutive concrete model was then introduced to consider the contribution of concrete in tension. Additionally, several aid functions were implemented, among which the following can be highlighted: a comprehensive, embedded reinforcement model to facilitate the introduction of complex rebar geometries; special support and load elements permitting an integrated and simple treatment of the boundary conditions imposed by them; and a simple design algorithm for the automatic determination of the required rebar areas based on calculated rebar stresses. Details of the tool are described in the second part of the document.

Three examples of applications to representative 3D D-regions are presented to show the capabilities of the tool and to shed some light on the behaviour of these elements. In particular, the analyses of fourteen four-pile caps, three socket base column-to-foundations connections and one anchorage block are described in the third part of the thesis. Results prove that realistic response predictions can be obtained considering relatively simple constitutive models. The capacity of the tool to configure consistent stress field models depending on the reinforcement arrangement is also demonstrated. The generation of rational reinforcement configurations by applying the implemented design algorithm is also shown.

A strut-and-tie-based method for the analysis and design of four-pile caps with rectangular geometries is proposed in the fourth part of the document. This model was derived based on conclusions obtained from finite element analysis with the developed tool and experimental data obtained from literature. The method is based on a refined 3D strut-and-tie model and the consideration of three potential modes of failure: exceeding the reinforcement strength, crushing of the diagonal strut at the base of the column with narrowing of the strut and splitting of the diagonal strut due to transverse cracking. The main innovation is that the strut inclination is not fixed as in current strut-and-tie-based design procedures, but determined by maximizing the pile cap strength. The method accounts for strength softening of cracked concrete, compatibility constraints and reinforcement details. Its application to 162 specimens of literature led to very good predictions of the ultimate strength and, to a lesser extent, of the mode of failure.

Resumen

El método de los elementos finitos es una potente herramienta de análisis que ha facilitado un mejor conocimiento del comportamiento de las estructuras de hormigón armado. Su uso en el ámbito de la investigación está ampliamente extendido y complementa los ensayos experimentales y el desarrollo de nuevos modelos analíticos. Su aplicación en la práctica ingenieril ha permitido la resolución de elementos complejos y la propuesta de diseños más consistentes. Sin embargo, el ingeniero estructural común todavía es reticente a usar la modelización por elementos finitos en su trabajo ya que considera que la mayoría de estos modelos son excesivamente sofisticados para sus necesidades y su conocimiento. Especialmente preocupante es que algunos de ellos usen herramientas de elementos finitos incluso cuando no entienden los fundamentos de las mismas, lo que puede representar un riesgo para la seguridad estructural. Para acercar la modelización por elementos finitos a la práctica profesional es necesario reconocer que las necesidades son diferentes de las del investigador y, por lo tanto, las herramientas y modelos deben ser adaptados. La complejidad de muchas herramientas de elementos finitos suele derivarse de la adopción de modelos constitutivos de hormigón avanzados. La implementación de modelos más sencillos podría facilitar su uso por usuarios menos experimentados.

En la práctica ingenieril el análisis con elementos finitos puede ser de gran utilidad para tratar aquellos elementos más problemáticos y/o donde la aplicación de los métodos de análisis tradicionales presenta limitaciones. Esto incluye las llamadas regiones D con comportamiento 3D, que están caracterizadas por campos de tensiones complejos provocados por cambios abruptos en la geometría de la estructura y/o cargas concentradas. El método de bielas y tirantes y el método de campos de tensiones son herramientas consistentes y racionales para el análisis y dimensionamiento de regiones D, pero mientras que su aplicación a elementos 2D está bien cubierta en la literatura, su extensión a 3D es problemática. Este hecho explica por qué se adoptan todavía hipótesis excesivamente conservadoras en el dimensionamiento de estos elementos. La propuesta de métodos analíticos y de diseño más adecuados o la modelización con elementos finitos podría conducir a soluciones más racionales, lo que a su vez reduciría las necesidades de material y los costes.

Como parte de esta tesis se ha desarrollado una herramienta de cálculo no lineal basada en el método de los elementos finitos orientada al análisis y dimensionamiento de regiones D tridimensionales por usuarios con menos experiencia en

la modelización con elementos finitos. En lo que respecta a la modelización del material, se ha adoptado un modelo ortotrópico para el hormigón para permitir el uso de relaciones uniaxiales de tensión-deformación. Sólo es necesario definir un único parámetro, la resistencia a compresión uniaxial del hormigón. Inicialmente la resistencia a tracción del hormigón era despreciada en los análisis siguiendo las hipótesis del método de bielas y tirantes y campos de tensiones. Se introdujo después un modelo constitutivo más avanzado, pero todavía simple, para considerar la contribución del hormigón en tracción. Adicionalmente, se han implementado varias funciones de ayuda, entre las que destacan: un modelo de armadura embebida para facilitar la introducción de geometrías de armado complejas; elementos especiales de apoyo y de carga que permiten un tratamiento integral y sencillo de las condiciones de contorno impuestas por ellos; y un algoritmo de diseño para la determinación de manera automática del área de armado necesaria en función de las tensiones calculadas.

Se presentan tres ejemplos de aplicación a regiones D 3D representativas para mostrar las capacidades de la herramienta y describir el comportamiento de estos elementos. En concreto, en la tercera parte del documento se describen los análisis de catorce encepados sobre cuatro pilotes, tres cálices de cimentación y un bloque de anclaje. Los resultados muestran que se pueden obtener predicciones bastante realistas considerando modelos constitutivos relativamente sencillos. También se demuestra la capacidad de la herramienta para configurar modelos de campo de tensiones consistentes dependiendo de la configuración de armado. Además se muestra la capacidad del algoritmo de diseño para configurar disposiciones de armado racionales.

En la cuarta parte del documento se propone un método basado en un modelo de bielas y tirantes para el análisis y dimensionamiento de encepados sobre cuatro pilotes con geometría rectangular. Este modelo se derivó a partir de las conclusiones obtenidas del análisis de elementos finitos con la herramienta desarrollada y los datos experimentales obtenidos de la literatura. El método se basa en un modelo 3D de bielas y tirantes refinado y la consideración de tres modos de fallo posibles: rotura del acero, aplastamiento de la biela diagonal en la base de la columna con estrechamiento de la misma y *splitting* de la biela diagonal debido a la fisuración transversal. La principal novedad es que el ángulo de la biela no se fija como en los modelos actuales de bielas y tirantes, sino que se determina mediante la maximización de la resistencia del encepado. El método considera el debilitamiento de la resistencia del hormigón fisurado, condiciones de compatibilidad de deformaciones y detalles de armado. Su aplicación a 162 especímenes dio lugar a la obtención de muy buenas predicciones de la resistencia última y, en menor grado, del modo de fallo.

Resum

El mètode dels elements finits és una potent eina d'anàlisi que ha facilitat un millor coneixement del comportament de les estructures de formigó armat. El seu ús en l'àmbit de la investigació està àmpliament estès i complementa els assajos experimentals i el desenvolupament de nous models analítics. La seua aplicació en la pràctica enginyeril ha permès la resolució d'elements més complexos i la proposta de dissenys més consistents. No obstant això, l'enginyer estructural comú encara és reticent a fer servir la per elements finits en el seu treball ja que considera que la majoria d'aquests models són excessivament sofisticats per a les seues necessitats i el seu coneixement. Especialment és que alguns d'ells fan servir eines d'elements finits fins i tot quan no entenen els fonaments en què es basen aquests models, el que pot representar un risc per a la seguretat estructural. Per apropar la modelització per elements finits a la pràctica professional cal reconèixer que les necessitats són diferents de les de l'investigador i, per tant, les eines i models han de ser adaptats. En concret, la complexitat de moltes eines d'elements finits sol derivar-se de l'adopció de models constitutius avançats de formigó. La implementació de models més senzills basats en la pràctica enginyeril podria facilitar el seu ús per a usuaris menys experimentats en la modelització amb elements finits.

A la pràctica enginyeril l'anàlisi amb elements finits pot ser de gran utilitat per a tractar aquells elements més problemàtics i/o on l'aplicació dels mètodes d'anàlisi tradicionals presenta limitacions. Això inclou les anomenades regions D amb comportament 3D, que estan caracteritzades per camps de tensió complexos provocats per canvis abruptes en la geometria de l'estructura i/o càrregues concentrades. El mètode de bieles i tirants i el mètode de camps de tensions són eines consistents i racionals per a l'anàlisi i dimensionament de regions D, però mentre que la seua aplicació a elements 2D està ben coberta en la literatura, la seua extensió a 3D és problemàtica. Aquest fet explica per què s'adopten encara hipòtesis excessivament conservadores en el dimensionament d'aquests elements. La proposta de mètodes analítics i de disseny més adequats o la modelització amb elements finits podria conduir a solucions més racionals, amb el que també es reduirien les necessitats de material i els costos.

Com a part d'aquesta tesi s'ha desenvolupat una eina de càlcul no lineal basada en el mètode dels elements finits orientada a l'anàlisi i dimensionament de regions D tridimensionals per a usuaris amb menys experiència en la modelització amb elements finits. Pel que fa a la modelització del material, s'ha adoptat

un model ortotròpic per al formigó per permetre l'ús de relacions uniaxials de tensió-deformació. Només cal definir un únic paràmetre, la resistència a compressió uniaxial del formigó. Inicialment la resistència a tracció del formigó era menyspreada en les anàlisis seguint les hipòtesis del mètode de bieles i tirants i camps de tensions. Es va introduir després un model constitutiu més avançat, però encara simple, per considerar la contribució del formigó a tracció. Addicionalment, s'han implementat diverses funcions d'ajuda, entre les quals destaquen: un model d'armadura embeguda per facilitar la introducció de geometries d'armat complexes; elements especials de suport i de càrrega que permeten un tractament integral i senzill de les condicions de contorn imposades per ells; i un algoritme de disseny per a la determinació de manera automàtica de l'àrea d'armat necessari en funció de les tensions calculades. Els detalls de l'eina es descriuen en la segona part del document.

Es presenten tres exemples d'aplicació a regions D 3D representatives per mostrar les capacitats de l'eina i descriure el comportament d'aquests elements. En particular, en la tercera part del document es descriuen les anàlisis de catorze enceps sobre quatre pilons, 3 calzes de fonamentació i un bloc d'ancoratge. Els resultats mostren que es poden obtenir prediccions prou realistes considerant models constitutius relativament senzills. També es demostra la capacitat de l'eina per configurar models de camp de tensions consistents depenent de la configuració d'armat. A més es mostra la capacitat de l'algoritme de disseny per configurar disposicions d'armat racionals.

En la quarta part del document es proposa un mètode basat en un model de bieles i tirants per a l'anàlisi i dimensionament d'enceps sobre quatre pilons amb geometria rectangular. Aquest model es va derivar a partir de les conclusions obtingudes de l'anàlisi d'elements finits amb l'eina desenvolupada i les dades experimentals obtingudes de la literatura. El mètode es basa en un model 3D de bieles i tirants refinat i la consideració de tres modes de fallada possibles: trencament de l'acer, aixafament de la biela diagonal a la base de la columna amb estrenyiment de la mateixa i splitting de la biela diagonal per causa de la fissuració transversal. La principal novetat és que l'angle de la biela no es fixa com en els models actuals de bieles i tirants, sinó que es determina mitjançant la maximització de la resistència de l'encep. El mètode proposat considera el debilitament de la resistència del formigó fissurat, condicions de compatibilitat de deformacions i detalls d'armat. La seua aplicació a 162 espècimens de la literatura va donar lloc a l'obtenció de molt bones prediccions de la resistència última i, en menor grau, del mode de fallada.

Acronyms and notation

Acronyms

D-region	discontinuity or disturbed region
FE	finite element
FESCA 3D	Finite Elements for Simplified Concrete Analysis in 3D
STM	strut-and-tie method
SFM	stress field method

Notation

- $\{ \}$ = column vector
 $\langle \rangle$ = row vector
 $[\]$ = matrix
 $[B]$ = strain-displacement matrix
 $\langle B_s^p \rangle$ = rebar strain-displacement matrix
 $[D]$ = constitutive matrix
 $[K_T]$ = tangent stiffness matrix
 $[k^e]$ = finite element stiffness matrix
 $\{r\}$ = nodal displacement vector
 $[T]$ = transformation matrix
 $\langle T_s^e \rangle$ = steel strain transformation vector
 $\langle T_s^f \rangle$ = steel force transformation vector
 $\{\epsilon\}$ = strain vector
 $\{\sigma\}$ = stress vector
 $\{\Psi\}$ = residual force vector
 b_w = pile cap width
 b_0 = perimeter of critical section for two-way shear
 c, c_x, c_y = column dimensions
 d = effective depth
 d_p = pile diameter
 e, e_x, e_y = pitch between centre of piles
 f_{c0} = uniaxial cylinder compressive strength of concrete
 f_{ce} = effective compressive strength of concrete
 f_{cp} = equivalent plastic strength of concrete

f_{ct}	=	tensile strength of concrete
f_{su}	=	steel ultimate stress
f_{sy}	=	steel yield stress
f_{syd}	=	design steel yield stress
l_x, l_y	=	side lengths of rectangular pile
w	=	shear span defined as horizontal distance from face of column to center of pile reaction
w_{ii}	=	crack opening
w_c	=	crack opening at zero stress
A_{cs}	=	cross-sectional area at one end of a strut in a strut-and-tie model, taken perpendicular to the axis of the strut
A_p	=	pile sectional area
A_s	=	rebar area
$A_{s,min}$	=	minimum rebar area
$A_{s,0}$	=	minimum rebar area to be considered in design
A_{sT}	=	total amount of horizontal reinforcement in one direction
A_{sp}	=	area of reinforcement over pile in one direction
A_{ts}	=	area of nonprestressed reinforcement of a tie
E	=	elastic modulus
E_s	=	steel elastic modulus
F_{ns}	=	nominal strength of a strut
F_{nt}	=	nominal strength of a tie
F_s	=	force in a strut
F_t	=	force in a tie
G	=	shear modulus
G_f	=	fracture energy
K	=	bulk modulus

M_u	=	factored moment at section
V_c	=	nominal shear strength provided by concrete
V_u	=	factored shear force at section
V_e	=	finite element volume
α_p	=	plastic factor
β_p	=	area factor of the projection of the pile perpendicular to the strut direction
$\theta_{s,x}^{2d}, \theta_{s,y}^{2d}$	=	strut angle projection in 2D at $y=\text{const}$ and $x=\text{const}$, resp.
θ_s^{3d}	=	3D strut angle
φ	=	angle between the tie in the x-direction and the horizontal projection of the diagonal strut
ϵ	=	strain ($\epsilon > 0$ tension)
ϵ_{c0}	=	strain at peak stress f_{c0}
ϵ_{ce}	=	strain at peak stress f_{ce}
ϵ_0	=	hydrostatic strain
ϵ_1	=	principal compressive strain
ϵ_3	=	principal tensile strain
γ_0	=	deviatoric strain
σ	=	stress ($\sigma > 0$ tension)
σ_0	=	hydrostatic stress
σ_1	=	principal compressive stress
σ_3	=	principal tensile stress
σ_s	=	steel stress ($\sigma > 0$ tension)
τ_0	=	deviatoric stress
ξ_c	=	softening coefficient for cracked concrete strength
ξ, η, μ	=	hexahedron natural coordinates
ν	=	Poisson's ratio

Contents

Acknowledgements	i
Abstract	iii
Resumen	v
Resum	vi
Acronyms	ix
Contents	xiii
I Introduction	1
1 Introduction	3
1.1 Application of finite element modelling to reinforced concrete	3
1.2 D-Regions and their importance	4
1.3 Motivation for this work	7
1.4 Objectives.	8
1.5 Outline of this document.	9

II	Implementation of the finite element model	13
2	A general overview of FESCA 3D	15
2.1	Introduction	15
2.2	What FESCA 3D is (and what is not)	16
2.3	FESCA 3D for analysis and for design	18
2.4	FESCA 3D and the FE method	22
2.5	On selecting a finite element for concrete	25
2.6	Generation of the FE mesh	27
2.7	Implementation	27
3	Concrete modelling	29
3.1	Introduction	29
3.2	Behaviour of concrete	30
3.3	Constitutive models for concrete	33
3.4	Proposed 3D constitutive model for concrete	43
3.5	Conclusions	53
4	Reinforcement modelling	55
4.1	Introduction	55
4.2	Behaviour of steel	56
4.3	Constitutive models for steel	57
4.4	Bond-slip interaction	57
4.5	Reinforcement representation	58
4.6	Proposed reinforcement model	62
4.7	Examples of applications	72
4.8	Conclusions	77
5	Load and support modelling	79
5.1	Introduction	79
5.2	Load modelling	80

5.3 Support modelling	88
5.4 Example of application	92
5.5 Conclusions.	100
III Examples of applications	101
6 Validation of FESCA 3D and analysis of pile caps	103
6.1 Introduction	103
6.2 Analysis of six scaled pile caps	104
6.3 Analysis of eight full-size pile caps	121
6.4 Conclusions.	129
7 Analysis of socket base column-to-foundation connections	131
7.1 Introduction	131
7.2 Description of the specimens, experimental setup and test observations.	132
7.3 Finite element model	135
7.4 Finite element analysis	136
7.5 Conclusions.	143
8 Analysis and design of an anchorage block	145
8.1 Introduction	145
8.2 Description of the structural model proposed by Bajo and Pérez-Fadón (2002) .	146
8.3 Analysis and design of the anchorage block with FESCA 3D	148
8.4 Conclusions.	162
IV Strut-and-tie modelling of 3D D-regions	163
9 Refined strut-and-tie model for predicting the strength of four-pile caps	165
9.1 Introduction	165

9.2 Design methods for pile caps	167
9.3 Proposed strut-and-tie model	174
9.4 Validation with test results	184
9.5 Verification with FE results	186
9.6 Comparison with existing methods	188
9.7 Design approach proposed	192
9.8 Conclusions	193
V Conclusions	201
10 Conclusions	203
10.1 Summary	203
10.2 Conclusions drawn from this work	204
10.3 Future work	208
Bibliography	209
Index	219

Part I

Introduction

Chapter 1

Introduction

A tool is as good as its producer, but it is valuable only in the hands of the skilled user ... The structural engineer has unlearned to choose the appropriate tool for a given job: sufficiently precise but not oversophisticated.

—J. Schlaich 1990

1.1 Application of finite element modelling to reinforced concrete

Reinforced concrete has been widely used as a structural material since the second half of the 19th century. First construction applications were based on a system of patents whose structural safety was checked by experimental testing. The use of reinforced concrete to other elements was extended with the appearance of theoretical models at the end of the 19th century and the publication of national norms in the 20th century. First structural models and design methods were simple, intuitive and resolvable by hand. A good example of this is the truss analogy introduced by Ritter (1899) and Mörsch (1908), where the behaviour of cracked reinforced concrete beams was assimilated to that of a steel truss.

Advances in computer technology during the second half of the 20th century permitted the handling of more complex structures and the development of more realistic models. An unprecedented level of modelling detail was achieved with the FE method (Zienkiewicz 1977) and its application in the analysis of reinforced concrete structures (Ngo and Scordelis 1967) (Rashid 1968). This

fostered the development of advanced nonlinear constitutive relationships and models that include complex phenomenon such as concrete cracking, slip of rebars or dynamic effects. Today the use of FE models as virtual laboratories permits a reduction in the time and cost associated with experimental testing and a better understanding of the response of reinforced concrete structures.

The development of commercial FE software packages has been a key element in the widespread application of the method. In the beginning, research centres and universities developed their own, quite specific, tools, whose application in the outside world was limited. Some examples in the field of structural concrete can be found in Committee on Concrete and Masonry Structures ASCE (1982). User-friendlier tools oriented to the market were developed afterwards. Today there is a relatively wide choice of programs. However, a great portion of practising engineers is still reluctant to use them as their application requires a relatively high level of expertise, which is hard to achieve when there are usually more immediate priorities.

In order to bring closer FE modelling to the structural engineer it is necessary to acknowledge that his needs are different to those of the researcher. On the one hand, the researcher aims to clarify and explain with the help of FE results the behaviour of a structure, especially the most uncertain aspects. Therefore, it is important that the FE model reflects the real conditions. On the other hand, the practitioner reduces the problem to the essentials and adopts conservative assumptions and models to guarantee that design requirements are fulfilled. Doing so the likelihood of committing mistakes is reduced. The advantages of FE modelling in structural engineering practice should not be dismissed though, especially when dealing with those more complex elements such as the so-called D-regions treated in next section.

1.2 D-Regions and their importance

Concrete structures can be subdivided into two types of regions: (i) those in which the Bernoulli hypothesis of plane strain distribution is assumed to be valid (B or Bernoulli regions) and (ii) those in which the strain distribution is nonlinear and, hence, the Bernoulli hypothesis is not valid (D- or discontinuity or disturbed regions). D-regions can be caused by abrupt changes in the geometry of the structure and/or concentrated loads, provoking disturbances in the internal flow of stresses and the development of complex stress fields in the critical region. D-regions can be delimited considering the St. Venant's

principle, which states that the length of the dispersion zone is approximately equal to the width or depth of the element.

1.2.1 Analysis and design methods for D-regions

Contrary to the rational and consistent analysis and design methods used for B-regions, the behaviour of D-regions was traditionally misunderstood and its design was contentious and mainly supported on rules of thumb or judgement based on past experience.

The strut-and-tie method (STM) (J. Schlaich, Schafer, and Jennewein 1987) and the stress field method (SFM) (Muttoni, Schwartz, and Thürlimann 1997) emerged to shed some light and rationality on the design of these critical regions. Both methods are closely related, although their origins are rather different. On the one hand, the STM is a generalisation of the truss analogy to apply it to any part of the structure. Strut-and-tie models consist of concrete struts carrying the compressive forces, steel ties carrying the tensile forces and nodal zones where they connect. On the other hand, the SFM is derived from the application of the theory of plasticity to reinforced concrete (Drucker 1961). Stress field models consist of compressive stress fields of finite dimensions.

Despite the differences between the STM and the SFM, they also have many characteristics in common: both methods are based on the lower-bound theorem of plasticity, which implies that different solutions can be in general adopted; they are not only useful tools to determine the required reinforcement quantities, but also to understand the internal behaviour of the element and to develop more rational solutions; and one of the main assumptions in both methods is neglecting the tensile strength of concrete. Indeed, strut-and-tie models can be viewed as a discrete representation of stress field models.

Stress field models provide a more accurate representation of the stress state inside the element than strut-and-tie models. However, due to its simplicity, the STM has become more popular in practice engineering, and major design codes include provisions and guidelines for its application (European Committee for Standardization 2004) (ACI Committee 318 2002) (Fédération Internationale du Béton 2013) (ACHE 2003).

Hand calculations are frequently sufficient to applied both the STM and SFM, although the application of the latter is generally more tedious. However, these calculations merely by hand are not free of difficulties (Tjhin and D. A. Kuchma 2002). Computer-based tools have been developed to overcome some of the barriers of strut-and-tie modelling (Anderheggen and M. Schlaich 1990)

(Tjhin and D. A. Kuchma 2007) (J.-w. Park et al. 2010) (Bairán García 2012) and stress field modelling (Fernández Ruiz and Muttoni 2007) (Lourenço and Almeida 2013). The application of these tools is oriented to elements with a 2D behaviour.

1.2.2 3D D-regions

Many D-regions can be treated as planar elements. This assumption is appropriate when the forces and stresses in one of the spatial directions are negligible. That can be the case for deep beams, beams with openings, dapped-end beams, corbels and joints, if loads act in the plane of the element. 2D models can be used for these regions, examples of which can be found in literature.

However, the response of other elements is clearly 3D. That is the case of pile cap foundations, socket base column-to-foundation connections, anchorage blocks or bridge diaphragms. Working with 3D models becomes much more complex. Indeed, the application of 3D strut-and-tie models in literature is mainly restricted to pile caps and no reference was found on 3D stress field models. The need for further research on the analysis of 3D D-regions was addressed in the fib bulletin 61:

“there are aspects concerning realization of 3D models, for which little or no guidance is found in the STM provisions. Often, the decomposition of a 3D region into planar models is sought to avoid complexity of 3D models. Such a 2D analogy is often possible, but where this is not the case, e.g. in large pile foundations, the formulation of a spatial model can be quite intricate as well as finding consistent geometries for the 3D nodal zones. For complex nodal geometry strength factors developed for biaxial stress state may be inappropriate. Further research should be performed on efficient concepts for developing 3D nodal zones as well as suitable failure criteria be defined the effective strength of 3D nodes.” (Reineck et al. 2011)

1.2.3 Nonlinear finite element analysis of D-regions

Nonlinear FE analysis can be a promising alternative to the STM and SFM (Amini Najafian and R. L. Vollum 2013a). Commercial FE software packages can be used, but, as mentioned earlier, their oversophistication can represent a barrier for the common structural engineer. More simplified tools have been developed by implementing the hypotheses of the STM and SFM in a FE environment. However, the application of these tools is limited to 2D problems.

Therefore, treatment of the more complex 3D D-regions by simplified methods or models has not been facilitated yet.

1.3 Motivation for this work

Analysis and design of typical 2D D-regions is well covered in scientific literature with many examples of applications of the STM and, to a lesser extent, of the SFM. However, guidelines and recommendations for the analysis of 3D D-regions are scarce. The application of the STM and the SFM to 3D D-regions presents several difficulties. On the one hand, generation of rational 3D strut-and-tie models can be tedious and strength determination of struts and nodal zones is subjected to uncertainties. On the other hand, development and calculation of 3D stress field models seems unapproachable without the help of computer methods. Indeed, no reference was found about this in literature. As a result, 3D D-regions are frequently treated as 2D elements and/or designed inconsistently.

Further study of the behaviour of 3D D-regions could derive in more rational design solutions. FE analysis can be appealing in this sense not only to understand better their behaviour, but also to draw conclusions which can be considered to develop more simple models and to propose guidelines and recommendations for their design.

In order to approach FE modelling to the common practising engineer it is necessary to acknowledge that his needs (and his requirements) are different to those of the structural researcher. Some simplifications must be introduced in the analysis, starting from adopting simple and intuitive concrete constitutive models.

1.4 Objectives

Development of a finite element-based tool for the analysis of 3D reinforced concrete elements

There are several advantages of developing an own computer tool, such as:

- full control on the internal operations of the program
- great flexibility to implement diverse constitutive models, including those adopted in simple analysis methods, hence permitting the assessment of their adequacy in a more systematic manner and the proposal of potential modifications
- adaptation of its functions to the user's needs
- development of additional functions and elements to facilitate its use and the interpretation of output results, in particular thinking in its application by the common practising engineer

This path is not free of difficulties though. Structural models and ideas need to be expressed first on paper. Their translation into computer code comes next and is usually more complicated than the previous step because different functions, elements and models need to be assembled appropriately and potential numerical issues must be accounted for. Data organisation is of great importance as well when dealing with large amounts of information as derived from FE modelling.

Study of 3D D-regions

Pile caps, socket base column-to-foundation connections, anchorage zones and bridge diaphragms are some examples of 3D D-regions. Rational guidelines and recommendations for their analysis are scarce. FE analysis can shed some light on the behaviour of these elements which could ultimately derive in more consistent designs.

Automatic generation of 3D stress field models

One of the complications when using the STM and the SFM is the selection of an appropriate model (Tjhin and D. A. Kuchma 2002). This can become a real challenge for complex elements, especially in 3D. The automatic generation of 3D stress field models through FE analysis can be useful to derive rational strut-and-tie models from which to determine the required reinforcement quantities and also to understand the internal resisting mechanism of the structural element.

Proposal of analysis models for pile cap foundations

Results obtained from FE analysis can be useful to develop simpler structural models. Pile caps are probably the most important element inside the group of 3D D-regions and several STM-based approaches have been proposed for their analysis. However, comparison of the predictions obtained by different methods shows a significant scatter in the results, which often leads to the adoption of excessively conservative solutions. More refined models can result in more optimal designs and substantial savings.

Implementation of design algorithms inside a finite element environment

Currently, the use of FE modelling in design is in general restricted to check the structural safety at the ultimate limit state and the response at the serviceability limit state of solutions obtained with traditional design procedures. However, implementation of design algorithms in an FE environment can permit taking advantage of FE results to determine design variables such as the required steel quantity.

1.5 Outline of this document

This document is divided into five parts and ten chapters, which are organised as follows:

Part I (*Introduction*) includes Chapter 1 and highlights the motivation and objectives of the thesis and addresses its contribution to the current state of knowledge.

Part II (*Implementation of the finite element model*) includes four chapters in which characteristics and fundamentals of the developed numerical tool are described. Each chapter treats interrelated, but rather differentiated topics (see below) and describes for each particular topic both the state of the art and the work undertaken in the thesis related to it. Therefore, none of these chapters is entirely dedicated to a state-of-the-art review.

- Chapter 2 introduces the main characteristics of FESCA 3D, describes its potential application for both analysis and design and discusses aspects related to its implementation. Important equations derived from the FE formulation are given and related with aspects treated in subsequent chapters of the thesis.
- Chapter 3 is dedicated to concrete modelling. The difficulties in proposing an adequate 3D constitutive model for concrete and uncertainties in extending them to real-life structures are outlined. The simplified, intuitive concrete model implemented in the tool based on the use of uniaxial stress-strain relationships is described in the last part of the chapter.
- Chapter 4 covers reinforcement modelling and highlights the necessity of a flexible, independent definition of complex rebar geometries. The comprehensive embedded reinforcement model implemented in the tool is described, including the simplified treatment of curved geometries and modelling of bond-slip between concrete and steel.
- Chapter 5 addresses the importance of the adequate modelling of the boundary conditions in the analysis of D-regions. Load and support models integrated in FESCA 3D to facilitate a consistent definition of these boundary conditions are described.

Part III (*Examples of applications*) includes three chapters and shows the capacity of FESCA 3D in the analysis and design of 3D D-regions through some example applications. Three structural element types classified as 3D D-regions are included.

- Chapter 6 shows the application of the tool for the analysis of pile cap foundations. Results predicted for fourteen four-pile cap specimens tested and reported in literature are presented and compared with the experimental ones. This result comparison shows the importance of the different aspects covered in previous chapters and proves that strength predictions obtained when adopting a relatively refined concrete model are very close to the experimental ones despite the simplicity of the model.

- Chapter 7 shows the capacity of FESCA 3D to automatically generate rational 3D stress fields through the analysis of three socket base column-to-foundation connections with different reinforcement configurations. Results obtained from both linear and nonlinear analysis are presented to highlight the advantages of the latter to identify the internal flow of forces near failure.
- Chapter 8 presents the application of the tool for the design of an anchorage block. The capacity of FESCA 3D in automatically obtaining a rational reinforcement arrangement is shown.

Part IV (*Strut-and-tie modelling of 3D D-regions*) includes Chapter 9 and presents a new, alternative STM-based approach for the analysis and design of four-pile caps without shear reinforcement. Strength predictions obtained by this approach and other five methods for 162 pile cap specimens are compared and discussed.

Part V (*Conclusions*) includes Chapter 10 and closes this document with a summary of the main conclusions drawn from this work and the proposal of future work.

Part II

Implementation of the finite element model

Chapter 2

A general overview of FESCA 3D

Different degrees of accuracy are required at different stages of a project or of assessment.

—Muttoni and Fernández Ruiz 2012

2.1 Introduction

The aim of structural analysis is to predict the response of a structure subjected to a certain load combination. This response is influenced by the geometry of the structure, the material properties, the support conditions and the applied loads. Structural models are useful because these factors are considered in a simplified manner. In particular, FE models have gained huge importance in recent decades thanks to their flexibility to introduce diverse factors.

Application of FE models to reinforced concrete structures can be traced back to the 1960s (Ngo and Scordelis 1967)(Rashid 1968). Many references with examples of applications and guidelines have been published since then (FIB bulletin 45 2008) and several FE software packages have been developed for a systematic application of the method, some of which have been commercialised (ABAQUS, ANSYS, DIANA, ATENA...). Although FE programs are progressively becoming an everyday tool in some design offices, its use is still more extended in the research field, where they are frequently used as actual virtual laboratories to save time and money in experimental testing.

Very realistic predictions can be obtained with some of the already existing FE programs. However, the use of some of them can become quite challenging for the general practising engineer. Moreover, obtaining sound results is not always straightforward as several factors need to be considered. For instance, some programs include in their formulation model-related parameters with no physical meaning which need to be calibrated in order to fit the test response. This approach is not adequate for engineering practice, where the fundamentals of the structural model must be clear to avoid mistakes and misunderstandings.

A new nonlinear FE-based tool named FESCA 3D (acronym of *Finite Elements for Simplified Concrete Analysis in 3D*) was developed in this thesis for the analysis and design of 3D reinforced concrete structures and structural elements. Simplifications regarding concrete material modelling were considered and self-developed functions were integrated to overcome some of the barriers that engineers may encounter when using FE programs. Main characteristics of the program are introduced in this chapter.

2.2 What FESCA 3D is (and what is not)

2.2.1 Object

FESCA 3D was developed to bring FE analysis of reinforced concrete closer to engineering practice, balancing the accuracy and adaptability of FE models, and the simplicity of design models and methods such as the STM and the SFM. Tools for 2D analysis with a similar purpose had been developed by other authors (Fernández Ruiz and Muttoni 2007)(Tjhin and D. A. Kuchma 2007)(J.-w. Park et al. 2010)(Bairán García 2012). For 3D elements Hartl and Beer (2000) proposed a FE-based tool to make advanced numerical methods available for engineers. 3D FE analysis of structural concrete had indeed attracted the attention of previous researchers (e.g. (González Vidosa, Kotsovos, and Pavlovic 1990)). However, it is believed that the approach proposed hereafter presents some innovations over previous ones, which makes it especially suitable for the analysis and design of 3D D-regions.

FESCA 3D is not a replacement of commercial FE programs, which may be in general more powerful and offer more analysis options. However, after improving the user interface, FESCA 3D could be an appealing alternative to these programs for practising engineers who do not have a high level of expertise in FE analysis, and for educational purposes.

2.2.2 Main characteristics of the tool

A simplified 3D model for concrete

A proper 3D characterisation of concrete entails several difficulties and is subjected to many uncertainties. Advanced concrete constitutive models are in general excessively oversophisticated for the general practising engineer and, moreover, such level of detail is in general not needed for the usual stages of design and assessment. Acknowledging this, a simplified, orthotropic constitutive model was adopted from the beginning in order to use intuitive equivalent uniaxial stress-strain relationships to characterise the 3D response. Diverse uniaxial models were considered throughout the development of the program as described below.

The initial assumption was to neglect the tensile strength of concrete, as is commonly done in practice design, and which is the main assumption of the STM and the SFM. In compression, elastic-perfectly plastic models were adopted. Similar assumptions had been previously considered by Fernández Ruiz and Muttoni (2007) in 2D for the development of elastic-plastic stress fields giving sound strength predictions. This assumption limited the scope of the tool to the ultimate limit state analysis and led to clear 3D stress fields which helped to understand the internal load path from which strut-and-tie models could be easily derived.

Comparison of FE and experimental results showed that neglecting the tensile strength of concrete can give excessively conservative strength predictions for large, lightly reinforced concrete elements, which is in fact a characteristic of most 3D D-regions. Moreover, it leads to unrealistic tensile strains and, therefore, the adoption of typical compressive softening models based on transverse tensile strains becomes inadequate. In order to obtain more realistic predictions the constitutive model was modified to account for the tensile stresses in concrete. Different tensile softening models were considered, with those based on fracture mechanics theory giving the most realistic results. In compression more refined nonlinear constitutive models were adopted as well. Confinement and cracking effects on the compressive strength were included. Details of the adopted concrete constitutive model can be found in Chapter 3.

Integrated tools to facilitate FE modelling

Some functions were developed to facilitate the definition of reinforcing bars, loads and support conditions. These elements are frequently a source of problems in the development of an FE model.

A comprehensive embedded reinforcement model was developed, allowing for a complete independence between the geometry of the reinforcement and the FE mesh. The model was complemented with an additional function to ease the introduction of rebars with complex, curved spatial geometries. Details of the reinforcement model are given in Chapter 4.

Additionally, several functions and models were implemented to permit a flexible, direct and consistent definition of load and support geometries and conditions, without having to include load and supports elements explicitly in the FE mesh, hence, reducing modelling efforts. Load and support models are described in more detail in Chapter 5.

2.3 FESCA 3D for analysis and for design

The structural engineer usually encounters two different types of problems: (i) the assessment of existing structures and (ii) the design of new ones. Although both problems are related to structural analysis, they should not be solved following the same approach (Muttoni, Fernández Ruiz, and Niketić 2015). On the one hand, the purpose of assessment is to estimate the element strength, compare it with the design loads and assess if strengthening is necessary. It is wise to start from simple, conservative models in order to avoid unnecessary levels of complexity. Development of more refined, sophisticated models is only justified if conservative strength estimations are below the acting loads in order to reduce or avoid potential retrofitting of the structure. On the other hand, the purpose of design is to determine the element dimensions and the reinforcement geometry and quantity to guarantee a sound response under service loads and the structural safety at the ultimate limit state. Element dimensions are in general fixed or can be modified only slightly and, therefore, efforts are focused on the determination of the reinforcement.

The FE method has been extensively used for analysis of reinforced concrete structures in the research field and also in engineering practice; however, application of FE modelling for design is usually limited to check if an already-developed design fulfils the design constraints. The use of FE results in a systematic manner can be appealing to configure a design solution as some

authors have proposed in literature: Tabatabai and Mosalam (2001) developed a computational platform for optimum reinforcement dimensioning of general spatial structures consisting of flat panels which worked in conjunction with a commercial FE program (TNO DIANA 2016); a more direct approach was proposed by Fernández Ruiz and Muttoni (2007) where rebar areas were calculated iteratively based on nonlinear FE results; a completely automatic procedure was proposed by Amini Najafian and R. L. Vollum (2013b) in which reinforcement quantity was initially determined from linear FE analysis and updated afterwards based on nonlinear FE results obtained with a commercial FE program (TNO DIANA 2016).

FESCA 3D can be used for both analysis and design purposes.

2.3.1 FESCA 3D for analysis

FESCA 3D can be used for predicting the response and maximum strength of 3D reinforced concrete structures. For assessment of existing structures it is recommended to start with a simplified FE analysis (a) neglecting the tensile strength of concrete, (b) assuming an elastic-perfectly plastic response in compression and (c) dismissing the effect of confinement on the concrete strength. Consideration of compressive softening due to transverse cracking depends on the existing reinforcement: if reinforcement is well distributed over the element, the magnitude of the resulting FE tensile strains may be reasonable despite having neglected the tensile strength of concrete and can be used to estimate this softening; otherwise, FE tensile strains will not be realistic and the use of traditional softening formulae can lead to excessively conservative results.

If boundary conditions and reinforcement arrangement have been properly defined, the maximum load predicted under the assumptions mentioned will be in general smaller than the actual one according to the lower-bound theorem of plasticity; this cannot be guaranteed though for lightly reinforced elements when compressive softening is not accounted for. If the design load is smaller than the predicted strength, refinement of the analysis is not necessary; otherwise, the concrete constitutive model should be refined to include the contribution of the tensile strength of concrete and the effect of confinement on the compressive strength of concrete. A more realistic, larger strength prediction may be obtained under these new assumptions, permitting to avoid or reduce potential retrofitting.

Displacements, 3D stress and strain fields, rebar stresses, concrete damage due to transverse tensile strains and other variables can be determined at each load step based on the FE results. These results can be represented graphically for a more direct and intuitive interpretation. The accuracy of these predictions depends on the assumptions made on material modelling and the refinement of the model.

2.3.2 FESCA 3D for design

A simple design algorithm was developed to automatically determine the required reinforcement quantity. This approach is equal to that adopted by Fernández Ruiz and Muttoni (2007). Rebar areas are calculated iteratively based on steel stresses obtained from nonlinear FE analysis where steel is modelled as perfectly elastic as follows:

$$A'_s = A_s \frac{\sigma_s}{f_{syd}} \begin{cases} \text{if } A'_s \leq A_{s,min} \rightarrow A'_s = A_{s,min} \\ \text{if } A'_s \leq A_{s,0} \rightarrow A'_s = 0 \end{cases} \quad (2.1)$$

where $A_{s,min}$ is the minimum rebar area for crack control, $A_{s,0}$ is the minimum rebar area to be considered and f_{syd} the design yield stress of steel.

Rebar areas can be updated considering every rebar as a homogeneous unit or as a compound of FEs: when the former, σ_s in equation 2.1 is taken equal to the maximum tensile stress of the rebar ($\sigma_s > 0$); when the latter, σ_s is taken equal to the tensile stress of the rebar FE.

Any constitutive law can be considered for concrete, but it is recommended to adopt a simple model assuming an elastic-perfectly plastic model in compression and neglecting the tensile strength. This concrete model is not only in accordance with design practice, but also speeds the convergence process compared to more refined models.

The criteria to accept a solution as valid at the end of each design step is based on the rebar stress ration σ_s/f_{syd} . The user must define a range of admissible values. The definition of this range must be reasonable, especially considering that the obtained solution will have to be rounded up to the next available commercial rebar diameters. Stress ratios between 0.90-0.95 and 1.05-1.10 can be adequate ($0.90 - 0.95 \leq \sigma_s/f_{syd} \leq 1.05 - 1.10$). Subsequent nonlinear FE analyses are undertaken until the design convergence criterion is fulfilled. In general, a reasonable solution is already attained within the first iteration as steel stresses vary slightly with reinforcement quantity.

If reinforcement geometry is not given, running a linear analysis to obtain the elastic stress field can be of interest. Indeed, dimensioning reinforcement based on linear elastic stresses is a common approach in design. This is also in agreement with the recommendation made by J. Schlaich, Schafer, and Jennewein (1987) in the STM, who proposed to orientate struts and ties with the elastic stress pattern to guarantee an adequate response under service loads and to increase the ductility. However, this approach does not account for the stress redistribution near failure.

Another appealing approach to generate a rational reinforcement layout which is possible with FESCA 3D is to define a blind reinforcement layout by introducing rebars in several locations and directions, without much reasoning and just considering construction aspects. Then, by means of the design algorithm the program eliminates those rebars which are less demanded (i.e. those whose calculated area is below $A_{s,0}$) and determines the required rebar area of the others. The capacity of this procedure will be shown in Chapter 8. It should be noted that initially-input rebar areas can affect to subsequent results and, therefore, to the final solution: zones with significantly higher initial reinforcement concentrations may attract larger forces at the expend of other zones with lower reinforcement concentrations; therefore, some load paths may be favoured over others and, in some cases, this may have an effect in the obtained solution.

2.3.3 Safety format for assessment and design

For design, the ultimate limit state should be verified by a partial safety factor method, in which design resistance is calculated using the design material values as input parameters for the nonlinear FE analysis, as proposed in MC 2010 (Fédération Internationale du Béton 2013). f_{co} , f_{ct} and f_{sy} should be hence substituted in the FE analysis by their corresponding design values f_{cd} , f_{ctd} and f_{syd} by dividing them by the partial safety factor for a material property γ_M . Partial factors γ_M proposed in MC 2010 for concrete and steel for persistent loads are 1.5 and 1.15, respectively.

The same approach and material safety factors should be considered for assessment purposes, even when this will derive in more conservative results.

2.4 FESCA 3D and the FE method

It is out of the scope of the present document to give a detailed description of the FE method, which can be found elsewhere (Zienkiewicz 1977). However, it is of interest to recall here some important equations derived from the method and to relate them with some aspects of FESCA 3D treated in next chapters.

Equilibrium equations between external and internal forces are the fundamental equations of structural analysis. In the FE method this equilibrium must be satisfied at the nodes of the FE mesh. A displacement state must be found for which the internal nodal force vector $\{F_{int}\}$ equals the external nodal force vector $\{F_{ext}\}$. The latter vector contains the values of the applied forces and reactions (section 2.4.2), and the former is obtained from the stresses induced by the displacements (section 2.4.3).

The direct stiffness method is the most popular implementation of the FE method in order to obtain the nodal displacement vector for which external and internal nodal forces are balanced. For structural systems with a nonlinear response the determination of this displacement vector is not direct and requires to follow an iterative procedure until equilibrium between external and internal forces is achieved (section 2.4.4). The difference between the external and the internal nodal force vector at each iteration step i is known as the residual nodal force vector $\{\Psi_i\}$:

$$\{\Psi_i\} = \{F_{ext}\} - \{F_{int,i}\} \quad (2.2)$$

The objective is hence to obtain a nodal displacement vector $\{r\}$ for which $\{\Psi_{i+1}\} = \{0\}$. Considering this, the displacement increment at each iteration step can be calculated as follows:

$$\{d\Psi\} = -\frac{\partial \{F_{int,i}\}}{\partial r} dr = \{\Psi_{i+1}\} - \{\Psi_i\} = -\{\Psi_i\} \quad (2.3)$$

This equation can also be written as:

$$\{\Psi_i\} = [K_{T,i}] \{dr\} \quad (2.4)$$

where $[K_{T,i}]$ is the tangent stiffness matrix, which is a function of the displacement state (section 2.4.1).

2.4.1 Building the tangent stiffness matrix

The tangent stiffness matrix $[K_T]$ is obtained by assembling accordingly the tangent stiffness matrices of each FE in which the structure is divided. The tangent stiffness matrix of an FE $[k^e]$ can be determined as:

$$[k^e] = \int_{V_e} [B]^T [D] [B] dV \quad (2.5)$$

where $[D]$ is the material constitutive matrix and $[B]$ is the strain-displacement matrix, which relates the FE nodal displacements $\{r^e\}$ with the strain vector $\{\epsilon\}$ at any point inside the FE. In general this integration is performed numerically by evaluating $[B]$ and $[D]$ at the Gauss integration points of the FE.

The strain-displacement matrix $[B]$ is a function of the FE geometry; the constitutive matrix $[D]$ is a function of the material properties and the current strain state. Concrete and steel present very different properties and are in general treated separately. Concrete presents a complex nonlinear response due to cracking and multi-axial effects; concrete modelling aspects are treated in Chapter 3. Steel can be characterised more easily, but the main issue when modelling reinforcing bars is how to include them in a model which is mainly defined by the concrete mass; reinforcement modelling aspects are discussed in Chapter 4.

2.4.2 Building the external nodal force vector

The external force vector includes the reactions induced at the supports, which can only be determined after displacements are obtained, and the loads applied on the structure, which are known.

In the FE method any force acting on the structure must be applied at the nodes. However, loads and reactions are frequently not punctual but distributed, and, therefore, it is necessary to transform them into equivalent nodal forces. These equivalent nodal forces depend on the magnitude, stress distribution and geometry of the load, but also on the geometry of the FE mesh.

Load modelling can significantly affect the obtained results, especially when load dimensions are relatively large (of the same order of magnitude) compared to the entire structural element, as it is actually the case in most D-Regions. For simplicity reasons it is frequently assumed that the stress distribution on

the loading surface is uniform; this is justified because in most cases stresses being applied are constant. However, the mere presence of the loading element makes the stresses which are actually being transmitted to the structure differ. Therefore, loading elements of significant dimensions should be introduced in the FE mesh if sound predictions are to be obtained.

The explicit definition of loading elements in an FE model can be tedious, especially if the geometry of the FE mesh needs to be adapted to the geometry of the loading element. An automatic function based on static condensation was implemented in FESCA 3D in order to reduce these modelling efforts. This function accounts for the effect of the loading element on the stress distribution and the stiffness of the system without having to include it explicitly in the FE mesh. A more detailed description of load modelling in FESCA 3D is given in Chapter 5.

2.4.3 *Building the internal nodal force vector*

Similarly to the tangent stiffness matrix, the internal nodal force vector $\{F_{int}\}$ is obtained by assembling accordingly the internal nodal force vector of each FE $\{f_{int}^e\}$. The latter can be determined as:

$$\{f_{int}^e\} = \int_{V_e} [B]^T \{\sigma\} dV \quad (2.6)$$

where $\{\sigma\}$ is the stress vector, which is a function of the strain vector $\{\epsilon\}$ and, hence, of the FE nodal displacements.

2.4.4 *Iterative procedure and convergence criteria*

Due to material nonlinearities an iterative process is in general needed until equilibrium between external and internal forces is attained. Different nonlinear resolution methods have been proposed in literature. The Newton-Raphson method, the Arc-length method and the displacement-controlled method were implemented in FESCA 3D.

In nonlinear analysis it is not realistic to seek for solutions where external and internal forces are perfectly balanced. A convergence criterion must be established to define the limit between unacceptable and acceptable solutions. Convergence strategies based on the maximum absolute value of the residual

nodal force vector, the norm of the residual force vector and energy increments were implemented in FESCA 3D.

2.4.5 Resolution of the system of equations

The tangent stiffness matrix $[K_T]$ is singular by nature. Boundary conditions imposed by the supports must be considered to solve the system of equations 2.4. This system of equations can be partitioned into restrained degrees of freedom (r) (known displacement) and free degrees of freedom (f) (unknown displacement):

$$\begin{bmatrix} \{d\Psi_f\} \\ \{d\Psi_r\} \end{bmatrix} = \begin{bmatrix} [K_{ff}] & [K_{fr}] \\ [K_{rf}] & [K_{rr}] \end{bmatrix} \begin{bmatrix} \{dr_f\} \\ \{dr_r\} \end{bmatrix} \quad (2.7)$$

Free displacements $\{dr_f\}$ can be obtained as:

$$\{dr_f\} = [K_{ff}]^{-1} (\{d\Psi_f\} - [K_{fr}] \{dr_r\}) \quad (2.8)$$

At least six appropriate degrees of freedom must be restrained in 3D problems to prevent the rigid motion of the structure. Imposing zero displacements on nodes located at the support locations is the most common approach in practice; however, this approach is not very realistic as supports and bearings are never perfectly rigid in reality. A more accurate modelling of the actual boundary conditions is necessary in some cases, especially when the dimensions of the supports and of the structural element are of the same order of magnitude; however, this can be laborious. Special support models were developed in FESCA 3D considering typical support conditions in order to facilitate a more flexible modelling of the boundary conditions imposed by them. These models are described in Chapter 5.

2.5 On selecting a finite element for concrete

The FE strain-displacement matrix $[B^e]$ is a function of the type of FE and the nodal coordinates. Four different FEs were implemented for concrete: the four-node tetrahedron, the ten-node tetrahedron, the eight-node hexahedron and the twenty-node hexahedron.

Initially the four-node tetrahedron was chosen due to its simplicity; concurrently reinforcing bars were modelled by discrete two-node bar elements linked

to the concrete nodes (Meléndez 2012). The embedded reinforcement model was then implemented so reinforcement geometry could be independent of the concrete FE mesh. To take full benefit of the advantages of the embedded model it was necessary to implement a higher-order concrete element because the four-node tetrahedron has only linear interpolation capacity and, therefore, the strain state inside the FE is constant.

The quadratic ten-node tetrahedron, the eight-node hexahedron and the twenty-node hexahedron were then implemented. Good results were obtained with the ten-node tetrahedron if the rebar trajectory ran on the FE faces, but spurious responses were observed if the rebar passed through them. The eight-node and the twenty-node hexahedrons gave sound results regardless of the location of the rebar.

Due to its higher interpolation capacity the twenty-node hexahedron was used in all the analyses presented in this document (figure 2.1). For expository reasons, all figures and formulations presented hereafter will refer to the twenty-node hexahedron. The shape functions of this element, from which the strain-displacement matrix can be derived, are given by:

$$\begin{aligned}
 N_i^e &= 1/8(1 + \xi\xi_i)(1 + \eta\eta_i)(1 + \mu\mu_i)(\xi\xi_i + \eta\eta_i + \mu\mu_i - 2) \text{ for corner nodes } i = 1\dots 8 \\
 N_i^e &= 1/4(1 - \xi^2)(1 + \eta\eta_i)(1 + \mu\mu_i) \text{ for midside nodes } i = 9, 11, 17, 19 \\
 N_i^e &= 1/4(1 - \eta^2)(1 + \xi\xi_i)(1 + \mu\mu_i) \text{ for midside nodes } i = 10, 12, 18, 20 \\
 N_i^e &= 1/4(1 - \mu^2)(1 + \xi\xi_i)(1 + \eta\eta_i) \text{ for midside nodes } i = 13, 14, 15, 16
 \end{aligned}
 \tag{2.9}$$

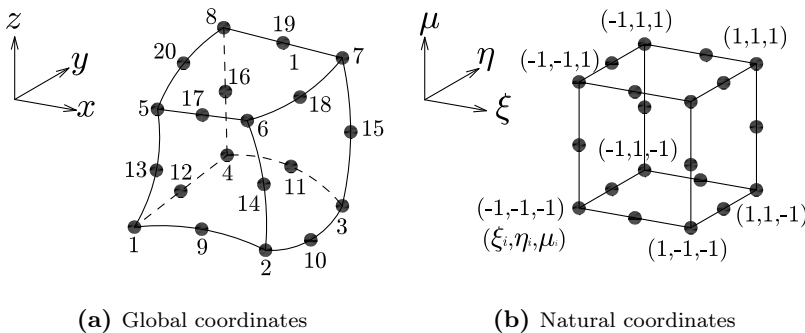


Figure 2.1: The 20-node hexahedron FE.

2.6 Generation of the FE mesh

Generation of the FE mesh is a challenge by itself. It was outside the scope of this work to develop an FE mesher. The open source platform Salome (CASCADE OPEN, CEA/DEN, and EDF R&D 2016) was used to generate the FE meshes adopted for the analyses presented in this thesis. Salome offers many options for pre- and post-processing data in numerical simulation. In particular, it can generate tetrahedral and hexahedral meshes adaptable to the geometry and restraints imposed by the user. The tetrahedron mesher is very versatile and can be applied to complex geometries like spheres; the hexahedron mesher imposes some limitations as volumes to be meshed must have six faces. Only the nodal coordinates and element connectivity of the mesh generated by Salome was exported to FESCA 3D.

It must be noted that development of powerful meshing algorithms has facilitated the generation of complex FE meshes and led to the development of more refined models which account for even the smallest geometric details. However, computational time increases exponentially when including more FEs: a balance between excessively refined and excessively coarse meshes must be found. Sometimes mesh refinement is justified by the need to adapt the concrete mesh to the reinforcement layout or the geometry of the loads and supports; the embedded reinforcement model and the load and support models integrated in FESCA 3D allow the removal of these causes of further refinement and, hence, coarser meshes can be potentially used.

2.7 Implementation

FESCA 3D was implemented entirely in the programming environment MATLAB (2014). Despite its limitations, this environment seems to be appropriate for the current purposes of the tool: MATLAB is optimised to work with vector and matrices, which are the main elements on which an FE model is based; its graphical user interface permits the generation of advanced plots to facilitate the analysis of the output results. MATLAB disadvantages are mainly related with computational inefficiency. However, this limitation is acceptable for a first approach where the objective was to check the feasibility of the tool rather than developing a final product. The code could always be rewritten in a more efficient programming language in the future if its use was to be extended.

Chapter 3

Concrete modelling

Much of the experimental data on concrete properties may turn out to be unreliable on account of the interaction between test machine and tested specimen. A simple technique that is both sound and consistent is provided by the ordinary uniaxial-compression cylinder test.

—Kotsovos and Pavlovic 1995

3.1 Introduction

The definition of a sound concrete material model has been considered a determinant factor to obtain a realistic prediction in the analysis of reinforced concrete structures and, therefore, has attracted the attention of many investigations over the years. The FE method has facilitated the development of advanced concrete models which account for several factors affecting its response. The ability of some of these models to accurately reproduce the behaviour of concrete structures is doubtless. However, the formulation of these advanced constitutive models is in general excessively sophisticated for the general structural engineer.

The use of complicated constitutive models may be justified by the complex nature of concrete behaviour. Concrete is usually subjected to a multiaxial stress state, with the response in the principal direction being affected by the strain state in secondary orientations. This influence is such that the variation of frictional stresses induced by the mere presence of the loading platens partly explains the difference observed in results obtained by different testing techniques of small-scaled specimens (Kotsovos 1983). This does not only reflect

the complex behaviour of concrete, but also the difficulties in characterising the material response and its extension to the structural level, where restraining conditions may be difficult to assess and different to those of the material test. The adequacy of using complex concrete material models in practice engineering can be questioned considering this.

This chapter describes briefly concrete behaviour and modelling before presenting the concrete constitutive model adopted in FESCA 3D. Several simplifications were undertaken in this model to facilitate its understanding. The uniaxial compressive strength of concrete f_{c0} is the only mandatory input parameter. The use of an orthotropic formulation permits the consideration of uniaxial stress-strain relationships, which are more familiar for the practitioner, to characterise the 3D response.

3.2 Behaviour of concrete

A brief description of concrete behaviour under uniaxial and multiaxial stress states is given in this section to highlight its main characteristics.

3.2.1 Uniaxial behaviour of concrete

Uniaxial compression

A typical stress-strain diagram of concrete in uniaxial compression is plotted in figure 3.1. The initial part of the ascending branch is almost linear up to about 30 percent of the maximum stress f_{c0} . Then microcracks start to propagate in a stable manner and the stress-strain curvature increases gradually. At about 70-90 percent of the ultimate load continuous macrocracks begin to form and the crack system becomes unstable. A descending branch is observed after the peak stress f_{c0} .

It is often believed that ductility observed in some concrete structures is related with the descending portion of the stress-strain diagram. However, after comparing stress-strain curves of specimens subjected to variable degrees of frictional restrains, Kotsovos (1983) concluded that the descending branch depends on the testing technique: the negative slope becomes steeper when reducing the frictional restraint and, indeed, the load would fall abruptly after f_{c0} in an ideal test with no friction; therefore, descending branches in concrete models must be considered with caution. Only the ascending branch provides a realistic description of the material behaviour (Kotsovos and Pavlovic 1995).

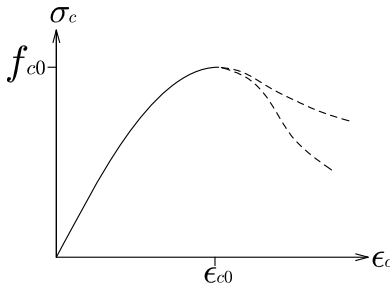


Figure 3.1: Stress-strain diagram for concrete in uniaxial compression.

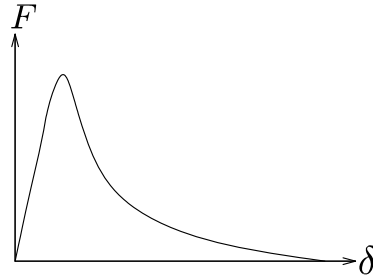


Figure 3.2: Load-deformation diagram for concrete in uniaxial tension.

Uniaxial tension

A typical load-deformation diagram of concrete in uniaxial tension is plotted in figure 3.2. It shows a linear response almost up to the peak load, which is followed by a pronounced descending branch. Strain distribution is fairly uniform for low deformations. Near the peak load strains start to localize around the weakest section, microcracks begin to appear within a narrow zone and the assumption of uniform strain distribution stops to be valid. These microcracks in the fracture zone widen while applying further deformations, and stresses transferred through the remaining ligaments reduce.

In early investigations concrete response in tension was described by means of stress-strain curves, as in compression, assuming that the strain and stress distribution was uniform (Hughes and Chapman 1966)(Madu 1975). Although this assumption is appropriate in the pre-peak regime, the specimen deformation after cracking corresponds to the sum of the crack opening in the fracture zone and the elastic strains outside it; therefore, working with average strains has no meaning and deformations should be used instead (Hordijk 1991).

3.2.2 *Biaxial behaviour*

Concrete behaviour is affected by secondary stress components. Compressive stress-strain $\sigma_1 - \epsilon_1$ diagrams obtained for different levels of transverse stresses σ_2 with $\sigma_3 = 0$ are plotted in figure 3.3. The effect of transverse stresses σ_2 on the compressive response in the longitudinal direction can be summarised as follows: under biaxial compression, strength can be up to approximately 25 percent higher than that observed in uniaxial compression, with strains at peak stress and ductility increasing with higher transverse compressive stresses;

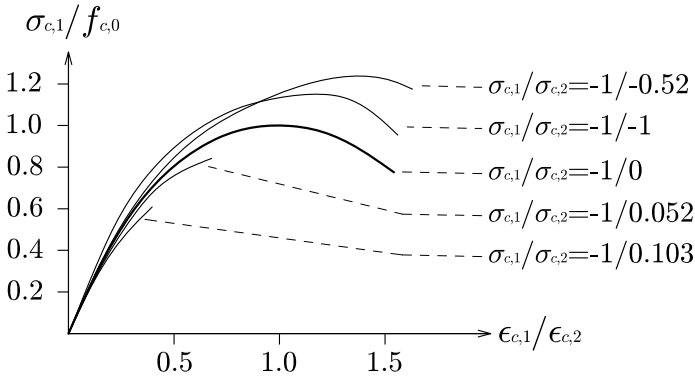


Figure 3.3: Relative stress-strain diagram for concrete under biaxial compression and combined tension-compression (after Kupfer, Hilsdorf, and Rusch (1969)). $\sigma_{c,1}$ = stress in principal compressive direction; $\sigma_{c,2}$ = transverse stress; (-) compression, (+) tension

under combined tension and compression the compressive strength and the strain at peak stress reduce with increments of the transverse tensile stress.

In biaxial tension the tensile strength is approximately equal to that observed in uniaxial tension, but the strain at the peak decreases with the transverse tensile stress (Kupfer, Hilsdorf, and Rusch 1969)).

3.2.3 Triaxial behaviour

Similarly to biaxial stress states, the combination of stresses applied in a second and third direction affects the response in the principal direction. First triaxial tests can be traced back to Richart, Brandtzaeg, and Brown (1928), where it was reported that the presence of lateral stresses could increase the specimen strength to approximately 4.1 times the magnitude of the lateral stresses. More triaxial test programmes have been undertaken since then, obtaining analogous qualitative conclusions as those mentioned above for biaxial stress states: strength increases with lateral compressive stresses and reduces with transverse tensile stresses.

Characterisation of triaxial behaviour of concrete has mainly been focused in studying the effect of transverse stresses on the principal compressive strength. A direct comparison of results obtained by different authors must be done with caution, because measured data depends not only on the material properties but also on the testing technique (Gerstle et al. 1978). Hannant (1974) already

acknowledged this fact when he proposed an approximate, likely conservative concrete failure surface expressed in principal stress space $\sigma_1 - \sigma_2 - \sigma_3$ based on experimental data published at that time. The purpose of his proposal was to enable the designer to estimate the proximity to failure in complex stress situations. Other authors preferred to represent the concrete failure surface by relating the octahedral normal stress σ_0 and the octahedral shear stress τ_0 at failure (Gerstle et al. 1978)(Kotsovos and Pavlovic 1995).

3.3 Constitutive models for concrete

Constitutive models describe material response in an idealised manner. In structural analysis this idealisation begins with neglecting the material microstructure, so principles of continuum mechanics are applicable. These models are known as macro-scale models, versus micro- and meso-scale models which consider the internal structure of the material. Concrete models presented hereafter belong to the group of macro-scale models.

A direct approach to develop a constitutive model is finding a mathematical expression which fits the experimental data. These models are known as empirical models and are appropriate to describe the concrete response under uniaxial conditions. However, the development of multiaxial models requires the assumption of some theoretical principles; by doing this the model can be applied to other arbitrary stress states and is not limited to the conditions it was derived from.

A large variety of concrete models has been proposed in literature. They can be classified based on three criteria: (i) the crack model (discrete or smeared), (ii) the assumption made on material properties variation with axes orientation (anisotropic, orthotropic or isotropic models) and (iii) the underlying theory (elasticity, plasticity or damage mechanics). These aspects are discussed in the next subsections.

3.3.1 *Classification based on crack model*

Discrete-crack approach

Ngo and Scordelis (1967) proposed to represent cracking by disconnecting the concrete FEs at both sides of a crack; this approach seems to be in accordance with the physical nature of cracking as it introduces a discontinuity in the concrete mass. Crack response, including aggregate interlocking effects, can

be simulated by using special linkage elements connecting adjoining elements. One of the disadvantages of this approach is that crack paths are constrained to pass along the element edges and, therefore, a mesh bias is introduced. Computational time can also be increased significantly as the topology of the mesh needs to be altered while cracking propagates (Miguel, Jawad, and Fernández 1990). Today the use of discrete-crack models is mainly limited to the research field and to specific problems where local cracking plays an important role in the structural response; otherwise, the smeared-crack approach described next is generally used.

Smeared-crack approach

Rashid (1968) proposed an alternative approach where the discontinuity induced by cracking was accounted for by considering cracked concrete as an orthotropic material; the axes of material orthotropy were determined by the cracking directions. This approach permitted leaving the original FE mesh unaltered throughout the whole analysis and did not restrain the cracking path. Initially Rashid proposed to reduce the elastic modulus in the cracking direction and the shear modulus on the cracked surface to zero straight after cracking. A shear retention factor β was found necessary by other authors to account for aggregate interlocking effects, with the proportion of the shear stiffness retained not being critical (Suidan and Schnobrich 1973). A gradual reduction of the elastic modulus after cracking was considered by other authors (Bažant and Oh 1983).

Smeared-crack models can be further classified based on how the axes of material orthotropy are established into (i) fixed, (ii) multi-directional fixed and (iii) rotating:

- In fixed crack models crack directions and, hence, axes of material orthotropy are fixed to the principal strain directions at cracking initiation. This approach leads to misalignment of principal stress and strain directions. Predicted responses tend to be too stiff (Rots 1989).
- The multi-directional fixed crack model permits the formation of several fixed cracks, the behaviour of which is monitored separately (Rots 1989). The model offers different solutions depending on the threshold angle defined to allow for subsequent cracks. Indeed, the multi-directional fixed model is very flexible and can be made to coincide with the fixed and the rotating approach in its extremes. However, this model is more complex and is not as intuitive as the fixed and rotating counterparts.

- In the rotating crack model the axes of material orthotropy rotate continuously with principal stress directions (Cope et al. 1980). This implies that microstructural defects are also rotated, which does not seem to be very realistic; despite this, the rotating crack approach has been used extensively in literature providing realistic predictions.

3.3.2 Classification based on variation of material properties with direction

The relation between the stress and strain tensor components σ_{ij} and ϵ_{ij} can be expressed in terms of a fourth-order tensor C_{ijkl} or in matrix form through the constitutive matrix $[D]$ as follows:

$$\sigma_{ij} = C_{ijkl}\epsilon_{kl} \quad (3.1)$$

$$\{\sigma\} = [D] \{\epsilon\} \quad (3.2)$$

with C_{ijkl} and $[D]$ being a function of the mechanical properties of the material.

For 3D problems the tensor C_{ijkl} is formed by 81 different values and the size of matrix $[D]$ is 9x9. The number of independent parameters can be reduced to 21 considering the symmetry of the stress and strain tensors, and that C_{ijkl} is equal to C_{klij} for Green elastic materials. Considering this, the constitutive matrix $[D]$ can be written as:

$$\begin{bmatrix} \sigma_{xx} \\ \sigma_{yy} \\ \sigma_{zz} \\ \tau_{xy} \\ \tau_{yz} \\ \tau_{xz} \end{bmatrix} = \begin{bmatrix} C_{1111} & C_{1122} & C_{1133} & C_{1112} & C_{1123} & C_{1113} \\ & C_{2222} & C_{2233} & C_{2212} & C_{2223} & C_{2213} \\ & & C_{3333} & C_{3312} & C_{3323} & C_{3313} \\ & & & C_{1212} & C_{1223} & C_{1213} \\ & \text{sym} & & & C_{2323} & C_{2313} \\ & & & & & C_{1313} \end{bmatrix} \begin{bmatrix} \epsilon_{xx} \\ \epsilon_{yy} \\ \epsilon_{zz} \\ \gamma_{xy} \\ \gamma_{yz} \\ \gamma_{xz} \end{bmatrix} \quad (3.3)$$

This is the constitutive matrix of an anisotropic material whose mechanical properties vary with orientation. The number of independent variables can be reduced further if some assumptions on the variation of material properties with direction are made.

If it is assumed that the material response is symmetric with respect to three mutually perpendicular axes (orthotropic material), the number of independent

values can be reduced to 9. The constitutive matrix $[D]$ expressed in the local coordinate system defined by the axes of orthotropy can be written as:

$$\begin{bmatrix} \sigma_{11} \\ \sigma_{22} \\ \sigma_{33} \\ \tau_{12} \\ \tau_{23} \\ \tau_{13} \end{bmatrix} = \begin{bmatrix} C_{1111} & C_{1122} & C_{1133} & 0 & 0 & 0 \\ & C_{2222} & C_{2233} & 0 & 0 & 0 \\ & & C_{3333} & 0 & 0 & 0 \\ & & & C_{1212} & 0 & 0 \\ & \text{sym} & & & C_{2323} & 0 \\ & & & & & C_{1313} \end{bmatrix} \begin{bmatrix} \epsilon_{11} \\ \epsilon_{22} \\ \epsilon_{33} \\ \gamma_{12} \\ \gamma_{23} \\ \gamma_{13} \end{bmatrix} \quad (3.4)$$

Furthermore, if interaction between the three orthogonal directions is neglected, the number of independent variables can be reduced further to 6 and $[D]$ can be written as:

$$\begin{bmatrix} \sigma_{11} \\ \sigma_{22} \\ \sigma_{33} \\ \tau_{12} \\ \tau_{23} \\ \tau_{13} \end{bmatrix} = \begin{bmatrix} E_{11} & 0 & 0 & 0 & 0 & 0 \\ & E_{22} & 0 & 0 & 0 & 0 \\ & & E_{33} & 0 & 0 & 0 \\ & & & G_{12} & 0 & 0 \\ & \text{sym} & & & G_{23} & 0 \\ & & & & & G_{13} \end{bmatrix} \begin{bmatrix} \epsilon_{11} \\ \epsilon_{22} \\ \epsilon_{33} \\ \gamma_{12} \\ \gamma_{23} \\ \gamma_{13} \end{bmatrix} \quad (3.5)$$

where E_{ii} is the elastic modulus which directly relates principal strains and stresses and G_{ij} is the shear modulus relating shear stresses and strains in the ij -plane.

Finally, if it is assumed that the material presents identical mechanical properties in any direction (isotropic material), only two independent variables are required. For an elastic material the constitutive matrix $[D]$ can be written in terms of the elastic Young's modulus E and the Poisson's ratio ν as:

$$\begin{bmatrix} \sigma_{xx} \\ \sigma_{yy} \\ \sigma_{zz} \\ \tau_{xy} \\ \tau_{yz} \\ \tau_{xz} \end{bmatrix} = \frac{E}{(1+\nu)(1-2\nu)} \begin{bmatrix} 1-\nu & \nu & \nu & 0 & 0 & 0 \\ & 1-\nu & \nu & 0 & 0 & 0 \\ & & 1-\nu & 0 & 0 & 0 \\ & & & \frac{1-2\nu}{2} & 0 & 0 \\ & \text{sym} & & & \frac{1-2\nu}{2} & 0 \\ & & & & & \frac{1-2\nu}{2} \end{bmatrix} \begin{bmatrix} \epsilon_{xx} \\ \epsilon_{yy} \\ \epsilon_{zz} \\ \gamma_{xy} \\ \gamma_{yz} \\ \gamma_{xz} \end{bmatrix} \quad (3.6)$$

When it is convenient to decouple the material response into hydrostatic (volumetric) and deviatoric (shape) changes, the last matrix is written as a function of the bulk modulus K and the shear modulus G as follows:

$$\begin{bmatrix} \sigma_{xx} \\ \sigma_{yy} \\ \sigma_{zz} \\ \tau_{xy} \\ \tau_{yz} \\ \tau_{xz} \end{bmatrix} = \begin{bmatrix} K + \frac{4}{3}G & K - \frac{2}{3}G & K - \frac{2}{3}G & 0 & 0 & 0 \\ & K + \frac{4}{3}G & K - \frac{2}{3}G & 0 & 0 & 0 \\ & & K + \frac{4}{3}G & 0 & 0 & 0 \\ & & & G & 0 & 0 \\ & \text{sym} & & & G & 0 \\ & & & & & G \end{bmatrix} \begin{bmatrix} \epsilon_{xx} \\ \epsilon_{yy} \\ \epsilon_{zz} \\ \gamma_{xy} \\ \gamma_{yz} \\ \gamma_{xz} \end{bmatrix} \quad (3.7)$$

where

$$K = \frac{\sigma_0}{3\epsilon_0} = \frac{E}{3(1-2\nu)} \quad (3.8)$$

$$G = \frac{\tau_0}{\gamma_0} = \frac{E}{2(1+\nu)} \quad (3.9)$$

The following subsections discuss the application of anisotropic, orthotropic and isotropic models in concrete.

Anisotropic models for concrete

Definition of anisotropic models presents difficulties due to the large number of independent values involved. The application of these models is very limited.

Orthotropic models for concrete

Orthotropic models have been popular in concrete FE analysis as they permit the use of uniaxial relationships to treat multi-axial problems. Moreover, orthotropic models are supported by experimental evidence to some extent: it is obvious that concrete behaviour on a cracked surface and in the direction normal to it differs significantly; and results on multiaxial compression specimens also show that the material response varies with direction, with principal material axes influenced by the direction of loading (Kupfer, Hilsdorf, and Rusch 1969).

The smeared-crack approach described previously is one of the first references of orthotropic-based models. Liu, Nilson, and Slate (1972) extended the appli-

cation of orthotropic models to uncracked 2D stress states and proposed the following relationship for biaxial states:

$$\begin{bmatrix} \sigma_1 \\ \sigma_2 \\ \tau_{12} \end{bmatrix} = \begin{bmatrix} \frac{E_1^2/E_2}{E_1/E_2 - \nu_1^2} & \frac{E_1\nu_1}{E_1/E_2 - \nu_1^2} & 0 \\ \frac{E_1\nu_1}{E_1/E_2 - \nu_1^2} & \frac{E_1}{E_1/E_2 - \nu_1^2} & 0 \\ 0 & 0 & \frac{E_1E_2}{E_1 + E_2 + 2E_2\nu_1} \end{bmatrix} \begin{bmatrix} \epsilon_1 \\ \epsilon_2 \\ \epsilon_{12} \end{bmatrix} \quad (3.10)$$

with the elastic modulus E_1 and E_2 accounting for confinement effects. Good correlation with experimental results was obtained, but it was recognised that experimental data to check the goodness of the shear modulus was scarce. Determination of the shear modulus in orthotropic models has been indeed controversial. Darwin and Pecknold (1977) proposed to adopt a shear modulus which would not favour any direction and that would be invariable with axes rotation. The value derived from this requirement was given by:

$$G = \frac{E_1 + E_2 - 2\nu\sqrt{E_1E_2}}{4(1 - \nu^2)} \quad (3.11)$$

Bažant (1983) suggested that if coaxiality between principal stress and strain directions was to be enforced, the shear modulus should be obtained as (figure 3.4):

$$G_{ij} = \frac{\sigma_{ii} - \sigma_{jj}}{2(\epsilon_{ii} - \epsilon_{jj})} \quad (3.12)$$

Despite this contribution Bažant (1983) critiqued the used of orthotropic models in FE programs because they are not tensorially invariant and, hence, the results depend on the choice of reference axes; he also stated that rotation of the axes of material orthotropy is inadmissible as it implies to rotate the microstructural defects. Despite these critiques, orthotropic models have been used extensively in FE modelling and practical applications show that they can provide realistic predictions.

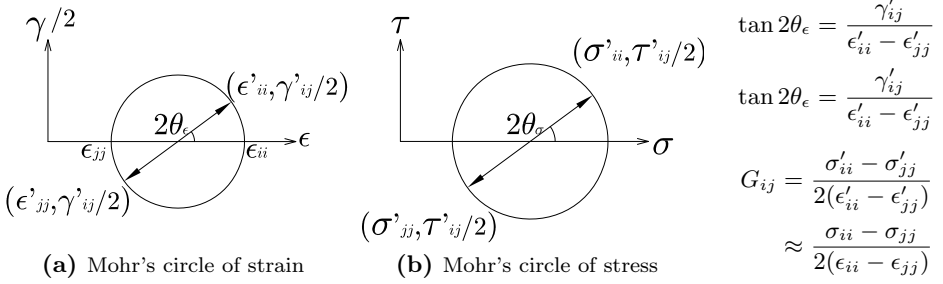


Figure 3.4: Tangent shear modulus G to enforce coaxiality between principal strain and stress directions as proposed by Bažant (1983).

Isotropic models for concrete

This approach was followed in the early FE studies for its simplicity (Ngo and Scordelis 1967), where it was also assumed that concrete response was linear-elastic. A more advanced nonlinear isotropic model was proposed later by Kotsovos and Pavlovic (1995), where the bulk modulus K and the shear modulus G vary with the hydrostatic stress σ_0 and the deviatoric stress τ_0 . Sound results were obtained by these authors.

3.3.3 Classification based on the underlying theory

Principles of the theory of elasticity and plasticity have been used to support most concrete constitutive models proposed in literature acknowledging that: concrete response in tension is essentially linear-elastic up to the peak stress and is followed by cracking, which is a nonlinear phenomenon; concrete response in compression is initially linear-elastic, but micro-cracking appearing at relatively low stress levels leads to nonlinear deformations, a portion of which are irrecoverable; under high multiaxial compressive states concrete can exhibit a ductile behaviour, which can be considered through the theory of plasticity. It must be noted that damage-based models (Grassl and Jirásek 2006) have been used to a lesser extent for concrete modelling as well, but they will not be treated in this section as they are not related with the model adopted in the thesis.

Elasticity theory

Elasticity is the property of materials to return to their original shape and size when the stress causing the deformation reduces to zero. Elastic models can be classified into two categories: (i) total stress-strain models (secant formulation) and (ii) hypoelastic or incremental models (tangent formulation) (Committee on Concrete and Masonry Structures ASCE 1982).

In total stress-strain models the stress state is path independent and deformations are completely reversible. Therefore, these models fail to capture inelastic deformations. The relationship between stress and strain is one-to-one:

$$\sigma_{ij} = F_{ij}(\epsilon_{kl}) \quad (3.13)$$

Arbitrary nonlinear functions may result in energy generation under certain loading-unloading cycles, but it can be demonstrated that if the elastic constitutive matrix is symmetric, the energy generation in a complete cycle is zero (Chen 1982). Constitutive models based on Green hyperelastic formulation avoids energy generation by assuming the existence of a strain energy-density function from which the relation between stress and strain can be derived.

In hypoelastic models deformations are only infinitesimally reversible and the stress state depends on the strain state and the stress path followed to reach that state. These models can capture inelastic deformations. The constitutive relation is not expressed in total values but in incremental form as follows:

$$\Delta\sigma_{ij} = F_{ij}(\Delta\epsilon_{kl}, \sigma_{mn}) \quad (3.14)$$

where σ_{mn} is the current stress tensor and $\Delta\sigma_{ij}$ and $\Delta\epsilon_{ij}$ are the stress and strain increments, respectively.

Elastic models can also be classified into (i) linear and (ii) nonlinear:

- The use of linear-elastic concrete models is widely extended in design practice due to its simplicity. Although the complete stress-strain curve of concrete is clearly nonlinear, concrete behaviour at relatively low stress levels in compression and up to cracking in tension is fairly linear; this explains why under certain circumstances the use of these models can be adequate. Linear-elastic models have also been adopted in FE analysis of reinforced concrete structures, especially in first studies (Ngo and Scordelis 1967). When combined with an appropriate failure criterion

they can provide reasonable strength predictions for certain problems (e.g. reinforced concrete elements whose response is mainly determined by concrete cracking).

- Nonlinear models can provide more realistic predictions. A wide spectrum of nonlinear compressive uniaxial stress-strain models can be found in literature, from the simple parabola equation (used by Hognestad (1951), Vecchio and Collins (1986), J.-w. Park et al. (2010) among others) to more refined models proposed elsewhere (Saenz 1964) (Popovics 1973). For the tension regime, although it has been a common approach to disregard the contribution of concrete in tension, several nonlinear tensile uniaxial models have been proposed as well; two types of models can be distinguished: (i) those expressed in terms of average strains (Scanlon 1971) (Vecchio and Collins 1986)(figure 3.5a) and (ii) those expressed in terms of crack widths (Hillerborg, Modeer, and Petersson 1976)(figure 3.5b) (Hordijk 1991)(figure 3.6d). Former models can lead to mesh-dependent results and, hence, are not objective (Bažant and Planas 1998); latter models are usually based on principles of fracture mechanics and permit overcoming mesh dependency problems. Examples of nonlinear biaxial and triaxial models can be found in literature as well (Liu, Nilson, and Slate 1972) (Kupfer and Gerstle 1973) (Darwin and Pecknold 1977) (Elwi and Murray 1979) (Kotsovos and Pavlovic 1995).

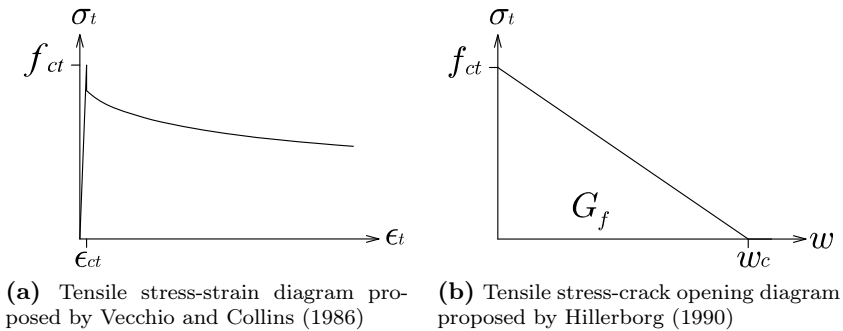


Figure 3.5: Concrete tensile models.

Plasticity theory

Experimental data shows that nonlinear deformations of concrete in compression are partly plastic and, therefore, after unloading, a portion of the total deformation is not recovered. Principles of plasticity theory can be applied to treat irreversible deformations. Two different plastic models can be distinguished: (i) perfectly plastic models, which admit changes of plastic strain under constant stress and (ii) work-hardening plastic models, which only admit changes of plastic strain with stress variation (Chen 1982).

The so called yield function $f(\sigma_{ij}) = k$ separates the domains of fully elastic and plastic deformations. Plastic deformations take place once the yield function is reached, with the stress state remaining on the yield surface in perfectly plastic models, and the increment stress vector moving outwards of the yield surface in work-hardening models. Several yield surfaces have been proposed in literature, a selection of which can be found elsewhere (Committee on Concrete and Masonry Structures ASCE 1982) (Chen 1982). The widely used Drucker-Prager surface, which will be introduced later in this chapter, is among them.

Relevance of the theory of plasticity in the field of reinforced concrete structures derives from the fact that the theory of plasticity forms the basis of limit analysis (Nielsen and Hoang 2011).

3.4 Proposed 3D constitutive model for concrete

Details of the concrete model developed in this thesis are given in this section. The proposed model describes the 3D response by using equivalent uniaxial stress-strain laws, such as those proposed in concrete design codes and which are familiar to practitioners. Only one single input variable, the uniaxial compressive strength f_{c0} , needs to be defined, allowing the engineer to focus on the analysis and/or design of the structure rather than on the definition of the parameters of the material model.

3.4.1 Crack model

A smeared crack representation was adopted. This approach is adequate for the purposes of the tool because the interest is to study the global response rather than the evolution of local cracking. This approach is simpler and facilitates modelling and analysis compared to the alternative discrete crack concept, which entails changes in the FE mesh, may introduce mesh bias and, therefore, requires a more careful modelling. The adoption of a smeared crack representation is in line with most existing FE software packages.

3.4.2 Variation of material properties with direction

An orthotropic model was adopted, permitting to decouple the three-dimensional response into three quasi-independent uniaxial directions (figure 3.6a). “Quasi-independent” means that interaction between uniaxial directions is considered somehow; in particular, the effect of confinement and transverse cracking on the uniaxial effective compressive strength of concrete is considered as detailed in section 3.4.3. It was assumed that the material axes of orthotropy are defined by the principal strain directions and rotate with them (Cope et al. 1980). The constitutive matrix $[D]$ in local orthotropic axes can be written as:

$$\begin{bmatrix} \Delta\sigma_{11} \\ \Delta\sigma_{22} \\ \Delta\sigma_{33} \\ \Delta\tau_{12} \\ \Delta\tau_{23} \\ \Delta\tau_{13} \end{bmatrix} = [D^L] \{\Delta\epsilon\} = \begin{bmatrix} E_{11} & 0 & 0 & 0 & 0 & 0 \\ 0 & E_{22} & 0 & 0 & 0 & 0 \\ 0 & 0 & E_{33} & 0 & 0 & 0 \\ 0 & 0 & 0 & G_{12} & 0 & 0 \\ 0 & 0 & 0 & 0 & G_{23} & 0 \\ 0 & 0 & 0 & 0 & 0 & G_{13} \end{bmatrix} \begin{bmatrix} \Delta\epsilon_{11} \\ \Delta\epsilon_{22} \\ \Delta\epsilon_{33} \\ \Delta\gamma_{12} \\ \Delta\gamma_{23} \\ \Delta\gamma_{13} \end{bmatrix} \quad (3.15)$$

¹In the following it is considered that $\epsilon_{11} < \epsilon_{22} < \epsilon_{33}$, with $\epsilon > 0$ in tension.

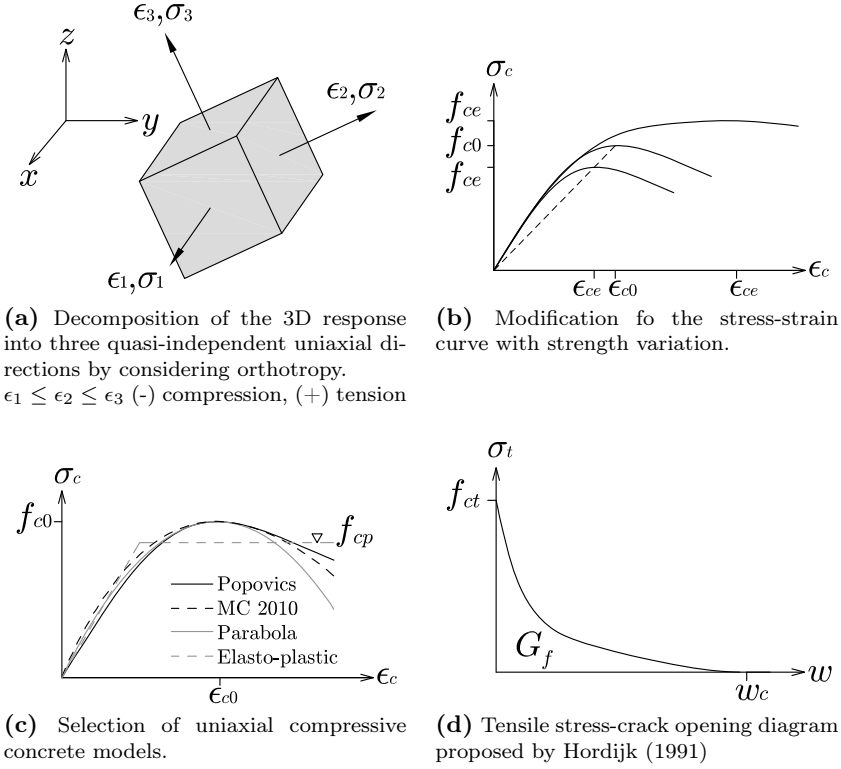


Figure 3.6: 3D characterization through uniaxial models.

where the elastic modulus E_{ii} is a function of the principal strain ϵ_{ii} and the adopted uniaxial stress-strain law. The tangent shear moduli G_{ij} are determined as detailed in the next subsection.

Tangent shear moduli G_{ij}

In general the tangent shear moduli G_{ij} are determined to enforce coaxiality between principal strain and stress directions. They are calculated according to Bažant (1983) as (figure 3.4):

$$G_{12} = \frac{\sigma_{11} - \sigma_{22}}{2(\epsilon_{11} - \epsilon_{22})} \quad G_{23} = \frac{\sigma_{22} - \sigma_{33}}{2(\epsilon_{22} - \epsilon_{33})} \quad G_{13} = \frac{\sigma_{11} - \sigma_{33}}{2(\epsilon_{11} - \epsilon_{33})} \quad (3.16)$$

For linear-elastic materials equation 3.16 gives $G_{ij} = E/2$. For nonlinear models, if the sign of the numerator is equal to the sign of the denominator (i.e. $\epsilon_{ii} > \epsilon_{jj}$ with $\sigma_{ii} \geq \sigma_{jj}$), the shear modulus will be non-negative; this condition is always achieved for elastic-perfectly plastic models. However, if the uniaxial stress-strain model includes a descending branch, it is possible to obtain negative shear modulus values once the peak stress is exceeded in one of the principal directions because larger strains do not imply larger stresses any more; indeed, in multiaxial tension, if the stress drops rapidly after cracking in one of the principal directions, obtaining a negative shear modulus is quite likely. This situation is less probable in multiaxial compression as high transverse compressive stresses imply high effective strengths; therefore, the peak stress will be rarely exceeded and, even if so, the stress drop in the principal compressive direction will not be abrupt.

A negative shear modulus does not have any physical reasoning and can only be explained by the artificial nature of the value adopted to enforce coaxiality. An alternative formulation is considered at cracked states if softening tensile models are adopted; the tangent shear modulus after cracking is obtained according to:

$$G_{ij} = G_0 \left(1 - \frac{w_{ii}}{w_c} \right) \quad (3.17)$$

where w_{ii} is the crack opening in the i direction, w_c is the crack opening at zero stress and G_0 the shear modulus at the uncracked state (taken equal to $E_c/2$). When the crack width increases the tangent shear modulus reduces, until it vanishes when the crack is fully open; this is in agreement with the physical response expected for a crack as aggregate interlocking effects diminish with crack opening. Exponential softening models may be adopted as well. Slight deviations in the principal directions can arise and the convergence process may be slowed down. However, as this formulation is only applied at cracked points, it does not seem to significantly affect global results and the convergence process.

Transformation into the global coordinate system

The constitutive matrix defined in equation 3.15 in local axes must be transformed into the global coordinate system by:

$$[D] = [T]^T [D^L] [T] \quad (3.18)$$

where $[T]$ is obtained as:

$$[T] = \begin{bmatrix} l_1^2 & m_1^2 & n_1^2 & l_1 m_1 & m_1 n_1 & l_1 n_1 \\ l_2^2 & m_2^2 & n_2^2 & l_2 m_2 & m_2 n_2 & l_2 n_2 \\ l_3^2 & m_3^2 & n_3^2 & l_3 m_3 & m_3 n_3 & l_3 n_3 \\ 2l_1 l_2 & 2m_1 m_2 & 2n_1 n_2 & m_1 l_2 + l_1 m_2 & n_1 m_2 + m_1 n_2 & n_1 l_2 + l_1 n_2 \\ 2l_2 l_3 & 2m_2 m_3 & 2n_2 n_3 & m_2 l_3 + l_2 m_3 & n_2 m_3 + m_2 n_3 & n_2 l_3 + l_2 n_3 \\ 2l_1 l_3 & 2m_1 m_3 & 2n_1 n_3 & m_1 l_3 + l_1 m_3 & n_1 m_3 + m_1 n_3 & n_1 l_3 + l_1 n_3 \end{bmatrix} \quad (3.19)$$

with l_i , m_i and n_i being the directional cosines of the principal strain directions.

Limitations of the rotating orthotropic model

The adoption of a rotating orthotropic model is justified for its simplicity, but some limitations must be acknowledged. Besides the critiques to orthotropic models made by Bažant (1983), it must be noted that the assumption of coaxiality between principal strain and stress directions is only valid when sufficient shear stress transfer can take place along the crack planes to rotate the material axes of orthotropy. This is not fulfilled in high-strength concrete elements, where cracks typically propagate through aggregates, producing smooth and flat cracks.

3.4.3 Underlying theory*An elasticity-based model*

The model is based on the theory of elasticity. Internal forces are determined assuming that strain and stress principal directions are parallel and each principal stress is directly calculated from its corresponding principal strain. Principal strain directions are obtained from the diagonalisation of the strain tensor, which is derived from the displacement vector obtained by accumulating

subsequent displacement increments obtained at each iteration step from the residual forces and using a tangent stiffness matrix.

A total stress-strain formulation is used to calculate the principal stress if the current principal strain ϵ_{ii}^t is larger in absolute terms than the maximum strain attained in that principal direction in previous converged solutions. An incremental formulation is used otherwise, where the principal stress increment $\Delta\sigma_{ii}^t$ is calculated based on the maximum absolute strain attained in previous steps in that principal direction, the principal stress σ_{ii}^n associated to this strain and the principal strain increment $\Delta\epsilon_{ii}^t$. Both formulations can be written as follows:

$$\sigma_{ii}^t = F_{ii}(\epsilon_{ii}^t) \text{ if } |\epsilon_{ii}^t| \geq \max_{n=1}^{n=t-1} |\epsilon_{ii}^n| \text{ (loading)} \quad (3.20)$$

$$\begin{aligned} \sigma_{ii}^t = \sigma_{ii}^{t-1} + \Delta\sigma_{ii}^t = \sigma_{ii}^{t-1} + f_{ii}(\Delta\epsilon_{ii}^t, \max_{n=1}^{n=t-1} |\epsilon_{ii}^n|, \sigma_{ii}^n) \\ \text{if } |\epsilon_{ii}^t| < \max_{n=1}^{n=t-1} |\epsilon_{ii}^n| \text{ (unloading)} \end{aligned} \quad (3.21)$$

It should be noted that even in monotonic analysis unloading is possible due to stress redistribution.

Interaction between uniaxial directions

Interaction between the three principal directions was accounted for by considering the effect of transverse strains/stresses on the effective compressive strength of concrete f_{ce} . Compression-compression and compression-tension interaction were considered separately.

- Compression-compression interaction

A Drucker-Prager yield surface was adopted to calculate the effective compressive strength f_{ce} of confined concrete. This surface is given by:

$$F = \sqrt{J_2} - \theta I_1 - k \quad (3.22)$$

where θ and k are parameters to be determined from experimental testing, J_2 is the second deviatoric stress invariant and I_1 is the first stress invariant, which are calculated as:

$$I_1 = \sigma_1 + \sigma_2 + \sigma_3 \quad (3.23)$$

$$J_2 = \frac{1}{6} \left[(\sigma_1 - \sigma_2)^2 + (\sigma_2 - \sigma_3)^2 + (\sigma_1 - \sigma_3)^2 \right] \quad (3.24)$$

Based on multiaxial experimental data collected and presented in Hannant (1974), the following parameters were adopted:

$$\theta = 0.23 \quad k = 0.35 f_{c0} \quad (3.25)$$

At the beginning of each load/displacement step, and given the current transverse principal stresses σ_2 and σ_3 , the effective compressive strength f_{ce} for each integration point is derived from equation 3.22 as the value σ_1 which leaves the stress coordinates on the yield surface.

- Tension-compression interaction

Presence of major tensile strains normal to the compressive direction reduces the strength and the stiffness of concrete in compression compared to those values obtained in a standard uniaxial cylinder test. The reduction factor adopted in FESCA 3D is based on the Modified Compression Field Theory (MCFT) (Vecchio and Collins 1986), where the following relation was proposed after testing reinforced concrete panels:

$$\frac{f_{ce}}{f_{c0}} = \frac{1}{0.8 + 170\epsilon_t} \leq 1 \quad (3.26)$$

where ϵ_t is the tensile strain transverse to the compressive direction.

The MCFT was later extended to 3D by Vecchio and Selby (1991), who proposed to take the greater tensile strain of the two transverse strains into equation 3.26; this implies neglecting the effect of the lowest tensile strain. In the model proposed in this thesis it was preferred to take ϵ_t as the sum of the two transverse tensile strains ϵ_2, ϵ_3 (or just ϵ_3 if $\epsilon_2 < 0$) for the sake of safety.

It should be noted that this strength reduction should not be applied in general when the tensile strength of concrete is neglected in the analysis of lightly reinforced specimens. In these cases, calculated FE tensile stresses at unreinforced areas are not realistic and concrete strength reduction may be excessively overestimated.

- Effect on the strain at peak stress

Not only the strength, but also the strain at peak stress is influenced by the presence of transverse stresses (see figure 3.3). When concrete strength is reduced due to transverse tensile strains, this effect is considered by assuming that the relationship between peak stress and strain at peak remains constant (figure 3.6b) and the strain at the effective compressive strength f_{ce} is calculated as:

$$\epsilon_{ce} = \frac{f_{ce}}{f_{c0}} \epsilon_{c0} \quad (3.27)$$

When concrete strength increases due to confinement, the model proposed by Mander, Priestley, and R. Park (1988) is considered (figure 3.6b):

$$\epsilon_{ce} = \epsilon_{c0} \left(1 + 5 \left(\frac{f_{ce}}{f_{c0}} \right) \right) \quad (3.28)$$

A selection of uniaxial stress-strain models

- Compressive models

A selection of some uniaxial models which can be potentially considered is plotted in figure 3.6c and is described next.

Adoption of an elastic-perfectly plastic model can be appropriate when the structural capacity is limited by steel yielding and large compressive concrete strains are not to be expected in the pre-peak regime. The suggestion made

by Muttoni, Schwartz, and Thürlimann (1997) of reducing the uniaxial compressive strength f_{c0} to an effective plastic value f_{cp} is considered in FESCA 3D when adopting this model; this reduction accounts for the increase in brittleness with concrete strength:

$$\begin{aligned} f_{cp} &= f_{c0} \text{ if } f_{c0} \leq 20 \text{ MPa} \\ f_{cp} &= 2.7 f_{c0}^{2/3} \text{ if } f_{c0} > 20 \text{ MPa} \end{aligned} \quad (3.29)$$

Further reductions should be applied for cases in which strains of different orders of magnitude may take place in the ultimate limit state.

The simplest nonlinear model is the Hognestad parabola, where the stress is obtained as:

$$\sigma_{ii} = f_{ce} \left(2 \frac{\epsilon_{ii}}{\epsilon_{c1}} - \left(\frac{\epsilon_{ii}}{\epsilon_{c1}} \right)^2 \right) \quad (3.30)$$

A more refined model is that proposed by Popovics (1973), which presents a more gradual descending branch:

$$\sigma_{ii} = f_{ce} \frac{\epsilon_{ii}}{\epsilon_{c1}} \frac{n}{n - 1 \left(\epsilon_{ii}/\epsilon_{c1} \right)^n} \quad (3.31)$$

with

$$n = 0.4 \times 10^{-3} f_{c0} 145 + 1 \text{ with } f_{c0} \text{ in MPa} \quad (3.32)$$

- Tensile models

FESCA 3D offers the option of neglecting the tensile strength of concrete, as it is a common assumption in practice design. This approach leads to clear 3D stress field models and provides a clear understanding of the resisting mechanism, which can be appealing for initial analyses and for educational purposes. However, neglecting the tensile strength of concrete can lead to predicted strengths that are significantly below the actual maximum loads when tensile stresses between cracks are significant or for structural elements with large volumes of unreinforced concrete in tension. In these cases it is necessary to include the tensile strength of concrete if a more accurate prediction is to be obtained.

If the tensile strength is to be considered, any tensile stress-strain law can be defined.

The softening tensile stress-strain model proposed in the MCFT (Vecchio and Collins 1986) (figure 3.5a) has been used by other authors for 2D analysis. This model was derived from reinforced concrete panels and, therefore, it is not appropriate when there are large volumes of unreinforced concrete that can be potentially in tension (as it is the case in 3D D-regions). FE results obtained with FESCA 3D are in agreement with this statement (Meléndez, Miguel, and Pallarés 2016). Moreover, results obtained with this model may exhibit mesh dependency as it is expressed in terms of strains.

Models based on fracture mechanics proved to be more adequate to model the tensile response of concrete. In particular, the softening tensile stress-crack opening model proposed by Hordijk (1991) was adopted for some of the analyses presented in this document and provided sound results; in this model the tensile stress after cracking is obtained from (figure 3.6d):

$$\frac{\sigma_{ii}}{f_{ct}} = \left(1 + \left(c_1 + \frac{w_{ii}}{w_c}\right)^3\right) e^{-c_2 \frac{w_{ii}}{w_c}} - \frac{w_{ii}}{w_c} (1 + c_1^3) e^{-c_2} \quad (3.33)$$

where w_{ii} is the crack opening and w_c is the crack opening at zero stress, which is determined by the fracture energy G_f . The best fit to experimental results was obtained for $c_1 = 3$ and $c_2 = 6.93$. The fracture energy is a material property, which can be estimated from the concrete compressive strength. The formula proposed in MC 2010 (Fédération Internationale du Béton 2013) is given by:

$$G_f = 73 f_{c0}^{0.18} \text{ with } f_{c0} \text{ in MPa, } G_f \text{ in N/m} \quad (3.34)$$

Equivalent crack band width for tensile stress-crack opening models

The equivalent crack band width concept (Bažant and Oh 1983) was used to transform crack openings w_{ii} into strain values ϵ_{ii} . This width is usually obtained as a function of the FE size. The proposal made in FESCA 3D is to determine the equivalent crack band width of each Gauss integration point as a function of the volume associated to that integration point, which can be calculated as:

$$V_{e,j} = |J_e| w_j \quad (3.35)$$

where $|J_e|$ is the determinant of the Jacobian matrix of the FE and w_j the weight of the integration point. Then, the crack band width is taken equal to the diagonal of a cube whose volume is $V_{e,j}$ (figure 3.7):

$$l_{eq,j} = \sqrt[3]{3|J_e| w_j} \quad (3.36)$$

FEs with large aspect ratios may exhibit some mesh sensitivity caused by distorted band widths. Therefore, FEs as square as possible are preferred.

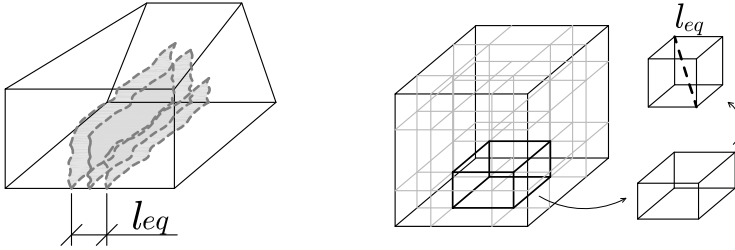


Figure 3.7: Determination of the equivalent length of an integration point.

Determination of plastic deformations

Plastic deformations were accounted for in a simplified manner by assuming that a constant portion of the maximum strain attained at an integration point is irrecoverable when unloading. The defined plastic factor α_p , i.e. the portion of the total deformation that is not recovered when the stress is reduced to zero, determines the elastic slope of the unloading-reloading branch (figure 3.8). This is a simplified approach which permits the assessment of loading and unloading at specific integration points due to stress redistribution. This approach was considered adequate for the current purposes of the tool as in general plastic deformations will not be relevant in the determination of the structural strength, which is the main objective of the tool. The adoption of different plastic factors α_p did not seem to have a significant effect on the final results.

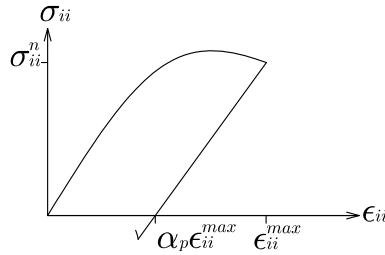


Figure 3.8: Plastic deformations.

3.5 Conclusions

This chapter described briefly the behaviour of concrete and different approaches for its modelling. Then, the model adopted in FESCA 3D was presented. Observing the existing problems related with obtaining reliable multiaxial test data and the complexity of current models, it was preferred to adopt some simplifications to at least facilitate the definition of the material model and the interpretation of the output results. The number of input parameters was reduced to the minimum; indeed, the compressive strength f_{c0} is the only mandatory input parameter as the rest of material parameters can be derived from this value. It could be thought that these simplifications may derive in a significant loss of accuracy of the FE results. However, as it is seen in next chapters, if relatively-refined uniaxial models are considered, the obtained predictions can be rather realistic.

Without neglecting the importance of concrete constitutive modelling, other factors which in general attract less attention such as the imposed boundary conditions can be more decisive to obtain sound results than the concrete constitutive model itself, especially in D-regions. This will be shown later in Chapter 6, where the effect of considering the tensile strength of concrete, or not, on the global results is compared with the influence of adopting different boundary conditions.

Square FEs and regular meshes are in general preferred, especially when using tensile models based on fracture mechanics. The geometry of the reinforcement, the applied loads and the support elements can interfere in the adoption of such FE meshes; an embedded reinforcement model (Chapter 4) and special load and support elements (Chapter 5) were developed and integrated in FESCA 3D to overcome these restrictions.

Chapter 4

Reinforcement modelling

In order to achieve the advantages of a regular mesh, and at the same time model complicated reinforcing details, an embedded representation of reinforcement appears to be the desirable approach.

—Elwi and Hrudey 1989

4.1 Introduction

Reinforcement influences the response of reinforced concrete structures not only because it is the main mechanism to sustain tensile forces, but also for its influence on the stress flow inside the concrete element. This is of special relevance in D-regions because the internal stress field is complex and easily influenced by the reinforcement layout. In order to obtain a sound response prediction it is important that the adopted reinforcement model reflects its actual geometry and characteristics.

Despite reinforcement relevance, concrete is still the main component in reinforced concrete structures and hence determines the principal aspects of the FE model, including the geometry of the FE mesh. The main issue in reinforcement modelling is not material characterisation, which does not entail much difficulties, but the way of introducing the steel rebars into the FE model without causing much distortion to it. One simple approach is to consider reinforced concrete as a composite material. However, it is more appropriate for general purposes to model reinforcing bars separately from concrete, which permits the treatment of non-uniform reinforcement distributions. Two approaches, the discrete and the embedded representation have been proposed in

literature; the main advantage of the embedded model over the discrete one is that the geometries of the steel bars and the concrete FE mesh are completely independent.

This chapter briefly describes general aspects of reinforcement modelling, including the bond-slip interaction with the surrounding concrete. The reinforcement model adopted in FESCA 3D is then presented; the embedded approach was followed in order to facilitate the introduction of any rebar geometry. The procedure to generate automatically the embedded rebar FEs from the intersections with the concrete mesh is described. Derivation of the FE formulation for both the perfect-bond and the bond-slip models is discussed. Two examples of applications at the end of the chapter show the capability of the implemented reinforcement model to deal with complex reinforcement geometries.

4.2 Behaviour of steel

A typical uniaxial stress-strain diagram of a hot-rolled steel rebar, valid for both tension and compression, is illustrated in figure 4.1. The curve is formed by an initial linear-elastic region up to the yielding stress f_{sy} , which is followed by a plastic plateau where strain increases while stress remains constant. The stress increases again for larger strains in the hardening region, until the maximum stress f_{su} is reached and the stress reduces.

The effect of transverse strains and stresses on the axial response of a steel rebar is negligible and is in general dismissed; therefore, there is not need for a multiaxial material characterisation as it was the case for concrete.

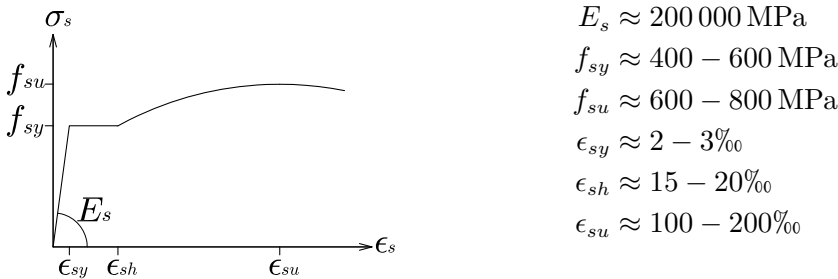


Figure 4.1: Stress-strain diagram for steel in tension and compression.

4.3 Constitutive models for steel

As it can be inferred from the behaviour described in the previous section, steel material modelling does not entail many difficulties: adoption of a uniaxial constitutive relationship is sufficient and the same stress-strain relation can be adopted for tension and compression.

It is a common approach to model steel as an elastic-perfectly plastic material, dismissing the strain-hardening branch (figure 4.2). Only two parameters are needed: the elastic modulus E_s and the yielding stress f_{sy} . This assumption is conservative and appropriate for most cases as strain-hardening occurs at relatively large strains which are rarely reached in practice. Despite this, when needed, strain hardening can be accounted for by adopting a positive slope E_h after yielding or a more refined model fitting the actual stress-strain curve.

The slope of the unloading-reloading branch is in general taken equal to the initial elastic modulus E_s .

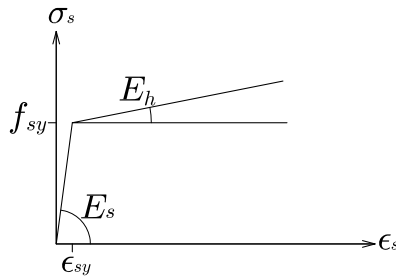


Figure 4.2: Elastic-perfectly plastic and elastic-hardening models for steel.

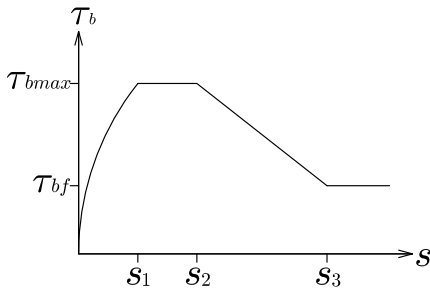
4.4 Bond-slip interaction

Bond is the mechanism of stress transfer between concrete and steel. This interaction is defined by relating bond stresses and slip displacements at the concrete-steel interface in the rebar direction. This mechanism permits the development of tensile stress in concrete between cracks and can be critical at anchorage zones if the bond strength is exceeded, leading to premature local failures.

The bond-slip relationship is influenced by the transverse stress state: compressive stress states increase the bond strength and transverse cracking weakens

it. Different constitutive models have been proposed in literature. The one proposed in MC 2010 (Fédération Internationale du Béton 2013) is given here for reference (figure 4.3):

$$\tau(s) = \begin{cases} \tau_{bmax} (s/s_1)^{0.4} & 0 \leq s \leq s_1 \\ \tau_{bmax} & s_1 \leq s \leq s_2 \\ \tau_{bmax} - (\tau_{bmax} - \tau_{bf}) \frac{(s-s_2)}{(s_3-s_2)} (s - s_2) & s_2 \leq s \leq s_3 \\ \tau_{bf} & s > s_3 \end{cases} \quad (4.1)$$



Values for good bond conditions

$$\tau_{bmax} = 2.5\sqrt{f_{c0}}$$

$$\tau_{bf} = 0.4\tau_{bmax}$$

$$s_1 = 1.0mm$$

$$s_2 = 2.0mm$$

$$s_3 = \text{clear distance between ribs}$$

$$\alpha = 0.4$$

Figure 4.3: Bond stress-slip displacement model (MC 2010 (Fédération Internationale du Béton 2013)).

4.5 Reinforcement representation

Three different approaches have been proposed in literature for reinforcement modelling: (i) the distributed or smeared representation, (ii) the discrete representation and (iii) the embedded representation.

Assuming perfect bond between concrete and steel is in general sufficient for most practical cases. However, if required, the discrete and the embedded representation can be refined further to introduce this interaction as discussed at the end of this section.

4.5.1 Distributed or smeared representation

Reinforced concrete is treated as a composite material; therefore, no additional FEs are introduced to include the reinforcement. A compound constitutive matrix needs to be determined, which will include the contribution of concrete and steel. Different concrete constitutive matrices were presented in Chapter 3. The steel counterpart can be calculated as:

$$[D_s] = \sum_{i=1}^n \int_{l_i} \langle T_{s,i}^\epsilon \rangle^T \rho_i E_s \langle T_{s,i}^\epsilon \rangle \quad (4.2)$$

where n is the number of rebars, ρ_i is the reinforcing ratio and $\langle T_{s,i}^\epsilon \rangle$ is the strain transformation vector from the global system (xyz) to the local coordinate system defined by the rebar axis and is given by:

$$\langle T_{s,i}^\epsilon \rangle = [l_{1,i}^2 \quad m_{1,i}^2 \quad n_{1,i}^2 \quad l_{1,i}m_{1,i} \quad m_{1,i}n_{1,i} \quad l_{1,i}n_{1,i}] \quad (4.3)$$

where $l_{1,i}$, $m_{1,i}$, $n_{1,i}$ are the directional cosines of the rebar axis.

This approach is simple and avoids the modification of the concrete FE mesh. However, it is only appropriate when reinforcing bars are uniformly distributed and treatment of more general cases where reinforcement is concentrated at specific areas of the element is problematic.

4.5.2 Discrete representation

Steel rebars are modelled by independent FEs whose nodes are coincident with those of the concrete FE mesh. Therefore, unless bond-slip interaction is considered, the number of nodes does not need to be increased. The most common and simple approach is to use unidimensional elements to represent the rebars (Rashid 1968). The stiffness matrix of a two-node bar element can be obtained as:

$$[k_s^e] = [T_s^f]^T [k_s^{e,L}] [T_s^f] = [T_s^f]^T \frac{E_s A_s}{l_s} \begin{bmatrix} 1 & -1 \\ -1 & 1 \end{bmatrix} [T_s^f] \quad (4.4)$$

where A_s and l_s are the area and the length of the element, respectively, and T_s^f is the force transformation matrix from the local rebar axis to the global coordinate system (x, y, z), which is given by:

$$[T_s^f] = \begin{bmatrix} l_{s1} & m_{s1} & n_{s1} & 0 & 0 & 0 \\ 0 & 0 & 0 & l_{s1} & m_{s1} & n_{s1} \end{bmatrix} \quad (4.5)$$

This stiffness matrix is then assembled into the global stiffness system at the corresponding concrete degrees of freedom. Instead of unidimensional elements, two- or three-dimensional FEs can be adopted as well if multiaxial effects on the rebar are to be considered (Ngo and Scordelis 1967). However, as mentioned previously, this is in general not necessary.

The major disadvantage of discrete models is that steel nodes must coincide with those of concrete. This implies that the concrete and the steel meshes are not independent. Therefore, either the reinforcement geometry must be adapted to the concrete mesh, or vice versa. For structural elements with a large number of rebars and/or complex geometries this disadvantage can become a real limitation for obtaining a regular and not excessively fine FE mesh.

4.5.3 *Embedded representation*

This approach overcomes the geometric constraints imposed by the discrete representation. Reinforcement is modelled by independent FEs as well, but concrete and steel nodes do not need to coincide. Embedded models were first proposed by Phillips and Zienkiewicz (1976); rebars had to be defined along one of the local coordinate axes of the concrete FE, limiting hence the flexibility of the model. The model proposed later by Elwi and Hruday (1989) was valid for arbitrary two-dimensional curved rebars, regardless of the geometry of the concrete FE.

With the embedded approach rebars can be defined in any position and orientation inside the concrete mesh. Every rebar FE is associated to a concrete FE in which it is embedded, which is known as its parent element. Similarly to the discrete representation, a stiffness matrix needs to be calculated for every rebar FE and then assembled into the global system accordingly. More details of the embedded representation are given in section 4.6 when describing the reinforcement model adopted for this work.

4.5.4 *Bond-slip representation*

Assuming perfect bond between concrete and reinforcement implies that steel strains coincide with those of concrete and, hence, they can be directly obtained from the nodal displacements of the concrete FEs. If bond-slip is to be considered, new nodes need to be generated along the rebar to account for the relative displacement between concrete and steel.

Discrete and embedded models can be adapted to include bond-slip interaction by introducing linkage or interface elements between the concrete nodes and the rebar nodes. The response of these additional elements is determined by the adopted bond-slip model (section 4.4). Linkage elements consisting of two orthogonal springs with no physical dimensions were used by Ngo and Scordelis (1967). The stiffness in the axial direction of the rebar was calculated from pull-out tests; in the transverse direction a relatively large value was arbitrarily assigned assuming an almost rigid connection. Other authors proposed later the use of interface elements instead of discrete elements to consider slip along the entire rebar and not just at the nodes (Groot, Kusters, and Monnier 1981).

An interesting, alternative bond-slip representation was proposed by Hartl and Beer (2000). Their approach is based on a supplementary interface model which accounts for slip at the material level without adding extra degrees of freedom to the global system.

4.6 Proposed reinforcement model

The reinforcement model integrated in FESCA 3D is based on the embedded approach described above. This approach is especially appropriate when a large number of rebars or complex reinforcement geometries are to be expected. Rebars can be defined in any position and orientation without affecting the concrete FE mesh. Moreover, it permits the consideration of slip between steel and concrete, which can be needed in certain analysis cases. Details of the adopted model, included the procedure followed for the generation of the rebar FEs from the intersections with the concrete mesh, are provided in this section.

4.6.1 FE formulation for perfect-bond and bond-slip

Perfect bond

If perfect bond between steel and concrete is assumed, the FE rebar strains can be directly determined from the nodal displacements of the concrete parent element because coincident steel and concrete coordinates experience the same displacement and, hence, strain. Considering this, the stiffness matrix of an embedded rebar FE can be obtained as follows:

$$[k_s^e] = \int_{V^e} [B^p]^T [D] [B^p] dV = A_s \int_{l^e} [B^p]^T [D] [B^p] dl \quad (4.6)$$

where A_s is the cross sectional area of the rebar, l_e is the length of the rebar FE and matrix $[B^p]$ relates the nodal displacements of the concrete parent element with the rebar strain state. In the local system defined by the rebar direction, this strain-displacement matrix $[B^p]$ can be substituted by a strain-displacement vector $\langle B_s^p \rangle$ relating nodal displacements of the concrete parent element with the rebar axial strain. The rebar strain-displacement vector $\langle B_s^p \rangle$ can be derived from a matrix transformation as follows:

$$\langle B_s^p \rangle = \langle T_s^c \rangle [B^p] \quad (4.7)$$

where $\langle T_s^c \rangle$ was given in equation 4.3. For curved rebars the variation of the axial direction needs to be considered when obtaining this transformation vector.

Equation 4.6 can now be rewritten as:

$$[k_s^e] = A_s \int_{l^e} \langle B_s^p \rangle^T E_s \langle B_s^p \rangle dl \quad (4.8)$$

The FE internal nodal force vector can be obtained similarly as:

$$\{f_s^e\} = A_s \int_{l^e} \langle B_s^p \rangle^T \sigma_s dl \quad (4.9)$$

Integration of equations 4.8 and 4.9 is performed numerically at the Gauss integration points of the bar. Inverse mapping of the rebar integration points to the natural coordinates of the parent element is needed first. The interpolation capacity of the bar is limited by the concrete parent element. For example, for a twenty-node hexahedron, which has a quasi-quadratic interpolation capacity, it is reasonable to use two- or three-node bar elements, but not higher-order elements. Two- and three-node bar elements were implemented in the model (figure 4.4).

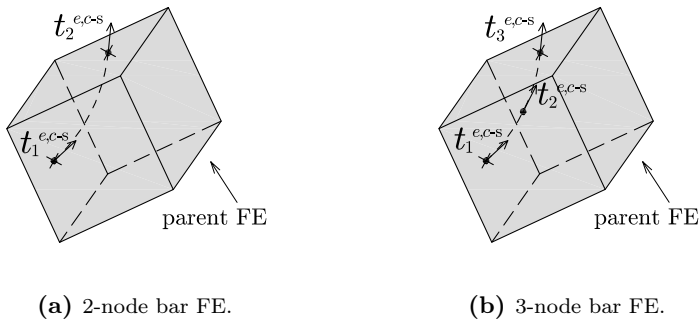


Figure 4.4: Embedded steel FE model.

Bond slip

The stiffness matrix of an embedded, slipping FE can be obtained by applying the incremental form of the principle of virtual work:

$$\Delta\delta W_{int} = \int_{V_s} \delta\epsilon_s \sigma_s dV + \int_{S_s} \delta r_{c-s} \tau_b dS \tag{4.10}$$

where σ_s and ϵ_s are the rebar axial stress and strain, respectively, and τ_b and r_{c-s} are the bond stress and the relative displacement between concrete and steel, respectively. The rebar axial strain (and hence the rebar stress) and the slip displacement (and hence the bond stress) are determined as follows.

If bond-slip is to be considered, additional nodes along the rebar are needed to account for the relative displacement between both materials (figure 4.5). Two different displacements must be distinguished: those of concrete $\{r_c\}$ and those of steel $\{r_s\}$. Concrete displacements can be directly obtained from the nodal displacements of the parent FE, as in the perfect-bond model:

$$\{r_c\} = [N^p] \{r_c^e\} \tag{4.11}$$

where $[N^p]$ is the shape function matrix of the parent FE.

Steel displacements $\{r_s\}$ can be obtained after calculating the relative displacement between concrete and steel $\{r_{c-s}\}$. In general only the relative displacement in the rebar axial direction, i.e. the slip, is of interest and one

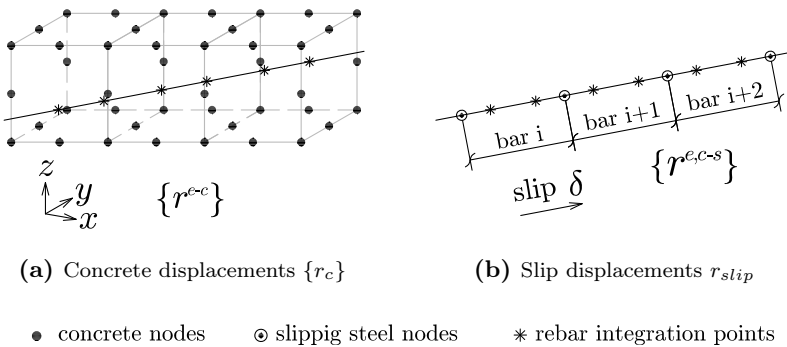


Figure 4.5: Slipping rebar model.

degree of freedom per node is sufficient. Slip displacements can be determined as:

$$r_{slip} = \langle N_s^b \rangle \{r_{c-s}^e\} \quad (4.12)$$

where $\langle N_s^b \rangle$ is a vector containing the shape functions of the bar element. Each displacement in $\{r_{c-s}^e\}$ must be expressed in the local coordinate system defined by the tangent direction to the curve at the node.

Considering the previous explanation, the axial strain at a certain rebar section can then be obtained by summing the components due to concrete ϵ_c and due to slip ϵ_{c-s} as:

$$\epsilon_s^e = \epsilon_c + \epsilon_{c-s} = \langle B_s^p \rangle \{r_c^e\} + \langle B_s^b \rangle \{r_{c-s}^e\} \quad (4.13)$$

where

$$\langle B_s^b \rangle = \frac{\partial \langle N_s^b \rangle}{\partial \xi} \frac{\partial \xi}{\partial x} \quad (4.14)$$

with ξ being the natural coordinate of the bar element.

Once steel strains and slip displacements are expressed as a function of nodal displacements equation 4.10 can be rewritten as follows:

$$\begin{aligned} \Delta \delta W_{int} &= A_s \int_{l^e} \delta \epsilon_s \sigma_s dl + O_s \int_{l^e} \delta r_{slip} \tau_b dl = \\ &= A_s \int_{l^e} (\delta \epsilon_c + \delta \epsilon_{c-s}) \sigma_s dl + O_s \int_{l^e} \delta r_{slip} \tau_b dl = \\ &= A_s \int_{l^e} \left(\{\delta r_c^e\}^T \langle B_s^p \rangle^T + \{r_{c-s}^e\}^T \langle B_s^b \rangle^T \right) \sigma_s dl + \\ &+ O_s \int_{l^e} \{\delta r_{c-s}^e\}^T \langle N_s^b \rangle^T \tau_b dl = \\ &= A_s \int_{l^e} \left(\{\delta r_c^e\}^T \langle B_s^p \rangle^T \right) E_s (\langle B_s^p \rangle \{\delta r_c^e\} + \langle B_s^b \rangle \{r_{c-s}^e\}) dl + \\ &+ O_s \int_{l^e} \{\delta r_{c-s}^e\}^T \langle N_s^b \rangle^T E_{slip} \langle N_s^b \rangle \{r_{c-s}^e\} dl \end{aligned} \quad (4.15)$$

where O_s is the rebar perimeter and E_{slip} is the tangential modulus of the bond stress-slip displacement relationship.

The total rebar displacement is split into two components in equation 4.15: that due to the concrete $\{r_c^e\}$ and that due to the relative displacement between concrete and steel $\{r_{c-s}^e\}$. Both vectors can be merged into one and equation 4.15 can be written in a more compact manner as:

$$\begin{aligned} \Delta\delta W_{int} = & A_s \int_{l^e} \begin{bmatrix} \{\delta r_c^e\} \\ \{\delta r_{c-s}^e\} \end{bmatrix}^T [\langle B_s^p \rangle \langle B_s^b \rangle]^T E_s [\langle B_s^p \rangle \langle B_s^b \rangle] \begin{bmatrix} \{r_c^e\} \\ \{r_{c-s}^e\} \end{bmatrix} dl + \\ & + O_s \int_{l^e} \{\delta r_{c-s}^e\}^T \langle N_s^b \rangle^T E_{slip} \langle N_s^b \rangle \{r_{c-s}^e\} dl \end{aligned} \quad (4.16)$$

From this equation it can be seen that the stiffness matrix of an embedded, slipping rebar can be obtained by assembling two matrices as follows:

$$\begin{aligned} [k_s^e] = & \left[A_s \int_{l^e} [\langle B_s^p \rangle \langle B_s^b \rangle]^T E_s [\langle B_s^p \rangle \quad \langle B_s^b \rangle] dl \right] + \\ & + \left[\begin{array}{cc} 0 & 0 \\ 0 & O_s \int_{l^e} \langle N_s^b \rangle^T E_{slip} \langle N_s^b \rangle dl \end{array} \right] \end{aligned} \quad (4.17)$$

The first term considers the rebar stiffness and the second the stiffness due to bond interaction.

The size of $[k_s^e]$ depends on the FE. For a three-node bar embedded in a twenty-node hexahedron the size of $[k_s^e]$ is 63×63 .

Rebar FE internal nodal forces $\{f_{int}^e\}$ can also be obtained by superposition of forces due to the axial stress and due to bond:

$$\{f_{int}^e\} = \left[A_s \int_{l^e} [\langle B_s^p \rangle \quad \langle B_s^b \rangle]^T \sigma_s dl \right] + \left[\begin{array}{c} 0 \\ O_s \int_{l^e} \langle N_s^{eb} \rangle^T \tau_b dl \end{array} \right] \quad (4.18)$$

4.6.2 Input data

Adopting an embedded approach allows for great flexibility in introducing complex reinforcement geometries in any position and orientation. In order to fully benefit from these advantages it is important to facilitate the definition of the reinforcement geometry by reducing the amount of required input data.

In FESCA 3D the user needs to define, for every rebar: (i) its diameter, (ii) the spatial coordinates of some relevant points (discussed below) and (iii) the stress-strain relationship. If slip is to be considered, the bond stress-slip model and the anchorage conditions at the end of the rebar (fixed or not fixed) must also be defined.

The rebar geometry is introduced as follows (figure 4.6): for straight bars, it is sufficient to define the coordinates of the end points (figure 4.6a); non-straight rebars can be introduced by entering a set of coordinates following the rebar geometry (figure 4.6b); for typical bent rebars, the user can directly enter the bending radius R^r and the coordinates of some master points (figure 4.6c). A function was implemented that automatically generates additional point coordinates at curved sections (figure 4.6d). This latter approach is not only a very simple way for introducing complex rebar geometries, but also permits a more accurate representation as it accounts for the variation of the rebar direction throughout the whole curve.

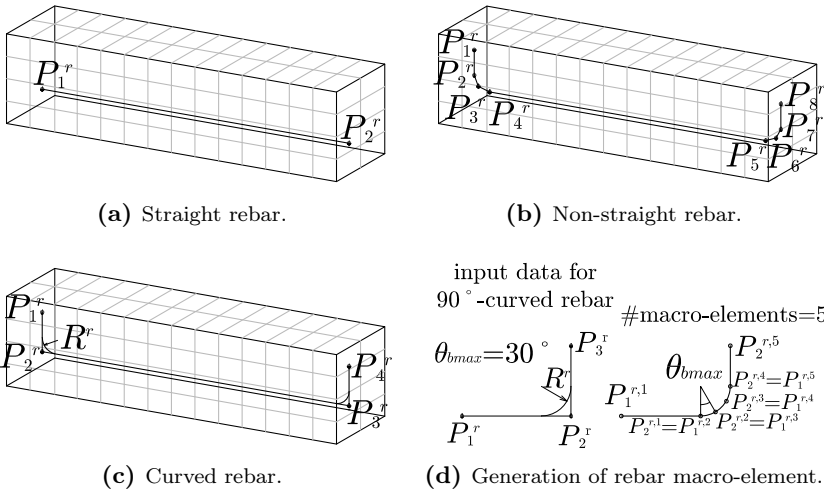


Figure 4.6: Input data for rebar geometry definition.

For closed rebars the first and last input rebar points must be coincident; this is important if slip between concrete and steel is to be considered because the first and last rebar FEs need to be connected.

The steel constitutive model is specified by a pair set of stress-strain points. Adopting an elastic-perfectly plastic model is in general sufficient for most practical cases. Unless defined otherwise, the elastic modulus for unloading and reloading is taken equal to the initial elastic modulus. Diverse models can be defined if the material properties do not coincide for all rebars.

Similarly, if slip is to be taken into account, the bond stress-slip displacement relationship is defined by a pair set of bond stress-displacement points.

4.6.3 Pre-processing of input geometric data

Input geometric data is pre-processed to facilitate the generation of rebar FEs in the next step. Each rebar is divided into one or more macro-elements which will be treated separately when finding the intersections with the concrete mesh. If no bending radius R^r is specified, the number of rebar macro-elements coincide with the number of straight segments delimited by the input points (for example, one and seven rebar macro-element in figures 4.6a and 4.6b, respectively). If a bending radius R^r is defined, curved segments are automatically generated between non-collinear stretches at bending sections (figure 4.6d). The user can define the maximum admissible rotating angle θ_{bmax} between adjacent macro-elements, which affects the refinement of the model ($\theta_{bmax} = 30^\circ$ was adopted in figure 4.6d).

4.6.4 Generation of rebar FEs

Rebar FEs are generated from the intersections between rebar macro-elements and concrete FEs. These intersections are obtained as follows.

Given two points $P_1^{r,m}$, $P_2^{r,m}$ defining the extremes of a macro-element m part of rebar r , four situations are possible (figure 4.7): (i) the segment goes through the volume (enters and exits) (figure 4.7a); (ii) the segment intersects with the volume only at one face, which implies that one end is inside the volume (figure 4.7b); (iii) the segment is fully embedded in the volume (figure 4.7c); (iv) the segment is external to the volume (figure 4.7d). A function was implemented to identify these situations and to find the intersecting coordinates if so. The procedure is based on the use of the Plücker coordinates as described below.

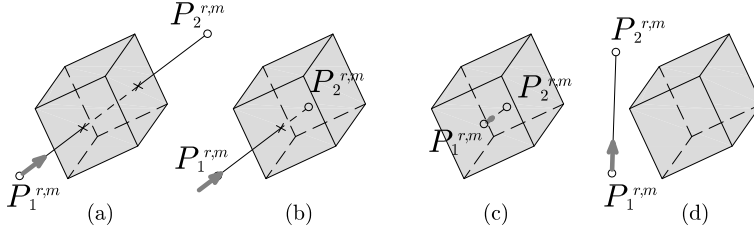


Figure 4.7: Relative position of rebar macro-element and concrete FE: (a) Segment enters and exits FE, (b) Segment enters but does not exit FE, (c) Segment embedded in FE, (d) Segment is external to FE.

Relative position of rebar macro-element and FE faces

A directed line r from A to B can be defined in the Plücker coordinate system by a vector of six homogeneous coordinates that are obtained as:

$$\{p_r\} = [\{v_{AB}\}, \{v_{OB}\} \times \{v_{AB}\}] \quad (4.19)$$

The side operator is a useful function in this coordinate system which permits to relate two directed lines in 3D space and is determined as follows:

$$\text{side}(r, s) = p_r(1)p_s(4) + p_r(2)p_s(5) + p_r(3)p_s(6) + p_r(4)p_s(1) + p_r(5)p_s(2) + p_r(6)p_s(3) \quad (4.20)$$

If $\text{side}(r, s) > 0$, the directed line r rotates counter-clockwise around s ; if $\text{side}(r, s) < 0$, the directed line r rotates clockwise around s ; and if $\text{side}(r, s) = 0$, line r intersects or is parallel to s .

This side operator can be used to study the relative position between the directed line defined by a rebar macro-element and the faces of an FE as described next. First, the directed lines defining the edges of a certain face (A, B, C, D) need to be expressed in the Plücker coordinate system; it is important that the directed lines defining the face edges rotate in the same direction around the polygon (counter-clockwise or clockwise).

$$\begin{aligned} \{p_{e_1}\} &= [\{v_{AB}\}, \{v_{OB}\} \times \{v_{AB}\}] \\ \{p_{e_2}\} &= [\{v_{BC}\}, \{v_{OC}\} \times \{v_{BC}\}] \\ \{p_{e_3}\} &= [\{v_{CD}\}, \{v_{OD}\} \times \{v_{CD}\}] \\ \{p_{e_4}\} &= [\{v_{DA}\}, \{v_{OA}\} \times \{v_{DA}\}] \end{aligned} \quad (4.21)$$

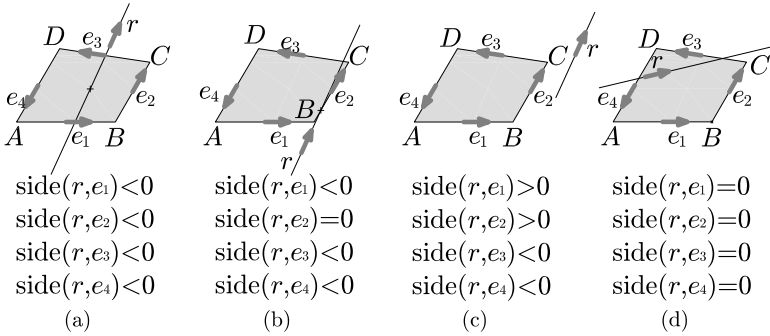


Figure 4.8: Relative position of spatial segment and polygon by using Plücker coordinates: (a) Rebar goes through FE face, (b) Rebar intersects with one FE edge, (c) Rebar trajectory is outside the FE face, (d) Rebar is parallel to the FE face.

The relative position of the rebar macro-element respect to the hexahedron face can be determined from the signs of the side operators $\text{side}(r, e_i)$. Four potential situations are represented in figure 4.8. Considering all possible combinations it can be concluded that if all non-zero side operators have the same sign, this means that the rebar is intersecting with the FE face, or at least one of its edges, and is not parallel to it.

Intersecting point coordinates

It can be demonstrated that the coordinates of the intersecting point between a plane defined by three points A, B, C and a ray r can be obtained as:

$$\{X_I\} = \text{side}(r, \overline{BC}) \{X_{P_A}\} + \text{side}(r, \overline{CA}) \{X_{P_B}\} + \text{side}(r, \overline{AB}) \{X_{P_C}\} \quad (4.22)$$

Therefore, the intersecting coordinates between the rebar and the FE face can be obtained easily from the side operator values obtained in the previous step. Moreover, the sign of the obtained side operators indicates if the rebar is entering or exiting the FE at that intersecting point. It must be checked though that the intersecting coordinates lie in-between the macro-element end points because thus far only the rebar direction was considered.

If vertexes of the FE face are coplanar, the coordinates of the intersecting point can be obtained by selecting any three vertexes of the face. For non-planar faces, the quadrilateral is divided into four triangles sharing a common vertex

at the centroid of the face. The procedure described above is repeated for the four triangles until an intersection is found. It should be noted that although the four planes intersect with the ray, only one of these intersections lies inside its corresponding triangle.

Relative position of rebar macro-element and FE

The process described in the two previous subsections is undertaken for every face of the FE and stops when both the entrance and exit points have been found. In some cases, after having checked all faces, only the entrance (exit) point may have been found; this implies that the second (first) macro-element end is inside the FE (figure 4.7b). In other cases no intersection is found because the rebar macro-element is fully embedded inside the concrete FE (figure 4.7c); to detect this situation it is sufficient to check if one of the rebar macro-element ends is inside the FE. If so, the other end is inside as well.

Efficient search algorithm

A search algorithm was developed to reduce the computational time required to find all the intersections between the concrete mesh and the reinforcing bars. For each rebar, the algorithm starts checking for potential intersections between the first macro-element and the concrete FEs, one by one. Similarly to Markou and Papadrakakis (2012), a geometrical constraint was introduced to limit the search space in the vicinity of the macro-element. The minimum distance from the centre of the hexahedron to the rebar macro element is computed. If this distance is larger than the distance from the centre of the hexahedron to its furthest vertex, the hexahedron is not considered further; otherwise, the intersection between the rebar macro-element and the FE may take place and the process described above based on the Plücker coordinates is performed.

After finding the first intersection the search domain is reduced to those hexahedrons sharing the entrance and/or exit faces (or the current hexahedron when the entrance and/or the exit points were not found). This avoids unnecessary checks and speeds the process. Lengths of each generated rebar FE are accumulated; when this accumulated magnitude is equal to the entire length of the macro-element the program jumps to the next macro-element. After completing the entire rebar the program proceeds with the next rebar, repeating the same procedure.

4.7 Examples of applications

4.7.1 Example 1: Definition of rebar geometry

An arbitrary rebar geometry was proposed in this example to show the ability of FESCA 3D to model complex reinforcement geometries with little input data. A simple $1\text{ m} \times 1\text{ m} \times 1\text{ m}$ concrete cube meshed by $10 \times 10 \times 10$ hexahedrons was considered. The rebar geometry was defined by the following coordinates (units in metres), which were directly input in FESCA 3D:

$$\begin{aligned} \{X_{P_1}\} &= [0.05 \quad 0.05 \quad 0.05]^T & \{X_{P_2}\} &= [0.95 \quad 0.05 \quad 0.05]^T \\ \{X_{P_3}\} &= [0.95 \quad 0.95 \quad 0.95]^T & \{X_{P_4}\} &= [0.05 \quad 0.95 \quad 0.95]^T \\ \{X_{P_5}\} &= [0.05 \quad 0.05 \quad 0.95]^T & \{X_{P_6}\} &= [0.05 \quad 0.05 \quad 0.05]^T \end{aligned} \quad (4.23)$$

The coordinates of the first and last input points coincided because the made-up rebar was closed. A bending radius R^r equal to 0.1 m was defined (otherwise the program would have assumed straight segments between the input points). Considering this input data, 72 rebar FEs were generated, which are represented in figure 4.9.

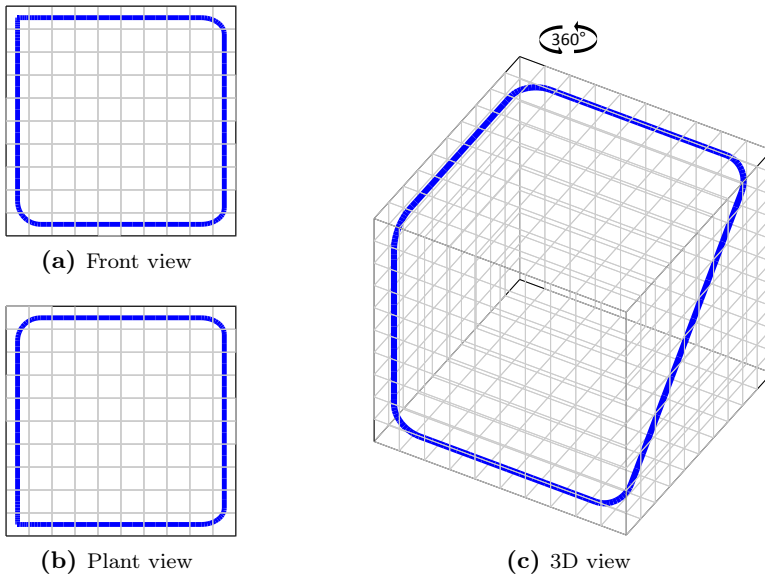


Figure 4.9: Discretisation of curved spatial rebar.

4.7.2 Example 2: Modelling continuous spiral stirrups

Certain designs can result in complex reinforcement geometries. That is the case for instance in circular piles, where the use of continuous spiral stirrups is extended as it can represent an improvement over plane stirrups. A correct definition of the actual reinforcement geometry is of importance in order to obtain a sound response prediction. The reinforcement model adopted in FESCA 3D permits the introduction of these complex reinforcement geometries in a simple manner as shown in this example.

Modelling and analysis of two beams with continuous spiral stirrups tested in one of the references (Karayannis and Chalioris 2013) is shown in this section. The specimens investigated correspond to beam specimens SP80 and SPA80: specimen SP80 presented a standard continuous spiral; specimen SPA80 presented an advanced geometry with stirrups oriented in a favourable position to resist shear (figure 4.10). The uniaxial cylinder compressive strength of concrete for both specimens was 28.5 MPa. The yield and ultimate stress of the horizontal steel rebars was equal to 550 MPa and 690 MPa, respectively. The yield and ultimate stress of the spiral stirrups was 310 MPa and 430 MPa, respectively.

A $40 \times 4 \times 6$ twenty-node hexahedron mesh was adopted. The geometry of the spiral rebars was introduced by defining the coordinates of the corners of the spiral. A bending radius of 5ϕ was assumed and the maximum transition angle between adjacent segments at bending sections was taken equal to 30° .

778 and 796 rebar FEs were generated for the spirals of beam SP80 and SPA80, respectively (figure 4.11 and 4.12).

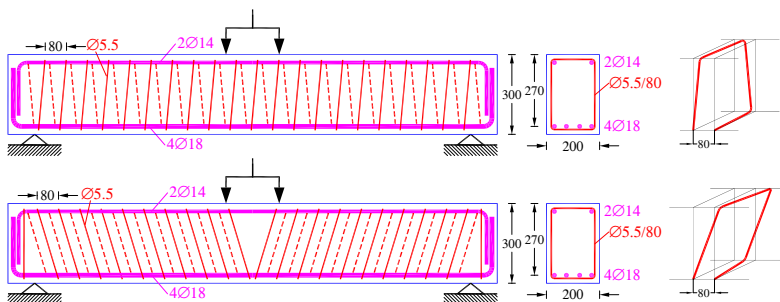


Figure 4.10: Geometry and reinforcement details of beam specimens with spiral reinforcement (from Karayannis and Chalioris (2013))

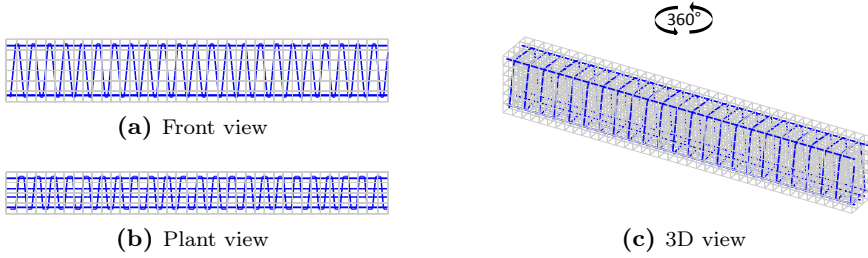


Figure 4.11: Discretisation of spiral rebar in beam SP80.

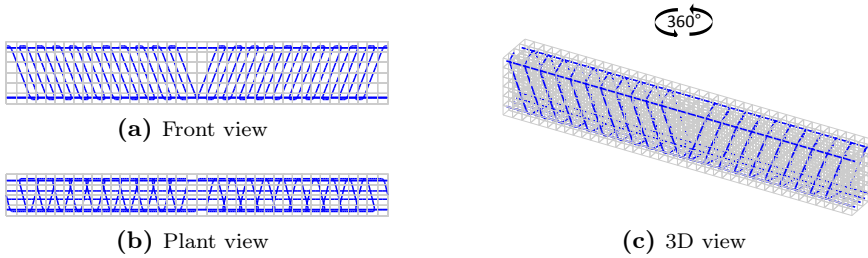


Figure 4.12: Discretisation of spiral rebar in beam SPA80.

A simple material model was adopted for concrete: tensile strength was neglected ($f_{ct} = 0$); in compression, an elastic-perfectly plastic response was adopted with $f_{cp} = 25.2$ MPa and $\epsilon_{cp} = -0.002$. Strength enhancement due to confinement was accounted for by a Drucker-Prager yield surface. Although the tensile strength of concrete was neglected, compressive softening due to transverse cracking was considered as the distribution of the reinforcement restricted the appearance of unrealistic tensile strains. The strength softening model proposed by Vecchio and Collins (1986) was adopted.

The horizontal rebars were modelled as elastic-perfectly plastic with $f_{sy} = 550$ MPa and $E_s = 200\,000$ MPa. The spiral stirrups were modelled as elastic up to the yield stress ($f_{sy} = 330$ MPa and $E_s = 200\,000$ MPa), followed by an horizontal plateau till $\epsilon = 0.01$ and a strain-hardening branch afterwards ($E_h = 8000$ MPa).

Two analyses were undertaken for each beam: one considering perfect bond and one considering bond slip interaction. When slip was accounted for, the bond stress-slip displacement law was defined according to MC 2010 (Fédération Internationale du Béton 2013).

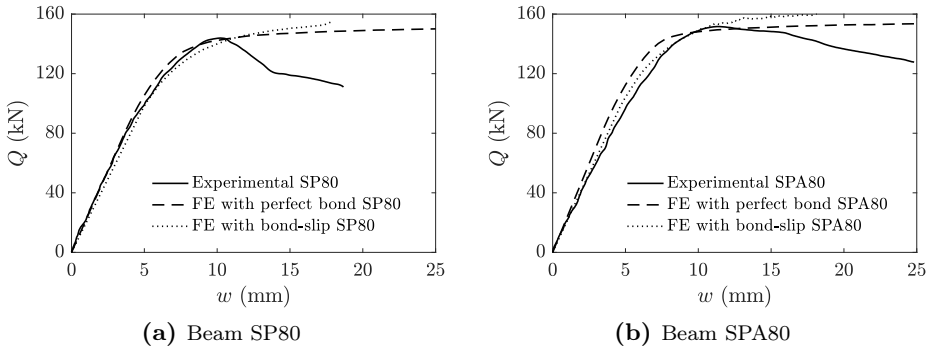


Figure 4.13: Experimental and FE load-deflection curves for beams with spiral stirrups.

Load-deflections curves obtained from FE analysis are compared with the experimental ones in figure 5.10, where Q refers to the shear force (equal to the reaction at the supports). The almost-horizontal plateau observed in the FE results is explained by the elastic-perfectly plastic model adopted for concrete in compression; no limitation was imposed to the maximum compressive strain, which explains why numerical results extended further than the experimental ones. Despite this, the FE strength predictions were close to the experimental results.

FE rebar stress profiles obtained along the first half of the spiral at $Q = 100$ kN are plotted in figure 4.14 (the grey vertical bands mark the location of the bending sections). These results show steel yielding of the vertical stretches. Lower tensile stresses were obtained at the horizontal portions, with even lower values at rebar sections at the upper sections of the beam. These results could not be compared with the experimental ones because steel strains were not measured, but they are consistent. Figure 4.14 also shows that steel stress varied abruptly at bending sections when the perfect-bond model was adopted (figures 4.14a and 4.14c). This stress variation was smoothed with the bond-slip model (figures 4.14b and 4.14d).

Figure 4.15 shows the FE principal compressive stress directions for beam SPA80 at $Q = 150$ kN obtained from the perfect-bond analysis. This load level is close to the almost-horizontal plateau of figure 5.10 and the maximum shear load reported by Karayannis and Chalioris (2013) (151.5 kN). Steel yielding of the vertical stretches of the spiral and concrete yielding of a large portion of the integration points in the load path between the load and the supports is observed (figure 4.15c); from these results it can be concluded that the maximum capacity of the specimen was (or was almost) exhausted at that load level.

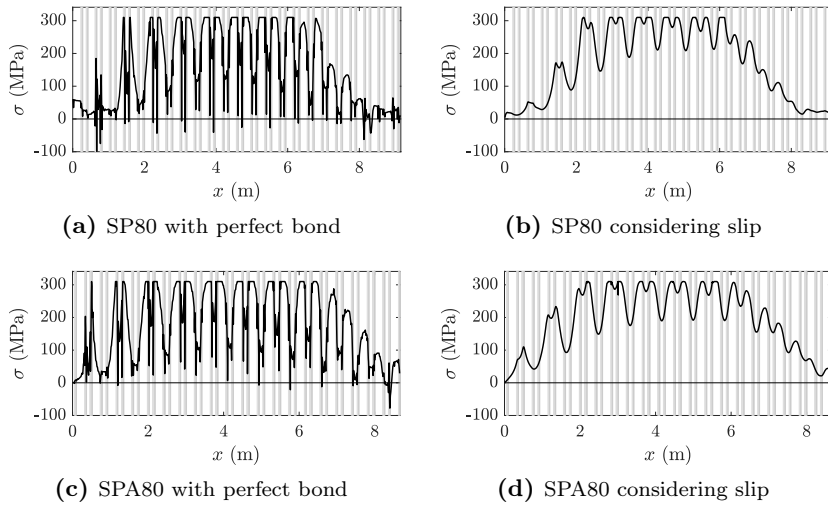


Figure 4.14: Steel stress profile along spiral stirrup.

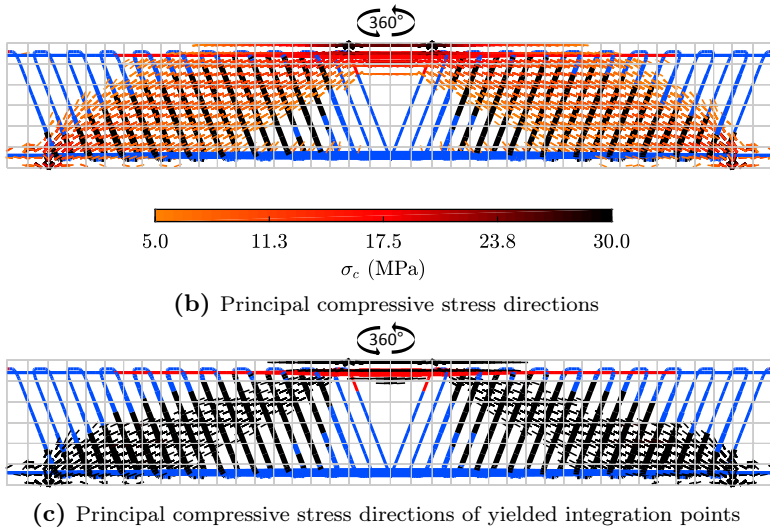


Figure 4.15: FE plot of concrete principal compressive stress directions for beam SPA80.

4.8 Conclusions

The inability of introducing the right reinforcement geometry should not be a limiting factor to obtain a sound response prediction in the analysis of reinforced concrete structures. This is of special relevance in the analysis of D-regions because the complex internal stress flow is easily influenced by the reinforcement configuration. Therefore, the adoption of an appropriate reinforcement model to facilitate a precise definition of the rebar geometry is important.

This chapter presented the details of the reinforcement model developed and integrated in FESCA 3D. The adopted model follows the embedded representation approach, which permits the consideration of any rebar position and orientation, completely independent of the concrete mesh. The formulation of both the perfect-bond and bond-slip models was presented. Although the former is in general sufficient for most practical cases, the model is ready to deal with more special cases where the stress transfer between concrete and steel can be relevant. The example of application to two beams with spiral reinforcement showed that the effect on the global response of considering bond-slip or not was almost negligible in this case; however, the bond-slip model permitted to obtain a more continuous, realistic rebar stress distribution.

Chapter 5

Load and support modelling

Decisions made regarding mesh layout, type of element used, representation of reinforcement details, support conditions, method of loading, convergence criteria, and selection of material behaviour model will produce a divergence of results.

—FIB bulletin 45 2008

5.1 Introduction

The stress field inside a D-region is affected by the geometry, position and restraint imposed by load and support elements. Slight variations of any of these factors can cause significant deviations in the results because the area of influence of these elements represents a significant portion of the whole critical region. Therefore, if sound predictions are to be obtained, it is necessary that the boundary conditions defined in the FE model reflect the actual restraints imposed by them.

Definition of boundary conditions has attracted little attention in FE analysis of reinforced concrete structures. Simple approaches such as fixing the degrees of freedom at the support areas or introducing the load by means of point loads are frequent in practice. These simplifications may be adequate when the dimensions of the whole structure or structural element are significantly larger than those of the loads and supports. However, in D-regions the dimensions of the latter, and hence their area of influence, are relevant. Therefore, simple modelling approaches as those mentioned above are not appropriate and can lead to erroneous results.

The most direct approach to consider appropriately the effect of load and support elements is by including them explicitly into the FE model. This requires to increase the size of the FE mesh and, in some cases, the refinement of the mesh to consider their distinctive geometric features. Therefore, introduction of these elements can be problematic for obtaining a regular and not excessively fine FE mesh. The common belief that the influence of these elements on the global response is not of such relevance and simplicity reasons may explain why load and support elements end up being omitted from the FE model in many cases.

Load and support models developed and implemented in FESCA 3D are described in this chapter. The importance of these elements in the internal stress field and the response of D-regions, the inadequacy of the commonly used boundary conditions to simulate the real conditions and the disadvantages of an explicit introduction of these elements in the FE mesh, were considered when proposing these models. They permit the omission of load and support elements in the FE model and a consistent approach is followed by which appropriate boundary conditions are inserted to account for their effect on the response. Load modelling is treated first: the procedure to determine the equivalent nodal forces of a distributed load and the condensed stiffness matrix of the loading substructure, regardless of the geometry of the FE mesh, is described. Support modelling is considered afterwards: the fundamentals of the implemented constant stress distribution support model and flexible support model are presented. One example of application to a pile cap foundation is shown at the end of the chapter to highlight the influence of load and support modelling on the predicted response, which shows strength variations of up to 100% depending on which model is adopted. It is also demonstrated that the commonly used fix support condition is the most inadequate approach.

5.2 Load modelling

The first part of this section outlines why load modelling is decisive for obtaining a sound response prediction in the analysis of D-regions (subsection 5.2.1). Derivation of the equivalent nodal forces of a uniform load, which is the most common practical case, is then discussed (subsection 5.2.2). The approach proposed in FESCA 3D to account for the effect of the loading substructure without modelling it explicitly is presented at the end of the section (subsection 5.2.3).

5.2.1 Importance of load modelling in D-regions

Loads acting on a structure cause a certain stress distribution at the element-load interface, which affects the stress field within the body. Slight variations of this stress distribution can have a notable effect on the response of D-regions, especially when the dimensions of the load area are of the same order of magnitude as the dimensions of the whole element. It is important that the FE stress distribution resultant from the forces applied in the model is similar to the real one in order to capture the actual picture of the internal stress field and to obtain realistic predictions.

Loads acting on a certain structural element frequently come from another component of the structure (for instance, loads acting on a column come from beams supported on them or loads acting on a pile cap come from a column). The effect of the latter on the response of the structural element object of study is sometimes considered in experimental testing by building stub elements adjacent to the main one, with the actuator then applying the load on these stub components.

Consideration of stub elements or loading substructures is of special importance in the analysis of D-regions. Indeed these elements are frequently inside the actual disturbed region, as it is inferred from St. Venant's principle: the length of the dispersion zone is approximately equal to the width or depth of the element. The mere presence of the loading substructure alters the stress distribution which is being transmitted to the main structural element.

Considering the previous paragraphs loading substructures should be introduced explicitly into the FE mesh in the analysis of D-regions. However, this is not always possible or convenient depending on the flexibility of the mesh. The simple example of considering a circular column inside a regular, quadrilateral mesh shows some of the issues that the FE user may encounter when introducing load elements into the model. A comprehensive load model was implemented in FESCA 3D to facilitate the introduction of typical load geometries regardless of the mesh (section 5.2.2). The use of static condensation principles and the implementation of a function that internally builds a supplementary FE mesh for the load elements permit the implicit consideration of their effect on the stress field and, hence, the response (section 5.2.3).

5.2.2 Equivalent nodal forces of a distributed load

In FE analysis external loads are considered by means of nodal forces which are introduced into the external nodal force vector $\{F_{ext}\}$ (equation 2.2). Concentrated (point) loads acting at the nodes can be directly introduced; distributed loads must be transformed first into a system of equivalent nodal forces. It must be noted that loads are never punctual, but under certain circumstances it can be acceptable to consider it so.

An excessively simplistic approach to model distributed loads is to divide the total load equally by the number of nodes located inside the loading area. A more precise approach is necessary for D-regions to obtain a sound stress field. Principles of the FE method, and in particular the properties of the shape functions, can be used to calculate the nodal forces equivalent to the applied load. As shown below, the approach which is proposed hereafter permits the consideration of any load geometry regardless of the geometry of the FE mesh.

The equivalent nodal force vector $\{f_{ext}\}$ of a distributed load $q(x, y)$ acting over an area S_q can be calculated as:

$$\{f_{ext}\} = \int \int_{S_q} q(x, y) \{N(x, y)\} dx dy \quad (5.1)$$

where $\{N\}$ is a vector containing the FE shape functions.

The most common situation is that the load is uniformly distributed over the loading area. When the latter, equation 5.1 can be written as:

$$\{f_{ext}\} = q \int \int_{S_q} \{N(x, y)\} dx dy \quad (5.2)$$

$\{f_{ext}\}$ is obtained by assembling the equivalent nodal forces determined for each FE located inside the loading area $\{f_{ext}^e\}$, which are calculated by integrating the FE shape functions over the corresponding portion of the load area S_q^e . Shape functions are usually expressed in the natural coordinate system of the FE (ξ, η for quadrilateral elements, figure 5.1). The FE equivalent nodal force vector $\{f_{ext}^e\}$ can be obtained as:

$$\{f_{ext}^e\} = q \int \int_{S_q^e} \{N(\xi, \eta)\} |J(\xi, \eta)| d\xi d\eta \quad (5.3)$$

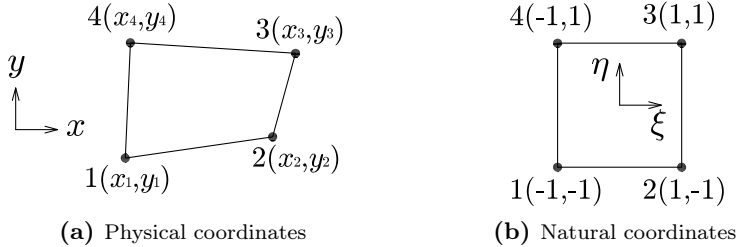


Figure 5.1: Coordinates mapping for quadrilateral element.

where $|J(\xi, \eta)|$ is the determinant of the Jacobian matrix given by:

$$[J] = \begin{bmatrix} \frac{\partial x}{\partial \xi} & \frac{\partial y}{\partial \xi} \\ \frac{\partial x}{\partial \eta} & \frac{\partial y}{\partial \eta} \end{bmatrix} = \begin{bmatrix} x_i \frac{\partial N_i}{\partial \xi} & y_i \frac{\partial N_i}{\partial \xi} \\ x_i \frac{\partial N_i}{\partial \eta} & y_i \frac{\partial N_i}{\partial \eta} \end{bmatrix} \quad (5.4)$$

The integration domain S_q^e is delimited by the FE edges and the function defining the external perimeter of the load area. The latter must be expressed in the natural coordinate system (ξ, η) if integration is to be undertaken in the natural coordinate system, which is the most appropriate approach. For rectangular areas, the integration domain in the natural coordinate system can be obtained from the transformation of the intersecting points between the FE edges and the perimeter of the load area. For circular geometries a transformation of the circumferential equation is needed (figure 5.2). Knowing that the coordinates of any point inside the FE can be expressed as a function of the FE nodal coordinates (x_i, y_i) and the FE shape functions $N_i(\xi, \eta)$ as:

$$\begin{aligned} x &= N_i(\xi, \eta)x_i = x(\xi, \eta) \\ y &= N_i(\xi, \eta)y_i = y(\xi, \eta) \end{aligned} \quad (5.5)$$

the equation of a circumference can be written in terms of the natural coordinates (ξ, η) as:

$$(x(\xi, \eta) - x_0^2) + (y(\xi, \eta) - y_0) = R^2 \quad (5.6)$$

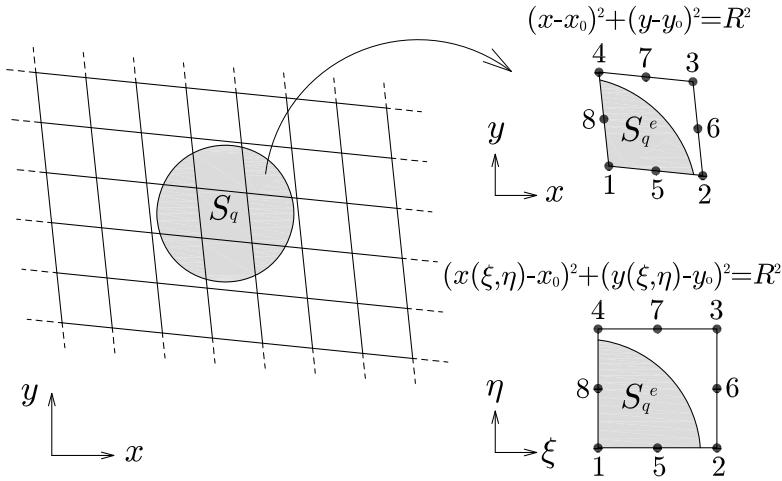


Figure 5.2: Determination of equivalent nodal forces of a distributed load.

The integration domain can be obtained by solving ξ as a function of η in equation 5.6, or vice versa.

For reference, the FE equivalent nodal forces for an 8-node quadrilateral subjected to a uniform load q which acts on its entire area are equal to:

$$\begin{aligned} f_{ext}^{e,i} &= -\frac{1}{12}A^e q \text{ for corner nodes } i = 1, 2, 3, 4 \\ f_{ext}^{e,i} &= \frac{4}{12}A^e q \text{ for midside nodes } i = 5, 6, 7, 8 \end{aligned} \quad (5.7)$$

where A^e is the area of the eight-node quadrilateral.

5.2.3 Static condensation of a loading substructure

As mentioned earlier, when the load is applied through an auxiliary component, the stress distribution which is actually being transmitted to the main element can differ from the one applied at the free extreme. The difference between both distributions depends on the stiffnesses of the loading element and the main element.

A load model based on static condensation was implemented in FESCA 3D to take into account the effect of the stiffness of the former without having to

include it explicitly into the FE model. The concept of static condensation permits to reduce the number of degrees of freedom by condensing those considered secondary. The latter are expressed in terms of the master (primary) degrees of freedom. If the master degrees of freedom of a substructure *sub* are denoted as *m* and the degrees of freedom to be condensed out as *c*, the global stiffness system (equation 2.4) can be rewritten as:

$$\begin{bmatrix} \{F_m^{sub}\} \\ \{F_c^{sub}\} \end{bmatrix} = \begin{bmatrix} K_{mm}^{sub} & K_{mc}^{sub} \\ K_{cm}^{sub} & K_{cc}^{sub} \end{bmatrix} \begin{bmatrix} \{r_m^{sub}\} \\ \{r_c^{sub}\} \end{bmatrix} \quad (5.8)$$

from which:

$$\{F_m^{sub}\} = [K_{mm}^{sub}] \{r_m^{sub}\} + [K_{mc}^{sub}] \{r_c^{sub}\} \quad (5.9)$$

$$\{F_c^{sub}\} = [K_{cm}^{sub}] \{r_m^{sub}\} + [K_{cc}^{sub}] \{r_c^{sub}\} \quad (5.10)$$

The to-be-condensed displacement vector $\{r_c^{sub}\}$ can be solved from equation 5.10 as:

$$\{r_c^{sub}\} = [K_{cc}^{sub}]^{-1} (\{F_c^{sub}\} - [K_{cm}^{sub}] \{r_m^{sub}\}) \quad (5.11)$$

$\{r_c^{sub}\}$ can then be substituted into equation 5.9 giving the reduced system of equations:

$$\begin{aligned} \{F_m^{sub}\} &= [K_{mm}^{sub}] \{r_m^{sub}\} + [K_{mc}^{sub}] [K_{cc}^{sub}]^{-1} (\{F_c^{sub}\} - [K_{cm}^{sub}] \{r_m^{sub}\}) \\ &= \left([K_{mm}^{sub}] - [K_{mc}^{sub}] [K_{cc}^{sub}]^{-1} [K_{cm}^{sub}] \right) \{r_m^{sub}\} + [K_{mc}^{sub}] [K_{cc}^{sub}]^{-1} \{F_c^{sub}\} \end{aligned} \quad (5.12)$$

where the displacements of the condensed degrees of freedom $\{r_c^{sub}\}$ have been eliminated. Equation 5.12 can also be written as:

$$\{\bar{F}_m^{sub}\} = [\bar{K}^{sub}] \{r_m^{sub}\} \quad (5.13)$$

FESCA 3D proceeds as follows to obtain the condensed stiffness matrix $[\bar{K}^{sub}]$ and the condensed force vector $\{\bar{F}^{sub}\}$ of the loading substructure. First, it

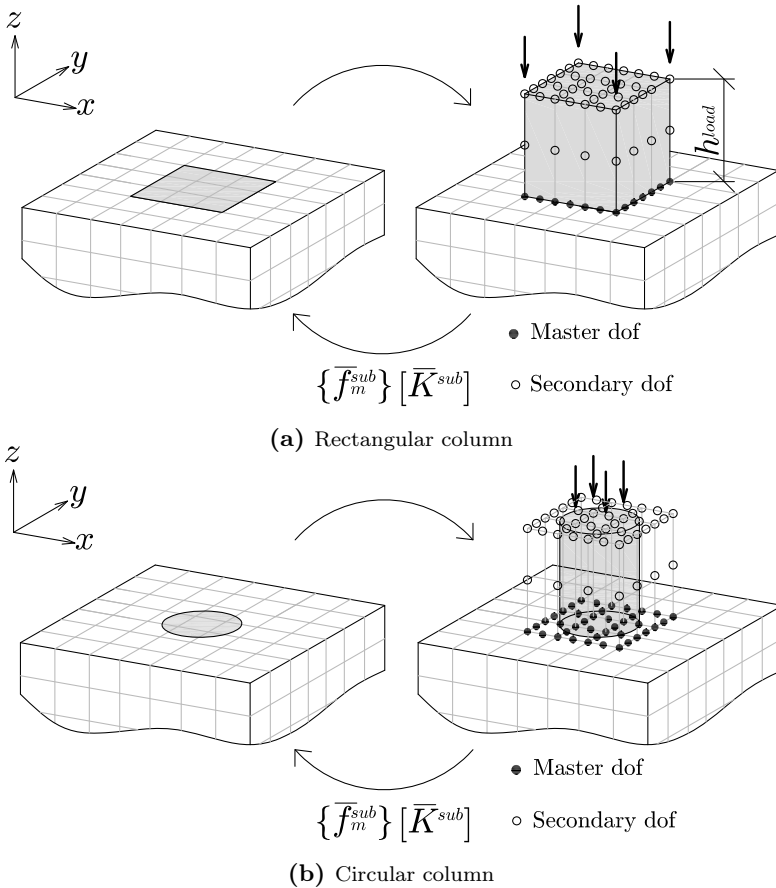


Figure 5.3: Static condensation of loading substructure.

builds an internal FE mesh which grows from the defined load area and considers the geometry of the original FE mesh of the main element (figure 5.3). The height of the substructure input by the user is considered (see next section). The master nodes of the new generated substructure coincide with the nodes of the main element. An isotropic, elastic material constitutive model is assumed for the substructure, which is a rather realistic assumption for elements which are expected to be under compression. The elastic modulus and Poisson's ration defined by the user (see next section) are considered to determine the constitutive matrix. The stiffness matrix of the loading substructure is obtained by assembling accordingly the stiffness matrices of the internally-generated FEs. The actual dimensions of the load element are considered and,

thus, integration is only performed in the load area domain (figure 5.3b). Nodal forces are applied at the upper, secondary degrees of freedom. The magnitude of these forces is determined assuming a uniform distribution as described in the previous section. The condensed stiffness matrix $[\bar{K}^{sub}]$ and the condensed force vector $\{\bar{F}^{sub}\}$ can be obtained once the stiffness matrix and the force vector of the substructure are determined. $[\bar{K}^{sub}]$ and $\{\bar{F}^{sub}\}$ are then assembled accordingly into the global stiffness matrix and the global external nodal force vector, respectively. During all this process the original FE mesh is not modified.

It must be noted that, if needed, the displacements of the condensed degrees of freedom $\{r_c^{sub}\}$ can be obtained with equation 5.11 once the displacements of the master degrees of freedom $\{r_m^{sub}\}$ are determined in the global system.

5.2.4 Required input data

Definition of a load in FESCA 3D requires: (i) the coordinates of the central point of the load area, (ii) the planar dimensions of the loading element (if it is circular, the radio, if it is rectangular, the side dimensions. For concentrated loads the user may assign a zero value to the plate dimensions), (iii) two orthogonal vectors $\{u_q\}, \{v_q\}$ defining the loading plane (for rectangular loads, $\{u_q\}$ and $\{v_q\}$ must be oriented in the direction of the sides) and (iv) a load vector $\{Q\}$ expressed in the orthonormal local system ($\{\hat{u}_q\}, \{\hat{v}_q\}, \{\hat{w}_q\}$), where $\{w_q\}$ is orthogonal to $\{u_q\}$ and $\{v_q\}$. If the loading element is not explicitly modelled but wants to be taken into account, the user must also define the height, the elastic modulus and the Poisson's ratio of the load element.

5.3 Support modelling

5.3.1 Importance of support modelling in D-regions

Supports induce reaction forces on the structure, the magnitude of which can only be determined once free displacements are obtained. Similarly to loads, the resultant FE stress distribution at support areas due to reaction forces affects the internal stress field and hence the predicted results, especially when the dimensions of the support areas are of the same order of magnitude as the dimensions of the whole element, as it is the case in most D-regions. To obtain a realistic prediction it is important that the FE stress distribution induced by the support elements is similar to the actual one.

It is a common approach in FE analysis to define the support conditions just by setting the displacements of the corresponding degrees of freedom of the nodes located inside the support area to zero. This implies treating supports as perfectly rigid elements. This assumption is realistic in only very few cases, but can be admissible for elements where the stress distribution at the supports is not of importance for the global response of the element; otherwise, consideration of the stiffnesses of the support elements and its effect on the stress field is relevant and should be considered in the FE model.

Supports are often omitted in the FE model for similar reasons as those exposed for the load counterparts. Special support models were integrated in FESCA 3D to permit a simple, but realistic modelling of the boundary conditions imposed by them. The fixed support model was implemented because it is the most commonly adopted approach, although its use in the analysis of D-regions is not recommendable as justified with the obtained results. The alternative and more convenient uniform-stress model and flexible support model described afterwards are more convenient and permit covering most practical cases.

5.3.2 Implemented support models

Fixed support

Displacements are forced to be zero at the nodes located inside the defined support area in one, two or three of the global directions (x, y, z). This support type can provide realistic predictions for structural elements whose dimensions are large compared to the dimensions of the supports and, indeed, it is fre-

quently used in practice due to its simplicity. However, this condition is not very realistic for most cases. Fixing the displacements leads to high concentrations of stresses in certain areas of the bearing and can lead to excessively stiff predictions. Moreover, this approach is very sensitive to the mesh geometry as only nodes which are inside the support area are restrained. Therefore, although fixed supports are frequently used in FE practice, they must be considered with care, especially when the support dimensions are significant in relation to the dimensions of the whole element. Indeed, considering the results obtained in this work, its use in the analysis of D-regions is in general not recommended.

Uniform-stress support

This support type enforces a uniform stress distribution at the support area, regardless of the geometry of the FE mesh. If the stress at the support area is to be uniform, the nodal reactions must be proportional to the equivalent nodal forces obtained for a uniform load with the same geometry. To enforce this, the concept of nodal tributary area is used. The nodal tributary area is defined as the ratio between the nodal equivalent force caused by a uniform load, and the total load. This area is a function of the geometry of the load and the FE mesh and does not depend on the magnitude of the load. Similarly to the determination of the equivalent nodal forces of a uniform load (equation 5.1), the tributary area of a node i can be obtained as:

$$A_{trib}^i = \sum_{e=1}^n \int \int_{S_b^e} N_i^e(\xi, \eta) |J^e(\xi, \eta)| d\xi d\eta \quad (5.14)$$

where n is the number of FEs the node belongs to and that are “touched” by the support area, S_b^e refers to the support area located inside the corresponding FE and N_i^e is the shape function of the node whose tributary area is being obtained.

The nodal tributary area is obtained for all nodes which form part of the FEs which are “touched” by the support area, even if that particular node is not enclosed inside the support perimeter. This calculation can derive in negative values of A_{trib}^i .

The total area of the support A_{sup} can be obtained by summing the obtained nodal tributary areas A_{trib}^i . This value must coincide with the area directly calculated from the defined perimeter.

Once the tributary nodal areas are obtained, the global stiffness matrix of the system $[K_T]$ is modified to enforce proportionality between nodal reactions and, hence, induce a uniform stress distribution at the support area. This modification is done as follows:

$$F_{3(i-1)+j} = K_{3(i-1)+j,k} r_k + \frac{A_{trib}^i}{A_{sup}} C_j r_k \approx \frac{A_{trib}^i}{A_{sup}} (C_j r_k) \propto \frac{A_{tri}^i}{A_{sup}} \quad (5.15)$$

where i is the node number, j the degree of freedom to which the support restrain applies, C_j is a constant large enough to dismiss the term $K_{3(i-1)+1,k} r_k$, and r_k is the displacement of a degree of freedom of reference. The node of reference proposed in the tool is the centre of the support. This permits the simulation of the rotation around the centre of the support, which is a typical condition of pinned supports, and also gives a physical meaning to the constant C_j in equation 5.15: it is the stiffness of an equivalent spring which substitutes the support. Indeed, the displacement of the central node multiplied by the stiffness value C_j gives the total reaction. This reaction is distributed between the support nodes according to the ratio A_{trib}^i/A_{sup} , enforcing a uniform stress distribution. In general the adoption of any arbitrary, relatively large value is appropriate for C_j . Three stiffness values can be defined for every support. Furthermore, directions of action do not necessarily need to coincide with the global directions (x, y, z) , because the stiffness state is transformed into the global coordinate system before being assembled into the global stiffness matrix.

Flexible support

This approach is based on the automatic development of an internal FE mesh for the support elements which is then assembled into the global FE model (figure 5.4). The procedure is similar to that presented for modelling loading substructures, although in this case the concept of static condensation cannot be used because reactions and, hence, $\{F_c\}$ and $\{F_m\}$ are unknown a priori. The height of the support, its elastic modulus and the Poisson's ratio are defined by the user considering the characteristics of the support element. An isotropic, elastic material constitutive model is assumed, which is a rather realistic assumption for elements which are expected to be under compression. The stiffness matrix of the support substructure is obtained by assembling accordingly the stiffness matrices of the internally-generated FEs. The actual dimensions of the load element are considered and integration is only performed in the support area domain. Instead of condensing the substructure,

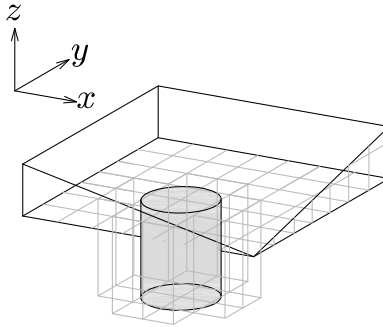


Figure 5.4: Automatic generation of auxiliary FEs to consider circular pile.

the calculated stiffness of the support substructure is assembled into the global stiffness system, whose size is increased to incorporate the new degrees of freedom. The boundary conditions at the based of the support can be defined as fixed or assuming a uniform stress distribution.

This flexible support model facilitates not only to account for the stiffness of these elements without including them “manually” into the model, but also to adopt support geometries that do not fit with the geometry of the FE mesh. As shown later, this can facilitate the introduction of a circular support in a model which is meshed with rectangular FEs.

5.3.3 Input data

Input data for the definition of a support element is: (i) the coordinates of the central point of the support, (ii) the planar dimensions (if it is circular, the radio and if it is rectangular, the side dimensions). For concentrated supports the user can assign a zero value for these dimensions), (iii) two orthogonal vectors $\{u_s\}$, $\{v_s\}$ defining the support plane (for rectangular loads $\{u_s\}$ and $\{v_s\}$ must be defined in the direction of the sides), (iv) a restraining vector $\{S\}$ with the directions of the reactions expressed in the orthonormal local system ($(\{\hat{u}_s\}, \{\hat{v}_s\}, \{\hat{w}_s\})$), with $\{w_s\}$ orthogonal to $\{u_s\}$ and $\{v_s\}$ and (v) the support type (fixed, uniform-stress or flexible).

For uniform-stress supports, a stiffness value must be also defined. In general any arbitrary, relatively large value is acceptable (the value obtained from dividing a realistic maximum reaction force by a small displacement, for instance 0.001 mm, can be a good reference value). For flexible supports the height, the material elastic modulus and the Poisson’s ratio of the support element must be input.

5.4 Example of application

The purpose of this section is to highlight the importance of a proper definition of the boundary conditions imposed by loads and supports in the analysis of D-regions. A deep four-pile cap tested by Suzuki, Otsuki, and Tsubata (1998) was taken as reference. Load and support models described in previous sections were adopted in different analysis cases. Results obtained from linear elastic FE analysis and nonlinear FE analysis are presented. The former show the effect on the elastic stress field of the different load and support models. The latter outline the influence of the adopted boundary conditions on the predicted strength and the importance of an adequate modelling of loads and supports elements in D-regions.

Specimen BPC-30-30-1 from reference (Suzuki, Otsuki, and Tsubata 1998) was considered. The dimensions of this element were $800 \times 800 \times 300$ mm. A $300 \times 300 \times 200$ mm stub column was cast on its top. The specimen was supported on four 150 mm-diameter supports, with almost zero resistance to rotation and horizontal displacement. The distance between support centres was 500 mm. The load was applied through the supports to make the four reactions equal. This column was fixed at its top to the testing machine. Reinforcement was bunched over the piles forming a square. Each band was formed by $4\phi 10$. Yield and ultimate stress of steel was 405 MPa and 592 MPa, respectively. The concrete compressive strength was 28.9 MPa.

Two alternative meshes were adopted. In the first one only the pile cap was modelled, using a $10 \times 10 \times 4$ twenty-node hexahedron mesh (figure 5.5). In the second one, the stub column was also included with $4 \times 4 \times 2$ additional twenty-node hexahedrons (figure 5.6). Hereafter these meshes are referred as Mesh 1 and Mesh 2, respectively.

Following engineering instinct the load was applied at the top of the cap in Mesh 1 and at the top of the column in Mesh 2, and supports were defined at the bottom of the cap regardless of the adopted model. This implies turning upside down the actual experimental setup. Despite this inversion, flexibility given by the implemented load and support models permits the simulation of similar conditions as those in the test.

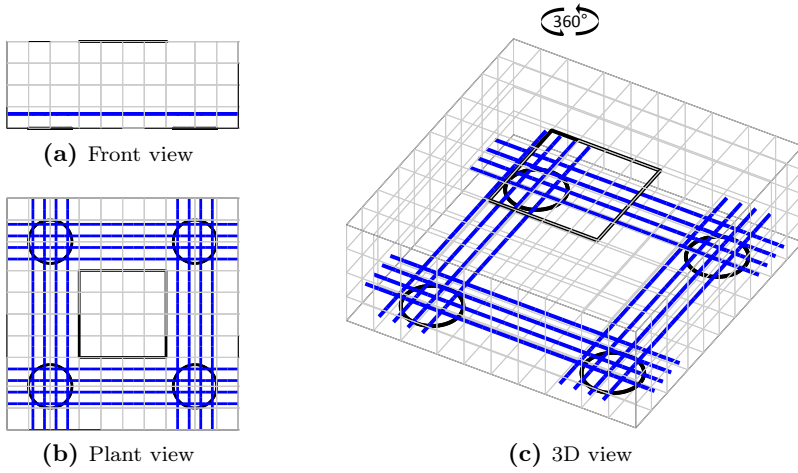


Figure 5.5: FE mesh for pile cap BPC-30-30-1. Column omitted.

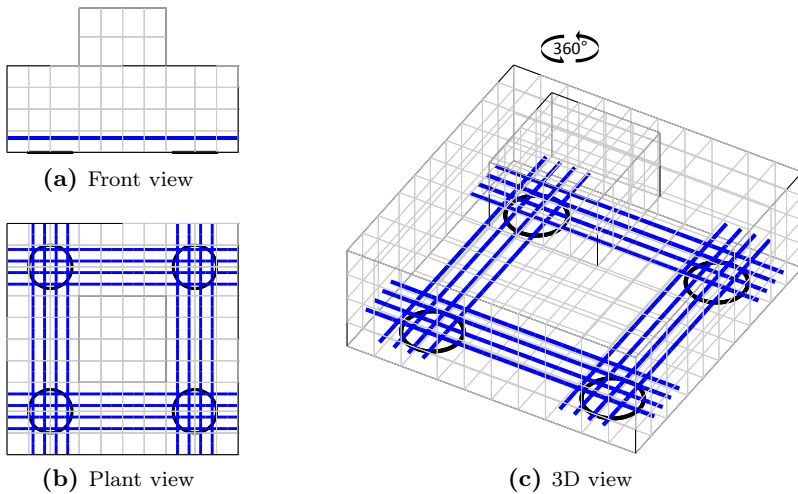


Figure 5.6: FE mesh for pile cap BPC-30-30-1. Column included.

5.4.1 Linear elastic finite element analysis

Load models

The influence of different load models on the stress distribution induced under the column is assessed in this subsection through the representation of the contour plots of the compressive vertical stress fields on the upper horizontal cap plane. All results were obtained for a vertical column load of 500 kN.

As discussed earlier, loading elements should be included in the model when their dimensions are of the same order of magnitude as the main element. This is the case in the considered pile cap. Despite this, the three potential approaches that can be followed to model the acting load were considered for assessing the differences: (i) neglect the importance of the stub column and adopt Mesh 1, (ii) adopt Mesh 1 but consider the effect of the column by static condensation and (iii) adopt Mesh 2.

Results obtained with the first approach are shown in figure 5.7. The stress distribution corresponding to the original load geometry is plotted in figure 5.7a). Three variations were proposed in addition: firstly, the square column was rotated 45° (figure 5.7b); secondly, a 300 mm-diameter column geometry was adopted (figure 5.7c); and thirdly, a 300 mm-diameter column geometry was adopted and the regular FE mesh was distorted (figure 5.7d). Plotted results demonstrate the flexibility of the model in representing typical load geometries regardless of the FE mesh. The resultant stress field is not corrupted even for distorted and arbitrarily-oriented meshes. This permits the definition of the FE mesh without having to attend to geometric details of the loads. It should be noted that these plots were generated by linear interpolation of the stress values obtained at the closest integration points, which explains why lower stress levels are observed near the load perimeter.

Neglecting the effect of the load element (the stub column in this case) is a common approach in practice, but inadequate for the analysis of D-regions. The resultant stress distribution varies importantly when considering the effect of the column (figure 5.8). Stresses concentrate at the column corners because the uniform stress distribution at the top of the column is deviated on the way to the cap. As discussed later in section 5.4.2, this stress concentration has a notable effect on the resultant strength and stiffness of the element. Almost equal results are obtained with the simple model based on static condensation (figure 5.8a) and the more complete FE Mesh 2 (figure 5.8b). This was expected in linear elastic analysis, but demonstrates that the implementation of the condensed model was correct.

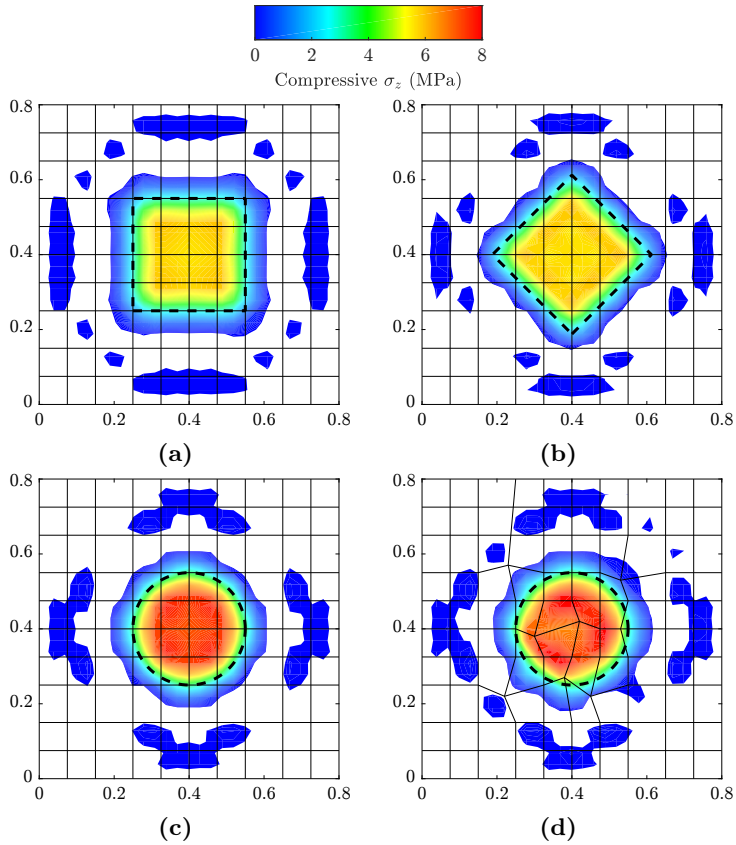


Figure 5.7: FE vertical stress field at loading area. Column effect not included: (a) uniform square load with parallel FE mesh, (b) uniform square load with arbitrary orientation, (c) uniform circular load with regular mesh, (d) uniform circular load with distorted mesh.

Support models

The influence of different support models on the stress distribution induced over the support areas is assessed similarly through the representation of the contour plots of the compressive vertical stress fields on these planes. All results were obtained for a vertical column load of 500 kN. Only the support model was varied from case to case while the support geometry remained unaltered (150mm-diameter bearings).

Figure 5.9 shows four contour plots of the vertical compressive stress field σ_z at the bottom section of the cap obtained by adopting: (i) the fixed support

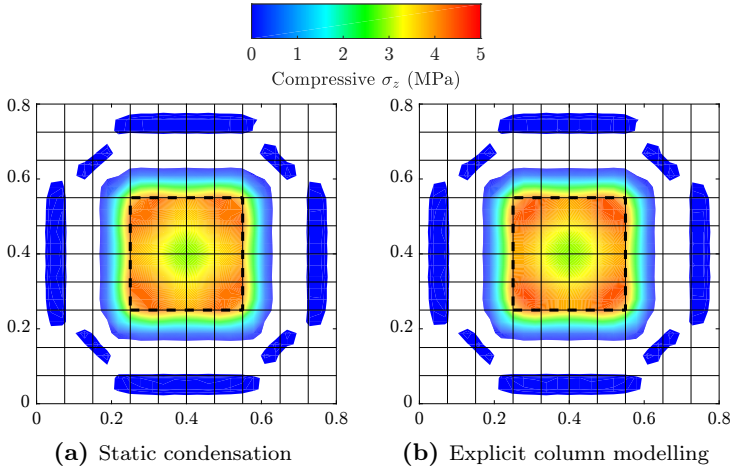


Figure 5.8: FE vertical stress field at loading area. Column effect included.

model (figure 5.9a), (ii) the uniform-stress support model (figure 5.9b), (iii) a flexible support model consisting of 50 mm-thick steel plates (figure 5.9c) and (iv) a flexible support model consisting of 200 mm-high concrete piles (figure 5.9d).

Stress concentration at the inner corners of the piles is observed for the fixed support model (figure 5.9a) and, to a lesser extent, for the flexible model with steel plates (figure 5.9c). The stress is not perfectly uniform for the uniform-stress support model, with slightly higher values around the centre of the pile (figure 5.9b). This is a consequence of the coarse mesh adopted because although the internal forces at the support base are forced to be equivalent to a uniform stress distribution, with few integration points inside the support area it cannot be guaranteed that stresses at integration points will reflect a uniform stress. More accurate results could have been obtained with little refinement of the mesh.

The effect of the support stiffness on the stress distribution can be observed by comparing figure 5.9c and 5.9d: results obtained for the steel plate supports (stiffer) show stress concentration at the inner corners, similar to the fixed supports; results obtained for the concrete pile supports (more flexible) show a fairly uniform stress distribution.

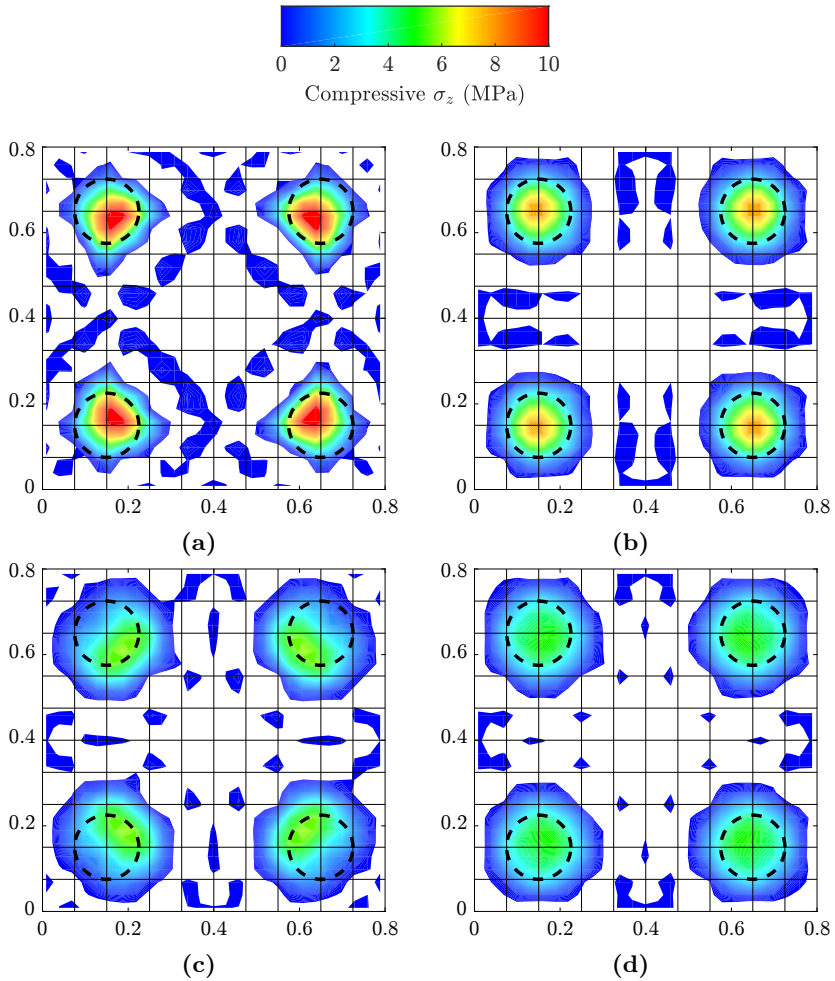


Figure 5.9: FE vertical stress field at support areas: (a) Fixed supports, (b) Uniform-stress supports (c) Flexible supports (steel plates), (d) Flexible supports (concrete piles).

5.4.2 Nonlinear finite element analysis

As shown in the previous subsections stress fields at the column and support areas are influenced by the load and support models. The effect of the variation of the stress field on the predicted strength and stiffness is assessed in this subsection. Nonlinear FE analyses were run for a more realistic comparison of the predictions. Tensile strength of concrete was neglected. An elastic-perfectly

plastic response was adopted for concrete in compression ($f_{cp} = 25.4$ MPa). Enhancement of concrete strength due to confinement was taken into account. Concrete strength softening due to transverse cracking was not considered as tensile strains are to be unrealistic due to the low reinforcement quantities and the neglect of the tensile strength of concrete.

Before presenting the FE results, a simple strut-and-tie model may facilitate the understanding of the influence of the load and support models through the stress field on the predicted strength and stiffness. FE models leading to stress concentration around the column corners and/or the support inner-corners result in more inclined equivalent strut angles than those giving a uniform stress distribution. Steeper struts result in lower forces at the ties for the same vertical load. Therefore, if the strength is limited by yielding of the ties as it often occurs, those models leading to more inclined strut angles will predict higher strengths. Considering this, a higher strength must be expected:

- for fixed supports than for uniform-stress supports
- the more rigid the support is
- if the column stiffness is taken into account

FE results can be presented after this discussion. The experimental and FE load-deflection curves obtained for the considered pile cap specimen are plotted in figure 5.10.

The following conclusions can be obtained regarding load modelling:

- If the column effect is disregarded, the response is more flexible and the yielding load is lower than the ones observed in the test (figure 5.10a).
- Significantly stiffer and stronger predictions are obtained if the effect of the column is considered (figure 5.10b,5.10c).
- Very similar results are obtained by using static condensation (figure 5.10b) and by including the column explicitly in the FE mesh (figure 5.10c).

The following conclusions can be obtained regarding support modelling:

- The variation of the FE results with the support models can be up to around 50%.

- As expected, uniform-stress supports lead to the weakest and more flexible response, and the response obtained with steel plate supports is stiffer and stronger than with the concrete piles.
- Fixed supports did not lead to the strongest and stiffest response in this case as it should be expected. The reason is found in the adopted FE mesh, which left a significant portion of the support area unrestrained as not many nodes were located inside the defined area. This evidences the inadequacy of the fixed support condition because a small variation of the support geometry can lead to large variations in the results depending on the number of nodes that are “captured” by the defined area.

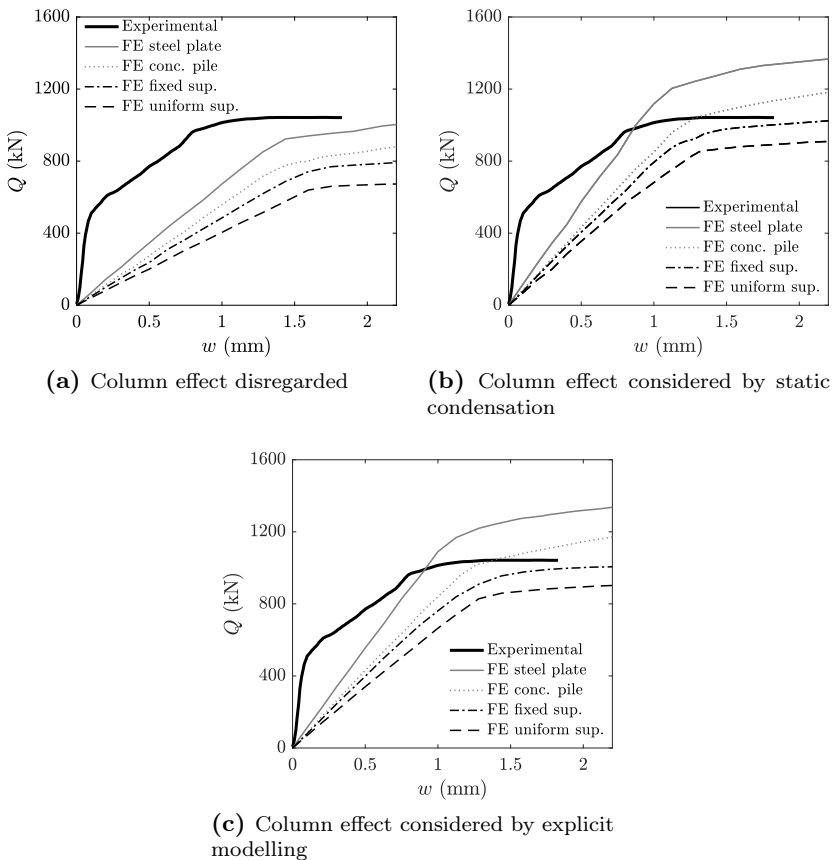


Figure 5.10: FE load-deflection curves for pile cap BPC-30-30-1 obtained under different load and support assumptions. $f_{ct} = 0$.

These results show the importance of a proper modelling of load and support elements. Results can vary about 100% depending on the adopted assumptions. Considering the experimental setup, the most appropriate assumptions should consider the column effect (either by static condensation or by including it in the FE model) and uniform-stress support model. Based on the results plotted in figure 5.10b-5.10c it is seen that under these conditions the predicted strength is lower than the experimental one. To obtain more realistic predictions the tensile strength needs to be accounted (see Chapter 6).

5.5 Conclusions

This chapter presented the fundamentals of the load and support models developed and integrated in FESCA 3D. Principles of static condensation were used to account for the effect of the loading substructure without having to include it explicitly in the FE mesh. Principles of the FE method were considered for the development of the uniform-stress distribution support model and the flexible support model. These models cover realistically most situations in engineering practice and experimental testing.

An example of application to a four-pile cap specimen was presented at the end of the chapter where different load and support models were adopted. Although it was known before the analyses that some of these models were not appropriate for the existing conditions, none of them was completely unpractical. Comparison of the results demonstrated the importance of an adequate definition of the boundary conditions in the analysis of D-regions, with result variations of up to 100% depending on the adopted assumptions. It was also justified why the frequently used fixed support model is inappropriate for the analysis of D-regions.

Part III

Examples of applications

Chapter 6

Validation of FESCA 3D and analysis of pile caps

As the pile caps are basic to the safety of structures and not open to visual inspection after service, a sound knowledge of their exact behaviour is essential. A complete and satisfactory solution can be achieved only by performing a nonlinear analysis of the pile caps throughout the entire load range, taking into account the loading history and several nonlinear effects.

—Sam and Iyer 1995

6.1 Introduction

Validation of any model must be done through comparison between model and experimental results. In general this entails the consideration of a relative large number of specimens to prove that the model is able to capture the effect of different factors on the element response. Access to well-documented experimental data is critical for this purpose. However, experimental programmes on 3D D-regions are scarce due to the difficulties in undertaking these tests. The only structural element which may be an exception in this dearth is pile cap foundations, which has been object of study in several experimental campaigns.

A pile cap is a foundation element commonly found in construction that is used to transfer loads from the superstructure to a group of piles. The cap often consists of a lightly reinforced concrete block with no shear reinforcement

which is cast on top of the piles. The number of piles depends on the load to be transferred and the soil capacity. Most pile caps in construction practice are supported by two, three or four piles, but foundations with several tens of piles also exist (Concrete Reinforcing Steel Institute 2008). Pile caps can be classified based on the shear span-to-depth ratio w/d as slender ($w/d > 1$) or deep (thick) ($w/d < 1$) (Gogate and Sabnis 1980). The latter constitute a D-region and, indeed, most pile caps in construction fall into this category. If piles are lined up (i.e. more than one row of piles exist in each direction), they can be treated as 2D elements; otherwise, the element behaviour is three-dimensional and should be treated as such.

It should be noted that FESCA 3D is a numerical tool and not only a numerical model. Different concrete constitutive models can be adopted (see Chapter 3), boundary conditions imposed by support and load elements can be accounted for in various manners (see Chapter 5) and permits the adoption of different FE meshes. These factors, and others, affect to the accuracy of its predictions. Therefore, instead of considering a large population of pile cap specimens and compare FE and experimental results, it was preferred to select a small, but representative sample to study the effect of different factors on the FE results and, to show ultimately that realistic predictions can be obtained when defining the variables of the FE model appropriately. Considering a small sample will also permit going deeper into other aspects such as the identification of the mode of failure based on the FE results. This sample is formed by fourteen four-pile cap specimens tested by two different groups of authors, which together represent a very large portion of the tests on pile caps. Firstly, results for six scaled specimens (Suzuki, Otsuki, and Tsubata 1998) obtained from six different analysis cases are presented to show the influence of concrete modelling and boundary conditions on FE results. Secondly, eight full-size specimens (Blévoit and Frémy 1967) were analysed with special emphasis on the identification of the mode of failure based on FE results.

6.2 Analysis of six scaled pile caps

6.2.1 Introduction

Suzuki and his colleagues undertook an extensive experimental campaign on four-pile caps to study the influence of bar arrangement, edge distance (shortest distance from the cap edge to the pile centre), cap depth and column width on the ultimate strength of pile caps (Suzuki, Otsuki, and Tsubata 1998) (Suzuki, Otsuki, and Tsubata 1999) (Suzuki, Otsuki, and Tsuchiya 2000) (Suzuki and

Otsuki 2002). Detailed experimental results and observations obtained for 94 scaled specimens were reported in the aforementioned references, being ideal to check the adequacy of any numerical model by comparing experimental and numerical results. FE results obtained with FESCA 3D for six of these specimens are presented in this section. Taking a small sample was considered sufficient for the current purposes and more convenient so results could be discussed in more detail. Six different analysis cases were undertaken to study the influence of concrete modelling and load modelling on predicted results.

6.2.2 Description of the specimens, experimental setup and test observations

The six specimens considered were: BP-20-30-2, BPC-20-30-2, BP-30-25-2, BPC-30-25-2, BP-30-30-2 and BPC-30-30-2, taken from Suzuki, Otsuki, and Tsubata (1998). Specimen geometry and characteristics are described in figure 6.1 and table 6.1. The specimen name was set up as follows: the first term refers to the reinforcement configuration (BP stands for uniform grid and BPC for bunched square arrangement over piles), the second refers to the cap depth (200 mm or 300 mm) and the third to the column width (250 mm or 300 mm).

Reinforcement quantity was determined in order to make the bending strength smaller than the shear strength, so flexural failure would precede shear failure. Reinforced rebars were disposed symmetrically in x- and y-direction (table 6.1). A hook was prepared at the rebar ends to prevent anchorage failures.

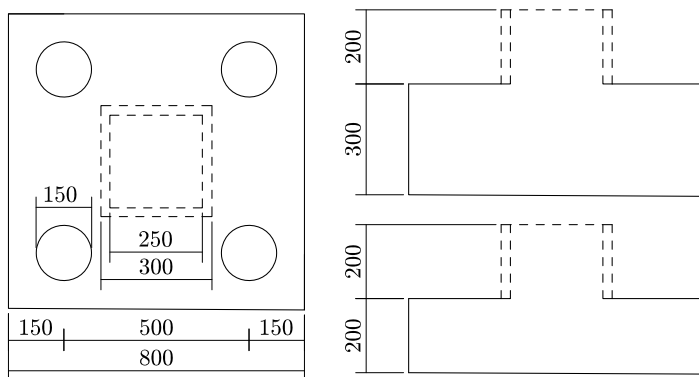


Figure 6.1: Geometry of specimens tested by Suzuki, Otsuki, and Tsubata (1998).

Table 6.1: Summary of specimens of Suzuki, Otsuki, and Tsubata (1998).

Specimen	h (mm)	c (mm)	f_{c0} (MPa)	Reinforcement	P_{test} (kN)	Fail.Mode
BP-20-30-2	200	300	29.8	$2 \times 6\phi 10$ (G)	480	y+s
BPC-20-30-2	200	300	29.8	$4 \times 3\phi 10$ (B)	495	y
BP-30-25-2	300	250	26.3	$2 \times 8\phi 10$ (G)	725	s
BPC-30-25-2	300	250	29.2	$4 \times 4\phi 10$ (B)	872	y+s
BP-30-30-2	300	300	28.5	$2 \times 8\phi 10$ (G)	907	y+s
BPC-30-30-2	300	300	30.9	$4 \times 4\phi 10$ (B)	1029	y+s

Reinforcement: (G)-grid reinf., (B)-bunched reinf.

Fail. mode: s-shear failure, f-flexural failure, y+s-shear failure after yielding.

The yield stress f_{sy} and the ultimate stress f_{su} of steel was 405 MPa and 592 MPa, respectively.

Each pile bearing consisted of a spherical support and two-stage rollers positioned orthogonal to each other, with almost zero resistance to rotation and horizontal displacement. The load was applied through the pile bearings so the four reactions were equal. Two loading beams were used for that purpose. The top of the stub column was fixed to the head of the testing machine.

Maximum loads measured during the tests and reported modes of failure are listed in table 6.1. The latter was judged by the authors of the reference based on the final failure status and the load-deflection curve as described below:

- Failure was classified as shear (s) when the column load decreased quickly after the maximum load and the deflection was small, showing one or two pile bearings thrusting into the slab and askew cracking on the two adjacent sides at the maximum load.
- Failure was classified as flexural (f) when the deflection grew quickly after a certain load and shear cracking did not occur until the maximum load.
- Specimens in which the deflection grew quickly near the maximum load but the load increased only slightly thereafter were reported as shear failures immediately after bending yield (y+s).

6.2.3 FE analysis cases

In structural analysis, the FE modeller and the general practitioner follow in general two different approaches. On the one hand, the FE modeller tries to obtain a response prediction as realistic as possible. This entails, among others, considering a refined concrete model accounting for tensile stresses and including secondary elements (e.g. stub columns, supporting elements) in the FE model that may have an effect on the response of the element object of analysis. On the other hand, the general practitioner is in general not interested in obtaining a “perfect” response prediction and adopts simplifications, like disregarding the tensile strength of concrete and/or neglecting the influence of secondary elements. Six different FE analysis cases were undertaken to account for both approaches: two different concrete constitutive models were considered and the effect of the stub column was accounted for in three different manners. Details of these models are given below.

Considered constitutive models for concrete (see Chapter 3):

- Simplified model: the tensile strength of concrete was neglected. The response in compression was modelled as elastic-perfectly plastic, with $f_{cp} = 2.7f_{c0}^{2/3}$ and $E_c = f_{cp}/0.002$. This model is in agreement with the hypotheses of the STM and the SFM. Strength enhancement due to confinement was considered through a Drucker-Prager yield surface. The strain at peak stress increased linearly with the effective strength so the elastic modulus E_c remained constant. Compressive softening due to transverse tensile strains was not accounted for.
- Refined model: concrete in tension was modelled by a linear elastic branch up to cracking and by a softening branch afterwards based on the model by Hordijk (1991). The concrete tensile strength f_{ct} was calculated as $0.21(f_{c0} - 8)^{2/3}$, which corresponds to the lower bound value of the characteristic tensile strength of concrete as defined in MC 2010. The elastic modulus E_c and the fracture energy G_f were taken equal to $E_c = 21\,500(f_{c0}/10)^{1/3}$ and $G_f = 73f_{c0}^{0.18}$ (G_f in N/m), as proposed in MC 2010. Concrete in compression was characterised by a nonlinear function following the model proposed by Popovics (1973). The strain at f_{c0} was taken equal to 0.002 regardless of the concrete strength for simplicity reasons. Strength enhancement due confinement was considered through a Drucker-Prager yield surface, and the strain at peak stress was modified following the model by Mander, Priestley, and R. Park (1988). Compressive softening due to transverse tensile strains was accounted for through the formulation proposed by Vecchio and Collins (1986).

Consideration of the stub column effect (see Chapter 5):

- Load model 1: the stub column was neither included in the FE mesh nor accounted for by static condensation. It was assumed that the load was applied directly on top of the cap with a constant stress distribution. A regular FE mesh formed by 1024 twenty-node hexahedrons ($16 \times 16 \times 4$) was adopted (figure 6.2a), whose nodal coordinates were modified accordingly to consider the different specimen depths.
- Load model 2: the stub column was not included in the FE mesh, but its effect was considered in the FE model by static condensation. The same FE mesh as in the previous case was used (figure 6.2a). Compared to the previous model, just the stub column height and its material elastic modulus had to be introduced when defining the load.
- Load model 3: the stub column was included explicitly in the FE mesh. The load was applied at the top of the column assuming a uniform stress distribution. A regular FE mesh formed by 1132 twenty-node hexahedrons was adopted (figure 6.2b). The geometry of the FE mesh was modified to consider the different specimen geometries. It was necessary to adapt not only the vertical coordinates, but also the horizontal one when the column width varied.

Considering the two concrete constitutive models and the three load models described above, six analysis cases were undertaken. For expository reasons, these analysis cases will be presented later as follows:

- FE analysis case 1: refined concrete constitutive model+load model 3.
- FE analysis case 2: simplified concrete constitutive model+load model 1.
- FE analysis case 3: simplified concrete constitutive model+load model 2.
- FE analysis case 4: simplified concrete constitutive model+load model 3.
- FE analysis case 5: refined concrete constitutive model+load model 1.
- FE analysis case 6: refined concrete constitutive model+load model 2.

Support conditions and reinforcement were defined in the same way in the six analysis cases. Supports were not included explicitly in the FE mesh. The uniform-stress support model described in Chapter 5 was adopted for

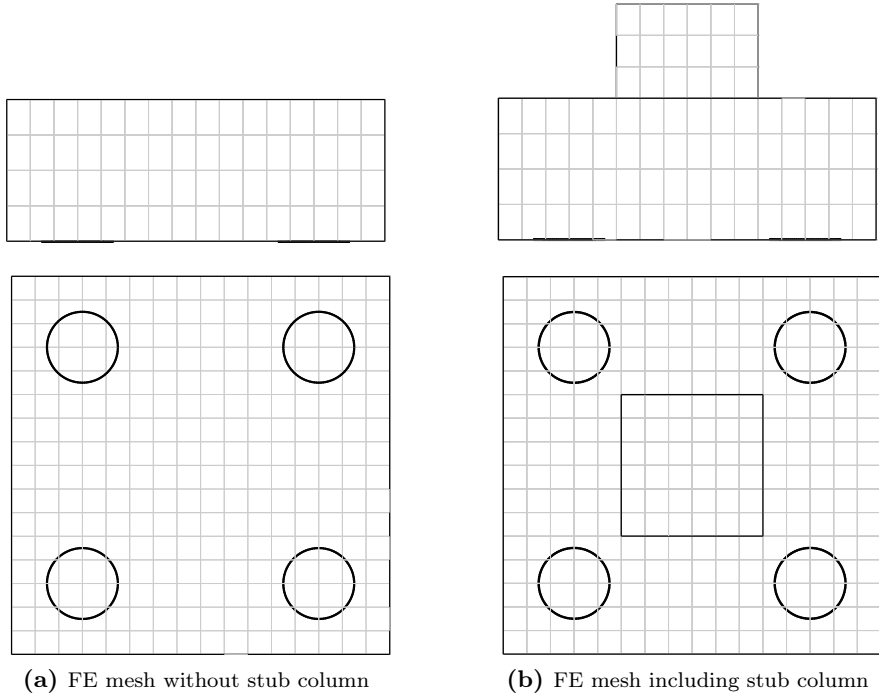


Figure 6.2: FE meshes for Suzuki's specimens.

the four supports. The vertical stiffness of each support was taken equal to $1 \times 10^{10} \text{ kN m}^{-1}$ (any other relatively large value could have been used) and the horizontal resistance was dismissed. This support model is in accordance with the bearing characteristics described in the reference. Reinforcing bars were introduced individually and it was assumed that they spanned the whole cap length, neglecting the anchorages hooks. Perfect bond between concrete and steel was assumed. Embedded rebar FEs were generated as three-node bar elements. Steel was modelled as elastic-perfectly plastic, ($f_{sy} = 405 \text{ MPa}$, $E_s = 200\,000 \text{ MPa}$).

It should be noted that the adopted FE model does not correspond with the actual experimental setup. In the test the load was applied through the piles to make the four reactions equal and the element was supported at the top of the stub column. These conditions were reproduced in the FE model, but without having to apply the load through the pile thanks to the elements implemented in FESCA 3D, such as the uniform-stress support model. In addition, this permitted the adoption of an FE model more in accordance with engineering

practice, with the cap supported by the piles and the load applied by the column.

A displacement-controlled method was used to determine subsequent load increments for the six analysis cases. An energy norm criterion (1%) was adopted to assess convergence in analysis cases 1, 5 and 6 (refined concrete model); a residual norm criterion (1%) was adopted for the rest (simplified concrete model).

6.2.4 FE results

Table 6.2 summarises maximum loads predicted for the six specimens in the six analysis cases and their corresponding strength ratio P_{test}/P_{FE} . Results obtained for each analysis case are discussed below.

Analysis case 1

This case was the most refine one. Predicted maximum loads were close to the experimentally measured for the six specimens and the strength was not overestimated for any of them. FE and experimental load-displacement curves can be compared in figure 6.3. In general the model predicted well the global response of the specimens. Only for specimens BPC-30-25-2 and BPC-30-30-2 the difference between predicted and experimental strengths was a bit larger. For these two specimens the maximum load in the FE analysis was limited by crushing initiation at the bottom section of the column after reinforcement yielding. It is believed that confinement effect on the column was being slightly underestimated in the FE model as the horizontal constraint imposed by the

Table 6.2: Summary of FE predicted strengths for Suzuki’s specimens.

Specimen	Anls.1		Anls.2		Anls.3		Anls.4		Anls.5		Anls.6	
	P_{FE} (kN)	$\frac{P_{test}}{P_{FE}}$										
BP-20-30-2	466	1.03	247	1.94	336	1.43	336	1.43	341	1.41	490	0.98
BPC-20-30-2	486	1.02	288	1.72	423	1.17	411	1.20	332	1.49	510	0.97
BP-30-25-2	720	1.01	465	1.56	684	1.06	600	1.21	685	1.06	794	0.91
BPC-30-25-2	803	1.09	599	1.46	825	1.06	736	1.18	600	1.45	854	1.02
BP-30-30-2	877	1.03	494	1.84	718	1.26	701	1.29	732	1.24	892	1.02
BPC-30-30-2	949	1.08	646	1.59	879	1.17	855	1.20	646	1.59	1030	1.00

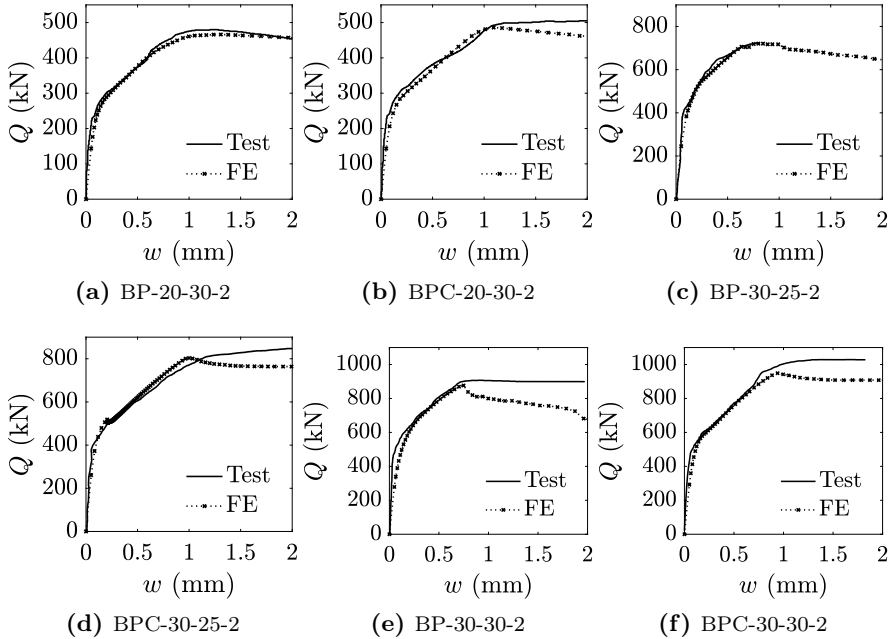


Figure 6.3: Experimental and FE load-displacement curves.

testing machine on the stub column was not considered. An additional analysis was undertaken in which now the horizontal displacements of the stub column were fixed. Load-displacements curves plotted in figure 6.4 were obtained under these conditions. Predicted maximum loads increased, especially in specimens whose cap depth was 300 mm, and approached to the experimental results.

Regarding modes of failure, (Suzuki, Otsuki, and Tsubata 1998) considered that, except for specimen BP-30-25-2, failure took place after reinforcement yielding (table 6.1). Rebar strains were not measured, so this statement was based on the observed global response. According to FE results, maximum loads were preceded by yielding of several or all rebars for the six specimens. For specimen BP-30-25-2 only small portions of the rebars closer to the edges had reached the yield stress, which could be in agreement with the observed mode of failure. For the other specimens a large percentage of reinforcing bars had yielded when reaching the maximum load.

FE principal compressive stress directions obtained near the maximum load for specimen BP-20-30-2 and BPC-30-30-2 are plotted for reference in figure 6.5

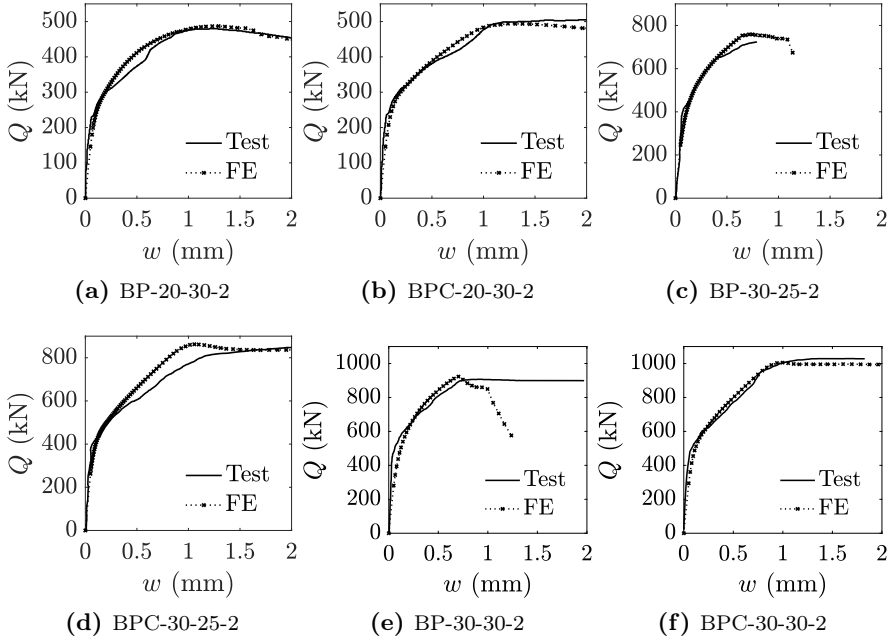


Figure 6.4: Experimental and FE load-displacement curves with constrained horizontal displacements at top of the column.

and 6.6, respectively. Spurious compressive stresses can be observed in certain areas, especially in specimen BP-20-30-2. It is believed that these spurious stresses are caused by the stiffness discontinuity that embedded rebars cause inside concrete FEs. Rebars do not disturb the stress field before cracking, but when the tensile strength is exceeded, concrete FEs in which a rebar FE is embedded suffer a strong discontinuity caused by the mere presence of the rebar, which affects the FE stress field. Despite this, spurious stresses were below 10MPa and concentrated at limited areas, and attending to the obtained results, they did not seem to affect the global response.

FE steel stresses at maximum load for specimens BP-20-30-2 and BPC-30-30-2 are plotted in figure 6.7. Rebars were numbered from the cap edge to the cap centre. Only three and four rebars were represented, respectively, as results were symmetric. Dotted vertical lines mark the edges of the piles and the column. All rebars had reached the yield stress at the maximum load for both specimens. Rebar 3 of specimen BP-20-30-2 (rebar located near mid-span) presented a slightly lower tensile stress at its centre. A constant stress

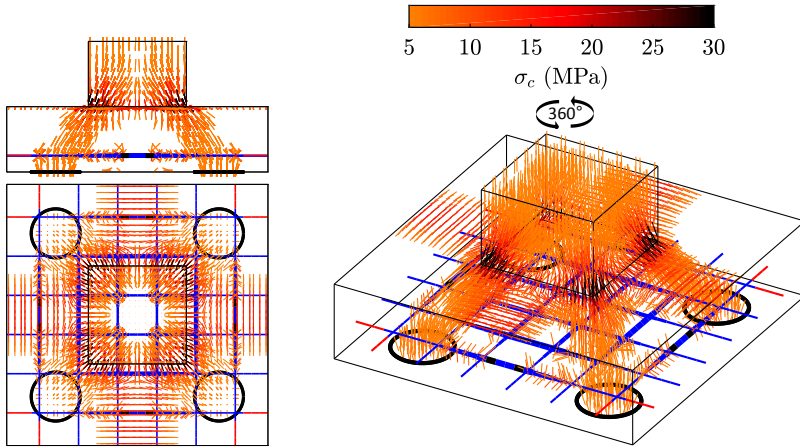


Figure 6.5: FE principal compressive directions for specimen BP-20-30-2 in analysis case 1. $P = 450$ kN

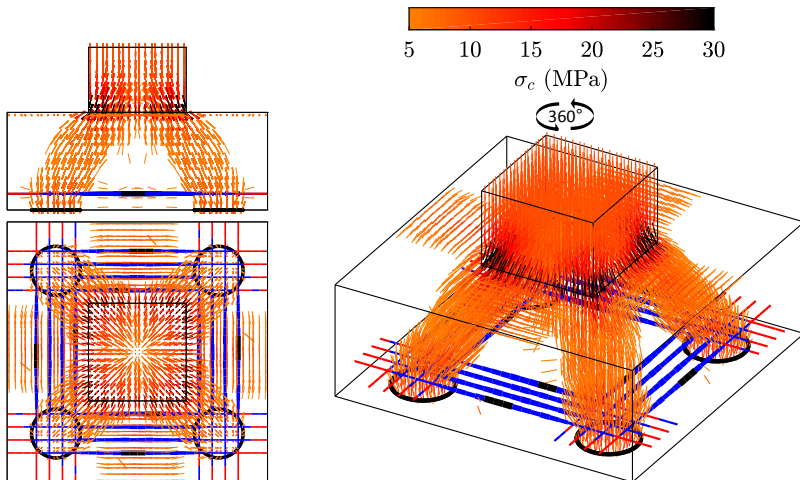


Figure 6.6: FE principal compressive directions for specimen BPC-30-30-2 in analysis case 1. $P = 900$ kN

should be expected, as this zone was severely cracked and no concrete stresses should exist to permit this rebar stress variation. The presence of spurious compressive concrete stresses seen in figure 6.5 causes this difference. Despite this, and as addressed earlier, this did not affect the global results as it only occurred at a relatively short length. This effect was not observed in rebars

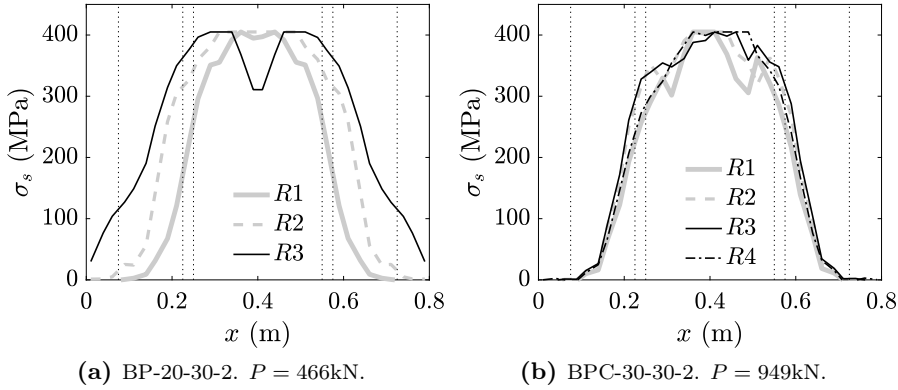


Figure 6.7: FE rebar stresses at maximum load.

of specimen BPC-30-30-2 as reinforcement concentration limited the areas of appearance of spurious stresses.

Analysis case 2

This analysis case was at the other extreme of analysis case 1, resembling the hypotheses of the STM and more in accordance with the approach that a general practitioner would follow. It was the most simple of the six considered and, hence, led to least accurate results. Pile cap strengths were underestimated between 50% and 100% (table 6.2), which may be considered excessively conservative. Two of the adopted assumptions caused this deviation: (i) neglecting the tensile strength of concrete and (ii) dismissing the effect of the column. It is clear that the former assumption is conservative. The latter is in on the safe side for specimens whose failure is influenced by reinforcement yielding as it underestimates the inclination of the compressive stress flow.

The assumption of neglecting the tensile strength of concrete led to clear three-dimensional stress field, with well-oriented principal directions and with no presence of spurious compressive stresses (figures 6.8 and 6.9). FE principal compressive stress directions for specimen BP-20-30-2 show that part of the compressive stresses was supported on mid-span rebars, and then the vertical component was transferred from the rebar ends to the supports. Although a bit peculiar, this solution is statically admissible.

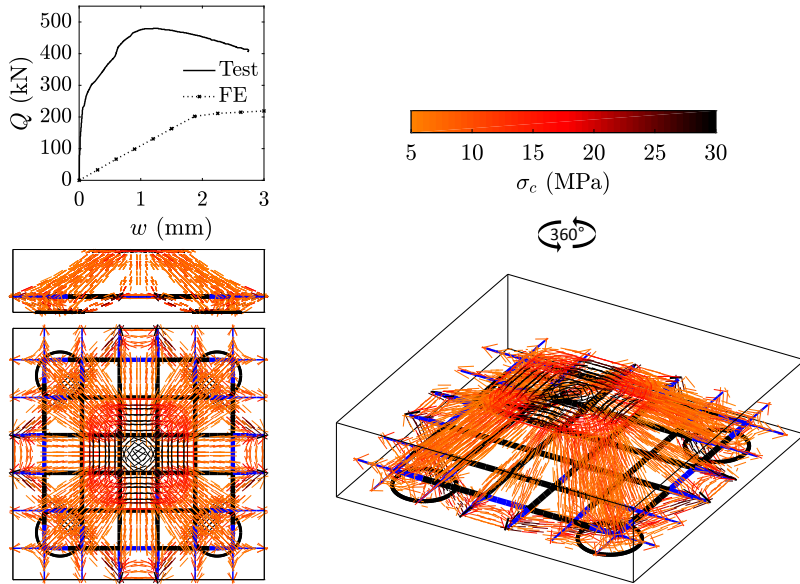


Figure 6.8: FE principal compressive directions for specimen BP-20-30-2 in analysis case 2. $P = 247\text{kN}$.

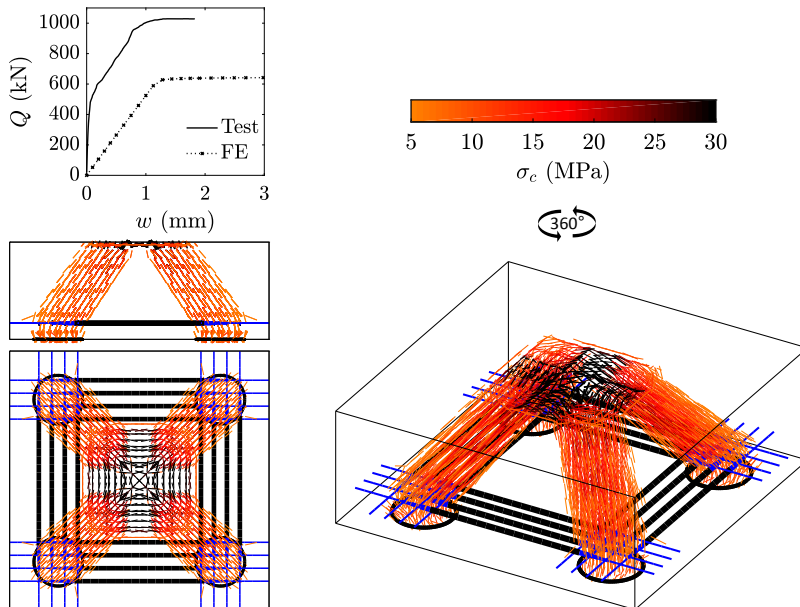


Figure 6.9: FE principal compressive directions for specimen BPC-30-30-2 in analysis case 2. $P = 646\text{kN}$.

Analysis case 3

Comparison of results obtained in analysis case 2 and 3 indicates that the consideration of the column effect improved predicted strength values significantly for all the specimens.

The effect on the compressive stress field can be seen in figures 6.10 and 6.11, with stresses concentrating at the column corners instead of the uniform distribution seen in figures 6.8 and 6.9. This means that the strut inclination increased compared to analysis case 2, and as failure was determined by reinforcement yielding in all specimens, predicted strengths increased.

FE steel stresses at the maximum load for specimens BP-20-30-2 and BPC-30-30-2 are plotted in figure 6.12. In specimen BP-20-30-2, with grid reinforcement, the two rebars closer to the edges (R1 and R2) had reached the yield stress. In specimen BPC-30-30-2, with bunched reinforcement over piles, all rebars had reached the yield stress at the maximum load, so it can be said that reinforcement capacity was being fully used. In this figure it is also seen that steel stresses were perfectly constant between the internal edges of the piles as in a truss model.

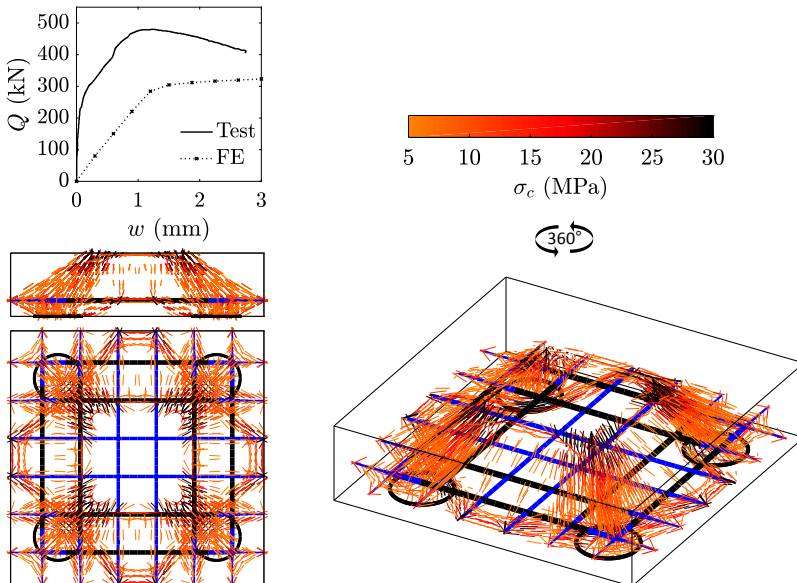


Figure 6.10: FE principal compressive directions for specimen BP-20-30-2 in analysis case 3. $P = 336\text{kN}$.

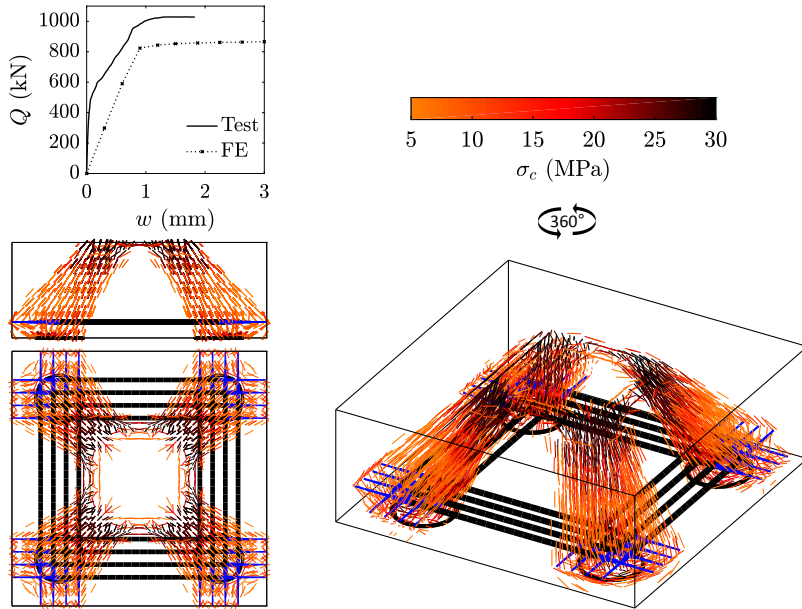


Figure 6.11: FE principal compressive directions for specimen BPC-30-30-2 in analysis case 3. $P = 879\text{kN}$.

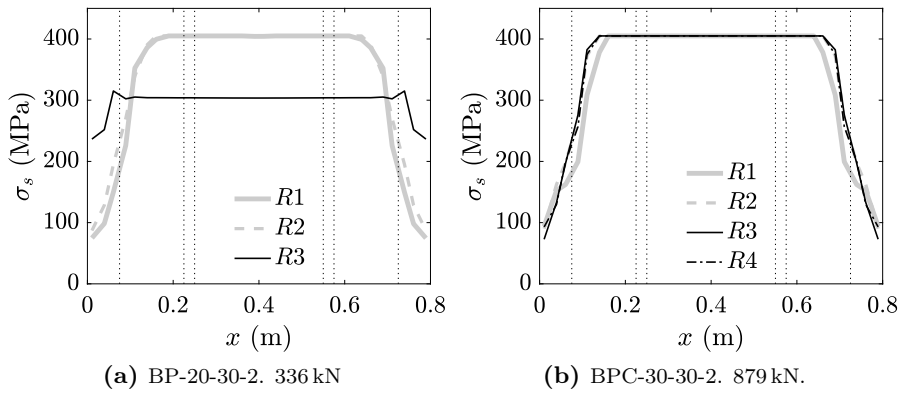


Figure 6.12: FE rebar stresses at maximum load.

Analysis case 4

Predicted maximum loads obtained when including the column explicitly in the FE model were close to, but lower than, those obtained in analysis case 3, where the column effect was accounted for by static condensation. As discussed later with analysis case 6, differences between both models derived from the fact that a linear elastic behaviour of the column was assumed when using static condensation, which may deviate from the real response at high load levels.

FE principal compressive stress directions obtained for specimens BP-20-30-2 and BPC-30-30-2 are plotted in figures 6.13 and 6.14, respectively and can be compared with those obtained in analysis case 3.

Analysis case 5

Compared to analysis case 2, consideration of tensile stresses in concrete led to significantly higher strengths for specimens with distributed reinforcement (BP), but the effect on specimens with bunched reinforcement over piles (BPC) was much lower, and, indeed, it was negligible on specimens BPC-30-25-2 and BPC-30-30-2. For BPC specimens, as reinforcement was concentrated, concrete tensile strains at non-reinforced areas were significantly large near the

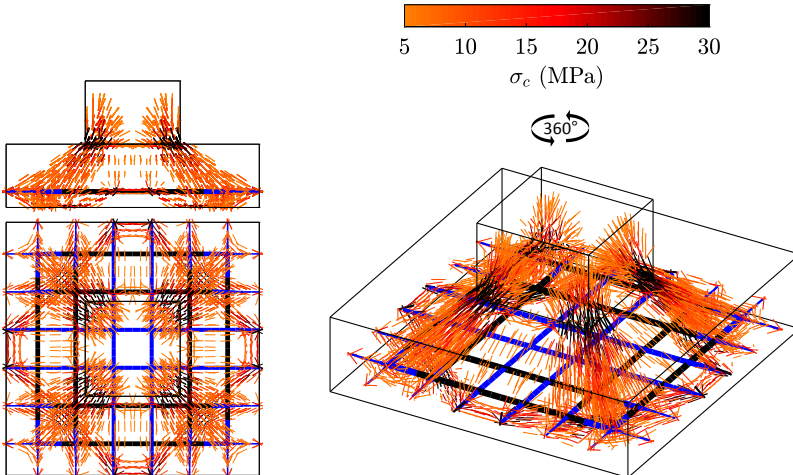


Figure 6.13: FE principal compressive directions for specimen BP-20-30-2 in analysis case 4. $P = 336$ kN

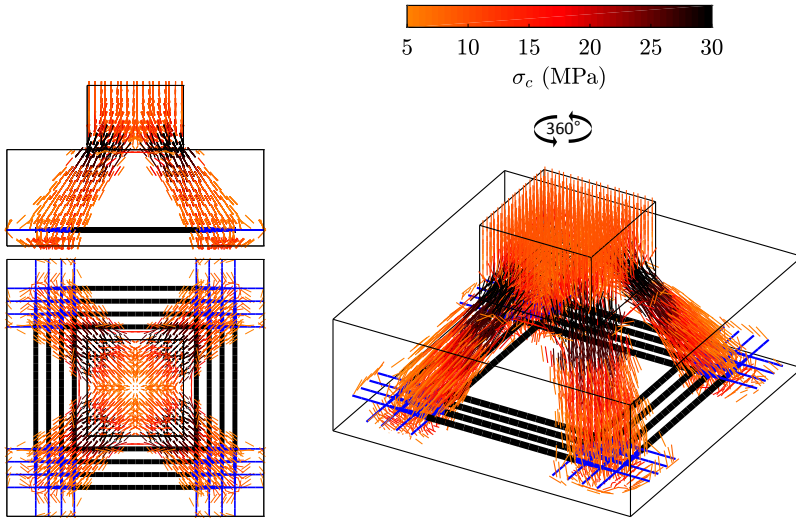


Figure 6.14: FE principal compressive directions for specimen BPC-30-30-2 in analysis case 4. $P = 855$ kN

maximum load, hence reducing the contribution of concrete in tension. Moreover, it must be noted that concrete softening due to transverse tensile strains was only considered with the refined concrete model and, therefore, includes a potential softening factor which was not accounted for in the simplified model of analysis case 2.

Analysis case 6

Compared to analysis case 1, considering the effect of the column by static condensation instead of by including it in the FE mesh affected only slightly the results. FE results obtained in analysis case 1 showed that the stresses on the interface column-cap influenced the response near the maximum load for some specimens as concrete at this interface started to crush after reinforcement yielding. Load model based on static condensation assumes a linear-elastic response and, therefore, these nonlinear effects are not accounted for. This led to higher predicted strengths in analysis case 6 compared to analysis case 1.

6.2.5 Conclusions

The obtained FE results showed that considering the stub column had a significant effect on the predicted results. Indeed, for specimens with concentrated reinforcement this effect was more important than considering or not the tensile stresses in concrete. These results highlight the importance of a proper modelling of the boundary conditions, rest importance to the adoption of complex concrete constitutive models and, hence, encourage the development of refined strut-and-tie models as that proposed later in Chapter 9.

Consideration of the tensile strength of concrete only affected the predicted maximum load of specimens with distributed reinforcement. However, if a realistic response prediction is to be obtained throughout the whole load history, tensile stresses in concrete need to be accounted for. Sound results fitting the experimentally measured load-displacement curves were obtained despite the relatively simplicity of the adopted constitutive model. The softening model proposed by Hordijk proved to be adequate to simulate the response after cracking.

Including the stub column, or any element interacting with the element object of study, permits to account for its nonlinear behaviour, which as shown above, may influence the response near the maximum load. However, it also imposes some restrictions on the FE mesh. Pile caps studied in this section had a square column section and the FE mesh could be adapted easily; it was only a bit more laborious to adapt the geometry when the column width changed. But if the column section had been circular and had been to be included in the FE mesh, such a regular FE mesh as that adopted here would not have been possible. It was proved here though, that the implemented model based on static condensation can be a good alternative as it does not affect the FE mesh.

6.3 Analysis of eight full-size pile caps

6.3.1 Introduction

Blévoit and Frémy (1967) reported the first experimental programme on pile caps. The purpose of their investigation was to study the adequacy of truss models to predict the strength of pile caps. This campaign is not only important for being one of the first, but also because represents still today the largest contribution to the existing experimental data base on pile caps. 116 specimens were tested, grouped as follows:

- 51 scaled four-pile caps
- 37 scaled three-pile caps
- 6 scaled two-pile caps
- 8 full-size four-pile caps
- 8 full-size three-pile caps
- 6 full-size two-pile caps

In order to prove the adequacy of FESCA 3D for the analysis of full-size specimens, FE results obtained for the eight full-size four-pile caps are shown in this section. It should be noted that most pile cap tested in literature were scaled to avoid difficulties in testing large specimens, so not many results on full-size specimens are available. However, pile caps may exhibit size effect and, therefore, it is important to check if the latter can be captured by the model.

6.3.2 Description of the specimens, experimental setup and test observations

Dimensions and characteristics of the eight full-size specimens considered can be found in figure 6.15 and table 6.3. Although it was not mentioned in the report, pictures of the specimens showed that the top of the cap was inclined, but only the maximum cap depth was given. The height of the stub column was not defined either. Four 350 mm × 350 mm piles supported the cap. In order to allow free rotation and displacement of the lower sections of the piles, Blévoit and Frémy (1967) planned initially to use a system formed by a steel sphere

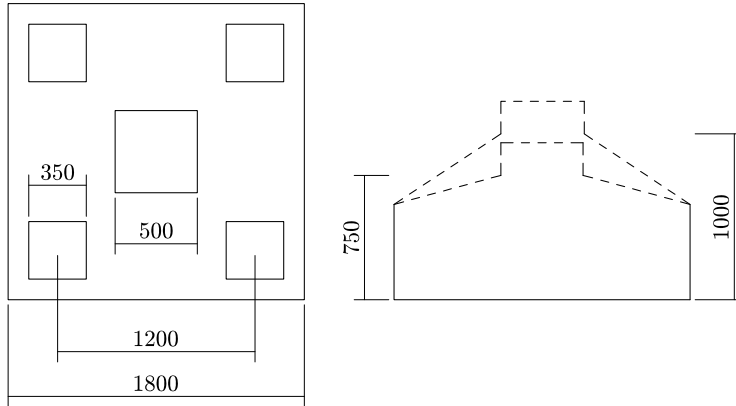


Figure 6.15: Geometry of specimens tested by Blévet and Frémy (1967).

Table 6.3: Summary of Blévet and Frémy (1967).

Specimen	h (mm)	f_{c0} (MPa)	Reinforcement	f_{sy} (MPa)	P_{test} (kN)	Fail.Mode
4N1	750	37.3	$4 \times 4\phi 32$ (B) $2 \times 7\phi 16$ (G)	276 279	7000	y+s
4N1bis	750	40.8	$4 \times 4\phi 25$ (B) $2 \times 7\phi 12$ (G)	443 517	6700	s
4N2	750	37.1	$4 \times 3\phi 32$ (B) $2 \times 4\phi 25$ (D)	279 300	6580	s
4N2bis	750	34.2	$4 \times 3\phi 25$ (B) $2 \times 4\phi 20$ (D)	498 475	7390	s
4N3	1000	34.2	$4 \times 2\phi 32$ (B) $4 \times 2\phi 25$ (B) $2 \times 8\phi 12$ (G)	251 281 293	6500	f
4N3bis	1000	49.3	$4 \times 2\phi 25$ (B) $4 \times 2\phi 20$ (B) $2 \times 8\phi 10$ (G)	485 446 430	9000	y+s
4N4	1000	35.4	$4 \times 4\phi 25$ (B) $2 \times 4\phi 25$ (D)	291 291	7530	y+s
4N4bis	1000	42.3	$4 \times 4\phi 20$ (B) $2 \times 4\phi 20$ (D)	486 486	8750	s

Reinforcement: (G)-grid reinf., (B)-bunched reinf.

Fail. mode: s-shear failure, f-flexural failure, y+s-shear failure after yielding.

and two rollers. This system caused some difficulties and was substituted by four 8 mm elastomeric pads on which piles were supported.

Two reinforcement configurations were adopted: (i) bunched reinforcement over piles (B) plus grid reinforcement (G), and (ii) bunched reinforcement over piles (B) plus diagonal bunched reinforcement (D) (table 6.3). Both plain, mild steel rebars and corrugated, high yield strength rebars were used.

Maximum loads measured during the tests are given in table 6.3. Modes of failure were judged based on the observations at failure described in the reference as follows: those failures triggered at one of the piles were classified as shear (s) if no reference was made to wide crack openings, assuming that the latter were not excessively large; those failures triggered at one of the piles with wide crack openings on the side faces were classified as shear failures after yielding (y+s); and failure of specimen 4N3, the only one classified as flexural (f), was identified as such because vertical cracks on the side faces were widely open at failure.

6.3.3 FE model

Some assumptions needed to be undertaken when developing the FE model as the information provided in the reference was not complete. The inclination of the cap top surface was disregarded, assuming a cuboid geometry. A mesh formed by 623 twenty-node hexahedrons was adopted. The stub column was included in the FE mesh assuming a height equal to 200 mm based on the pictures. The load was applied at its top assuming a uniform stress distribution. It was assumed that the height of the piles (which was not defined) was long enough so the stress distribution at the cap interface was uniform and that the resistance to rotation and horizontal displacement at its bottom was negligible. Similarly to the previous example, the uniform-stress support model described in Chapter 5 was adopted for the four supports. The vertical stiffness of each support was taken equal to $4 \times 10^5 \text{ kN m}^{-1}$ (any other relatively large value could have been used) and the horizontal resistance was dismissed.

Only one analysis case was considered. Concrete in tension was modelled by a linear elastic branch up to cracking and by a softening branch afterwards following the model by Hordijk (1991), with $f_{ct} = 0.21(f_{c0} - 8)^{2/3}$, $E_c = 21\,500(f_{c0}/10)^{1/3}$ and $G_f = 73f_{c0}^{0.18}$ (G_f in N/m). In compression, the nonlinear model by Popovics (1973) was adopted. Strength enhancement due to confinement was considered through a Drucker-Prager yield surface and softening due to transverse tensile strains was accounted for through the for-

mulation proposed by Vecchio and Collins (1986). This concrete model was hence the same as the refined model considered in the previous example of this chapter.

Reinforcing bars were introduced individually. It was assumed that they spanned the whole cap length/diagonal. Perfect bond between concrete and steel was assumed. Embedded rebar FEs were generated as three-node bar elements. Steel was modelled as elastic-perfectly plastic.

A displacement-controlled method was used to determine subsequent load increments. An energy norm criterion (1%) was adopted to determine convergence of the iterative process.

6.3.4 FE results

Predicted maximum loads and modes of failure based on FE results are given in table 6.4. Predicted modes of failure were judged from the FE load-displacements curves (figure 6.16) and FE rebar and concrete stresses as described below.

All strength predictions are close to the experimental ones, except for specimens 4N2bis and 4N3bis, which present strength ratios P_{test}/P_{FE} slightly deviated from the rest (1.17 and 1.16, respectively). Factors which could have caused this difference are discussed later in this section.

Table 6.4: FE predictions for Blévet and Frémy's specimens.

Specimen	P_{FE} (kN)	$\frac{P_{test}}{P_{FE}}$	Fail.Mode
4N1	6588	1.06	y+s
4N1bis	6721	1.00	y+s
4N2	6518	1.01	y+s
4N2bis	6296	1.17	s
4N3	6577	0.99	f
4N3bis	7728	1.16	f
4N4	7868	0.96	y+s
4N4bis	8497	1.03	s

Mode of failure: s-shear failure, f-flexural failure, y+s-shear failure after yielding.

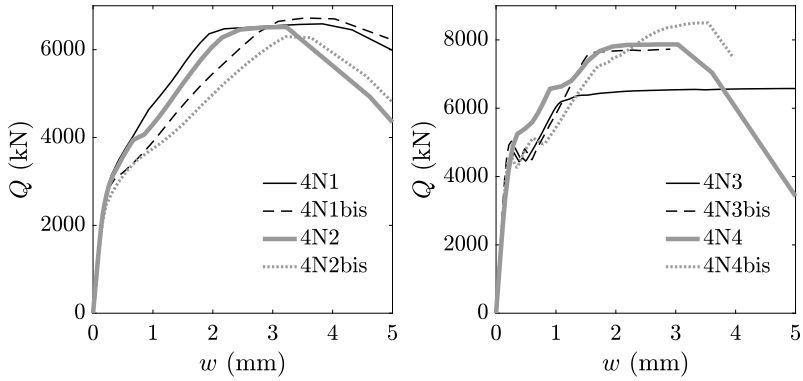


Figure 6.16: FE load-displacements curves for Blévet and Frémy specimens.

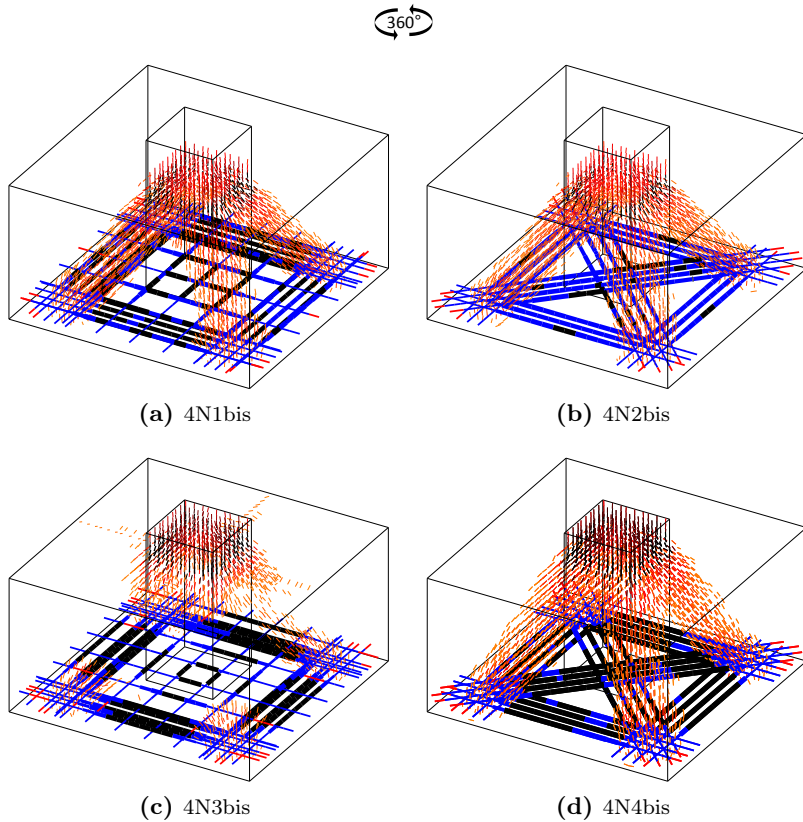


Figure 6.17: FE compressive stress directions for Blévet and Frémy specimens at maximum load. In black, yielded rebars.

Except specimens 4N2bis and 4N4bis, all elements exhibited a horizontal plateau at the maximum load, indicative of apparent reinforcement yielding at maximum load. This was confirmed by looking at FE rebar stresses. Principal compressive stress directions for four of the specimens at maximum load are plotted in figure 6.17, where yielded rebar segments are marked in black. Except in specimen 4N2bis, the majority of reinforcing bars had yielded when reaching the maximum load. A more detailed description on the identification of the mode of failure for specimens 4N2bis, 4N3bis and 4N1 is given next.

The maximum load in specimen 4N2bis was limited by concrete failure of the inclined strut. This can be seen in figure 6.18 showing three different contour plots representing the stress and strength state of concrete in compression on the cap diagonal plane when reaching the maximum load. Based on these results it can be stated that the capacity of the strut was exceeded when reaching the maximum load (figure 6.18b) with a significant strength reduction due to tensile strains transverse to the inclined strut (figure 6.18c). The load could not be increased further even when the rebars had still capacity left (figure 6.17b). This type of failure was identified as shear. No pictures were

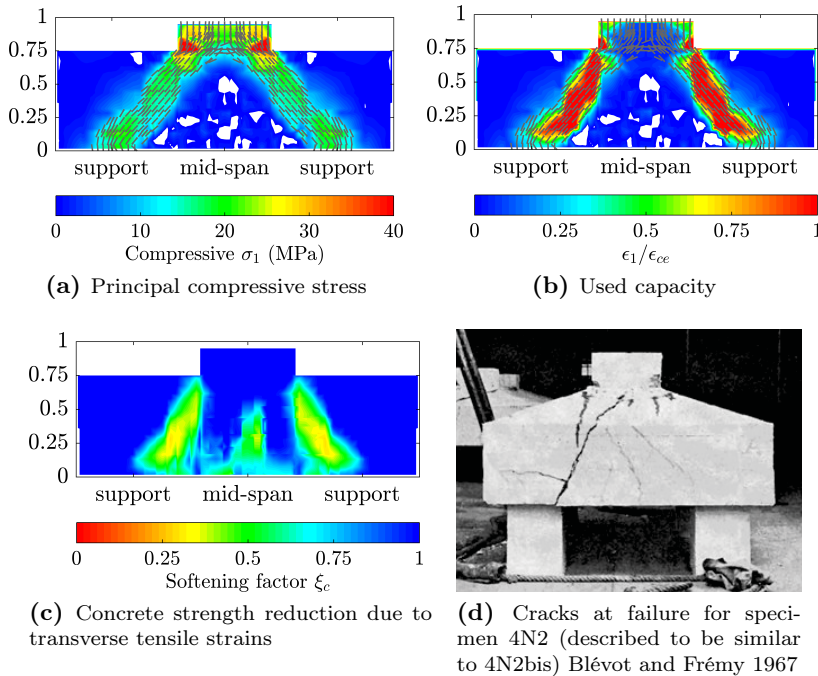


Figure 6.18: FE results for specimen 4N2bis at maximum load on the diagonal plane.

provided of specimen 4N2bis after failure, but it was said in the reference that it was similar to that of specimen 4N2, which is given here for reference (figure 6.18d). Cracks in this figure are consistent with FE results showing exhaustion of the strut capacity. After noting that the specimen failed in shear, the difference observed between FE predicted and experimental strength may be justified by the difficulties inherent of this type of failure.

The FE load-displacement curve of specimen 4N3bis exhibited a long plateau after reaching the maximum load, with all rebars having yielded. This was identified as a flexural failure. FE results plotted in figure 6.19 show that the inclined strut had still sufficient additional capacity to increase the load

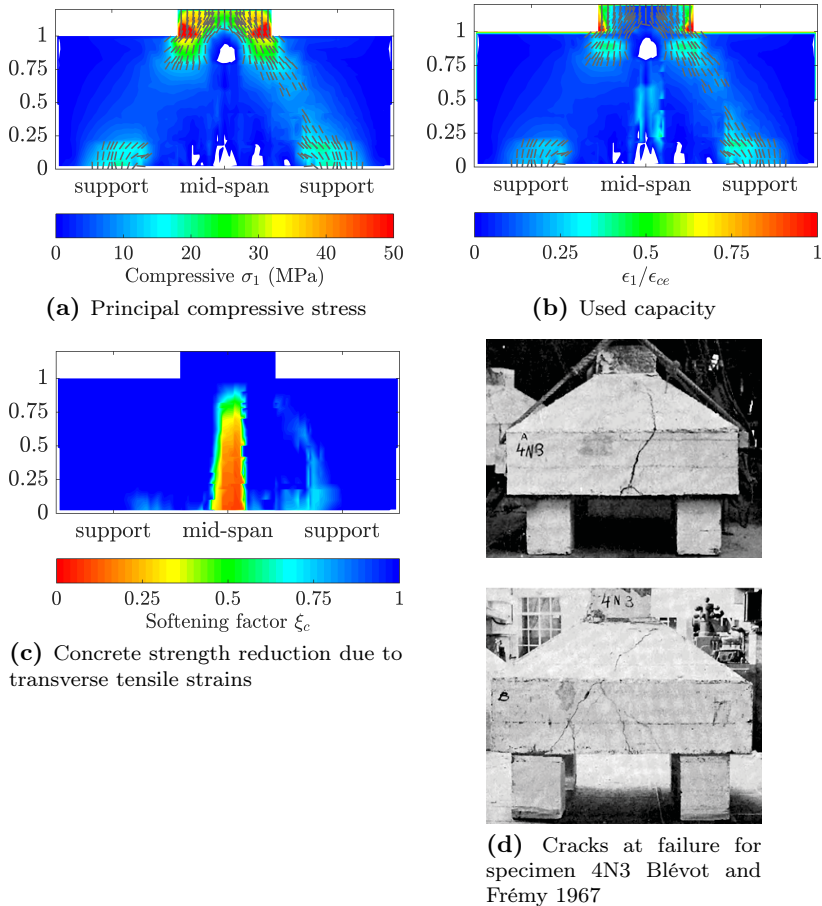


Figure 6.19: FE results for specimen 4N3bis at maximum load on the diagonal plane.

further and its strength had not been weakened by transverse cracking, which concentrated only at mid-span areas. The presence of a long vertical crack can be inferred from figure 6.19c. No pictures were provided of specimen 4N3bis after failure. Cracks at failure for specimen 4N3 are given for reference (figure 6.19d). FE predicted strength was significantly lower than the experimental one (7728 kN vs. 9000 kN). This difference might be explained by having assumed in the model a constant stress distribution at the pile-cap interface and not having considered frictional forces at the supports. Support conditions in the tests by Blévoit and Frémy (1967), especially for the full-size specimens, were not as ideal as in Suzuki, and it is likely that stress distribution at the top of the piles was not constant, but leaning slightly inwards, as it was seen in Chapter 5 when discussing different flexible support conditions. As mentioned in this chapter, a slight deviation of the reaction can cause a significant variation of the tie force. As for this specimen the maximum load was limited merely by reinforcement yielding, the predicted strength was significantly underestimated.

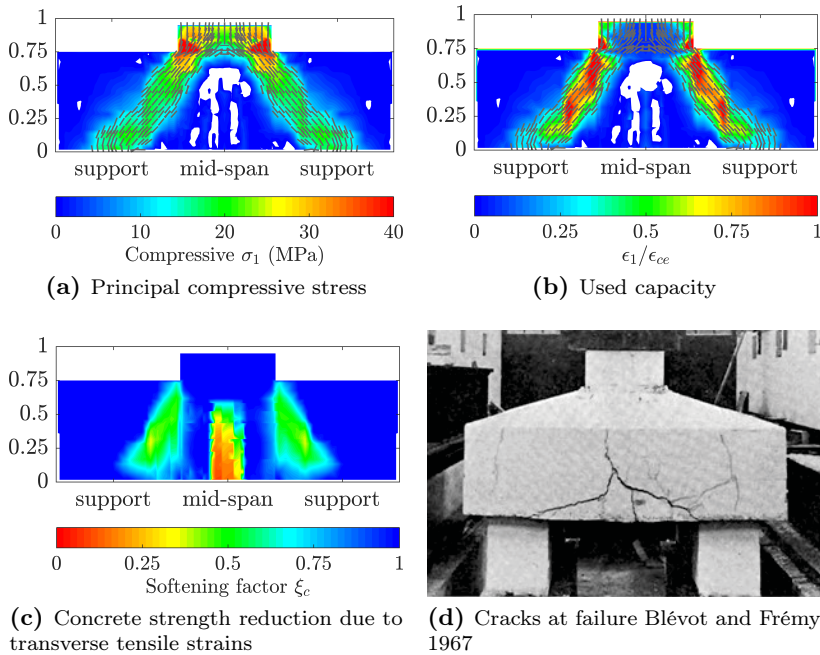


Figure 6.20: FE results for specimen 4N1 at maximum load on the diagonal plane.

The FE load-displacement curve of specimen 4N1 presented a plateau, but significantly shorter than that of specimen 4N3. Most rebars had yielded when reaching the maximum load. FE results on the diagonal plane (figure 6.20) are similar to those of specimen 4N2bis, but in this case the strut strength was not completely exhausted and, therefore, the load did not fall straight after the maximum. But with further displacement increments, as transverse tensile strains increased, the load started to fall. This failure was identified consequently as shear failure after yielding.

6.4 Conclusions

This chapter was presented to prove the adequacy of FESCA 3D for the analysis of 3D D-regions. Pile cap specimens were considered as this is the 3D D-region for which a more extensive experimental data base exists.

The accuracy of the predictions of any tool depends on the conditions adopted in the model, as it was shown in section 6.2 where results obtained in six different analysis cases were presented. Although it is acknowledged that the size of the considered sample is too small, it should be noted that FESCA 3D is a tool, and as such, the accuracy of its predictions will depend on the adopted model.

FE results obtained with FESCA 3D in the analysis of fourteen pile cap specimens showed the adequacy of the developed tool for the analysis of this 3D D-region. Strength predictions obtained when adopting a relatively refined concrete model including tensile stresses in concrete were very close to the experimental ones.

Different analysis cases were considered in the first example of application, showing the importance of considering the effect of the stub column to obtain sound predictions. Indeed, this factor was more determinant than the consideration of tensile stresses in concrete for some of the specimens. The analysis of eight full-size specimens focused on the identification of the modes of failure based on FE results. In general predicted modes of failure proved to be consistent with experimental observations despite the difficulties to classify some of the observed modes of failure.

Chapter 7

Analysis of socket base column-to-foundation connections

The stress field in a body (and consequently its overall behaviour) depends on the actual reinforcement layout and is thus not exclusively determined by its geometry and load pattern.

—Fernández Ruiz and Muttoni 2007

7.1 Introduction

Another frequent 3D D-region are socket base column to foundation connections, whose use in construction is increasing with the growth of precast concrete structures. This element consists in a concrete block, which can be cast-in-situ or precast, with a cavity in its upper part where a precast column is embedded. Its behaviour is often misunderstood and it is frequently designed by inconsistent rules of thumb or based on past experience. Consideration of 3D strut-and-tie models can be a more rational approach leading to more optimal designs.

One of the advantages, but also complications, of the STM is that there is no unique solution. The proposal of a rational strut-and-tie model for simple elements like pile caps is straightforward, but can entail more difficulties for more complex elements like socket base column-to-foundation connections. The ade-

quacy of the STM for the design of these elements and the effectiveness of different reinforcement arrangements was studied in two research projects conducted inside the group (projects BIA2009-11369 and BIA2012-32300)(Gutiérrez Vela 2015). Three alternative strut-and-tie models were proposed, from which nine different reinforcement configurations were derived. Test results showed that some strut-and-tie-based configurations were more efficient than others, but all of them improved the strength of the element designed according to general practice design.

Results from linear FE analysis can be used to derive strut-and-tie models from the elastic stress trajectories (J. Schlaich, Schafer, and Jennewein 1987), but this approach does not account for the stress redistribution due to material nonlinearities, mainly caused by concrete cracking. Nonlinear FE analysis can be a more appealing approach, but requires to know the reinforcement geometry in advance. Results obtained for three representative specimens tested by Gutiérrez Vela (2015) are presented in this chapter to show the capacity of FESCA 3D to generate automatically rational nonlinear stress fields, which vary consistently depending on the reinforcement arrangement, and from which 3D strut-and-tie models can be easily derived. These results are compared with those obtained from linear FE analysis.

7.2 Description of the specimens, experimental setup and test observations

The experimental campaign referred hereafter was led by Dr. Pedro F. Miguel and Dr. Luis Pallarés and conducted by Moisés Gutiérrez at Instituto de Ciencia y Tecnología del Hormigón (ICITECH) at Universitat Politècnica de València (figure 7.1). A brief description is given here. More detailed information can be found in the reference (Gutiérrez Vela 2015).

The experimental campaign consisted of ten full-size specimens of dimensions $1.4\text{ m} \times 1.4\text{ m} \times 1\text{ m}$ (xyz) with a cavity located centrally at its upper part of $0.6\text{ m} \times 0.5\text{ m} \times 0.6\text{ m}$ (xyz). Three base strut-and-tie models were proposed to design the reinforcement (figure 7.2). A force system formed by a pair of horizontal forces and a vertical load, acting on two opposite vertical walls and at the bottom of the cavity, respectively, was considered to account for both the axial force and the bending moment transferred by the column. Strut and tie forces were determined assuming a value of 690 kN for the two horizontal loads and 550 kN for the vertical load.



Figure 7.1: Test view (Gutiérrez Vela 2015).

Nine different reinforcement layouts were configured from these three models. Reinforcement in specimens X2, X3 and X7 was established directly from models 1, 2 and 3, respectively. Reinforcement in specimens X4, X5, X6, X8, X9 and X10 was obtained combining two of the strut-and-tie models with different contribution percentages (80%-20%, 50%-50% or 20%-80%). And specimen X1 was designed in accordance with general practice design. A design yield stress of steel equal to 550 MPa was assumed to calculate the required steel quantity. $\phi 8$, $\phi 12$, $\phi 16$ or $\phi 20$ mm rebars were considered. Only specimens X2, X3 and X7 were analysed in this chapter as they were considered representative of the others.

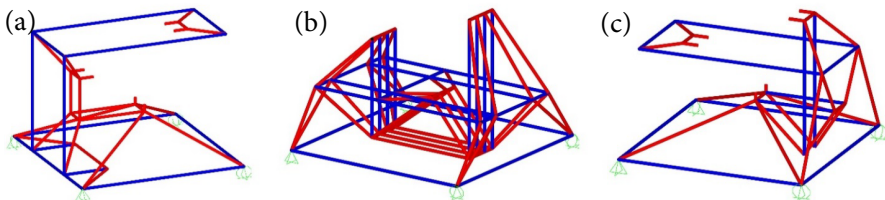


Figure 7.2: Proposed base strut-and-tie models: (a) Model 1, (b) Model 2, (c) Model 3. (Gutiérrez Vela 2015)

Loading was applied by means of a reusable steel column, as the objective was to study the response of the foundation element rather than the interaction with the column. Two horizontal loads on the vertical walls of the hole and one vertical load at the base of the cavity were transferred to the foundation element by applying an eccentric load on the column. Two vertical and one horizontal steel plates were used to fix the contact points between the column and the cavity at the walls and at the base, respectively. Eight load cells were employed to measure the loads transferred to the block: two at each vertical plate and four at the horizontal plate.

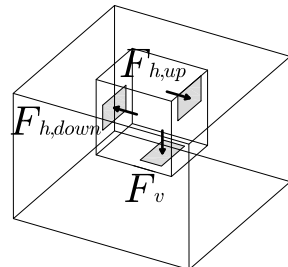
The block was supported at its bottom corners on 150 mm × 150 mm steel plates. The horizontal displacement was restrained to limit displacements caused by unbalanced horizontal loads introduced by the inclination of the column.

The uniaxial compressive strength of concrete and the total amount of reinforcement for the considered specimens are given in table 7.1. Measured forces applied by the column at the moment of failure are also given in this table ($F_{h,down}$ for specimen X7 was not given in the reference due to failure of one of the load cells). Failure was defined by the moment when the horizontal upper load $F_{h,up}$ was maximum.

Experimental results showed that specimen X7 (corresponding to strut-and-tie model 3) was the most efficient of the three as it provided the largest strength with the lowest amount of reinforcement. However, it must be acknowledged that the contribution to this strength increment of its higher compressive strength was difficult to assess.

Table 7.1: Column forces at failure (after (Gutiérrez Vela 2015))

Specimen	f_{c0} (MPa)	Steel (kg)	$F_{h,up}$ (kN)	$F_{h,down}$ (kN)	F_v (kN)
X2	28.0	124	861	908	770
X3	27.4	142	753	-	843
X7	43.1	99	934	950	1020



7.3 Finite element model

An FE mesh of 1875 twenty-node hexahedrons was adopted for the three specimens (figure 7.3a). Four 150 mm \times 150 mm vertically-fixed supports were defined at the corners. Three horizontal degrees of freedom were restrained as well to avoid rigid body displacements. Loading areas were defined considering the dimensions and locations of the steel plates used in the test to fix the contact between the column and the block. The centre of gravity of the vertical load was moved 80 mm-right from the centre to account for the eccentricity observed in the test. It was further assumed that the relation between the two horizontal and the vertical load introduced by the column was constant for each specimen and equal to that observed at failure (for specimen X3 it was assumed that both horizontal loads were equal).

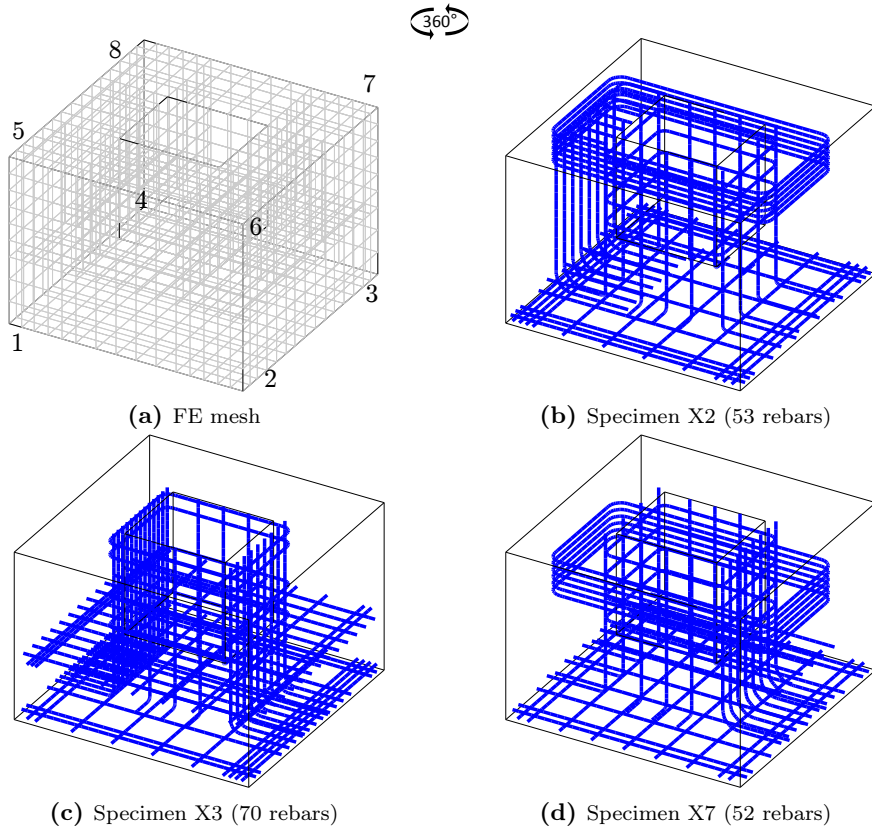


Figure 7.3: FE model for socket base column-to-foundation connections.

Reinforcement bars were introduced one by one and considering bending radii equal to 6ϕ (figures 7.3b, 7.3c, 7.3d). Perfect bond between concrete and steel was assumed. An elastic-perfectly plastic model was adopted for steel with $f_{sy} = 530$ MPa and $E_s = 200\,000$ MPa.

7.4 Finite element analysis

J. Schlaich, Schafer, and Jennewein (1987) proposed to treat both the ultimate and service limit state with one unique strut-and-tie model in order to guarantee a sound response in both states. The geometry of the strut-and-tie model was to be obtained by orienting the truss geometry at the elastic stress fields, i.e. struts and ties must be arranged parallel to the principal compressive stress directions and principal tensile stress directions, respectively. This approach can be adequate to propose a first strut-and-tie model, but does not account for the stress redistribution near the ultimate state. Moreover, for complex elements the elastic stress trajectories may be excessively diffused to infer a clear resisting mechanism.

Results obtained from nonlinear analysis considering stress distribution due to concrete cracking can be more conclusive regarding the flow of forces near the ultimate state. For this analysis it is necessary to define the reinforcement geometry, which will influence the stress field within the body.

Linear and nonlinear FE results obtained for specimens X2, X3 and X7 are presented in this section to show the differences between both analyses.

7.4.1 Linear elastic analysis

An isotropic, elastic model was adopted for concrete, with $E_c = 21.5 (f_{c0}/10)^{1/3}$ (f_{c0} in MPa, E_c in GPa) as proposed in MC 2010 (Fédération Internationale du Béton 2013).

Obtained FE principal compressive and tensile stress directions for an upper horizontal load of 700 kN are represented in figure 7.4. It was already known that the influence of the reinforcement arrangement was going to be negligible in the elastic analysis, as the elastic stress field is determined almost uniquely by the geometry of the concrete element (and the loads and supports). Despite this, results for the three specimens X2, X3 and X7 are plotted to highlight later the differences with nonlinear analysis results. Only one half of the specimen was represented, permitting a better visualisation of the internal stress field.

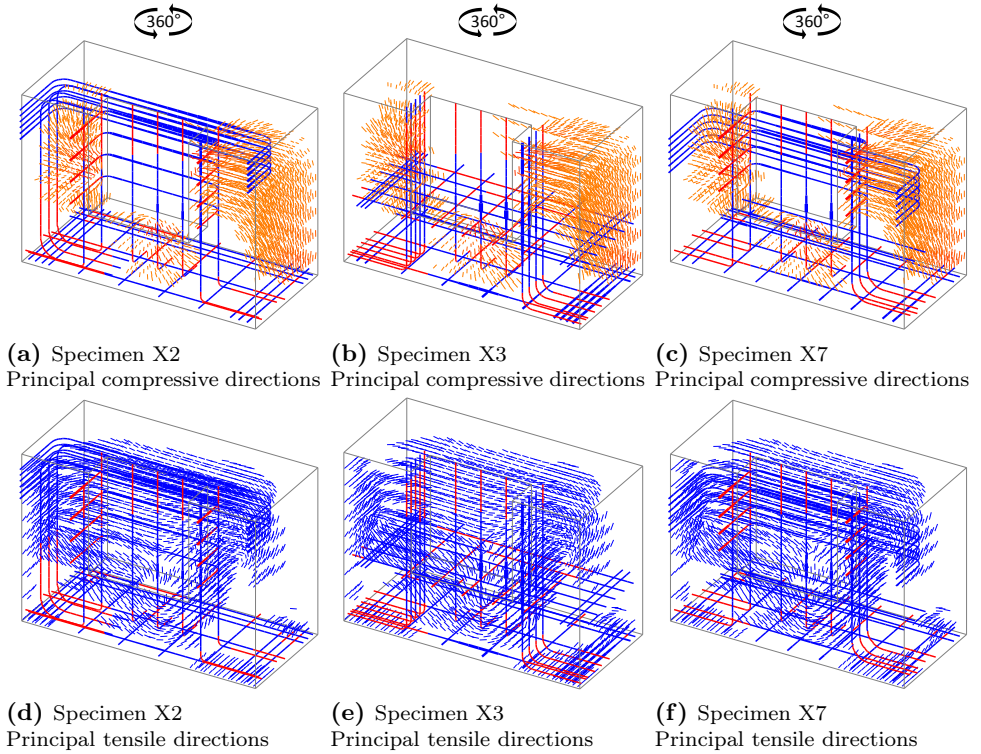


Figure 7.4: Linear FE results for socket base column-to-foundations connection specimens.

Only principal directions of integration points where the compressive or tensile principal stress was larger than 1 MPa, and with a maximum of 10 integration points per FE, were plotted for clarity reasons.

Elastic FE results for the three specimens are practically identical, as it was expected. Indeed, it would have not been necessary to define any reinforcement for the linear elastic analysis. The principal compressive stress trajectories are rather diffused and the identification of strut elements from these results seems tough. The principal tensile stress directions were not conclusive either, although it is seen that major tensile stresses appear around the cavity and below it.

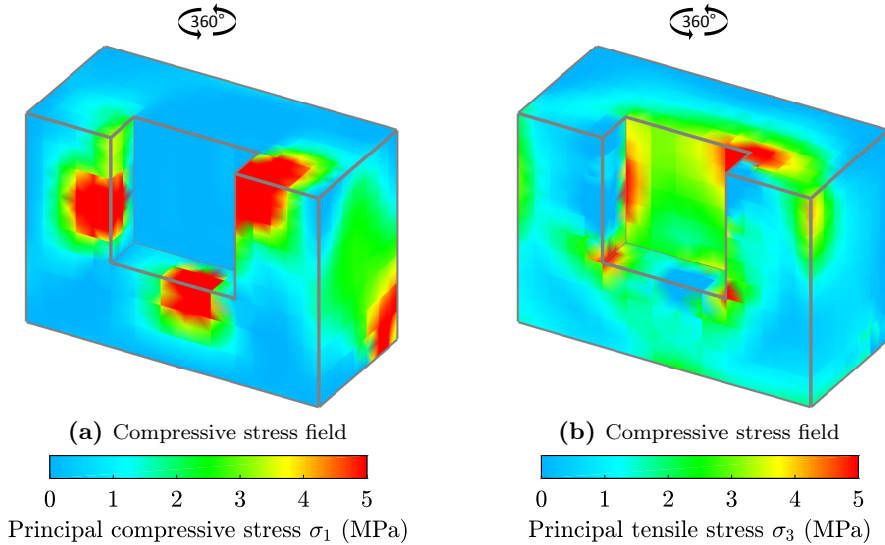


Figure 7.5: Elastic stress fields for socket base column-to-foundation connection X2.

The compressive and tensile stress fields in figure 7.5 show the magnitude of the obtained elastic stresses for specimen X2 (almost identical representations were obtained for specimens X3 and X7). From this figure and the previous one, it can be inferred that:

- reinforcement should be concentrated below the cavity and, especially, around the cavity, where the largest tensile stresses concentrate
- vertical reinforcement should be provided at the front wall ¹ to deviate the horizontal upper load to the supports of the front
- horizontal reinforcement should be provided between supports at the front wall and at the back wall ²
- an inclined tensile stress trajectory goes from the back wall to the front. Materialisation of this tie is not doable though as using inclined rebars is against practical reinforcement arrangements. Therefore, an alternative load path must be found

¹Wall parallel and closer to face 2367 (figure 7.3a)

²Wall parallel and closer to face 1458 (figure 7.3a)

The main advantage of the elastic analysis is that reinforcement slightly affects the results and, therefore, it is not necessary to propose or know the reinforcement geometry in advance. However, although elastic FE results provided a better understanding of the element behaviour and clarified which areas should be obligatorily reinforced, the identification of the internal resisting mechanism and flow of forces can still be uncertain for the less experienced engineer. The proposal of strut-and-tie models such as those developed by Gutiérrez Vela (2015) does not seem straightforward without further reasoning.

7.4.2 *Nonlinear finite element analysis*

Nonlinear FE results obtained for the same three specimens are presented in this subsection. Contrary to the linear elastic analysis, the consideration of the reinforcement arrangement was mandatory and, as shown later, decisive for the results.

A simplified concrete constitutive model was considered. Concrete tensile strength was neglected. In compression, an elastic-perfectly plastic model was adopted, with $f_{cp} = 2.7f_{c0}^{2/3}$ and $E_c = f_{cp}/0.0023$. Concrete softening due to transverse cracking was not accounted for. Strength enhancement due to confinement effect was considered by means of a Drucker-Prager yield surface. This simple constitutive model was considered sufficient for the purpose of this chapter.

FE principal compressive stress directions obtained for the three specimens for an upper-horizontal load of 700 kN are plotted in figures 7.6, 7.7 and 7.8. Compared to linear elastic results, the internal flow of forces is now clearly visible and derivation of the corresponding strut-and-tie model is straightforward from these results. Tensile forces in reinforcing rebars are now necessary for the internal equilibrium as concrete cannot sustain tensile stresses and, therefore, the reinforcement layout affects the compressive stress flow and, hence, the resulting strut-and-tie model. These strut-and-tie configurations are in accordance with those initially proposed by Gutiérrez Vela (2015) and from which reinforcement was determined (see figure 7.2).

Although it was not the main purpose of the analyses to predict the maximum strength of the elements, comparison of numerical and experimental results can still be of interest. The maximum upper horizontal loads predicted by FESCA 3D for specimens X2, X3 and X7 were 811 kN, 810 kN and 878 kN, respectively. These values can be compared with the experimental ones in table 7.1. Considering the complexity of the test and the simplifications and

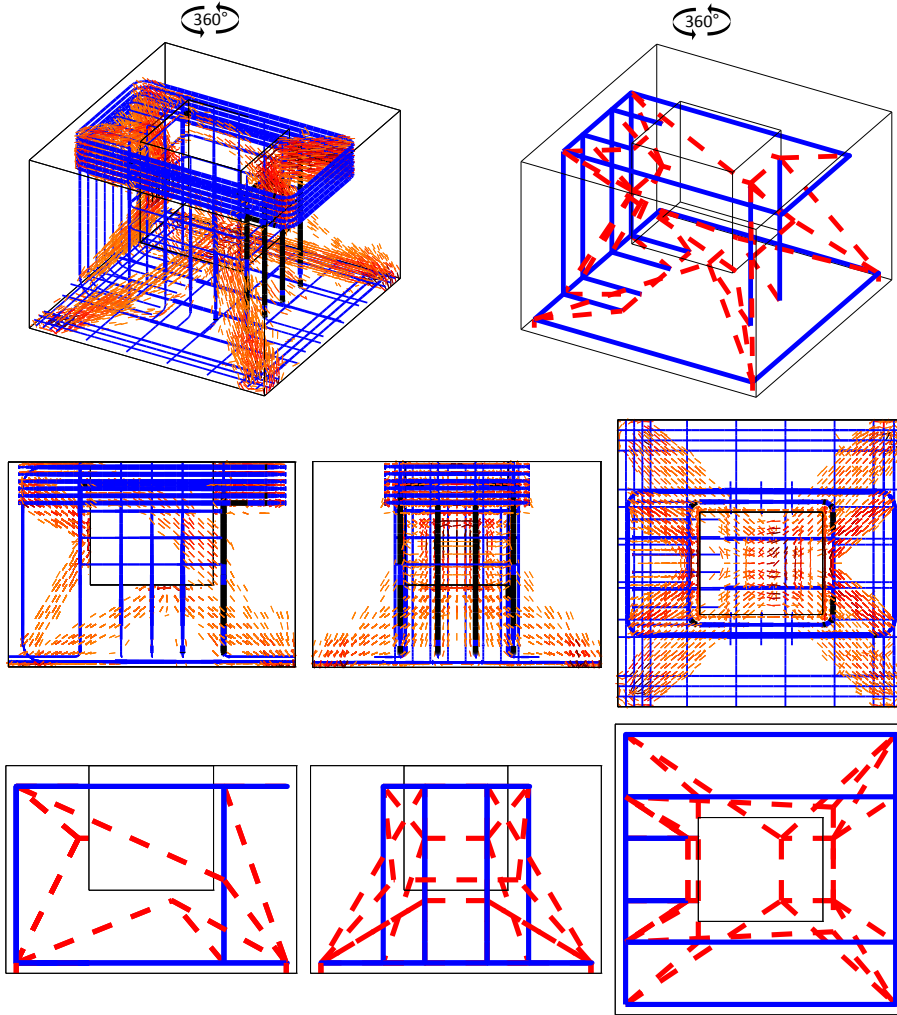


Figure 7.6: FE results and STM model for specimen X2.

assumptions undertaken in the model, differences between predicted and experimental strengths are acceptable. Strength in specimens X2 and X7 was limited by yielding of the horizontal stirrups around the cavity, whose initiation can already be observed in figures 7.6 and 7.8. The maximum load of specimen X3 was limited by yielding of the horizontal rebars under the cavity in the longitudinal direction, whose initiation can already be observed in figures 7.7, and the vertical rebars at the front wall. These failure modes are in agreement with experimental observations.

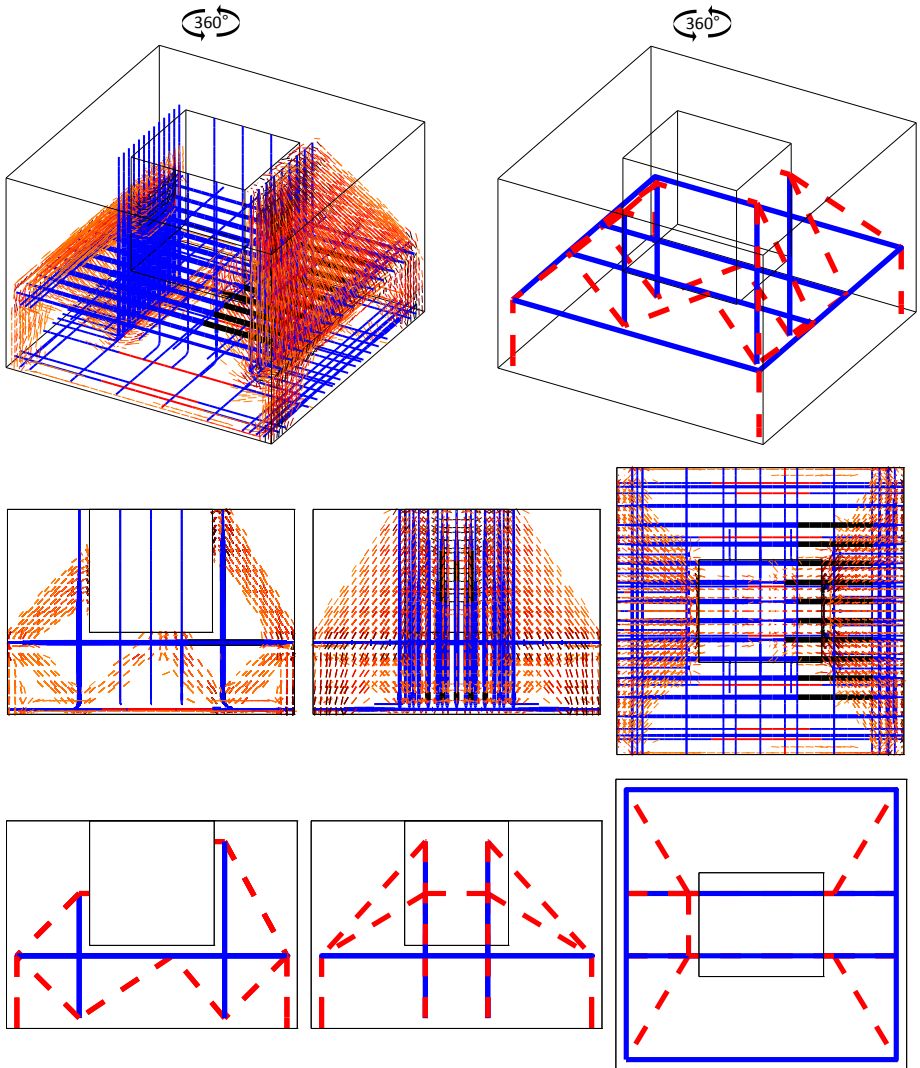


Figure 7.7: FE results and STM model for specimen X3.

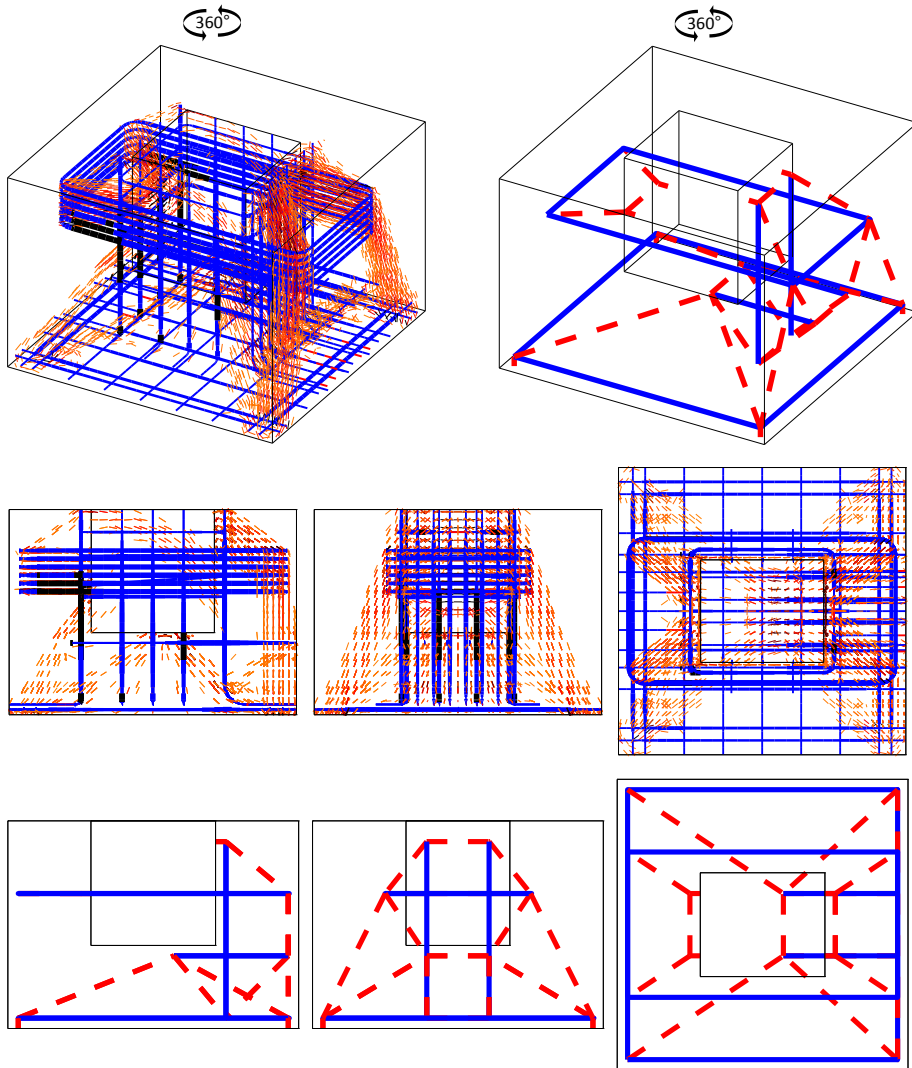


Figure 7.8: FE results and STM model for specimen X7.

7.5 Conclusions

The capacity of FESCA 3D to generate automatically rational three-dimensional stress fields which are consistent with the introduced reinforcement geometry was demonstrated. Representation of the principal compressive stress directions obtained from nonlinear FE analysis facilitates the proposal of rational 3D strut-and-tie models.

Comparison of linear and nonlinear results showed that the latter leads to the generation of clearer stress fields than the former and, therefore, facilitates a better understanding of the resisting mechanism. It must be noted though that, contrary to linear FE analysis, nonlinear FE analysis requires the definition of the reinforcement, which is the main unknown in design. Reinforcement configuration could have been determined based on a 3D strut-and-tie models (as in Gutiérrez Vela (2015)) or based on past experience. When the former, nonlinear FE results could then be useful to confirm the adequacy of the proposed model and, ultimately, to point out deficiencies of the model or alternative load paths. When the latter, nonlinear FE results could clarify if the proposed reinforcement is rational at all. Additionally, the practitioner could reasonably introduce rebars at different locations and observe how this affect the stress field. This seems a rather trial and error approach, but still not prohibitive thanks to the functions implemented permitting a flexible definition of the reinforcement. A more appealing approach is presented in Chapter 8, where the user introduces rebars at diverse locations without much reasoning and then the implemented design algorithm eliminates rebars that are not required and calculates the area of the others.

This example also showed the importance of the reinforcement layout in the resulting stress field within the body. There is not a unique solution, but the final response of the element will be determined by the reinforcement geometry.

The specimens considered in this example had a relatively large number of reinforcing bars, some of them with curved geometries. Thanks to the comprehensive reinforcement model implemented in FESCA 3D, introducing all these rebars one by one was not a limitation and, hence, it was possible to account for more realistically the actual reinforcement geometry.

Although it was not the main purpose of the analysis, predicted strengths were acceptable when compared with experimental values. Test results were not conclusive regarding the contribution of the tensile strength of concrete to the capacity of the elements. The numerical model did not account for this contribution and still provided not-excessively conservative results. It must

be noted that the maximum load in the three specimens was limited by steel yielding, and it is believed that the contribution to this resisting mechanism of potential concrete ties at those strain levels was probably negligible.

Chapter 8

Analysis and design of an anchorage block

Designers are often uncomfortable with the flexibility allowed by the STM. This concern increases with the complexity of the design, especially as the number of truss elements becomes large and if the truss is highly statically indeterminate.

—J.-w. Park et al. 2010

8.1 Introduction

Anchorage zones are typical D-regions where the prestressing force is treated as a concentrated load acting on the concrete element. A rational design is important to avoid local failures and to facilitate an effective spread out of the prestressing forces over the entire cross-section. Strut-and-tie models facilitate the development of consistent reinforcement arrangements.

Tendons can be positioned inside the concrete section or external to it. When the latter, auxiliary anchorage elements are cast at certain sections to transfer prestressing forces to the main structure. The dimensions of these elements are relatively small compared to the global dimensions of the structure and they are subjected to large forces giving for complex stress states. 3D strut-and-tie models can be useful for understanding the internal resisting mechanisms and for determining the required reinforcement quantities, but their proposal can entail difficulties. An example of application of the STM for the design of anchorage blocks was presented by Bajo and Pérez-Fadón (2002) as part of the

design of a concrete box girder bridge. Assuming a statically indeterminate system of reactions induced by the web and the bottom slab of the bridge, these authors proposed a 3D strut-and-tie model, determined the element forces and calculated the required reinforcement quantity. Their approach was relatively simple despite the complexity of the problem, but also subjected to some uncertainties, starting from the determination of the element forces in a statically indeterminate system.

This chapter presents the application of FESCA 3D for the design of an anchorage block following the example studied by Bajo and Pérez-Fadón (2002). Firstly, a simplified FE model is developed resembling truss model conditions following the structural model proposed by Bajo and Pérez-Fadón, i.e. similar reaction locations and directions (see section 8.3.1). Acknowledging the benefits, but also limitations of this model, a second, more realistic FE model is proposed afterwards to take advantage of further options offered by FESCA 3D (see section 8.3.2). The capacity of FESCA 3D for automatically obtaining a rational reinforcement arrangement by eliminating or reducing the area of less demanded rebars is shown in both FE models.

8.2 Description of the structural model proposed by Bajo and Pérez-Fadón (2002)

This section presents the anchorage block and the structural model for its design considered in the original reference by Bajo and Pérez-Fadón (2002). Anchorage blocks were located at the corners of the hollow section of a box girder bridge (figure 8.1a). The dimensions of the block considered in the reference are given in figure 8.1b, where direction-y corresponds to the longitudinal direction of the bridge. In this figure the surface in contact with the slab corresponds to face 1234 and the web is parallel to face 1458. The anchorage force was introduced by two point forces acting at the upper right front node: the one in y-direction corresponds to the actual anchor force and the one in x-direction accounts for tendons not being parallel to the web (the point of application of the load considered by these authors is not in agreement with general practice, as the load should have been applied at the centre of gravity of the anchorage plate, but this is a conservative assumption).

Seven point reactions were considered giving for a statically indeterminate system (figure 8.1c). The position and direction of these reactions was defined “based on the real spread of the anchorage force”. The vertical support was provided by the web and the horizontal support by both the slab and the web.

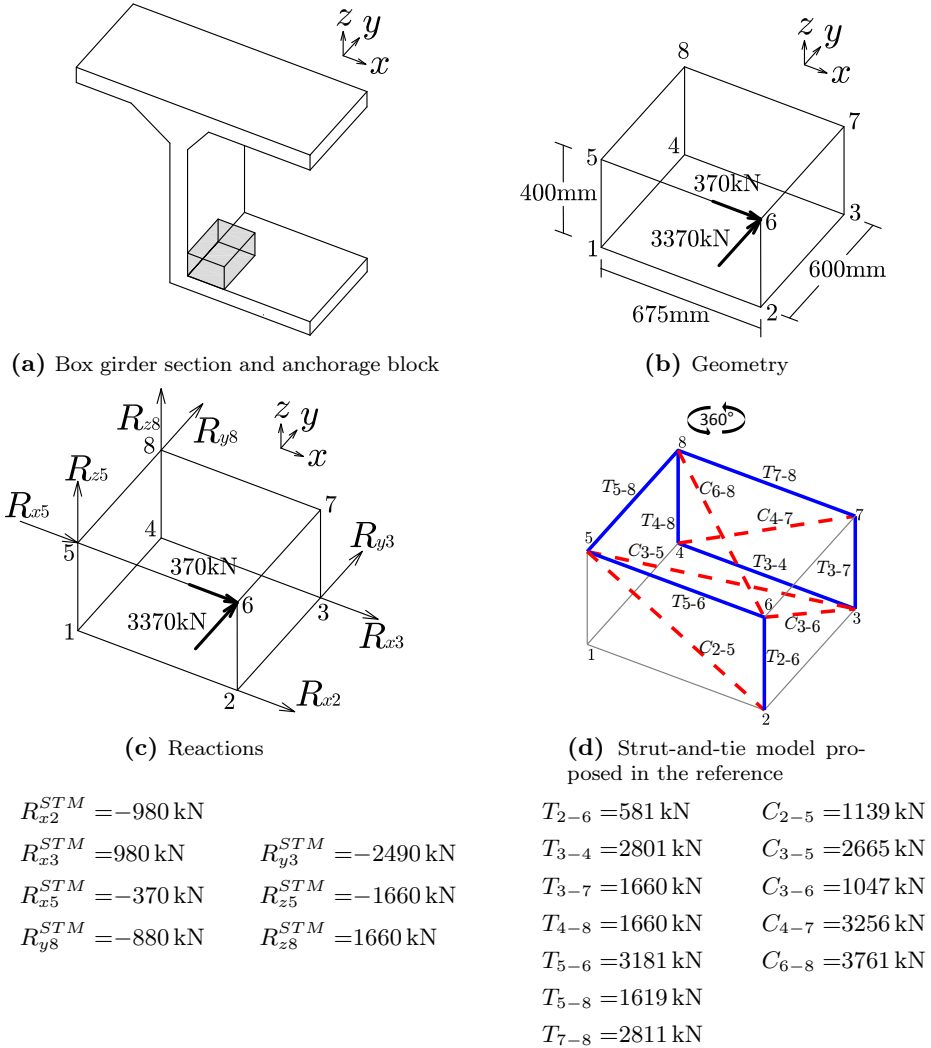


Figure 8.1: Description of anchorage block and strut-and-tie model (after Bajo and Pérez-Fadón 2002).

The 3E strut-and-tie model of figure 8.1d was proposed to represent the internal flow of forces and to determine the required reinforcement quantity. This model can be explained as follows. Prestressing force acting on y-direction (3370 kN) is deviated by ties T_{2-6} and T_{5-6} and transmitted to support at 3 through C_{3-6} and to support at 8 through C_{6-8} . The y-reaction at 8 is smaller than

the y-component of C_{6-8} and, hence, the excess must be transferred to support 3 through T_{5-8} and C_{3-5} . The x-component of C_{6-8} is transmitted to support 3 through $T_{7-8} - C_{4-7} - T_{3-4}$. The x-component of T_{5-6} is transferred to 2 by C_{2-5} and to 3 by C_{3-5} . The vertical components of C_{3-6} and T_{2-6} are transmitted to support at node 5 through C_{2-5} and C_{3-5} and to support at 8 through $T_{3-7} - C_{4-7} - T_{4-8}$. The force applied in the x-direction (370 kN) is directly supported by node 5 through horizontal tie T_{5-6} .

As the system is statically indeterminate, reactions and element forces depend on the stiffnesses of the truss elements. Values of the reactions and element forces considered in the reference are given in the figure. It was not mentioned in the reference though if the stiffness of the truss elements had been considered or how the adopted values were obtained.

8.3 Analysis and design of the anchorage block with FESCA 3D

The analysis of the anchorage block described in the previous section presents two of the complications that may appear when using the STM: the selection of an appropriate model, and the treatment of statically indeterminate systems (Tjhin and D. A. Kuchma 2002). The first issue can be overcome with experience, but for those practising engineers lacking inspiration, plotting of principal compressive stress directions obtained with FESCA 3D can be helpful as shown in Chapter 7. The second issue can only be solved considering the stiffness of the truss elements. Tie stiffness can be obtained directly from rebar areas, but determination of the strut stiffness requires making assumptions on their sectional areas, and this is not always straightforward, especially in 3D. FESCA 3D helps to overcome this problem as the stiffness of the elements is considered implicitly when calculating the stiffness of the FEs.

Two FE models with different levels of detail are considered in this section. Firstly, a simplified FE model was adopted where support and load dimensions were defined relatively small to resemble truss model conditions (section 8.3.1). Secondly, a more refined model was developed in which the load dimensions were accounted for and the contact between the anchorage block and the web and the slab was modelled more realistically by nonlinear elastic point supports distributed over the contact surface (section 8.3.2). It must be noted that it was not the purpose of this section to present a rigorous FE analysis, but to show the potential benefits of considering FE modelling for design. For a more precise FE analysis it would have been necessary to consider more accurately

the conditions imposed by the bridge on the block. One option to undertake the latter is briefly commented in section 8.3.2.

8.3.1 Simplified finite element model resembling truss model conditions

Description of finite element model

A simplified FE model was adopted following the assumptions undertaken in the structural model adopted by Bajo and Pérez-Fadón. Load and support areas were defined finite, to avoid stress localisation, but relatively small compared to the element dimensions, to resemble point loads and reactions inherent of truss models. Adopting a $50\text{ mm} \times 50\text{ mm}$ area was considered appropriate for this purpose.

The dimensions of the block were enlarged to $725\text{ mm} \times 650\text{ mm} \times 450\text{ mm}$ so the centres of gravity of the support and load areas coincided with the nodal coordinates of the truss model (figure 8.2a). An FE mesh formed by $14 \times 12 \times 8$ twenty-node hexahedrons was adopted (figure 8.2b).

Support and load locations and directions were considered as in the reference model. Fixed support conditions were considered. A uniform stress distribution was assumed over the loading area in both the x- and y-direction.

Without further reasoning, reinforcement was defined by arranging rebars along the twelve edges of the block (figure 8.3), as an engineer with scarce intuition on the element behaviour would do to be on the safe side. These

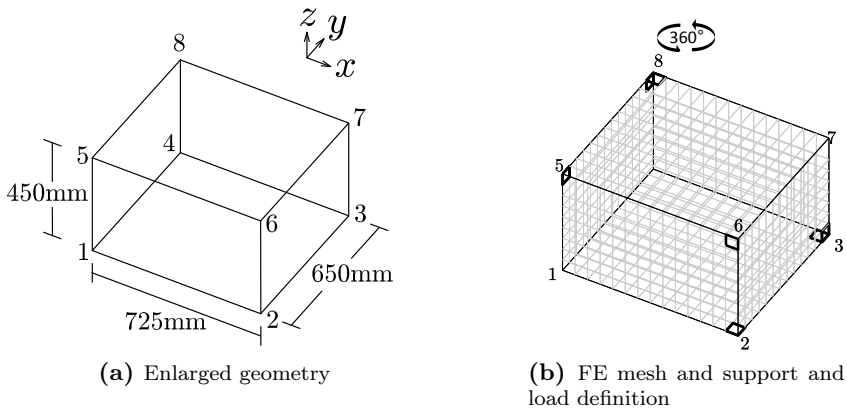


Figure 8.2: Details of simplified FE model

rebars were placed 25 mm inwards from the external perimeter, centred with the support and load areas and coinciding with the position of the ties of the truss model. An area of 80 cm^2 was defined for each one, considering that tie forces would be of the same order of magnitude as the applied load. Perfect bond between steel and concrete was assumed. The strut-and-tie model proposed by Bajo and Pérez-Fadón (figure 8.1d) could have been considered to adopt a more rational reinforcement geometry and, indeed, it is an advisable approach to consider simple structural models when developing FE models (and also vice versa). But the problem here was tackled from the perspective of an engineer lacking the time or the inspiration to propose a suitable reinforcement configuration, as if the strut-and-tie model proposed in the reference was unknown.

Material properties of concrete were defined as follows. Tensile strength of concrete was neglected in agreement with design practice. In compression, a perfectly elastic model was adopted to avoid that the compressive strength of concrete became a limiting factor. Considering the defined load and support dimensions, it can be seen that very large compressive stresses must be expected (for instance, at the loading plate 1350 MPa just from the force in the y-direction). This is obviously not realistic and is a consequence of having reduced load and support areas, but it is inevitable if the model is to be kept

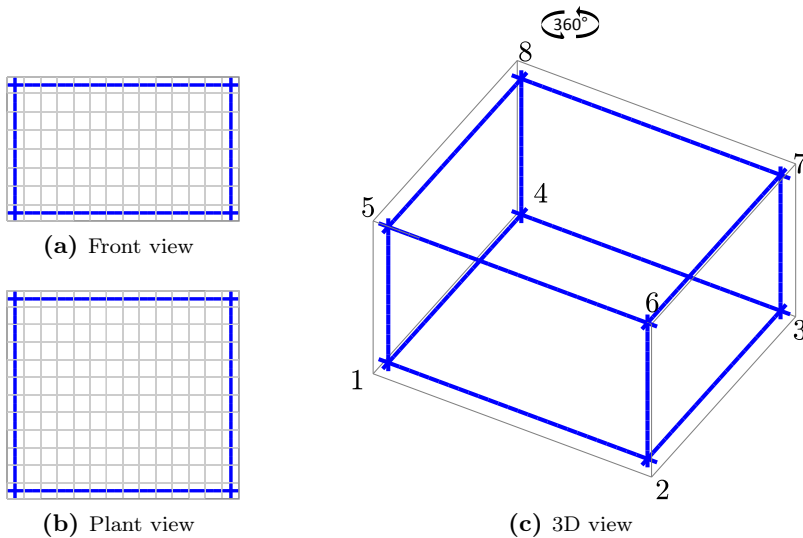


Figure 8.3: Reinforcement arrangement for simplified FE model.

similar to a truss model. Adoption of such model is not always necessary, but in this case it was because the undertaken simplifications not only affected the concrete model but also the geometry of the boundary conditions. In general it is recommended to use an elastic-perfectly plastic model for concrete in compression for design, as it is done in the next FE model. The elastic modulus for concrete E_c was taken equal to 750 GPa. This high magnitude is justified to, first, prevent excessively large compressive concrete strains associated with large compressive stresses and, second, avoid distortion of the stress field caused by extreme reinforcement concentration, especially at nodal areas. The latter aspect is discussed further when presenting the FE results.

For steel, an elastic-perfectly plastic model was adopted, with $f_{syd} = 400$ MPa and $E_s = 200\,000$ MPa.

Design procedure

The simple design algorithm implemented in FESCA 3D was used to determine the required steel quantity based on the calculated rebar stresses (section 2.3.2). Only the maximum tensile rebar stress was considered to calculate the required rebar area (i.e. every reinforcing bar was considered as a entire, indivisible unit). Both the minimum rebar area $A_{s,min}$ and the minimum rebar area to be considered $A_{s,0}$ were taken equal to 0. It was established that the stress ratio $\sigma_{s,i}^{max}/f_{syd}$ for all rebars at the design load should be between 0.95 and 1.05 to accept a solution as valid.

The design load was reached by increasing the load stepwise, with load steps equal to ten percent of the design load.

Finite element analysis results

Only two design iterations were needed until the acceptance criteria were satisfied (table 8.1). Indeed, a good estimation was already obtained in the first iteration. Rebar areas determined from tie forces of the strut-and-tie model in figure 8.1 (A_{STM}) are also given in this table for comparison. Obtained values are discussed later in this section.

FE principal compressive stress directions of those integration points whose compressive stress was larger than 100 MPa at the design load for the final design configuration (A_{s2}) are plotted in figure 8.4. In this figure rebar widths are proportional to the rebar diameter and the colour intensity is proportional to the ratio σ_s/f_{syd} . The analogy with the strut-and-tie model proposed in

Table 8.1: Calculated rebar areas based on FE and STM results

	A_{s0}	A_{s1}	A_{s2}	A_{STM}
T_{1-2}	80 cm ²	18 cm ²	14 cm ²	—
T_{1-4}	80 cm ²	12 cm ²	8 cm ²	—
T_{1-5}	80 cm ²	15 cm ²	8 cm ²	—
T_{2-3}	80 cm ²	20 cm ²	14 cm ²	—
T_{2-6}	80 cm ²	35 cm ²	33 cm ²	14 cm ²
T_{3-4}	80 cm ²	58 cm ²	57 cm ²	70 cm ²
T_{3-7}	80 cm ²	37 cm ²	36 cm ²	41 cm ²
T_{4-8}	80 cm ²	49 cm ²	49 cm ²	41 cm ²
T_{5-6}	80 cm ²	63 cm ²	62 cm ²	79 cm ²
T_{5-8}	80 cm ²	32 cm ²	28 cm ²	40 cm ²
T_{6-7}	80 cm ²	10 cm ²	7 cm ²	—
T_{7-8}	80 cm ²	50 cm ²	50 cm ²	71 cm ²
Steel vol.	536 000 cm ³	22 571 cm ³	20 717 cm ³	21 087 cm ³

the reference is evident. Only the strut C_{3-5} cannot be identified in the FE compressive stress field.

Before comparing FE-designed and STM-designed areas it is necessary to note that numerical results obtained from FE models are sometimes not as “disciplined and perfect” as one would desire, especially if one is trying to resemble a truss model with solid elements. Despite the apparent regularity of the principal compressive stress directions in figure 8.4, some shortcomings can be noticed when looking at FE results in more detail.

Considering the analogy with a truss model, constant steel stresses should be expected at rebars, which are progressively transferred to concrete and supports at nodal areas. This was indeed the case for the pile caps treated in Chapter 6 (see figure 6.12). But in this example, with unlimited compressive stresses in concrete, extremely concentrated reinforcement and nodal zones subjected to large stresses, the idealisation of constant steel stresses was not met by all ties. FE rebar stresses at the design load for the final solution (A_{s2}) are plotted in figure 8.5. The desired behaviour seems to be accomplished by ties T_{3-4} , T_{5-6} , T_{7-8} and T_{2-6} , but not by the others, for which stress plateaus at mid-length are accompanied by noticeable jumps near rebar ends. These jumps are explained by numerical issues caused by not-perfectly-aligned principal compressive directions at nodal areas. This effect is especially remarkable in this example as reinforcement was highly concentrated, giving for a significant heterogeneous stiffness distribution. Deviations of principal directions

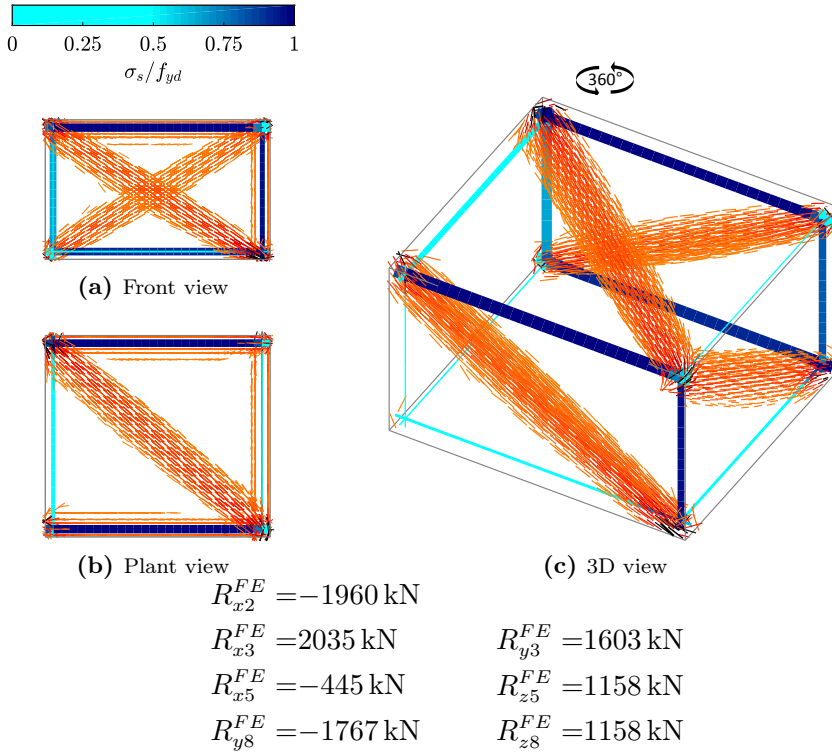


Figure 8.4: FE principal compressive stress directions and reactions obtained from the simplified model.

can be observed when looking in detail at some nodal areas in figure 8.4 and, associated with large compressive stresses, can cause significant rebar force variations, which ultimately led to overestimating the area required for some of the rebars. The largest overestimation took place for tie T_{5-8} , with an abrupt jump and a non-negligible area. In this case the y-component of C_{6-8} to be withstood by support 8 was partly being transferred through T_{5-8} , instead of directly to the support itself. For the rest of the ties these stress variations did not affect significantly final results either because their areas were relatively small, or because the stress jump was not excessive. Comparison of FE and STM results can be undertaken next after this discussion.

FESCA 3D did not eliminate any tie, but calculated areas for ties T_{1-2} , T_{1-4} , T_{1-5} , T_{2-3} and T_{6-7} were significantly smaller than the others and could be

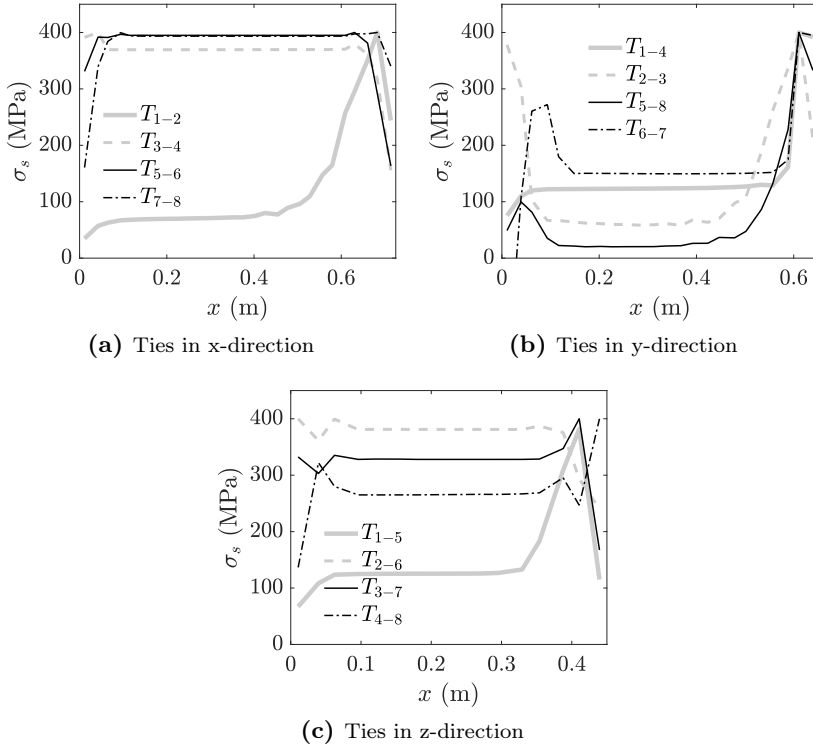


Figure 8.5: FE steel stresses obtained from the simplified model.

probably dismissed (especially after the discussion of the previous paragraph). These rebars coincide with the ties which were not included in the truss model proposed in the reference. The total steel volume obtained was very similar in both solutions, but the distribution differed with the internal distribution of forces.

Comparison of rebar areas (tie forces) and reaction values in both models is useful to identify the differences between the two internal load paths. The load path of the strut-and-tie model adopted by Bajo and Pérez-Fadón was already described in section 8.2, so only the differences will be mentioned here. In the FE model:

- the y-reaction at 8 was significantly larger than in the reference strut-and-tie model (1767 kN vs. 880 kN) and, hence, $|R_{z5}^{FE}| = |R_{z8}^{FE}| \leq |R_{z5}^{STM}| = |R_{z8}^{STM}|$.

- the y-component of C_{6-8} could be fully withstood by support 8 and did not need to be re-transferred to support 3 (hence, C_{3-5} was not noticed in the stress field). Therefore, and despite the numerical issues mentioned above, $A_{T_{5-8}}^{FE}$ was still smaller than $A_{T_{5-8}}^{STM}$.
- the force that is transferred directly to support 3 through C_{3-6} is larger than in the reference strut-and-tie model (hence, $A_{T_{2-6}}^{FE} > A_{T_{2-6}}^{STM}$, $A_{T_{5-6}}^{FE} < A_{T_{5-6}}^{STM}$, $A_{T_{7-8}}^{FE} < A_{T_{7-8}}^{STM}$, $A_{T_{3-4}}^{FE} < A_{T_{3-4}}^{STM}$, and $|R_{x2}^{FE}| > |R_{x2}^{STM}|$, $|R_{x3}^{FE}| > |R_{x3}^{STM}|$).
- tie areas of T_{3-7} and T_{4-8} should be equal to that of T_{2-6} and, hence, smaller than the ones obtained with the strut-and-tie model. Nevertheless, due to the numerical issues mentioned above, $A_{T_{4-8}}^{FE}$ was slightly larger than $A_{T_{4-8}}^{STM}$.

Evolution of the compressive stress field

The anchorage block treated in this chapter presents a complex behaviour and the development of a strut-and-tie model may not be so evident at first sight. The strut-and-tie model proposed in the reference was coherent, but less experienced engineers may have encountered some difficulties to arrive to this solution. It was shown that FESCA 3D arrived to a rational solution and proved to be a useful design-aid as the resisting mechanism could be clearly identified from the FE principal compressive stress directions. This section shows the evolution of the compressive strength field throughout the iterative process, which starts from a linear-elastic solution and ends with a well-defined stress field.

Figure 8.6 shows the FE compressive stress field obtained at different iteration steps when applying the first load step. Principal compressive directions of those integration points whose principal compressive stress was larger than 30 MPa are also plotted. The compressive stress field is diffused in the first iterations, giving for low compressive stresses. Principal compressive stress directions orient themselves while the iterative process advances in order to reduce residual forces caused by the assumption of neglecting the tensile strength of concrete. The tangent shear modulus of concrete plays an important role in this early phase. Despite the complexity of the problem, a quite clear resisting system starts to emerge between the 8th and the 10th iteration. The compressive stress field is refined further in subsequent iterations, until the convergence criterion is achieved and the next load step can be applied. The number of iterations needed in subsequent load steps is much lower as the resisting mechanism already took shape in the first load step.

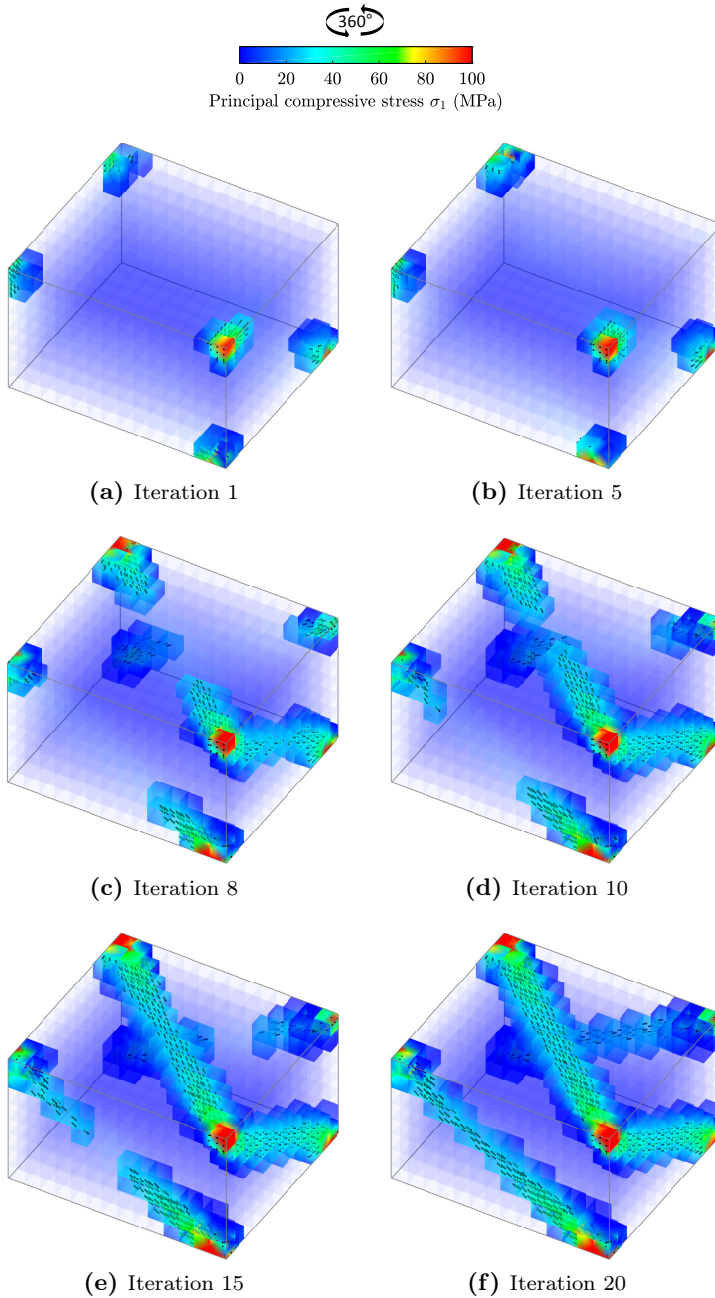


Figure 8.6: Evolution of the three-dimensional compressive stress field through out the iteration process.

8.3.2 Refined finite element model

Description of the finite element model

A second, more refined FE model was considered afterwards defining more realistic boundary conditions at the contact surface between the anchorage block and the bridge section. Considering problems and actual benefits of excessively detailed models, that not many details were given in the reference and the actual purpose of this chapter, some simplifications were still undertaken when defining them. It was assumed that the block was cast in the web (400 mm thickness) and the bottom slab (300 mm thickness) (figure 8.7a). To consider this, the dimensions of the block were enlarged and taken equal to 1075 mm \times 600 mm \times 700 mm.

An FE mesh formed by 16 \times 10 \times 9 twenty-node hexahedrons was adopted. The geometry of the supports was defined as shown in figure 8.7b considering the thickness of the web and the bottom slab. Punctual supports acting perpendicular to these areas were defined (figure 8.7c). These supports were defined as nonlinear-elastic, acting only against compressive forces and with their capacity limited by the compressive strength of concrete. The elastic modulus of the supports was determined based on the stiffness of the bridge section to axial and transverse forces. The stiffness considered in each direction was $K_x = 1.8 \times 10^4 \text{ kN m}^{-1}$, $K_y = 5 \times 10^5 \text{ kN m}^{-1}$ and $K_z = 2 \times 10^3 \text{ kN m}^{-1}$. These values were then distributed to each node based on their tributary area in an automatic manner. A more realistic option could have been to model the entire bridge and then obtained a condensed stiffness matrix at the degrees of freedom of the contact surface between the bridge section and the anchorage block by static condensation, and assume a linear elastic behaviour (see section 5.2.3). Then this condensed matrix could have been used to define the support conditions in the FE model of the anchorage block. This option was not carried out as such level of detail was not necessary for the purposes of the chapter.

Based on the pictures of the reference, a loading are of diameter equal to 300 mm was defined (figure 8.7b). A uniform distribution was assumed over this area.

Similarly to the previous model, reinforcement was defined without further reasoning by arranging rebars in the x-, y- and z-directions separated 100 mm from each other (figure 8.7d). 140 rebars were introduced in total. A diameter

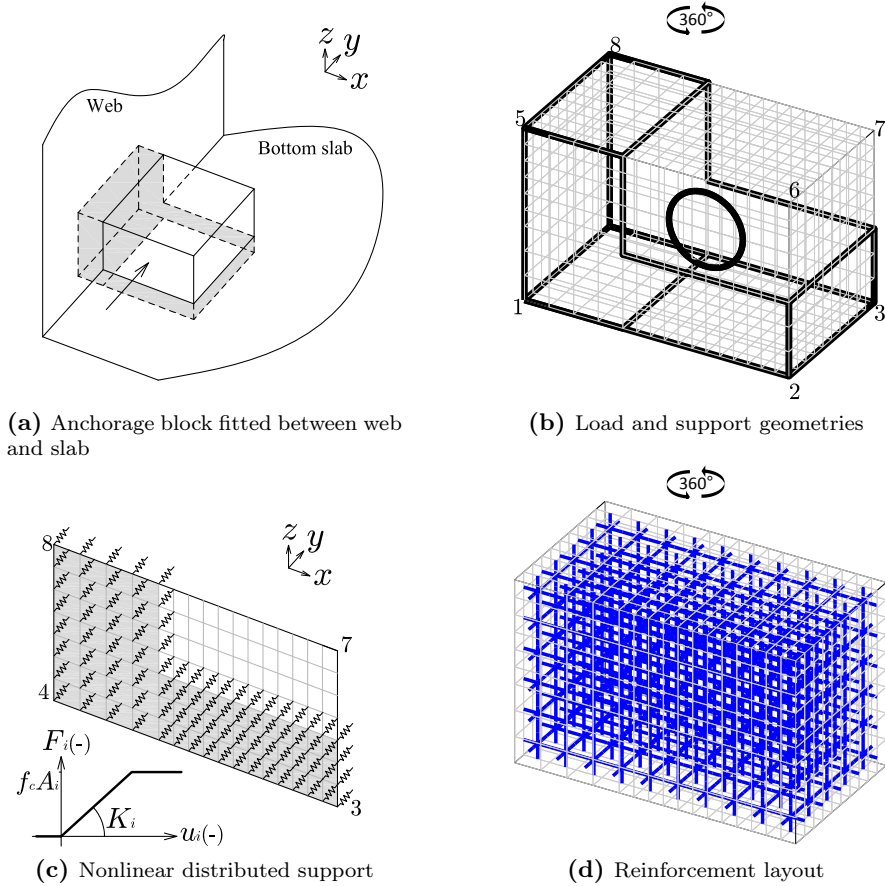


Figure 8.7: Details of refined FE model.

of $\phi 25$ was defined for each rebar. Perfect bond between steel and concrete was assumed.

Material properties were defined as follows. For steel, a design yield stress of 400 MPa was adopted, with $E_s = 200\,000$ MPa. Tensile strength of concrete was neglected. In compression, an elastic-perfectly plastic model was adopted, with $f_{cp} = 50$ MPa and $E_c = 30$ GPa.

Design procedure

The maximum tensile rebar stress was considered to determine the area required for each rebar. The minimum rebar area $A_{s,min}$ was taken equal to zero. The minimum rebar area to be considered $A_{s,0}$ was taken equal to $154\text{ mm}^2(\phi 14)$. It was established that the stress ratio $\sigma_{s,max}/f_{yd}$ for all rebars should be between 0.95 and 1.05 to accept a solution as valid.

The load was increased by load steps equal to ten percent of the design load.

Finite element analysis results

For simplicity reasons results presented in this section were obtained considering only the y-component of the applied force (3370 kN), assuming that the x-component was directly transferred to the web through horizontal rebars whose area could be easily determined.

FE principal compressive stress directions obtained for the final solution at the design level are plotted in figure 8.8a. Analogies with the strut-and-tie model and the simplified FE model presented before can be observed. For instance, vertical rebars located at the back of the block transfer the vertical component of the inclined compressive stress field going to the bottom corner, as tie T_{3-7} did in truss models with C_{3-6} . The main difference is the appearance of an additional support point in the y-direction at corner 1 and, consequently, two struts C_{1-3} and C_{1-8} .

The resulting reinforcement configuration is clearer in figures 8.8b and 8.8c. Ten iterations were needed until convergence criteria were achieved, but it must be noted that the differences between solutions after the fourth iteration were slight and affected only a few of the bars. Many of the rebars were eliminated during the process and “only” 49 of the bars introduced initially remained. The diameters of these rebars rounded up to the next available commercial diameters are given in figure 8.8c (due to the inability to transfer text data to the interactive file, bars for this view were coloured: red for $\phi 32$, green for $\phi 25$, blue for $\phi 20$ and yellow for $\phi 16$). A more practical reinforcement arrangement is proposed in this same figure based on the calculated rebar areas. The resulting total amount of reinforcement is equal to $16\,200\text{ cm}^3$, which can be compared with that obtained from the simplified model ($20\,717\text{ cm}^3$).

The magnitude of the principal compressive stresses within the body can be observed in the 3D compressive stress field represented in figure 8.9.

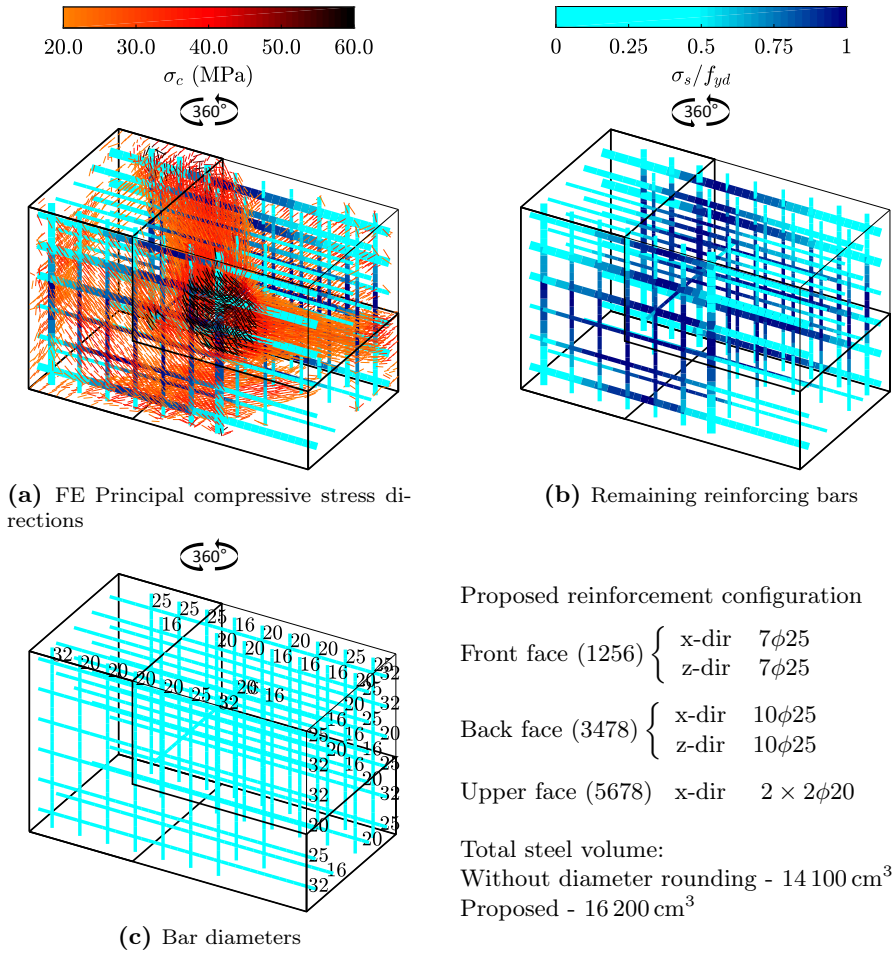


Figure 8.8: FE principal compressive stress directions for anchorage block obtained from refined FE model at the design load

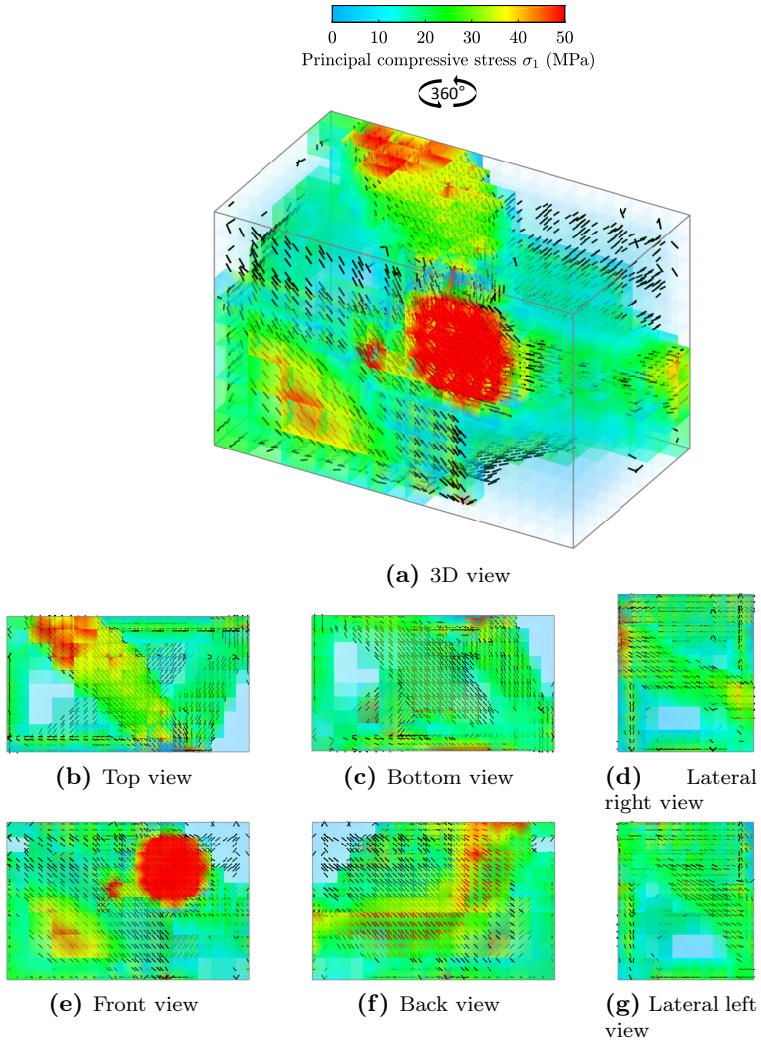


Figure 8.9: FE compressive stress field for anchorage block obtained from refined FE model at design load.

8.4 Conclusions

Differences between FE models and simplified analysis models such as strut-and-tie and stress field models are such that in practice they are frequently treated as different, isolated problems. It is forgotten that both approaches can complement each other and potential synergies that could be obtained considering both approaches simultaneously are wasted.

On the one hand, the FE modeller tries to develop a detailed FE model to simulate the element and its interaction with surrounding elements as realistic as possible. Sometimes this requires the adoption of fine meshes to adapt to complex geometries, modelling contact surfaces between different materials and/or including secondary elements interacting with the element object of study. Most commercial FE software packages permit achieving high levels of detail, but always at the cost of simplicity. Sound FE results may be obtained from these models, but the likelihood of making mistakes, some of which difficult to identify, also increases. Moreover, for a practising engineer FE results are meaningless if they do not shed some light on the element behaviour and internal force distribution as these aspects are critical in the development of rational reinforcement arrangements.

On the other hand, when using the STM the engineer proposes a suitable truss model to represent the internal flow of forces, which is much simpler than an FE model, but also more clarifying for design purposes. Furthermore, required reinforcement quantity can be calculated directly from tie forces.

FE models and strut-and-tie and stress field models can complement each other if the existing gap between both approaches is bridged. FESCA 3D was conceived with this idea in mind. The anchorage block described above is a good example of application to show this as the element behaviour was relatively more complex than elements treated in previous chapters.

This example also showed the difficulties that an engineer can encounter when applying the STM to hyperstatic systems, and the influence that adopting different assumptions on the internal force distribution can have on final design results. One of the main difficulties of hyperstatic strut-and-tie models is the determination of the stiffness of the struts. In an FE model this is directly accounted for when calculating the FEs stiffness.

Part IV

Strut-and-tie modelling of 3D D-regions

Chapter 9

Refined strut-and-tie model for predicting the strength of four-pile caps

Current design procedures for pile caps do not provide engineers with a clear understanding of the physical behaviour of these elements. Strut-and-tie models, on the other hand, can provide this understanding and hence offer the possibility of improving current design practice.

—Adebar, D. Kuchma, and Collins 1990

9.1 Introduction

As mentioned in Chapter 6, pile cap foundations are the 3D D-region which has attracted more attention of all. This interest has been reflected both in the experimental field and in the proposal of analytical methods. However, the design of these elements has been traditionally contentious. A significant progress was made in the last decades with the proposal of more rational design methods. Most of these methods were proposed after experimental testing and are based on truss or strut-and-tie models (Blévot and Frémy 1967) (Clarke 1973) (Adebar, D. Kuchma, and Collins 1990) (Adebar and Zhou 1996) (J. Park, D. Kuchma, and Souza 2008) (Souza et al. 2009). Although these methods represent an improvement over the traditional procedures based on test results, rules of thumb and past experience which were frequently followed in the past, it must be noted that comparison of the predictions obtained by them shows

a significant scatter in the results. This is a sign that uncertainties on the behaviour of these elements still exist, especially regarding the determination of the shear strength, which is systematically overestimated by some of these methods and explains why simplifications and excessively conservative assumptions are still common in design practice. Refinement of current analytical and design approaches could derive in more efficient designs of foundations.

Strut-and-tie models are adequate for representing the stress field inside pile cap foundations. As mentioned above, several analytical models for pile cap analysis and design based on 3D truss models have been proposed in scientific literature (Adebar, D. Kuchma, and Collins 1990) (Adebar and Zhou 1996) (J. Park, D. Kuchma, and Souza 2008) (Souza et al. 2009) (Guo 2015). Most of these references focused on the proposal of different formulae to limit the concrete strength of the diagonal strut in order to reproduce accurately the failure load. Little attention was paid on the truss geometry despite its influence on the resulting strut forces, and a predefined truss geometry was assumed by these authors. The use of more refined models derived by iteration of the truss geometry could lead to better initial predictions, which in turn will reduce the need of using correcting or empirical factors (Sagaseta and R. Vollum 2010).

This chapter presents a new, alternative STM-based approach for the analysis and design of four-pile caps with rectangular geometries, without shear reinforcement and loaded by a square column. Although from this description it might seem that its application is rather restrained, it must be noted that many of the pile caps found in practice fulfil these conditions. Traditional design methods for pile caps are described in the first part of the chapter. The proposed method is presented afterwards. A refined truss geometry is considered and the strut inclination is not predefined but determined by maximizing the pile cap strength considering different failure conditions. The proposed model satisfies equilibrium, strain compatibility and considers compressive strength softening of cracked concrete. It also accounts for the effect of reinforcement area and configuration (distribution and anchorage conditions) to estimate the shear strength, factors which are not considered in previous models. Strength predictions obtained by the proposed and other five methods of 162 pile cap specimens are compared and discussed in the last part of the chapter. The adequacy of the adopted model is further verified by means of 3D FE analysis.

The work included in this chapter was developed in collaboration with Dr. Juan Sagaseta during a research stay at the University of Surrey. This chapter was written together with an article draft which will be submitted to the ACI Structural Journal, which explains why the ACI Code is recurrently referred throughout the text.

9.2 Design methods for pile caps

9.2.1 Deep and slender pile caps

Pile cap behaviour depends significantly on its shear span-to-depth ratios w/d : slender pile caps ($w/d > 1$ Gogate and Sabnis (1980)) behave similarly to a beam, while in deep pile caps ($w/d < 1$) arching action is the predominant resisting mechanism. The boundary $w/d = 1$ is a reference and the response variation with w/d is gradual.

Experimental programs and design methods have mainly focused on deep pile caps as their treatment presents more difficulties. Interaction between flexural and shear failures is frequent in these elements and difficults the determination of the failure load and mode of failure. For instance, most deep pile caps tested in literature (Blévyot and Frémy 1967) (Clarke 1973) (Adebar, D. Kuchma, and Collins 1990) (Suzuki, Otsuki, and Tsubata 1998) (Suzuki, Otsuki, and Tsubata 1999) (Suzuki, Otsuki, and Tsuchiya 2000) (Suzuki and Otsuki 2002) were reported to fail in two-way shear, with or without reinforcement yielding, although many of them had been designed to fail in flexure.

Similarly to what happens with slender and deep beams, the difference in behaviour between slender and deep pile caps has implications on which structural model is more appropriate. A sectional force approach seems adequate for slender pile caps; however, it is contentious (Adebar, D. Kuchma, and Collins 1990) (Adebar and Zhou 1996) whether the approach is also valid for deep pile caps because some of the main assumptions of sectional analysis do not apply (i.e. flexural compression is not uniform along the cap width, plane sections do not remain plane and application of a constant shear stress limit for the whole depth does not seem adequate as shear stresses concentrate around the diagonal strut). Strut-and-tie models seem more adequate for deep pile caps as they represent better the internal flow of forces. Sectional force approaches and STM-based approaches are accepted in major design codes. Their application is discussed next.

9.2.2 Existing truss-based models for pile cap design

The STM is a valuable tool for the analysis of D-regions which has shed rationality in the design of these elements. The application of the method is conceptually simple: after defining the truss geometry, forces at the truss elements are obtained from equilibrium and compared with their corresponding estimated strengths to determine the maximum admissible load. Although the initial purpose of the STM was to provide a lower-bound solution of the element strength, further research made possible to improve also the accuracy of these predictions.

The STM has also been applied for the analysis and design of pile cap foundations. Several strut-and-tie-based methods have been proposed in literature. The geometric shape of the truss models adopted by different authors is fundamentally similar and is formed by inclined struts expanding from the column to the piles and horizontal ties extending between the piles. However, the location of the nodes, and hence the resulting strut inclination, do not always coincide. Most authors agree to locate the lower nodes at the centre of the piles at the reinforcement level, but several alternatives were proposed for the upper nodes (e.g., at the column centre (figure 9.1a) or at the column quarter points; at the cap surface or at half depth of the compressive stress block). It must be noted that calculated strut and tie forces depends on the adopted geometry. To cover all possible geometries it is useful to express the truss forces as a function of the strut inclination. The following formulae can be obtained from equilibrium:

$$F_s = \frac{P}{4 \sin \theta_s^{3d}} \quad (9.1)$$

$$F_{t,x} = \frac{P \cos \varphi}{4 \tan \theta_s^{3d}} = \frac{P}{4 \tan \theta_{s,x}^{2d}} \quad (9.2)$$

$$F_{t,y} = \frac{P \sin \varphi}{4 \tan \theta_s^{3d}} = \frac{P}{4 \tan \theta_{s,y}^{2d}} \quad (9.3)$$

where θ_s^{3d} is the angle of the inclined strut respect to the horizontal plane (figure 9.1a), and $\theta_{s,x}^{3d}$ and $\theta_{s,y}^{3d}$ are the angles of that the strut projection onto a vertical plane parallel to the x- and y-axis, respectively (figure 9.1b).

It should be noted that, despite having obtained the above equations from the equilibrium of a 3D model, equations 9.2 and 9.3 are equal to those obtained

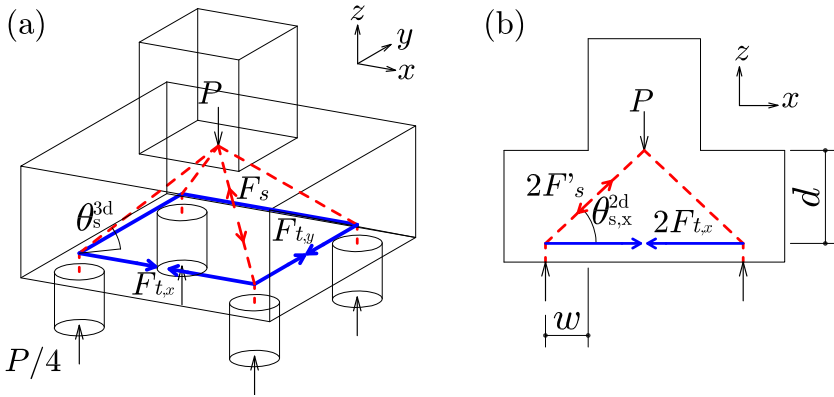


Figure 9.1: Strut-and-tie model for four-pile cap without shear reinforcement: (a) 2D model; (b) 3D model.

from a 2D model (figure 9.1b). If reinforcement area is determined based on tie forces as it is done in practice, this implies that same reinforcement quantities will be obtained considering 2D and 3D trusses. The calculation of F_s does reflect the 3D nature of the problem, but it rarely determines the final design. Therefore, some models presented as 3D in theory may be 2D in real practice.

The work undertaken by previous researchers on pile cap analysis with the STM is summarised next in chronological order.

The simplified design method proposed by Blévoit and Frémy (1967) is one of the first references of the application of truss models in pile cap analysis. These authors undertook an extensive experimental campaign to check the adequacy of these models in predicting the strength of pile caps. For four-pile caps they proposed a truss model with four lower nodes located at the centre of the piles at the reinforcement level and four upper nodes at the column quarter points on the cap surface. This model was then followed by most researchers. From test results they suggested to limit the steel stress to $3/5$ the steel yield stress f_{sy} and the bearing stress at the piles and the column to $0.9f_{c0} \sin^2 \theta_s^{3d}$.

Adebar, D. Kuchma, and Collins (1990) tested six full-size pile caps to study the suitability of 3D strut-and-tie models and the sectional approach of the ACI Building Code in pile cap design, concluding that the latter approach was not adequate for the design of deep pile caps. The adopted truss model was formed by four upper nodes and considered the depth of the compressive stress block under the column. To evaluate the flexural capacity the steel stress was limited

to the yield stress f_{sy} . Experimental observations showed that shear failures occurred after splitting of the compression strut. To prevent this failure it was suggested to limit the maximum bearing stress to the concrete compressive strength f_{c0} .

Adebar and Zhou (1996) proposed an alternative bearing stress limitation to prevent shear failures of deep pile caps. Their proposal was based on the study of the strength of idealised struts confined by plain concrete. It was proposed that concrete strength should be limited to:

$$f_b \leq 0.6f_{c0} + \alpha\beta 6\sqrt{f_{c0}} \quad (9.4)$$

where factors α and β account for confinement of the strut and height-to-width ratio, respectively. The adopted truss model was identical to that proposed by Blévoit and Frémy (1967).

J. Park, D. Kuchma, and Souza (2008) developed a more refined 3D strut-and-tie-based approach that considered strain compatibility and a nonlinear constitutive model for concrete. A compression-softening model was adopted to account for compression softening caused by transverse tensile strains. Additionally, the model also considered the contribution of tension stiffening effect to the tie strength. The upper nodes of the truss model were located at the column quarter points at half depth of the compressive stress block. Three different failure conditions were considered: crushing or splitting of the diagonal concrete strut; crushing of the horizontal compression zone at the base of the column; and yielding of the longitudinal reinforcement.

Souza et al. (2009) proposed a simpler truss geometry, with only one node at the upper section located at the centre of the column on the cap surface (figure 9.1a). This simplification implied a significant change in the strut inclination compared to previous authors and, hence, in the forces resulting from the truss system. To determine the flexural strength the following equation was proposed:

$$P = \frac{4\phi_y d A_{sT} f_{sy}}{e} \quad (9.5)$$

where factor ϕ_y is a calibration factor to be obtained in order to provide the lowest possible coefficient of variation when comparing test data and model predictions. A value of 2.05 was derived based on the investigated specimens. To predict the shear strength the model by Siao (1993) was adopted:

$$P = 2.08cd_f^{2/3} \quad (9.6)$$

This model assumed that shear failures of pile caps were caused by splitting of the compressive struts. Splitting strength was obtained by replacing the inclined strut by a 3D strut-and-tie prism and assuming concrete tensile stresses along the entire strut.

Guo (2015) developed a strut-and-tie-based method for evaluating punching strength of pile caps with uniform grid reinforcement. The adopted truss model was formed by one upper central node at 0.1 times the effective depth from the cap surface and four lower nodes at the reinforcement level slightly displaced from the centre of the piles. The punching shear strength was determined by the strut bearing load as follows:

$$P = 4 \sin \theta_s^{3d} F_s = 4 \sin \theta_s^{3d} (0.6\pi d_p^2 f_{ce}) = 4 \sin \theta_s^{3d} (0.6\pi d_p^2 \alpha (f_{c0}) \beta (w/d) f_{c0}) = \quad (9.7)$$

9.2.3 The STM in the ACI 318-14 (ACI Committee 318 2014)

The STM is also accepted in major design codes for the analysis and design of pile cap foundations. Regarding the ACI Building Code, the current version ACI 318-14 accepts its application regardless of the slenderness ratio (at least, no reference is made to it). However, preceding ACI 318-02, ACI 318-08 and ACI 318-11 restricted the application of the STM only to deep pile caps, for which the distance between pile axes and column axis was equal or less than two times the height of the cap (section 15.5.3). Application of the STM must be in accordance with the general guidelines of ACI 318-14, which are included in chapter 23. The area of reinforcement is calculated from the tie forces obtained and the factored yield strength. The compressive stresses in the struts must not exceed $0.51f_{c0}$ assuming that no confinement reinforcement is present in the pile caps. No special provisions are given for 3D nodal zones. Considering general guidelines for 2D elements, the concrete compressive stress in the nodal zone underneath the column shall be limited to $0.85f_{c0}$ and in the nodal zone over the piles to $0.51f_{c0}$. It should be noted that the purpose of these stress limitations is enabling yielding of the reinforcement prior failure rather than providing an accurate shear strength prediction.

9.2.4 The sectional method in the ACI 318-14 (ACI Committee 318 2014)

Although strut-and-tie models are gaining importance for the design of pile cap foundations supported by several references proving their adequacy (Adebar, D. Kuchma, and Collins 1990) (Adebar and Zhou 1996), the traditional design procedure considered in major design codes (European Committee for Standardization 2004) (ACI Committee 318 2014) is based on a sectional force approach. As mentioned above, the application of this approach to deep pile caps is controversial and has been subject of critiques (Adebar, D. Kuchma, and Collins 1990) (Adebar and Zhou 1996), but it is still accepted.

In the ACI Code the application of the sectional method to pile caps is similar to two-way slabs and footings. The flexural and shear strength are evaluated separately.

The flexural strength is governed by the amount of longitudinal reinforcement and is obtained assuming that plane sections remain plane and that the concrete compressive block extends to the entire pile cap width. As discussed previously, adequacy of these assumptions for deeper elements is contentious. The critical section to calculate the flexural strength is located at the face of the column.

The shear strength is governed by the cap depth and the concrete strength and is determined by the most restrictive condition considering one-way (section 22.5) and two-way shear (section 22.6):

$$V_c = 0.17\lambda\sqrt{f_{c0}}b_w d \quad (9.8)$$

$$V_c = 0.33\lambda\sqrt{f_{c0}}b_0 d \quad (9.9)$$

For one-way and two-way shear the critical sections are located at d and $d/2$ from the column face, respectively.

According to section 13.4.2.5 of ACI 318-14 the shear produced by the pile reaction at the critical sections shall be accounted for as follows: (i) when the pile centre is located $d_p/2$ or more inside the section, the reaction produces no shear on that section; (ii) when the pile centre is located $d_p/2$ or more outside the section, the entire pile reaction shall be considered; (iii) for intermediate positions, the portion of the pile reaction is obtained from a linear interpolation. An upper limit on the shear strength at a section adjacent to the column

face shall be considered as recommended in Concrete Reinforcing Steel Institute (2008) to avoid excessive/unlimited shear strengths when some/all piles are located inside the critical section. The following limits are proposed in the guidelines of the CRSI Handbook:

$$V_c = \frac{d}{w} \left(3.5 - 2.5 \frac{M_u}{V_u d} \right) \left(0.16 \lambda \sqrt{f_{c0}} + 17 \rho \frac{V_u d}{M_u} \right) b_w d \leq 0.83 \sqrt{f_{c0}} b_w d \quad (9.10)$$

$$V_c = \frac{d}{w} \left(1 + \frac{d}{c} \right) \frac{1}{6} \sqrt{f_{c0}} b_0 d \leq 2.67 \sqrt{f_{c0}} b_0 d \quad (9.11)$$

where b_0 in equation 9.11 is now the perimeter of the column.

9.3 Proposed strut-and-tie model

The proposed STM-based approach for the analysis and design of four-pile caps with rectangular geometries, without shear reinforcement and loaded by a square column is presented in this section. Details of the adopted truss geometry are described first. Derivation of the limit functions associated to the modes of failure considered in the method is presented next. Finally, determination of the predicted maximum load and mode of failure from these functions is discussed.

9.3.1 Equilibrium in the three-dimensional model

A statically determinate 3D truss model was adopted to represent the resisting mechanism of the element (figure 9.2). Unlike previous truss-based models, the adopted model considered that the strut inclination is unknown a priori. The position of the four lower nodes was fixed at the centre of the piles at the reinforcement level. The upper nodes were located inside the column and on the cap surface, but the horizontal position was not assumed beforehand, which implies that the strut inclination θ_s^{3d} is a geometrical variable. Therefore, not only the maximum load is an unknown, but also the strut inclination. Both values are obtained simultaneously by maximizing the element strength as described later.

As mentioned above, forces at diagonal struts and horizontal ties can be calculated from equilibrium (equations 9.1 to 9.3). For simplicity reasons, the formulae presented hereafter were derived for a square-shape cap, which applies to most four-pile caps in practice. Formulae for rectangular-shape caps could be obtained similarly. Considering symmetry, equations 9.2 and 9.3 can be merged into one as:

$$F_t = F_{t,x} = F_{t,y} = \frac{P}{4 \tan \theta_s^{2d}} = \frac{P}{4\sqrt{2} \tan \theta_s^{3d}} \quad (9.12)$$

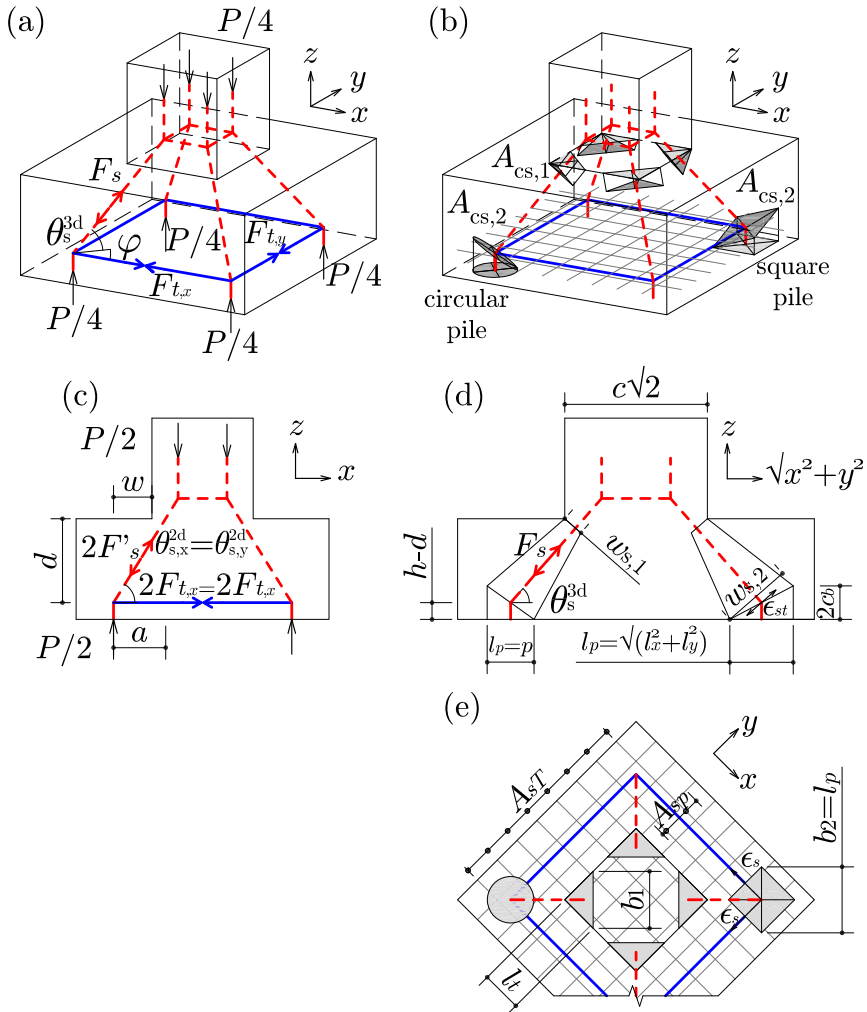


Figure 9.2: Proposed strut-and-tie model: (a) truss 3D view; (b) truss 2D side view; (c) 3D view of strut and tie details; (d) strut projection onto cap diagonal plane and (e) plan view of strut and tie details.

9.3.2 Considered failure modes and definition of corresponding limit functions

Three potential modes of failure were considered to determine the element strength:

- mode (i) accounts for exceeding the reinforcement strength when reaching the steel ultimate stress f_{su}
- mode (ii) accounts for crushing of the diagonal strut at the base of the column with narrowing of the strut
- mode (iii) accounts for splitting of the diagonal strut due to transverse cracking

If the truss geometry was fixed, the maximum admissible load would be given by the minimum value of these three modes of failure. However, in the proposed model the strut inclination θ_s^{3d} is unknown a priori and, therefore, forces at the truss elements, the geometry of the strut section and the maximum load associated to each mode of failure cannot be determined directly. However, it is possible to determine the relationship existing between θ_s^{3d} and the maximum load corresponding to each mode of failure. The functions giving these relationships were denoted as limit functions (one for each mode) and are obtained by equating the force acting on the ties (mode(i)) or struts (mode (ii) and mode (iii)) and the strength estimated for these elements. These functions are derived as follows:

Mode (i)

Given a vertical load P , the force acting on a tie of a four-pile cap can be determined from equilibrium as a function of the strut inclination (equation 9.12). The tie strength can be estimated from the tie area A_{ts} and the steel stress limit. The steel yield stress f_{sy} is usually considered for the latter. However, to obtain more realistic predictions, it is proposed in this approach to limit the steel stress to the steel ultimate stress f_{su} instead. A_{ts} can be determined considering that reinforcement is distributed symmetrically in each horizontal direction, i.e. $A_{ts} = A_{sT}/2$ with A_{sT} the total amount of reinforcement in the considered direction (figure 9.2d). Then the nominal tensile strength of a tie F_{nt} can be calculated in terms of the total amount of reinforcement A_{sT} as:

$$F_{nt} = A_{ts}f_{su} = \frac{A_{sT}}{2}f_{su} \quad (9.13)$$

The maximum column load limited by reinforcement failure can be derived then by equating equations 9.12 and 9.13:

$$P_{nt} = 4\sqrt{2} \tan \theta_s^{3d} F_{nt} = 2\sqrt{2} \tan \theta_s^{3d} A_{sT} f_{su} = P_{nt} (\theta_s^{3d}) \quad (9.14)$$

This limit function expresses the maximum strength of the pile cap limited by mode (i) in terms of the strut inclination θ_s^{3d} . It must be noted that the maximum admissible load of the pile cap limited by reinforcement failure increases as the strut inclination θ_s^{3d} increases because the force at the tie reduces.

Mode (ii)

Given a vertical load P , the force acting on a diagonal strut of a four-pile cap can be determined from equilibrium as a function of the strut inclination (equation 9.1). The strut strength can be estimated from the compressive strength of concrete and the strut area A_{cs} . Two different failure conditions evaluated at two different sections were considered in the approach: crushing (mode (ii)) and splitting (mode (iii)). Derivation of the limit function for mode (ii) is treated first.

The critical section to estimate the strength against crushing was defined at the top of the diagonal strut where it narrows at the intersection between the pile cap and the column. This top region was not considered as a node, but rather as a critical section of the strut. The strut strength limited by crushing of this section $F_{ns,1}$ can be obtained as:

$$F_{ns,1} = A_{cs,1} f_{cp} \quad (9.15)$$

where

$$A_{cs,1} = \frac{1}{2} w_{s,1} b_1 \quad (9.16)$$

$$w_{s,1} = l_t \frac{\sqrt{2}}{2} \sin \theta_s^{3d} = 3 \left(\frac{d}{\sqrt{2} \tan \theta_s^{3d}} - w \right) \frac{\sqrt{2}}{2} \sin \theta_s^{3d} \quad (9.17)$$

$$b_1 = l_t \sqrt{2} = 3 \left(\frac{d}{\sqrt{2} \tan \theta_s^{3d}} - w \right) \sqrt{2} \quad (9.18)$$

$$f_{cp} = \begin{cases} f_{c0} & \text{if } f_{c0} \leq 20 \text{ MPa} \\ 2.7 f_{c0}^{2/3} & \text{if } f_{c0} > 20 \text{ MPa} \end{cases} \quad (9.19)$$

Assuming an uncracked uniaxial compressive state at the top region, the compressive strength of concrete was taken as the plastic strength f_{cp} (Muttoni, Schwartz, and Thürlimann 1997). This assumption was justified based on experimental observations showing that this region remains uncracked until failure and was further verified using 3D FE analysis as shown in Chapter 6. The strut area $A_{cs,1}$ was obtained from the projection of a horizontal triangle expanding from the column corner onto a plane perpendicular to the strut passing through the centre of the column as shown in figure 9.2c. The stresses in the strut are assumed to be constant within area $A_{cs,1}$. The strut inclination determines the centre of gravity of the triangular stressed area and, hence, its side length l_t (figure 9.2). Considering equations 9.16 to 9.19 the nominal strength of the top narrow section of the strut is given by:

$$F_{ns,1} = 4.5 \left(\frac{d}{\sqrt{2} \tan \theta_s^{3d}} - w \right)^2 \sin \theta_s^{3d} f_{cp} \quad (9.20)$$

The maximum admissible vertical load limited by crushing of the diagonal strut at its top section is obtained from equations 9.1 and 9.20 giving:

$$P_{ns,1} = 4 \sin \theta_s^{3d} F_{ns,1} = 18 \left(\frac{d}{\sqrt{2} \tan \theta_s^{3d}} - w \right)^2 \sin^2 \theta_s^{3d} f_{cp} = P_{ns,1} (\theta_s^{3d}) \quad (9.21)$$

It must be noted that the maximum admissible load of the pile cap limited by crushing of the strut reduces as the strut inclination θ_s^{3d} increases because the strut becomes narrower (figure 9.2).

Mode (iii)

The critical section to estimate the strength of the diagonal strut against splitting was defined at its bottom where the strut meets the flexural reinforcement. Concrete strength at this section is reduced to the effective concrete strength f_{ce} to account for transverse cracking leading to splitting of the strut. The nominal strength of the strut against splitting $F_{ns,2}$ can be estimated from the following expression:

$$F_{ns,2} = A_{cs,2} f_{ce} = A_{cs,2} \xi f_{cp} \quad (9.22)$$

where

$$A_{cs,2} = \beta_p w_{s,2} l_p \quad (9.23)$$

$$w_{s,2} = l_p \sin \theta_s^{3d} + 2c_b \cos \theta_s^{3d} \quad (9.24)$$

$$c_b = h - d \quad (9.25)$$

$A_{cs,2}$ is obtained by projecting the pile section onto a plane perpendicular to the inclined strut passing through the lower node of the strut as shown in figure 9.2c. If the pile section is circular, the projection is an ellipse with minor and major axis equal to d_p and $w_{s,2}$, respectively (i.e. $\beta_p = \pi/4$ and l_p is the diameter of the pile d_p). If the pile section is rectangular, the projection is a rhombus of diagonals equal to the diagonal of the square section and $w_{s,2}$ (i.e. $\beta_p = 0.5$ and l_p is the diagonal of the pile section). For slender pile caps ($e/d > 2$), where the behaviour is closer to a beam and the stresses in the strut near the bottom node are relatively constant compared to deep pile caps, factor β_p should be taken equal to 1 (rectangular projection) for both circular and square piles, which ultimately increases the capacity.

The concrete softening coefficient ξ_c accounts for compression softening due to the presence of tensile strains. Several softening models have been proposed in literature (Vecchio and Collins 1993). The well-known model proposed for reinforced concrete panels by Vecchio and Collins (1986) was adopted:

$$f_{ce} = \xi f_{cp} = \frac{f_{cp}}{0.8 + 170\epsilon_{st}} \leq f_{cp} \quad (9.26)$$

where ϵ_{st} is the transverse tensile strain.

To extend this relationship to 3D, it was assumed that the two principal strains perpendicular to the strut ($\epsilon_{st,1}, \epsilon_{st,2}$) contribute equally to softening of the diagonal strut and ϵ_{st} in equation 9.26 was replaced by $\epsilon_{st,1} + \epsilon_{st,2}$. This sum can be obtained from the first invariant of the strain tensor:

$$\epsilon_x + \epsilon_y + \epsilon_z = \epsilon_{tx} + \epsilon_{ty} + \epsilon_z = \epsilon_{st,1} + \epsilon_{st,2} + \epsilon_s \quad (9.27)$$

This equation introduces a strain compatibility condition into the model. The average compressive strain in the z-direction ϵ_z and the average compressive strain of the strut ϵ_s can be estimated as:

$$\epsilon_z = \frac{-P/4}{E_c A_p} \quad (9.28)$$

$$\epsilon_s = \frac{-F_s}{E_c A_{cs,2}} = \frac{-P}{4 \sin \theta_s^{3d} E_c A_{cs,2}} \quad (9.29)$$

The average tensile strain in the x- direction can be derived from the steel strain as:

$$\epsilon_{tx} = \epsilon_t = \frac{F_t}{E_s A_{sp,x}} = \frac{P}{4 \tan \theta_s^{2d} E_s A_{sp,x}} = \frac{P}{4\sqrt{2} \tan \theta_s^{3d} E_s A_{sp,x}} \quad (9.30)$$

and ϵ_{ty} can be obtained similarly. $A_{sp,x}$ and $A_{sp,y}$ are the areas of reinforcement over the pile in the x and y directions respectively, which can be written as a fraction of the total reinforcement area A_{sT} . For bunched, symmetrical reinforcement, the area of reinforcement in each direction ($A_{sp,j}$) is taken as half the total reinforcement area $A_{sT,j}$, assuming that all reinforcement bars are placed over the piles. For grid layouts with hook and nill anchorages, $A_{sp,j}$ can be calculated as:

$$A_{sp,j} = A_{sT,j} \frac{d_p + c_b}{e + d_p} \text{ for circular piles} \quad (9.31)$$

$$A_{sp,j} = A_{sT,j} \frac{l_j + c_b}{e + l_j} \text{ for square and rectangular piles} \quad (9.32)$$

assuming that rebars are distributed uniformly between the outside edges of the piles and considering the spread of the diagonal strut at the reinforcement level. For grid layouts with full anchorage, $A_{sp,j}$ is taken equal to half the total reinforcement area $A_{sT,j}$ to consider confinement effects.

The maximum admissible vertical load limited by splitting of the diagonal strut is obtained from equation 9.1 and equations 9.22 to 9.32 and is given by:

$$P_{ns,2} = 4 \sin \theta_s^{3d} F_{ns,2} = \frac{4 \sin \theta_s^{3d} \beta_p (l_p \sin \theta_s^{3d} + 2c_b \cos \theta_s^{3d}) l_p f_{cp}}{0.8 + 170 (2\epsilon_t + \epsilon_z - \epsilon_s)} = P_{ns,2} (\theta_s^{3d}) \quad (9.33)$$

It must be noted that the maximum admissible load of the pile cap limited by splitting of the strut increases as the strut inclination θ_s^{3d} increases because

transverse tensile strains reduce (variation of the strut area $A_{cs,2}$ depends on the geometry, but for typical values it usually increases as well).

9.3.3 Evaluation of the strength

The three limit functions ($P_{ns,t}, P_{ns,1}, P_{ns,2}$) given by equations 9.14, 9.21 and 9.33 are plotted in figure 9.3 for a certain pile cap. These functions define an area of admissible loads and strut inclinations in which failure will not occur (grey region in figure 9.3). Considering the lower-bound theorem, the predicted pile cap strength P_{pred} corresponds to the maximum admissible load, which is the peak load of the area defined by the limit functions. The peak point can be determined by finding the lowest load between two intersection points: one defined by $P_{nt}(\theta_s^{3d})$ and $P_{ns,1}(\theta_s^{3d})$ (P_f); and the other one by $P_{ns,1}(\theta_s^{3d})$ and $P_{ns,2}(\theta_s^{3d})$ (P_s).

The strut inclination at failure θ_{pred}^{3d} is obtained simultaneously when determining the pile cap strength. The adoption of a variable strut angle θ_s^{3d} permits the realignment of the compressive stresses to steeper inclinations while concrete cracks. This realignment is possible because the stress distribution at the bottom of the stub column is not uniform, and permits to increase the element strength as long as the strength of the top section of the diagonal strut is not exceeded while narrowing.

9.3.4 Evaluation of the mode of failure

The predicted mode of failure can be assessed based on which intersection point governs in each case: if P_f governs (figure 9.3a), failure is identified as flexural; if P_s governs (figure 9.3b-c), failure is identified as shear. Shear failure can take place prior reinforcement yielding (figure 9.3b) or after (figure 9.3c). This is assessed considering the tie yielding function P_{yt} which can be obtained just by replacing the steel ultimate stress f_{su} by the steel yield stress f_{sy} in equation 9.14:

$$P_{yt}(\theta_s^{3d}) = 2\sqrt{2} \tan \theta_s^{3d} A_{sT} f_{sy} \quad (9.34)$$

If the tie yielding function P_{yt} at the calculated strut angle at failure θ_{pred}^{3d} is smaller than the predicted maximum load P_{pred} , the reinforcement will yield prior shear failure.

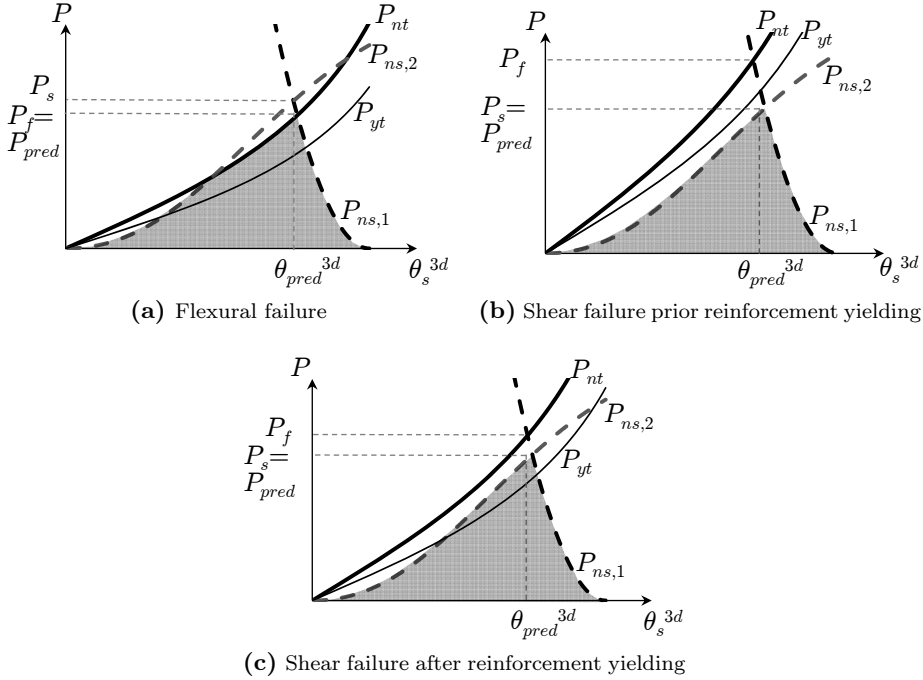


Figure 9.3: Limit functions P_{nt} , $P_{ns,1}$ and $P_{ns,2}$ and yielding function P_{yt} to predict pile cap strength.

Finding the predicted strength and mode of failure using the proposed model can be done by hand or numerically using a simple spreadsheet. It must be noted though that equation 9.33 is implicit because strains ϵ_t , ϵ_z and ϵ_s are a function of the column load P , which is unknown a priori. To simplify the solution procedure it is suggested to assign an initial value P_{est} to P in order to estimate strains in equations 9.29 to 9.30. A good initial value is P_f , which is obtained independently of $P_{ns,2}(\theta_s^{3d})$. Given P_{est} , $P_{ns,2}(\theta_s^{3d})$ can be determined and, hence, a first estimation of P_s . If P_s differs significantly from the estimated load P_{est} , the latter can be updated with P_s to obtain a new $P_{ns,2}(\theta_s^{3d})$ and estimate again P_s . This iterative process can be finished when convergence between P_s and P_{est} is achieved.

9.3.5 Relevance of the method

To highlight the relevance of the proposed model it is necessary to describe briefly first the approach followed by existing STM-based methods to predict the strength of a pile cap. In existing methods the flexural and shear strength is evaluated separately by using two independent equations: the former is determined by the tie elements and the latter by the struts. Reinforcement quantity only affects the flexural strength through the strength of the ties. Fixing the truss geometry permits the direct calculation of truss element forces and strengths, and hence the flexural and shear capacity. Then, the pile cap strength is determined by the minimum value of the two.

The model presented here considers that the strut inclination θ_s^{3d} is unknown a priori and, therefore, the flexural and shear strength cannot be obtained directly. The introduction of an additional variable required the definition of one extra equation. This extra equation was given by the limit function $P_{ns,1}(\theta_s^{3d})$, which accounts for crushing of the diagonal strut at its top section. The intersection of this function with the limit functions associated to the traditionally considered modes of failure (P_{nt} for flexure and $P_{ns,2}$ for shear) determines the predicted flexural and shear strength, respectively.

Moreover, the proposed model accounts for the reinforcement area and its layout to determine the shear strength, factors which proved to have an effect on the shear strength (Souza et al. 2009) but which were not considered in existing models. In the proposed approach the reinforcement area and its layout influence the shear strength in $P_{ns,2}$ through the effective concrete compressive strength f_{ce} . Only the reinforcement area located over the piles A_{sp} and which is assumed to contribute to resist the tensile stresses over the piles, should be considered. For bunched layouts, the total amount of reinforcement contributes to resist the tensile stresses over the piles and, hence, the estimated steel tensile strains are lower than for grid layouts; this assumption is consistent with experimental observations reporting higher failure loads for bunched reinforcement configurations compared with grid layouts with the same total amount of reinforcement (Blévoit and Frémy 1967) (Clarke 1973) (Adebar, D. Kuchma, and Collins 1990) (Suzuki, Otsuki, and Tsubata 1998).

Consideration of (a) a more refined truss geometry and (b) the reinforcement area and layout in the shear strength determination partly explains why predictions obtained by the proposed model exhibit a significantly lower scatter in the results compared to predictions from existing models. This is shown in the following sections.

9.4 Validation with test results

162 pile cap tests reported in literature (Blévoit and Frémy 1967) (Clarke 1973) (Suzuki, Otsuki, and Tsubata 1998) (Suzuki, Otsuki, and Tsubata 1999) (Suzuki, Otsuki, and Tsuchiya 2000) (Suzuki and Otsuki 2002) (Chan and Poh 2000) were considered to validate the proposed model. All specimens had a square shape in plan, had no shear reinforcement and were loaded at a centred square column. Table 9.1 shows the dimensions, material characteristics, reinforcement details (area, type of layout and anchorage conditions), and maximum load and mode of failure observed in the tests. Three failure modes are distinguished in this table: flexural (f), shear (s) and shear after reinforcement yielding (y+s). It is recognised though that the experimental evidence in some of the specimens investigated is not conclusive regarding the failure mode obtained and the identification of a dominant failure mode is uncertain or problematic in those cases. Indeed, the failure of many of the specimens may be more accurately described as a combination of bending and shear. Some specimens of the previously noted references were not included in the study because the tests presented some deficiencies. These tests are: 1,1; 1,2, 1,3, 1,4; 1,5 and 2,1 from Blévoit and Frémy (1967), which were reported by the authors as imperfect tests; 2,5 and 3,5 from Blévoit and Frémy (1967), specimens without flexural reinforcement; and B2 from Clarke (1973), which did not fail during the test.

Equation 9.12 to calculate tie forces was derived assuming that reinforcement was parallel to the cap sides. This configuration corresponds to the majority of the tests in Table 1. However, some the investigated specimens had diagonal reinforcement (denoted with D in the table). For these specimens, it was necessary to calculate first an equivalent tie area to consider this difference. This area was obtained by projecting the tie forces onto the x- and y-axis; for symmetrical cases this results into multiplying the area of diagonal rebars by a factor of $\sqrt{2}/2$.

Regarding the elastic moduli of steel and concrete, and to be consistent with the ACI 318-14, the following values were adopted for all the specimens: for steel, E_s was taken equal to 200 000 MPa; for concrete, E_c was calculated from the concrete compressive strength as $4750\sqrt{f_{c0}}$.

Table 9.1 and figure 9.4 show for each specimen the obtained ratio between the maximum load in the test and the predicted strength (P_{test}/P_{pred}) and failure mode. The average value of P_{test}/P_{pred} for the 162 tests is 1.08 with a coefficient of variation equal to 0.12. The maximum and minimum P_{test}/P_{pred} ratio is 1.55 and 0.74, respectively. The minimum value corresponds to specimen 11,1a of

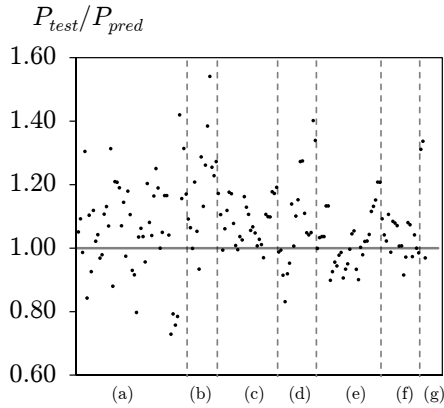


Figure 9.4: Ratio of test-to-predicted strengths P_{test}/P_{pred} for 162 specimens by the proposed method.

Blévoit and Frémy (1967). Similar specimens 11,1b; 11,2a; 11,2b also presented relatively low P_{test}/P_{pred} values compared to other tests. The experimental results for these specimens seem odd though as failure was lower than almost identical tests from the same authors with thinner caps (specimens 12,1a to 12,2b).

Predicted and observed modes of failure are compared next. This comparison shows a correct estimation of the failure mode in 55% of the specimens. This seems reasonable considering (a) the uncertainty in identifying the failure mode from test data in many cases and (b) the fact that the predicted shear and flexural strengths were very close to each other in many tests (see next-to-last column in table 9.1 where the ration $P_{s,pred}/P_{f,pred}$ is given). It must be recognised that in many specimens distinction between shear failure with and without reinforcement yielding was merely based on the description given of the crack pattern; in other specimens (those tested by Suzuki et al.) the load-displacement curve was measured and determination of steel yielding was better supported by experimental evidence; but in any test rebar strains were actually measured to conclude if reinforcement had yielded at failure and, if so, how many of the rebars. Considering the difficulties in correctly identifying these two modes of failure in the specimens investigated, if shear failure with and without yielding of the reinforcement are considered as one mode of failure, then the predicted and observed failure modes coincide in 75% of the specimens.

It is important to remark that only 5 specimens (3%) which failed in shear without yielding were predicted to fail in flexure and only for one of these

specimens the predicted load was larger than the real one (see specimen 3A,3, with $P_{pred}/P_{test} = 0.97$). This scenario is the most concerning of all as it could lead to a brittle shear failure of a specimen designed to fail in a ductile flexural manner.

Based on the results presented in this section it can be concluded that the proposed model predicts the strength and failure modes with reasonable accuracy for the considered specimens.

9.5 Verification with FE results

Results obtained in FE analysis of pile cap foundations were already presented in Chapter 6. Additional FE results are presented in this section for a more direct comparison with the assumptions and results of the proposed strut-and-tie model in order to ultimately demonstrate the adequacy of the latter. Results obtained for specimen BP-30-30-2 from Suzuki, Otsuki, and Tsubata (1998) are used for this purpose.

The following assumptions were considered regarding material modelling: concrete in tension was modelled using Hordijk's softening curve after cracking with the tensile strength given by $f_{ct} = 0.21f_{c0}^{2/3}$ (MPa units) and the fracture energy $G_f = 73f_{c0}^{0.18}$ (N/m and MPa units, respectively) as defined in MC 2010 (Fédération Internationale du Béton 2013); concrete in compression was modelled using a parabolic relationship with a reduction factor due to transverse tensile strains as proposed by Vecchio and Collins (1986) (equation 9.26); enhancement of the compressive strength of concrete due to confinement was taken into account using a Drucker-Prager yield surface; reinforcement steel was modelled as an elastic-hardening plastic material assuming perfect bond between the concrete and the steel.

Figure 9.5 shows the FE results obtained for the considered specimen. Figure 9.5b and 9.5c show the principal compressive stress field and trajectories in the cap diagonal plane at maximum load and after failure, respectively. The proposed strut-and-tie model resulted in a strut inclination of $\theta_s^{3d} = 48.64^\circ$, giving a strut geometry as that superimposed in the plot. In general, the predicted widths of the strut and the FE compressive stress field were similar. The predicted strut inclination is also consistent with the stress trajectories obtained numerically, although in the numerical results the stress direction can be steeper nearer the column and the pile compared to the strut-and-tie model. This is possible thanks to the tensile stresses and confinement enhancement considerations in the numerical model which permits the localisation of stresses

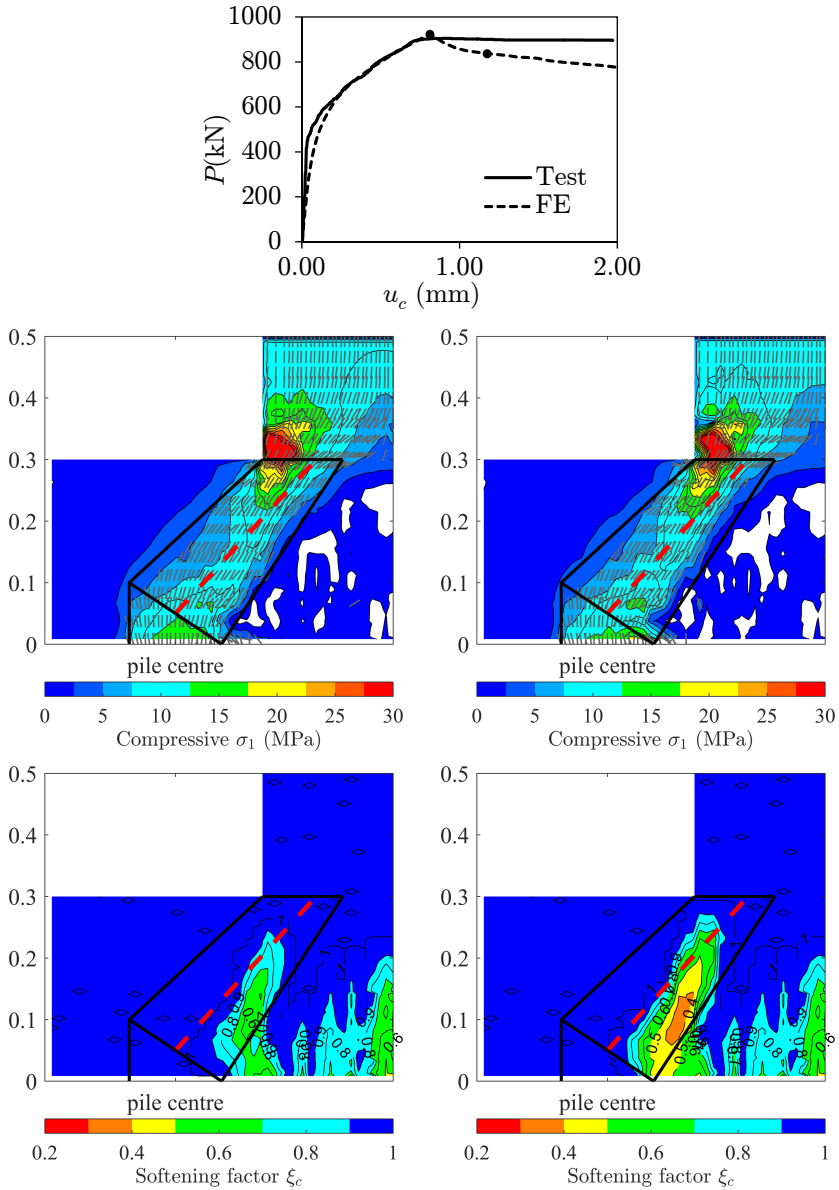


Figure 9.5: FE results for four-pile cap BP-30-30-2: (a) comparison of measured/predicted load-deflection curve; at the diagonal cap plane, superimposed to the strut-and-tie geometry obtained from the proposed method ($\theta_s^{3d} = 48.54^\circ$); (b) FE contour plot of compressive stress field and principal compressive directions at maximum load; (c) FE contour plot of compressive stress field and principal compressive directions after failure; (d) FE contour plot of concrete softening coefficient ξ_c at maximum load; (e) contour plot of concrete softening coefficient ξ_c after failure.

at the column corners. It is worth noting that assuming a fixed inclination of the strut, with the node at the top of the cap at the column quarter points and at the centre of the column, would result in strut angles of 45.28° and 35° , respectively. Both angles are significantly flatter than those obtained numerically and analytically in this work. It must be reminded that flatter angles lead to larger tie forces and lower strut forces, hence affecting the calculated flexural and shear strengths.

Figures 9.5d and 9.5e show the contour plot of the concrete softening coefficient ξ_c obtained from FE analysis in the diagonal plane of the cap at the maximum load and immediately afterwards. As mentioned earlier, the proposed method assumes (a) an uncracked state at the top region of the diagonal strut and adopts ξ equal to 1 and (b) compressive softening at the bottom section due to the transverse cracking (equation 9.26). For the considered specimen the latter resulted in $\xi = 0.5$. These assumptions and the resulting ξ values are consistent with numerical predictions shown in figures 9.5d and 9.5e.

Regarding the mode of failure, the proposed method predicted a shear failure after yielding, and agreed with experimental observations. The numerical model predicts that yielding of the steel and crushing of the concrete near the column govern the failure load. Strut softening initiates at the bottom due to steel yielding and propagates to the top, but not to the full depth (figures 9.5d and 9.5e). This weakening of the strut results in a stress redistribution with a realignment of the strut which becomes steeper and narrower in the region near the column. Therefore, numerical results are consistent with the predicted failure mode using the limit functions proposed in this work.

9.6 Comparison with existing methods

Results obtained for the 162 specimens investigated in the previous section by five other existing methods are presented in this section. In particular, the ACI sectional force approach (ACI Committee 318 2014), the ACI STM approach (ACI Committee 318 2014), the STM-based model by Adebar and Zhou (1996), the STM-based model by Souza et al. (2009) and the STM-based model by J. Park, D. Kuchma, and Souza (2008)) were considered. These methods were described in section 9.2. The accuracy of the predictions was expected to vary from one method to another as the design philosophy and complexity behind each approach is considerably different. Therefore, a direct comparison of the obtained results can be unfair and must be done with care. For example, the ACI STM approach was expected to provide a lower-bound

solution with no focus on the scatter of the results whereas the model by Souza et al. (2009) considers more variables and hence it aims at reducing the coefficient of variation, even if some of the predictions are unconservative.

The results of P_{test}/P_{pred} obtained using these approaches are summarised in figure 9.6.

Regarding the ACI sectional approach, the majority of the specimens are predicted to fail in flexure whereas in reality many tests failed in shear (figure 9.6a). Provisions for shear design with the ACI sectional approach, considering the stress limits from the CRSI Handbook (Concrete Reinforcing Steel Institute 2008), overestimate the shear strength lead. This results in many of the analyses giving unconservative predictions. This is of special concern as it can lead in some cases to brittle shear failures in elements designed to fail in a ductile flexural manner. Inadequacy of sectional-based approaches for the analysis of deep pile caps was already addressed by previous authors (Adebar, D. Kuchma, and Collins 1990) (Adebar and Zhou 1996).

The ACI STM approach provides conservative predictions of all specimens as shown in figure 9.6b, but the high level of conservatism in some cases (maximum $P_{test}/P_{pred} = 3.93$) can be questioned due to its economic implications in design. The shear strength is significantly underestimated in some cases as rather conservative assumptions regarding the concrete strength are adopted.

Predictions obtained with the approach by Adebar and Zhou (1996) (figure 9.6c) have a relatively low scatter ($COV = 21\%$) and only a few analyses result in unconservative predictions. However, most failures are predicted incorrectly as flexural. The proposed bearing stress limit governs in 17 out of 162 specimens. For these 17 specimens the average strength ratio P_{test}/P_{pred} is 1.03, with a coefficient of variation of 20%. These results are remarkable, especially considering the simplicity of the method.

Predictions by the simplified and calibrated model proposed by Souza et al. (2009) (figure 9.6d) also have a low scatter ($COV = 23\%$) with an average value of the P_{test}/P_{pred} ratio of 1.01. It must noted though that this method, and in particular the formula for estimating the flexural strength, was calibrated with experimental results, most of which were included in the current study. The shear design formula proposed by Souza et al. (2009) overestimates the contribution of d to determine the shear strength, similarly to the ACI sectional approach. The reason behind this overestimation is due to the fact that both approaches assume that the whole depth contributes to resist the transverse

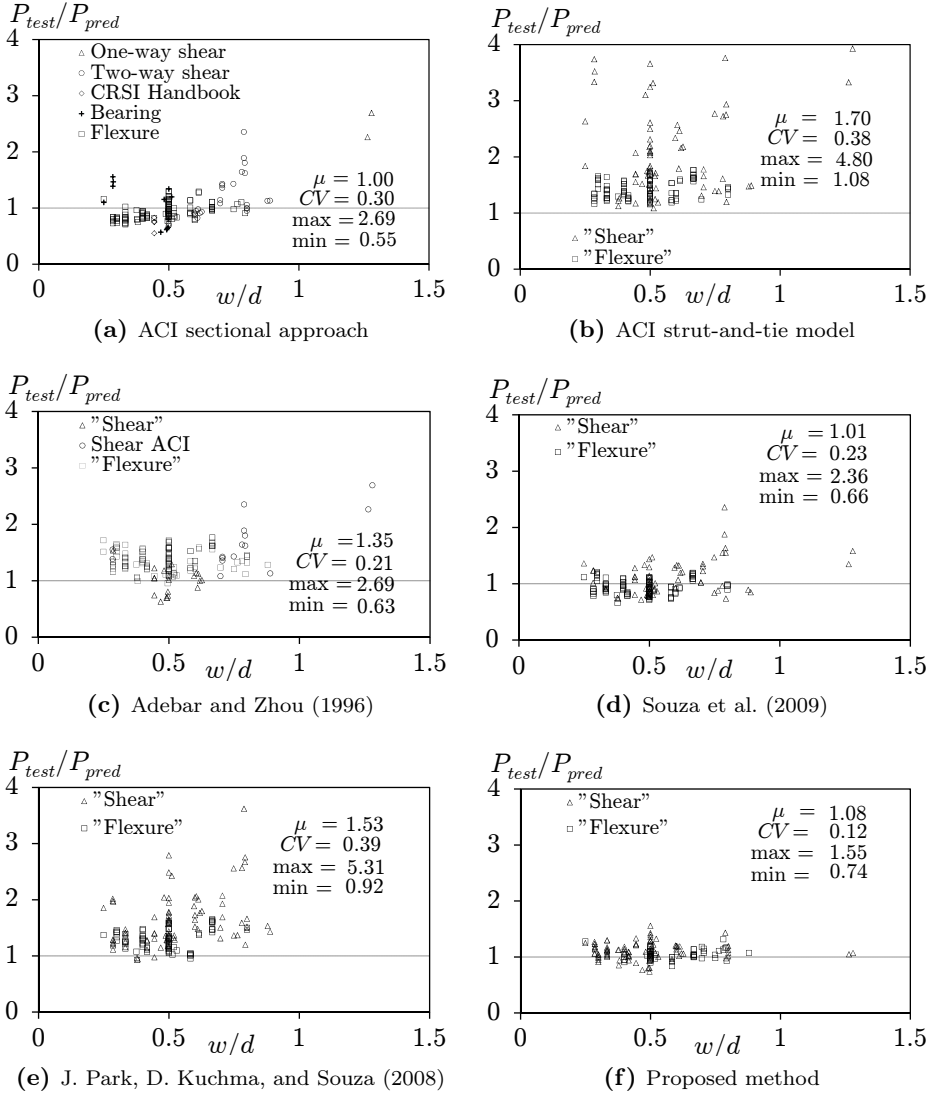


Figure 9.6: Ratio P_{test}/P_{pred} for 162 specimens obtained from the considered methods.

tensile stresses; however, in reality only a portion of this depth contributes to this resistance as it can be inferred from the stress flow.

In the model proposed by J. Park, D. Kuchma, and Souza (2008) (figure 9.6e) the shear strength is clearly underestimated, resulting in excessively large P_{test}/P_{pred} ratios in some of the specimens. For instance, the analyses of specimens 6,1 and 6,2 result in P_{test}/P_{pred} equal to 4.23 and 5.31, respectively. The low concrete strength of these specimens of around 13 MPa is behind these excessively conservative predictions..

Figure 9.6f shows the P_{test}/P_{pred} ratio of the proposed approach using the same axes to facilitate the comparison of the predictions. The proposed method has the lowest coefficient of variation ($COV = 12\%$) and the average value is slightly above one (1.08). As discussed in previous sections, (a) the refinement of the strut-and-tie geometry and (b) consideration of reinforcement details in the determination of the effective strut strength are behind the accuracy in the strength predictions. The relevance of the former is justified next.

Equation 9.35 gives the inclination of a fixed strut assuming that the upper nodes are located at the top of the cap at quarter points at the column:

$$\tan \theta_0^{3d} = \frac{d}{\sqrt{2}(e/2 - c/4)} \quad (9.35)$$

Figure 9.7 compares the simple fixed strut inclination θ_0^{3d} with the one obtained analytically in the proposed model θ_{pred}^{3d} . The latter was obtained by maximizing the strut capacity according to the limit functions. The differences between the angles shown in the figure are generally lower than 5° . Although this value may not seem significant, it must be noted that such an angle difference can result in a variation of the tie forces of around 20-25% and in the strut forces between 5-20%, depending on the strut inclination. These differences can be even larger if the strut inclination is fixed using an upper node at the centre of the column (Souza et al. 2009) or if the nodes are fixed at a section below the cap surface (Comisión Permanente del Hormigón 2008).

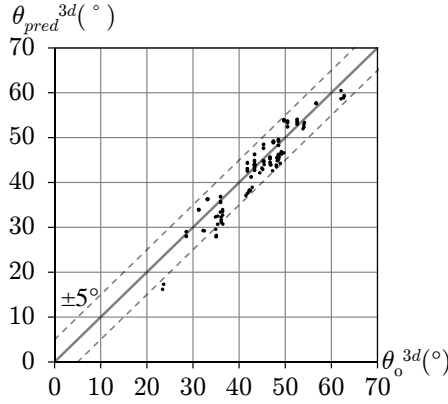


Figure 9.7: Fixed strut angle θ_0^{3d} adopted by other truss models vs. predicted strut angle at failure θ_{pred}^{3d} by the proposed model for 162 specimens.

9.7 Design approach proposed

Based on the method and limit functions described above, a design approach is proposed here to obtain the area of flexural reinforcement needed for a given design load P_u . For design, the steel yield stress f_{sy} will be used rather than the steel ultimate stress f_{su} .

For a given design load P_u , the reinforcement area can be calculated considering $P_{ns,1}$ and P_{yt} . Firstly, the strut angle θ_s^{3d} is determined from equation 9.21 introducing the design load P_u in $P_{ns,1}$. Secondly, the reinforcement area can be obtained introducing the previously calculated strut angle θ_s^{3d} in P_{yt} (equation 9.34). A close formulation can be obtained using this approach from which the required reinforcement quantity can be determined:

$$A_{sT} = \frac{P_u}{4f_{sy}} \frac{18dwf_{cp} + \sqrt{18P_u f_{cp} (d^2 + 2w^2) - 2P_u^2}}{9d^2 f_{cp} - P_u} \quad (9.36)$$

After determining the required steel quantity it is important to check that shear failure without yielding of the reinforcement will not occur. To warrant this it must be checked that the shear strength is larger than the flexural strength. This can be done as follows. Firstly, the predicted strut angle at failure is obtained by equating $P_{ns,1} = P_u$. This angle is then substituted in $P_{ns,2}$ (equation 9.33). If the obtained load is larger than P_u , then the shear

strength is larger than the flexural strength; otherwise, the geometry of the pile cap (e.g. increase the cap depth) or the concrete properties should be modified to increase the strength.

9.8 Conclusions

An adequate design of pile cap foundations is critical, especially considering that these elements are not open to visual inspection after service. Empirical approaches, rules of thumb and sectional-based methods were traditionally used for their design. Although the STM emerged as a more consistent and rational alternative for pile cap design, comparison of the predictions obtained by different STM-based methods proposed in literature shows a significant scatter in the results, a sign that uncertainties on the behaviour of these elements still exist.

This chapter described a new STM-approach which is applicable for the analysis and design of four-pile caps without shear reinforcement. One of the main innovations of this model is the use of a variable strut angle; existing models assume a fixed inclination of the strut using approximate rules. The other main innovation is the use of limit functions to account for different modes of failure. Three potential modes of failure were considered: (i) exceeding the reinforcement strength, (ii) crushing of the diagonal narrowing strut at the base of the column and (iii) splitting of the diagonal strut near the pile due to transverse tensile strains. The intersections between these three functions permits not only the determination of the pile cap strength, but also gives information on the predominant mode of failure. The model also takes into account the effect of the reinforcement area and the type of reinforcement layout on the shear strength, factors which were not considered in existing models.

The application of the method to 162 specimens from literature resulted into very good strength predictions. Five existing methods were considered as well and their results were compared with those obtained with the proposed one. The proposed model had the lowest coefficient of variation from all the methods investigated ($COV = 12\%$) with an average P_{test}/P_{pred} ratio of 1.08. Results obtained from nonlinear FE analysis were also shown to justify the validity of some of the undertaken assumptions.

Although the STM was initially conceived to provide a lower-bound solution, it can be concluded that the use of more refined geometries and formulae to estimate the concrete effective strength can provide more accurate predictions of pile cap strength, which in turn will derive in more economic designs.

Table 9.1: Experimental data and obtained predictions for the considered specimens.

Specimen	$f_{c0} f_{sy} f_{su}$ (MPa)	$h d e c d_p$ (mm)	$A_{sT}(\text{mm}^2) $ Arrangmt. Anch. cond.	P_{test} (kN) Fail.mode	$\frac{P_{test}}{P_{pred}}$ Fail.mode	$\frac{P_{s,pred}}{P_{f,pred}}$	θ_{pred}^{3d}
Blévoet and Frémy 1967							
4N1	37.3 277 401	750 675 1200 500 350 □	7843 B,hook	7000 y+s	1.07 y+s	0.82	43.0
4N1bis	40.8 455 774	750 682 1200 500 350 □	4824 B,hook	6700 s	1.11 y+s	0.64	44.1
4N2	37.1 285 416	750 660 1200 500 350 □	7602 B+D,hook	6580 s	1.00 y+s	0.84	42.2
4N2bis	34.2 491 803	750 670 1200 500 350 □	4816 B+D,hook	7390 s	1.32 s	0.60	43.3
4N3	34.2 257 387	1000 926 1200 500 350 □	6085 B,hook	6500 f	0.85 y+s	0.90	52.4
4N3bis	49.3 452 781	1000 931 1200 500 350 □	3941 B,hook	9000 y+s	1.12 y+s	0.72	53.4
4N4	35.4 291 413	1000 919 1200 500 350 □	6702 B+D,hook	7530 y+s	0.94 y+s	0.83	52.0
4N4bis	42.3 486 811	1000 926 1200 500 350 □	4384 B+D,hook	8750 s	1.13 s	0.63	53.0
2,2	32.8 355 428	300 277 420 150 140 □	639 B,hook	810 f	1.02 f	1.06	45.7
2,3	31.6 312 409	300 259 420 150 140 □	636 B+D,hook	740 y+s	1.04 f	1.18	44.0
2,4	31.0 330 425	300 261 420 150 140 □	628 C,hook	705 f	0.97 f	1.14	43.9
3,1	32.1 469 643	200 180 420 150 140 □	402 B,hook	475 y+s	0.98 f	1.37	33.6
3,2	37.2 447 589	200 177 420 150 140 □	444 D,hook	540 f	1.11 f	1.48	33.4
3,3	30.9 442 590	200 173 420 150 140 □	424 B+D,hook	510 y+s	1.13 f	1.46	32.5
3,4	32.6 474 638	200 154 420 150 140 □	402 C,hook	435 y+s	1.07 f	1.57	29.3
1A,1	26.6 493 580	300 270 420 180 140 □	766 B,hook	1150 s	1.33 s	0.71	46.4
1A,2	36.8 505 566	300 270 420 180 140 □	755 D,hook	900 s	0.89 s	0.82	46.8
1A,2 bis	33.3 505 566	300 270 420 180 140 □	755 D,hook	1178 s	1.22 s	0.79	46.7
1A,3	36.6 508 584	300 270 420 180 140 □	656 B+D,hook	1185 s	1.22 s	0.86	47.0
1A,4	32.9 497 567	300 270 420 180 140 □	766 C,hook	1158 s	1.21 s	0.78	46.6
3A,1	29.2 506 580	200 170 420 180 140 □	766 B,hook	815 s	1.07 f	1.08	31.2
3A,2	39.2 505 582	200 170 420 180 140 □	755 D,hook	900 s	1.14 f	1.20	32.3
3A,3	32.0 499 572	200 172 420 180 140 □	656 B+D,hook	665 s	0.97 f	1.21	32.8
3A,3bis	46.1 499 572	200 172 420 180 140 □	656 B+D,hook	843 f	1.18 f	1.37	34.0
3A,4	32.4 493 572	200 170 420 180 140 □	766 C,hook	845 s	1.11 f	1.14	31.7
Q,1	33.9 460 608	200 170 420 150 140 □	403 G,hook	408 f	0.93 f	1.29	32.3

Q,2	30.8	342	442	300	272	420	150	140	□	628	G,hook	650	y+s	0.93	y+s	0.89	45.6
Q,2bis	21.0	325	464	300	273	420	150	140	□	806	G,hook	510	y+s	0.81	s	0.65	45.0
6,1	13.2	498	592	140	107	420	150	140	□	628	B,hook	250	s	1.05	s	0.80	17.4
6,2	13.2	461	535	140	106	420	150	140	□	1232	B,hook	290	s	1.07	s	0.63	16.3
6,3	22.1	512	593	200	180	420	150	140	□	628	B,hook	650	f	1.04	f	1.01	30.8
6,4	30.6	476	558	200	171	420	150	140	□	1232	B,hook	850	s	0.97	s	0.88	28.1
6,5	18.4	518	618	300	264	420	150	140	□	905	B,hook	842	s	1.22	s	0.55	42.7
6,6	18.4	468	555	300	280	420	150	140	□	1608	B,hook	810	s	1.09	s	0.39	44.3
9A,1	22.6	459	636	500	474	420	150	140	□	904	B,hook	1200	s	1.05	s	0.48	59.4
9A,2	33.9	467	595	500	471	420	150	140	□	1608	B,hook	1900	s	1.18	s	0.43	58.9
9A,3	28.6	465	616	500	474	420	150	140	□	1809	B+G,hook	1700	s	1.26	s	0.32	59.4
10,1a	28.7	446	605	250	226	420	150	140	□	904	B,hook	850	s	1.20	s	0.63	39.0
10,1b	35.8	468	593	250	221	420	150	140	□	888	B+D,hook	800	s	1.01	s	0.72	38.4
10,2a	28.2	453	615	250	218	420	150	140	□	904	B,hook	750	s	1.06	s	0.64	37.6
10,2b	26.1	471	592	250	220	420	150	140	□	886	B+D,hook	800	s	1.19	s	0.65	38.0
10,3a	23.6	462	630	250	223	420	150	140	□	904	B,hook	760	s	1.19	s	0.57	38.3
10,3b	27.7	472	601	250	215	420	150	140	□	886	B+D,hook	740	s	1.06	s	0.67	37.2
11,1a	22.3	311	431	300	272	420	150	140	□	904	B,hook	563	y+s	0.74	s	0.76	44.0
11,1b	16.2	311	431	300	272	420	150	140	□	904	B,nil	493	y+s	0.80	s	0.65	43.6
11,2a	25.6	445	545	300	288	420	150	140	□	628	B,hook	558	s	0.77	s	0.75	46.7
11,2b	24.9	441	546	300	275	420	150	140	□	628	B,nil	585	y+s	0.80	s	0.79	44.9
12,1a	17.3	319	436	200	171	420	150	140	□	904	B,hook	840	f	1.43	y+s	0.99	28.0
12,1b	18.2	319	436	200	171	420	150	140	□	904	B,nil	693	f	1.16	f	1.02	28.2
12,2a	27.0	436	541	200	173	420	150	140	□	628	B,hook	750	y+s	1.31	f	1.21	30.7
12,2b	21.7	432	543	200	170	420	150	140	□	628	B,nil	640	y+s	1.17	f	1.13	29.6

Clarke 1973

A1	21.3	410	590	450	400	600	200	200	●	785	G,hook	1110	s	1.11	y+s	0.77	46.1
A2	27.6	410	590	450	400	600	200	200	●	785	B,hook	1420	s	1.08	y+s	0.98	45.7
A3	30.8	410	590	450	400	600	200	200	●	778	D,hook	1340	s	1.00	f	1.03	45.9
A4	21.4	410	590	450	400	600	200	200	●	785	G,nil	1230	s	1.23	y+s	0.77	46.1
A5	27.7	410	590	450	400	600	200	200	●	785	B,nil	1400	s	1.06	y+s	0.98	45.7
A6	26.9	410	590	450	400	600	200	200	●	778	D,nil	1230	s	0.95	y+s	0.98	45.7

A7	25.2	410	590	450	400	600	200	200	●	785	G,full	1640	s	1.30	y+s	0.95	45.6
A8	27.6	410	590	450	400	600	200	200	●	785	B,hook	1510	s	1.15	y+s	0.98	45.7
A9	27.7	410	590	450	400	600	200	200	●	785	G,hook	1450	s	1.29	y+s	0.84	46.4
A10	18.8	410	590	450	400	600	200	200	●	785	G,full+bob	1520	f	1.40	y+s	0.85	45.3
A11	18.0	410	590	450	400	600	200	200	●	785	G,full	1640	f	1.55	y+s	0.83	45.3
A12	26.3	410	590	450	400	600	200	200	●	785	G,full+bob	1640	f	1.28	y+s	0.96	45.7
B1	27.8	410	590	450	400	400	200	200	●	628	G,full	2080	s	1.25	y+s	0.97	58.8
B3	34.0	410	590	450	400	400	200	200	●	471	G,full	1770	f	1.27	f	1.20	60.5

Suzuki, Otsuki, and Tsubata 1998

BP-20-1	21.3	413	606	200	150	540	300	150	●	570	G,hook	519	y+s	1.19	y+s	0.84	29.1
BP-20-2	20.4	413	606	200	150	540	300	150	●	570	G,hook	480	y+s	1.12	y+s	0.83	29.1
BPC-20-1	21.9	413	606	200	150	540	300	150	●	570	B,hook	519	y+s	1.01	y+s	0.98	28.2
BPC-20-2	19.9	413	606	200	150	540	300	150	●	570	B,hook	529	y+s	1.07	y+s	0.96	28.0
BP-25-1	22.6	413	606	250	200	540	300	150	●	713	G,hook	735	s	1.14	y+s	0.76	37.0
BP-25-2	21.5	413	606	250	200	540	300	150	●	713	G,hook	755	s	1.19	y+s	0.74	36.9
BPC-25-1	18.9	413	606	250	200	540	300	150	●	713	B,hook	818	y+s	1.19	y+s	0.83	35.6
BPC-25-2	22.0	413	606	250	200	540	300	150	●	713	B,hook	813	y+s	1.09	y+s	0.88	35.9
BP-20-30-1	29.1	405	592	200	150	500	300	150	●	428	G,hook	485	y+s	1.01	f	1.10	33.9
BP-20-30-2	29.8	405	592	200	150	500	300	150	●	428	G,hook	480	y+s	1.00	f	1.10	34.0
BPC-20-30-1	29.8	405	592	200	150	500	300	150	●	428	B,hook	500	f	1.04	f	1.29	34.0
BPC-20-30-2	29.8	405	592	200	150	500	300	150	●	428	B,hook	495	f	1.03	f	1.29	34.0
BP-30-30-1	27.3	405	592	300	250	500	300	150	●	570	G,hook	916	s	1.18	y+s	0.76	48.6
BP-30-30-2	28.5	405	592	300	250	500	300	150	●	570	G,hook	907	y+s	1.15	y+s	0.77	48.6
BPC-30-30-1	28.9	405	592	300	250	500	300	150	●	570	B,hook	1039	y+s	1.12	y+s	0.90	47.7
BPC-30-30-2	30.9	405	592	300	250	500	300	150	●	570	B,hook	1029	y+s	1.08	y+s	0.92	47.8
BP-30-25-1	30.9	405	592	300	250	500	250	150	●	570	G,hook	794	y+s	1.09	y+s	0.82	44.3
BP-30-25-2	26.3	405	592	300	250	500	250	150	●	570	G,hook	725	s	1.07	y+s	0.77	44.1
BPC-30-25-1	29.1	405	592	300	250	500	250	150	●	570	B,hook	853	y+s	1.02	y+s	0.94	43.4
BPC-30-25-2	29.2	405	592	300	250	500	250	150	●	570	B,hook	872	y+s	1.04	y+s	0.94	43.4
BDA-70x90-1	29.1	356	501	300	250	500	250	150	●	570	G,hook	784	y+s	1.02	y+s	0.99	43.8
BDA-70x90-2	30.2	356	501	300	250	500	250	150	●	570	G,hook	755	y+s	0.97	f	1.01	43.9
BDA-80x90-1	29.1	356	501	300	250	500	250	150	●	570	G,hook	858	y+s	1.11	f	1.02	43.8

BDA-80x90-2	29.3	356	501	300	250	500	250	150	●	570	G,hook	853	y+s	1.10	f	1.02	43.8
BDA-90x90-1	29.5	356	501	300	250	500	250	150	●	570	G,hook	853	y+s	1.10	f	1.05	43.8
BDA-90x90-2	31.5	356	501	300	250	500	250	150	●	570	G,hook	921	y+s	1.18	f	1.07	44.0
BDA-100x90-1	29.7	356	501	300	250	500	250	150	●	570	G,hook	911	y+s	1.17	f	1.08	43.9
BDA-100x90-2	31.3	356	501	300	250	500	250	150	●	570	G,hook	931	y+s	1.19	f	1.10	44.0

Suzuki, Otsuki, and Tsubata 1999

TDL1-1	30.9	356	501	350	300	600	250	150	●	285	G,hook	392	f	0.99	f	1.30	44.5
TDL1-2	28.2	356	501	350	300	600	250	150	●	285	G,hook	392	f	0.99	f	1.25	44.3
TDL2-1	28.6	356	501	350	300	600	250	150	●	428	G,hook	519	f	0.91	f	1.02	43.1
TDL2-2	28.8	356	501	350	300	600	250	150	●	428	G,hook	472	f	0.83	f	1.02	43.1
TDL3-1	29.6	356	501	350	300	600	250	150	●	570	G,hook	608	f	0.93	y+s	0.89	42.6
TDL3-2	29.3	356	501	350	300	600	250	150	●	570	G,hook	627	f	0.96	y+s	0.89	42.6
TDS1-1	25.6	356	501	350	300	450	250	150	●	428	G,hook	921	f	1.15	y+s	0.97	54.1
TDS1-2	27.0	356	501	350	300	450	250	150	●	428	G,hook	833	f	1.02	y+s	0.97	54.2
TDS2-1	27.2	356	501	350	300	450	250	150	●	570	G,hook	1005	f	1.12	y+s	0.85	53.6
TDS2-2	27.3	356	501	350	300	450	250	150	●	570	G,hook	1054	f	1.17	y+s	0.85	53.7
TDS3-1	28.0	356	501	350	300	450	250	150	●	784	G,hook	1299	y+s	1.29	s	0.73	53.1
TDS3-2	28.1	356	501	350	300	450	250	150	●	784	G,hook	1303	y+s	1.29	s	0.73	53.1
TDM1-1	27.5	383	522	300	250	500	250	150	●	285	G,hook	490	f	1.11	f	1.25	46.4
TDM1-2	26.3	383	522	300	250	500	250	150	●	285	G,hook	461	f	1.05	f	1.23	46.2
TDM2-1	29.6	383	522	300	250	500	250	150	●	428	G,hook	657	f	1.04	f	1.04	44.9
TDM2-2	27.6	383	522	300	250	500	250	150	●	428	G,hook	657	f	1.05	f	1.01	44.7
TDM3-1	27.0	370	528	300	250	500	250	150	●	1270	G,hook	1245	s	1.42	s	0.57	42.8
TDM3-2	28.0	370	528	300	250	500	250	150	●	1270	G,hook	1210	s	1.36	s	0.58	42.8

Suzuki, Otsuki, and Tsuchiya 2000

BDA-20-25-70-1	26.1	358	496	200	150	450	250	150	●	285	G,hook	294	f	1.00	f	1.54	36.3
BDA-20-25-70-2	26.1	358	496	200	150	450	250	150	●	285	G,hook	304	f	1.03	f	1.54	36.3
BDA-20-25-80-1	25.4	358	496	200	150	450	250	150	●	285	G,hook	304	f	1.04	f	1.51	36.2
BDA-20-25-80-2	25.4	358	496	200	150	450	250	150	●	285	G,hook	304	f	1.04	f	1.51	36.2
BDA-20-25-90-1	25.8	358	496	200	150	450	250	150	●	285	G,hook	333	f	1.13	f	1.53	36.3
BDA-20-25-90-2	25.8	358	496	200	150	450	250	150	●	285	G,hook	333	f	1.13	f	1.53	36.3

BDA-30-20-70-1	25.2	358	496	300	250	450	200	150	●	428	G,hook	534	f	0.90	f	1.05	44.7
BDA-30-20-70-2	24.6	358	496	300	250	450	200	150	●	428	G,hook	549	y+s	0.93	f	1.05	44.6
BDA-30-20-80-1	25.2	358	496	300	250	450	200	150	●	428	G,hook	568	f	0.96	f	1.05	44.7
BDA-30-20-80-2	26.6	358	496	300	250	450	200	150	●	428	G,hook	564	f	0.94	f	1.08	44.9
BDA-30-20-90-1	26.0	358	496	300	250	450	200	150	●	428	G,hook	583	f	0.98	f	1.06	44.8
BDA-30-20-90-2	26.1	358	496	300	250	450	200	150	●	428	G,hook	588	f	0.99	f	1.06	44.8
BDA-30-25-70-1	28.8	383	522	300	250	450	250	150	●	428	G,hook	662	y+s	0.91	f	1.02	49.1
BDA-30-25-70-2	26.5	383	522	300	250	450	250	150	●	428	G,hook	676	y+s	0.95	y+s	0.99	48.9
BDA-30-25-80-1	29.4	383	522	300	250	450	250	150	●	428	G,hook	696	y+s	0.95	f	1.02	49.2
BDA-30-25-80-2	27.8	383	522	300	250	450	250	150	●	428	G,hook	725	y+s	1.00	f	1.00	49.0
BDA-30-25-90-1	29.0	383	522	300	250	450	250	150	●	428	G,hook	764	y+s	1.05	f	1.03	49.2
BDA-30-25-90-2	26.8	383	522	300	250	450	250	150	●	428	G,hook	764	f	1.06	y+s	0.99	49.0
BDA-30-30-70-1	26.8	358	496	300	250	450	300	150	●	428	G,hook	769	y+s	0.94	y+s	0.99	54.0
BDA-30-30-70-2	25.9	358	496	300	250	450	300	150	●	428	G,hook	730	y+s	0.91	y+s	0.98	53.9
BDA-30-30-80-1	27.4	358	496	300	250	450	300	150	●	428	G,hook	828	y+s	1.01	y+s	1.00	54.0
BDA-30-30-80-2	27.4	358	496	300	250	450	300	150	●	428	G,hook	809	y+s	0.98	y+s	1.00	54.0
BDA-30-30-90-1	27.2	358	496	300	250	450	300	150	●	428	G,hook	843	y+s	1.03	y+s	0.99	54.1
BDA-30-30-90-2	24.5	358	496	300	250	450	300	150	●	428	G,hook	813	y+s	1.05	y+s	0.96	53.9
BDA-40-25-70-1	25.9	358	496	400	350	450	250	150	●	570	G,hook	1019	s	1.06	y+s	0.80	57.7
BDA-40-25-70-2	24.8	358	496	400	350	450	250	150	●	570	G,hook	1068	y+s	1.13	y+s	0.78	57.7
BDA-40-25-80-1	26.5	358	496	400	350	450	250	150	●	570	G,hook	1117	f	1.15	y+s	0.80	57.8
BDA-40-25-80-1	25.5	358	496	400	350	450	250	150	●	570	G,hook	1117	y+s	1.17	y+s	0.79	57.7
BDA-40-25-90-1	25.7	358	496	400	350	450	250	150	●	570	G,hook	1176	f	1.23	y+s	0.79	57.7
BDA-40-25-90-2	26.0	358	496	400	350	450	250	150	●	570	G,hook	1181	f	1.23	y+s	0.80	57.7

Suzuki and Otsuki 2002

BPL-35-30-1	24.1	353	505	350	300	500	300	150	●	642	G,hook	960	s	1.11	y+s	0.75	53.4
BPL-35-30-2	25.6	353	505	350	300	500	300	150	●	642	G,hook	941	s	1.06	y+s	0.76	53.5
BPB-35-30-1	23.7	353	505	350	300	500	300	150	●	642	G,full+bob	1029	y+s	1.04	y+s	0.86	52.5
BPB-35-30-2	23.5	353	505	350	300	500	300	150	●	642	G,full+bob	1103	y+s	1.12	y+s	0.85	52.5
BPH-35-30-1	31.5	353	505	350	300	500	300	150	●	642	G,hook	980	s	1.00	y+s	0.82	53.7
BPH-35-30-2	32.7	353	505	350	300	500	300	150	●	642	G,hook	1088	y+s	1.09	y+s	0.83	53.8
BPL-35-25-1	27.1	353	505	350	300	500	250	150	●	642	G,hook	902	y+s	1.09	y+s	0.81	49.3

BPL-35-25-2	25.6	353	505	350	300	500	250	150	●	642	G,hook	872	s	1.08	y+s	0.79	49.3
BPB-35-25-1	23.2	353	505	350	300	500	250	150	●	642	G,full+bob	911	y+s	1.02	y+s	0.89	48.4
BPB-35-25-2	23.7	353	505	350	300	500	250	150	●	642	G,full+bob	921	y+s	1.02	y+s	0.89	48.4
BPH-35-25-1	36.6	353	505	350	300	500	250	150	●	642	G,hook	882	s	0.94	y+s	0.89	49.7
BPH-35-25-2	37.9	353	505	350	300	500	250	150	●	642	G,hook	951	s	0.99	y+s	0.90	49.7
BPL-35-20-1	22.5	353	505	350	300	500	200	150	●	642	G,hook	755	s	1.09	y+s	0.78	45.4
BPL-35-20-2	21.5	353	505	350	300	500	200	150	●	642	G,hook	735	s	1.08	y+s	0.77	45.3
BPB-35-20-1	20.4	353	505	350	300	500	200	150	●	642	G,full+bob	755	y+s	0.99	y+s	0.87	44.6
BPB-35-20-2	20.2	353	505	350	300	500	200	150	●	642	G,full+bob	804	y+s	1.06	y+s	0.86	44.6
BPH-35-20-1	31.4	353	505	350	300	500	200	150	●	642	G,hook	813	s	1.02	y+s	0.87	45.7
BPH-35-20-2	30.8	353	505	350	300	500	200	150	●	642	G,hook	794	s	1.00	y+s	0.86	45.7
Chan and Poh 2000																	
A	39.7	481	601	400	325	600	200	150	●	628	G,full	1230	f	1.31	f	1.11	41.3
B	38.3	481	601	400	325	600	200	150	●	628	G,full	1250	f	1.34	f	1.10	41.2
C	36.4	481	601	300	225	600	200	150	●	942	G,full	870	y+s	0.97	f	1.05	29.3

Pile shape: □ - square; ● - circular

Reinforcement arrangement: B - square bunched over piles; D - diagonal bunched; G - grid; C - continuous bunched.

Mode of failure: s - shear failure; f - flexural failure; y+s - reinforcement yielding followed by shear failure

Part V

Conclusions

Chapter 10

Conclusions

From a practical point of view, true simplicity can only be achieved if solutions are accepted with sufficient (but not perfect) accuracy.

—J. Schlaich, Schafer, and Jennewein 1987

10.1 Summary

This document summarises the work undertaken by the author to develop a 3D nonlinear FE-based tool for the analysis and design of reinforced concrete elements. The name of this tool is FESCA 3D, acronym of *Finite Elements for Simplified Concrete Analysis in 3D*. This tool was conceived as an alternative, simpler approach to already existing advanced FE software packages. Although the capabilities of the latter for obtaining very realistic predictions is unquestionable, it must be acknowledged that they are usually excessively sophisticated for the practising engineer, who is generally used to simpler and more intuitive methods and models as those proposed in design codes.

Several examples of applications were shown to highlight the relevance of a more simplified FE analysis as that proposed with FESCA 3D. These examples focused on D-regions with a 3D behaviour, whose study is not well covered in literature and for which the application of the STM and the SFM presents limitations. Both analysis and design cases were treated: on the one hand, comparison of experimental and numerical results demonstrated that, despite the simplifications adopted in the tool regarding concrete modelling, realistic predictions can be obtained in analysis if the right factors are considered

appropriately; on the other hand, application of the tool for design purposes showed its capacity for the generation of rational reinforcement arrangements in an automatic manner.

The application of the FE tool facilitated a better understanding of the internal response of 3D D-regions. This knowledge was used to develop a refined 3D strut-and-tie model for the analysis and design of four-pile caps with rectangular geometries. Very good strength predictions were obtained for the 162 specimens investigated.

10.2 Conclusions drawn from this work

A summary of the conclusions drawn from this work is given in this section.

Concrete modelling (Chapter 3)

Observing the existing problems related with obtaining reliable multiaxial test data on concrete and that the use of excessively complicated constitutive models is one of the main barriers that practising engineers encounter when using advanced FE programs, it was preferred to adopt some simplifications to at least facilitate the definition of the material model and the interpretation of the output results.

A 3D orthotropic, rotating model was implemented, permitting the use of simple uniaxial stress-strain relationships to characterise the 3D behaviour. The number of input parameters was reduced to the minimum and, indeed, the familiar uniaxial compressive strength f_{c0} is the only mandatory input parameter. Any uniaxial stress-strain model can be defined, giving flexibility to the user.

If relatively-refined uniaxial models are considered, the obtained predictions can be rather realistic. In particular, the adoption of the nonlinear compressive model proposed by Popovics (1973) (modified to account for the effect of cracking on the compressive strength (Vecchio and Collins 1986) and strength enhancement due to confinement considering a Drucker-Prager yield surface) and the tensile model proposed by Hordijk (1991) provided realistic response predictions for the specimens investigated.

Neglecting the tensile strength of concrete is a common assumption in engineering practice. Adoption of this hypothesis in FE analysis leads to conservative strength predictions and, what is more relevant, provides a clear picture of

the internal stress flow near the ultimate state. Development of rational strut-and-tie models from these results becomes straightforward. However, this assumption introduces a strong nonlinearity into the model, which required the implementation of robust resolution methods.

Reinforcement modelling (Chapter 4)

A comprehensive embedded reinforcement model was implemented allowing for a great flexibility in the definition of complex rebar geometries regardless of the geometry of the FE mesh. An additional function was integrated to facilitate the introduction of curved geometries by just defining the bending radio and a selection of master points.

The perfect-bond model proved to be sufficient for determining the global response in the conducted analyses. However, it is worth mentioning that a bond-slip model was implemented as well, which can be useful for analysis cases in which anchorage conditions present deficiencies that may affect the global response and/or to account for tension stiffening effects and/or to determine rebar stresses along curved sections more realistically.

Significance of the boundary conditions (Chapter 5)

The attention attracted by concrete modelling contrasts with the little importance given to the definition of the boundary conditions imposed by loads and supports. It is true that relevance of the latter may not be significant when load and support dimensions are relatively small compared to the global dimensions of the whole element (in simply supported beams, for instance) as long as they are placed reasonably well. However, in D-regions load and/or support dimensions and the dimensions of the critical region are usually of the same order of magnitude. Therefore, special attention must be given when defining the boundary conditions in FE analysis of these elements; results can be significantly distorted if they are not defined adequately (Chapter 5). Indeed, this factor can have a higher impact in the global response than adopting a simpler or a more refined concrete model (Chapter 6).

It was recognised that a sound definition of the boundary conditions can be time-consuming, especially when the geometry of the boundary elements does not fit the geometry of the FE mesh (for instance, the existence of circular piles in a pile cap foundation meshed by regular hexahedrons). Special load and support models were developed to facilitate the definition of most typical boundary conditions in D-regions: on the one hand, a load model based on

static condensation was implemented to permit the consideration of the column effect on the global response without having to include it explicitly in the FE model; on the other hand, a uniform-stress support model and a flexible support model were developed allowing for the generation of consistent stress distributions at the support areas without having to include support elements explicitly into the FE mesh.

Looking for a sufficient level of accuracy in engineering practice

The structural engineer usually encounters two different types of problems: (i) the design of new structures and (ii) the assessment of existing ones. Two different approaches should be followed to solve these problems. On the one hand, for design, both the ultimate limit state and the serviceability limit state must be considered; conservative assumptions are undertaken to guarantee the structural safety and an appropriate response under service loads; conservatism takes priority over accuracy. On the other hand, for assessment, only the ultimate limit state usually needs to be considered. The strength of the existing structure or element must be determined and compared with the design actions. The ultimate objective in assessment is to avoid or reduce as much as possible potential retrofiting. Therefore, it is wise to start with simple, conservative models providing a lower-bound solution. If the calculated strength is larger than the design actions, the accuracy of the prediction is sufficient for assessment purposes and there is no need of further refinement; otherwise, the model should be refined to provide a more realistic, higher strength. Therefore, it must be highlighted that there is no need to start with complex models if simpler, more conservative ones are sufficient.

Discussion in the previous paragraph must be considered in FE analysis of reinforced concrete structures. A common, simple, conservative assumption in engineering practice is neglecting the tensile strength of concrete. Results showed that including this assumption in FE analysis does not only provide a lower-bound solution, but can also be appealing for understanding better the internal flow of forces and for generating rational strut-and-tie models.

Automatic generation of consistent 3D stress fields

The capacity of the tool to generate consistent compressive stress field adaptable to different reinforcement configurations was demonstrated. FE results also showed the effect of the reinforcement geometry on the internal stress field (Chapter 7).

Rational strut-and-tie models can be easily derived after plotting the principal compressive stress directions obtained from nonlinear FE analysis neglecting the tensile strength of concrete. This information can be useful for the structural engineer to find out if the proposed reinforcement is rational and/or to identify the stress field within the body.

Finite elements for design

Undertaking simplified FE analyses reduces computational times and, therefore, makes acceptable the implementation of iterative design procedures inside the FE environment. A simple design algorithm was implemented by which rebar areas are updated based on rebar stresses obtained from nonlinear FE analysis (section 2.3.2). Results for an anchorage block showed the capacity of this simple algorithm to configure automatically a rational reinforcement arrangement by eliminating those rebars which are less demanded (Chapter 8).

Refined 3D strut-and-tie model for four-pile caps

A refined 3D strut-and-tie model for rectangular four-pile caps was developed based on FE results and experimental observations reported in scientific literature. One of the main innovations of this model is the use of a variable strut angle, contrary to the general trend in existing models, which assume a fixed inclination of the strut using approximate rules. The proposed approach also gives information on the predominant mode of failure, which is consistent with test observations and 3D FE simulations. Three potential modes of failure were considered: (i) exceeding the reinforcement strength, (ii) crushing of the diagonal, narrowing strut at the base of the column and (iii) splitting of the diagonal strut near the pile due to transverse tensile strains. The model takes into account the refined inclination of the strut, the effect of the reinforcement area and the type of reinforcement layout. These refined considerations resulted into very good strength predictions of the 162 tests investigated. The proposed model had the lowest coefficient of variation from all the methods investigated ($COV = 12\%$) with an average P_{test}/P_{pred} ratio of 1.08.

10.3 Future work

Accessibility of FESCA 3D

As mentioned in the document FESCA 3D was developed in MATLAB (2014) and, therefore, must be run on this platform. This presents many advantages, but also some limitations. Now that the fundamentals of the tool were proved, it would be appealing to translate this code into a more efficient programming language and to develop a proper user environment to facilitate its application by external users.

Concrete stress distortion due to reinforcement discontinuity

The implementation of the embedded reinforcement model provided a great flexibility in the definition of the rebar geometry. But this model also causes a strong stiffness discontinuity inside those concrete elements in which they are embedded. This can lead to local stress distortion under certain conditions. Although it seems that global results are not affected by this, it is necessary to study this further in detail.

Study of 3D D-regions

3D D-regions need further study both analytically and experimentally, same way as D-regions needed it before the appearance of the STM and the SFM. Current design procedures are in general excessively conservative due to the existing uncertainties. A better understanding of these elements could derive in more optimal designs, reducing material requirements and costs. Importance of 3D D-regions is specially remarkable for those elements such as pile caps and socket base column-to-foundation connections that are not open to visual inspection after service.

Guidelines for 3D strut-and-tie models

A refined 3D strut-and-tie model was proposed for four-pile caps with rectangular geometries subjected to a rectangular column load. Although a large portion of pile caps in practice fulfils these conditions, it must be acknowledged that its application is limited to a rather specific element. Additional general guidelines should be proposed for the application of the STM to 3D elements, especially on the determination of the strength of struts and nodal zones.

Bibliography

- ACHE (2003). *Monografía M-6. Método de Bielas y Tirantes*, p. 187 (cit. on p. 5).
- ACI Committee 318 (2002). *Building Code Requirements for Structural Concrete (ACI 318-02) and Commentary (ACI 318R-02)*. Farmington Hills: American Concrete Institute, p. 443 (cit. on p. 5).
- (2014). *Building Code Requirements for Structural Concrete (ACI 318-14) and Commentary (ACI 318R-14)*. Farmington Hills: American Concrete Institute, p. 520 (cit. on pp. 171, 172, 188).
- Adebar, P., Kuchma, D., and Collins, M. P. (1990). “Strut-and-Tie Models for the Design of Pile Caps: An Experimental Study”. In: *ACI Structural Journal* 87.1, pp. 81–92. ISSN: 08893241 (cit. on pp. 165–167, 169, 172, 183, 189).
- Adebar, P. and Zhou, L. (1996). “Design of Deep Pile Caps by Strut-and-Tie Models”. In: *ACI Structural Journal* 93.4, pp. 1–12 (cit. on pp. 165–167, 170, 172, 188–190).
- Amini Najafian, H. and Vollum, R. L. (2013a). “Design of planar reinforced concrete D regions with nonlinear finite element analysis”. In: *Engineering Structures* 51, pp. 211–225. ISSN: 01410296. DOI: 10.1016/j.engstruct.2013.01.022 (cit. on p. 6).
- (2013b). “Optimising reinforcement design in D regions using non-linear finite-element analysis”. In: *Magazine of Concrete Research* 65.4, pp. 234–247. ISSN: 0024-9831. DOI: 10.1680/macr.12.00063 (cit. on p. 19).

- Anderheggen, E. and Schlaich, M. (1990). “Computer-aided design of reinforced concrete structures using the truss model approach”. In: *Computer Aided Analysis and Design of Concrete Structures*, pp. 539–550 (cit. on p. 5).
- Bairán García, J. M. (2012). “Generación automática de esquemas de bielas y tirantes considerando criterios constructivos”. spa. In: *Hormigón y acero* 63.264, pp. 67–79. ISSN: 0439-5689 (cit. on pp. 6, 16).
- Bajo, C. and Pérez-Fadón, S. (2002). “Examples. Bridge of Lekeitio”. In: *FIB Bulletin No.16. Design examples for the 1996 FIP recommendations - Practical design of structural concrete*. Fédération Internationale du Béton (fib), p. 198. ISBN: 978-2-88394-056-8 (cit. on pp. 145–147).
- Bažant, Z. P. (1983). “Comment on Orthotropic Models for Concrete and Geomaterials”. In: *Journal of Engineering Mechanics* 109, pp. 849–865 (cit. on pp. 38, 39, 44, 46).
- Bažant, Z. P. and Oh, B. H. (1983). “Crack band theory for fracture of concrete”. In: *Matériaux et Constructions* 16.3, pp. 155–177. DOI: 10.1007/BF02486267 (cit. on pp. 34, 51).
- Bažant, Z. P. and Planas, J. (1998). *Fracture and size effect in concrete and other quasibrittle materials*. CRC Press, p. 640. ISBN: 9780849382840 (cit. on p. 41).
- Blévot, J. and Frémy, R. (1967). “Semelles sur Pieux”. In: *Institute Technique du Batiment et des Travaux Publics* 20.230, pp. 223–295 (cit. on pp. 104, 121, 122, 126–128, 165, 167, 169, 170, 183–185, 194).
- CASCADE OPEN, CEA/DEN, and EDF R&D (2016). *Salome: The Open Source Integration Platform for Numerical Simulation*. Guyancourt (France) (cit. on p. 27).
- Chan, T. K. and Poh, C. K. (2000). “Behaviour of precast reinforced concrete pile caps”. In: *Construction and Building Materials* 14, pp. 73–78 (cit. on pp. 184, 199).
- Chen, W.-F. (1982). *Plasticity in Reinforced Concrete*. New York: McGraw-Hill, p. 474. ISBN: 0070106878 (cit. on pp. 40, 42).

- Clarke, J. L. (1973). *Behaviour and Design of Pile Caps with Four Piles*. Tech. rep., Tech. Rpt. 489 (cit. on pp. 165, 167, 183, 184, 195).
- Comisión Permanente del Hormigón (2008). *EHE-2008. Instrucción de hormigón estructural*. Ed. by Fomento, M. de. Madrid, Spain, p. 704 (cit. on p. 191).
- Committee on Concrete and Masonry Structures ASCE (1982). *Finite element analysis of reinforced concrete structures*. ASCE, p. 544 (cit. on pp. 4, 40, 42).
- Concrete Reinforcing Steel Institute (2008). *CRSI Handbook*. Schaumburg, Illinois, p. 1605 (cit. on pp. 104, 173, 189).
- Cope, R. et al. (1980). “Modelling of Reinforced Concrete Behaviour for Finite Element Analysis of Bridge Slabs”. In: *Numerical Methods for Nonlinear Problems 1*, pp. 457–470 (cit. on pp. 35, 43).
- Darwin, D. and Pecknold, D. (1977). “Nonlinear Biaxial Stress-Strain Law for Concrete”. In: *Journal of the Engineering Mechanics Division* 103.EM2, pp. 229–241 (cit. on pp. 38, 41).
- Drucker, D. (1961). “On structural concrete and the theorems of limit analysis”. In: *Publ. Int. Assoc. Bridge Struct. Eng.* 21, pp. 49–59 (cit. on p. 5).
- Elwi, A. E. and Hrudey, T. M. (1989). *Finite Element Model for Curved Embedded Reinforcement*. DOI: 10.1061/(ASCE)0733-9399(1989)115:4(740) (cit. on pp. 55, 60).
- Elwi, A. E. and Muray, D. (1979). “A 3D hypoelastic concrete constitutive relationship”. In: *Journal of the Engineering Mechanics Division* 105.4, pp. 623–641 (cit. on p. 41).
- European Committee for Standardization (2004). *Eurocode 2: Design of Concrete Structures - Part 1-1: General rules and rules for buildings*, p. 225 (cit. on pp. 5, 172).
- Fédération Internationale du Béton (2013). *Model Code 2010*. Lausanne, p. 434 (cit. on pp. 5, 21, 51, 58, 74, 136, 186).

- Fernández Ruiz, M. and Muttoni, A. (2007). “On Development of Suitable Stress Fields for Structural Concrete”. In: *ACI Structural Journal* 104, pp. 495–502. DOI: <http://dx.doi.org/10.14359/18780> (cit. on pp. 6, 16, 17, 19, 20, 131).
- FIB bulletin 45 (2008). *Practitioners’ guide to finite element modelling of reinforced concrete structures*, p. 339 (cit. on pp. 15, 79).
- Gerstle, K. et al. (1978). “Strength of Concrete under Multiaxial Stress States”. In: *Douglas McHenry International Symposium on Concrete and Concrete Structures*. Vol. SP-55. Detroit: American Concrete Institute, pp. 103–131. DOI: 10.14359/6611 (cit. on pp. 32, 33).
- Gogate, A. B. and Sabnis, G. M. (1980). “Design of Thick Pile Caps”. In: *ACI Journal* 77.1, pp. 18–22 (cit. on pp. 104, 167).
- González Vidosa, F., Kotsovos, M., and Pavlovic, M. (1990). “Three-dimensional finite element analysis of structural concrete”. In: *Computer Aided Analysis and Design of Concrete Structures*, pp. 1029–1040 (cit. on p. 16).
- Grassl, P. and Jirásek, M. (2006). “Damage-plastic model for concrete failure”. In: *International Journal of Solids and Structures* 43.22-23, pp. 7166–7196. ISSN: 00207683. DOI: 10.1016/j.ijsolstr.2006.06.032 (cit. on p. 39).
- Groot, A. de, Kusters, G., and Monnier, T. (1981). “Numerical modelling of bond-slip behaviour”. In: *Heron* 26.1a, pp. 1–90 (cit. on p. 61).
- Guo, H. (2015). “Evaluation of Column Load for Generally Uniform Grid-Reinforced Pile Cap Failing in Punching”. In: *ACI Structural Journal* 112.2, pp. 123–134 (cit. on pp. 166, 171).
- Gutiérrez Vela, M. (2015). “Estudio Experimental de Cálices de Hormigón Armado Mediante Modelos de Bielas y Tirantes Tridimensionales (MSc Thesis)”. PhD thesis. Universitat Politècnica de Valencia (cit. on pp. 132–134, 139, 143).
- Hannant, D. J. (1974). “Nomograms for the failure of plain concrete axial stresses”. In: *The Structural Engineer* 52.5, pp. 151–165 (cit. on pp. 32, 48).

- Hartl, H. and Beer, G. (2000). “Computational modelling of reinforced concrete structures”. In: *Festschrift zum 60. Geburtstag von Lutz Sparowitz*. Ed. by Freytag, B. and Stebernjak, B. Graz: TU-Graz, pp. 105–114 (cit. on pp. 16, 61).
- Hillerborg, A. (1990). “Fracture mechanics concepts applied to moment capacity and rotational capacity of reinforced concrete beams”. In: *Engineering Fracture Mechanics* 35.1, pp. 233–240. ISSN: 00137944. DOI: 10.1016/0013-7944(90)90201-Q (cit. on p. 41).
- Hillerborg, A., Modeer, M., and Petersson, P. (1976). “Analysis of Crack Formation and Crack Growth in Concrete by Means of Fracture Mechanics and Finite Elements”. In: *Cement and Concrete Research* 6.6, pp. 773–782. DOI: [http://dx.doi.org/10.1016/0008-8846\(76\)90007-7](http://dx.doi.org/10.1016/0008-8846(76)90007-7) (cit. on p. 41).
- Hognestad, E. (1951). *A study of combined bending and axial load in reinforced concrete members*. Tech. rep., p. 128 (cit. on p. 41).
- Hordijk, D. (1991). “Local approach to fatigue of concrete”. Doctor Dissertation. Delft University of Technology (cit. on pp. 31, 41, 44, 51, 107, 123, 204).
- Hughes, B. and Chapman, G. (1966). “The complete stress-strain curve for concrete in direct tension”. In: *RILEM Bulletin* 30, pp. 95–97 (cit. on p. 31).
- Karayannis, C. G. and Chalioris, C. E. (2013). “Shear tests of reinforced concrete beams with continuous rectangular spiral reinforcement”. In: *Construction and Building Materials* 46, pp. 86–97. ISSN: 09500618. DOI: 10.1016/j.conbuildmat.2013.04.023 (cit. on pp. 73, 75).
- Kotsovos, M. (1983). “Effect of testing techniques on the post-ultimate behaviour of concrete in compression”. In: *Matériaux et Constructions* 16.1, pp. 3–12. DOI: 10.1007/BF02474861 (cit. on pp. 29, 30).
- Kotsovos, M. and Pavlovic, M. (1995). *Structural concrete. Finite-element analysis for limit-state design*. London: Thomas Telford, p. 550. ISBN: 9780727720276 (cit. on pp. 29, 30, 33, 39, 41).

- Kupfer, H. and Gerstle, K. (1973). “Behavior of Concrete Under Biaxial Stresses”. In: *Journal of the Engineering Mechanics Division* 99.EM4, pp. 853–866 (cit. on p. 41).
- Kupfer, H., Hilsdorf, H., and Rusch, H. (1969). “Behavior of Concrete Under Biaxial Stresses”. In: *ACI Journal Proceedings* 66.8, pp. 656–666. DOI: 10.14359/7388 (cit. on pp. 32, 37).
- Liu, T., Nilson, A., and Slate, F. (1972). “Biaxial stress-strain relations for concrete”. In: *Journal of Structural Division ASCE* 98.ST5, pp. 1025–1034 (cit. on pp. 37, 41).
- Lourenço, M. S. and Almeida, J. F. (2013). “Adaptive Stress Field Models : Formulation and Validation”. In: *ACI Structural Journal* 110.1, pp. 71–81 (cit. on p. 6).
- Madu, R. (1975). “Characterizaion of the stress-strain curves for reinforced concrete under uniaxial tension”. In: *Magazine of Concrete Research* 27.93, pp. 210–218. DOI: 10.1680/macrc.1975.27.93.210 (cit. on p. 31).
- Mander, J. B., Priestley, M. J. N., and Park, R. (1988). “Theoretical Stress-Strain Model for Confined Concrete”. In: *Journal of Structural Engineering* 114.8, pp. 1804–1826. DOI: 10.1061/(ASCE)0733-9445(1988)114:8(1804) (cit. on pp. 49, 107).
- Markou, G. and Papadrakakis, M. (2012). “An efficient generation method of embedded reinforcement in hexahedral elements for reinforced concrete simulations”. In: *Advances in Engineering Software* 45.1, pp. 175–187. ISSN: 09659978. DOI: 10.1016/j.advengsoft.2011.09.025 (cit. on p. 71).
- MATLAB (2014). *version 8.4.0 (R2014b)*. Natick, Massachusetts: The Math-Works Inc. (cit. on pp. 27, 208).
- Meléndez, C. (2012). *Modelo Numérico de Elementos Finitos para el Estudio de Regiones D Tridimensionales mediante Modelos de Bielas y Tirantes (MSc. Thesis)* (cit. on p. 26).

- Meléndez, C., Miguel, P. F., and Pallarés, L. (2016). “A simplified approach for the ultimate limit state analysis of three-dimensional reinforced concrete elements”. In: *Engineering Structures* 123, pp. 330–340. ISSN: 01410296. DOI: 10.1016/j.engstruct.2016.05.039 (cit. on p. 51).
- Miguel, P. F., Jawad, M., and Fernández, M. (1990). “A discrete-crack model for the analysis of concrete structures”. In: *Computer Aided Analysis and Design of Concrete Structures*. Ed. by Bicanic, N. and Mang, H., pp. 897–908 (cit. on p. 34).
- Mörsch, E. (1908). *Reinforced Concrete Construction, Theory and Application (Der Eisenbetonbau, seine Theorie und Anwendung)*, p. 376 (cit. on p. 3).
- Muttoni, A., Fernández Ruiz, M., and Niketić, F. (2015). “Design versus Assessment of Concrete Structures Using Stress Fields and Strut-and-Tie Models”. In: *ACI Structural Journal* 112.5, pp. 605–616. ISSN: 0889-3241. DOI: 10.14359/51687710 (cit. on p. 18).
- Muttoni, A., Schwartz, J., and Thürlimann, B. (1997). *Design of concrete structures with stress fields*. Birkhäuser Verlag (cit. on pp. 5, 50, 178).
- Muttoni, A. and Fernández Ruiz, M. (2012). “Levels-of-Approximation Approach in Codes of Practice”. In: *Structural Engineering International* 22.2, pp. 190–194. ISSN: 10168664. DOI: 10.2749/101686612X13291382990688 (cit. on p. 15).
- Ngo, D. and Scordelis, A. (1967). “Finite Element Analysis of Reinforced Concrete Beams”. In: *ACI Journal Proceedings* 64.3, pp. 152–163. DOI: 10.14359/7551 (cit. on pp. 3, 15, 33, 39, 40, 60, 61).
- Nielsen, M. P. and Hoang, L. C. (2011). *Limit analysis and concrete plasticity*. CRC Press. ISBN: 9781439803967 (cit. on p. 42).
- Park, J., Kuchma, D., and Souza, R. (2008). “Strength predictions of pile caps by a strut-and-tie model approach”. In: *Canadian Journal of Civil Engineering* 35, pp. 1399–1413 (cit. on pp. 165, 166, 170, 188, 190, 191).
- Park, J.-w. et al. (2010). “Automated Finite-Element-Based Validation of Structures Designed by the Strut-and-Tie Method”. In: *Journal of Structural*

Engineering 136.2, pp. 203–210. DOI: 10.1061/(asce)0733-9445(2010)136:2(203) (cit. on pp. 6, 16, 41, 145).

Phillips, D. and Zienkiewicz, O. (1976). “FINITE ELEMENT NON-LINEAR ANALYSIS OF CONCRETE STRUCTURES.” In: *Proceedings of the Institution of Civil Engineers, Part 2* 61.1, pp. 59–88. DOI: 10.1680/iicep.1976.3503 (cit. on p. 60).

Popovics, S. (1973). “A numerical approach to the complete stress-strain curve of concrete”. In: *Cement and Concrete Research* 3.5, pp. 583–599. DOI: 10.1016/0008-8846(73)90096-3 (cit. on pp. 41, 50, 107, 123, 204).

Rashid, Y. (1968). “Ultimate strength analysis of prestressed concrete pressure vessels”. In: *Nuclear Engineering and Design* 7.4, pp. 334–344. ISSN: 00295493. DOI: 10.1016/0029-5493(68)90066-6 (cit. on pp. 3, 15, 34, 59).

Reineck, K. et al. (2011). “Gaining Experience with Strut and Tie Models for the Design of Concrete Structures”. In: *Design Examples for Strut-and-Tie Models, fib bulletin 61*, pp. 197–216 (cit. on p. 6).

Richart, F. E., Brandtzaeg, A., and Brown, R. L. (1928). *A study of the failure of concrete under combined compressive stresses*. Tech. rep. Urbana, p. 104 (cit. on p. 32).

Ritter, W. (1899). “Die Bauweise Hennebique”. In: *Schweizerische Bauzeitung* 17, pp. 41–43, 49–52, 59–61 (cit. on p. 3).

Rots, J. (1989). “Computational Modeling of Concrete Fracture”. PhD thesis. Universiteit Delft, p. 132 (cit. on p. 34).

Saenz, L. (1964). “Discussion of Equation for the stress-strain curve of concrete by Desayi and Krishnan”. In: *ACI Journal Proceedings* 61.9, pp. 1229–1235 (cit. on p. 41).

Sagaseta, J. and Vollum, R. (2010). “Shear design of short-span beams”. In: *Magazine of Concrete Research* 62.4, pp. 267–282. DOI: 10.1680/macr.2010.62.4.267 (cit. on p. 166).

-
- Sam, C. and Iyer, P. (1995). “Nonlinear finite element analysis of reinforced concrete four-pile caps”. In: *Computers & Structures* 57.4, pp. 605–622. DOI: 10.1016/0045-7949(95)00068-R (cit. on p. 103).
- Scanlon, A. (1971). *Time dependent deflections of reinforced concrete slabs*. Tech. rep. Edmonton, Canada: University of Alberta, p. 247 (cit. on p. 41).
- Schlaich, J. (1990). “On the relevance of sophisticated modelling techniques on the design of real concrete structures”. In: *Computer Aided Analysis and Design of Concrete Structures*. Ed. by Bicanic, N. and Mang, H., pp. 1273–1281 (cit. on p. 3).
- Schlaich, J., Schafer, K., and Jennewein, M. (1987). “Toward a Consistent Design of Structural Concrete”. In: *PCI Journal* 32.May-June, pp. 74–150. DOI: 10.15554/pcij.05011987.74.150 (cit. on pp. 5, 21, 132, 136, 203).
- Siao, W. B. (1993). “Strut-and-Tie Model for Shear Behavior in Deep Beams and Pile Caps Failing in Diagonal Splitting”. In: *ACI Structural Journal* 90.4, pp. 356–363 (cit. on p. 170).
- Souza, R. et al. (2009). “Adaptable Strut-and-Tie Model for Design and Verification of Four-Pile Caps”. In: *ACI Structural Journal* 106.2, pp. 142–150 (cit. on pp. 165, 166, 170, 183, 188–191).
- Suidan, M. and Schnobrich, W. (1973). “Finite element analysis of reinforced concrete”. In: *Journal of the Structural Division* 99.10, pp. 2109–2122 (cit. on p. 34).
- Suzuki, K. and Otsuki, K. (2002). “Experimental Study on Corner Shear Failure of Pile Caps”. In: *Transactions of the Japan Concrete Institute* 23, pp. 303–310 (cit. on pp. 104, 167, 184, 198).
- Suzuki, K., Otsuki, K., and Tsubata, T. (1998). “Influence of Bar Arrangement on Ultimate Strength of Four-Pile Caps”. In: *Transactions of the Japan Concrete Institute* 20, pp. 195–202 (cit. on pp. 92, 104–106, 111, 167, 183, 184, 186, 196).

- Suzuki, K., Otsuki, K., and Tsubata, T. (1999). “Experimental Study on Four-Pile Caps with Taper”. In: *Transactions of the Japan Concrete Institute* 21, pp. 327–334 (cit. on pp. 104, 167, 184, 197).
- Suzuki, K., Otsuki, K., and Tsuchiya, T. (2000). “Influence of Edge Distance on Failure Mechanism of Pile Caps”. In: *Transactions of the Japan Concrete Institute* 22, pp. 361–368 (cit. on pp. 104, 167, 184, 197).
- Tabatabai, S. and Mosalam, K. (2001). “Computational platform for non-linear analysis/optimal design of reinforced concrete structures”. In: *Engineering Computations* 18.5/6, pp. 726–743. DOI: doi.org/10.1108/EUM0000000005785 (cit. on p. 19).
- Tjhin, T. N. and Kuchma, D. A. (2002). “Computer-Based Tools for Design by Strut-and-Tie Method : Advances and Challenges”. In: 99 (cit. on pp. 5, 9, 148).
- Tjhin, T. N. and Kuchma, D. A. (2007). “Integrated analysis and design tool for the strut-and-tie method”. In: *Engineering Structures* 29.11, pp. 3042–3052. ISSN: 01410296. DOI: 10.1016/j.engstruct.2007.01.032 (cit. on pp. 6, 16).
- TNO DIANA (2016). *Finite Element Analysis User’s Manual. Release 10.1* (cit. on p. 19).
- Vecchio, F. J. and Collins, M. P. (1986). “The Modified Compression-Field Theory for Reinforced Concrete Elements Subjected to Shear”. In: *ACI Journal Proceedings* 83.2, pp. 219–231. ISSN: 00028061. DOI: 10.14359/10416 (cit. on pp. 41, 48, 51, 74, 107, 124, 179, 186, 204).
- (1993). “Compression Response of Cracked Reinforced Concrete”. In: *Journal of Structural Engineering* 119.12, pp. 3590–3610 (cit. on p. 179).
- Vecchio, F. J. and Selby, R. (1991). “Toward Compression-Field Analysis of Reinforced Concrete Solids”. In: *Journal of Structural Engineering* 117.6, pp. 1740–1758 (cit. on p. 49).
- Zienkiewicz, O. (1977). *The Finite Element Method*. London: McGraw-Hill, p. 787 (cit. on pp. 3, 22).

List of Figures

2.1	The 20-node hexahedron FE.	26
3.1	Stress-strain diagram for concrete in uniaxial compression. . . .	31
3.2	Load-deformation diagram for concrete in uniaxial tension. . . .	31
3.3	Relative stress-strain diagram for concrete under biaxial compression and combined tension-compression (after Kupfer, Hilsdorf, and Rusch (1969)). $\sigma_{c,1}$ = stress in principal compressive direction; $\sigma_{c,2}$ = transverse stress; (-) compression, (+) tension	32
3.4	Tangent shear modulus G to enforce coaxiality between principal strain and stress directions as proposed by Bažant (1983). .	39
3.5	Concrete tensile models.	41
3.6	3D characterization through uniaxial models.	44
3.7	Determination of the equivalent length of an integration point.	52
3.8	Plastic deformations.	53
4.1	Stress-strain diagram for steel in tension and compression. . . .	56
4.2	Elastic-perfectly plastic and elastic-hardening models for steel. .	57
4.3	Bond stress-slip displacement model (MC 2010 (Fédération Internationale du Béton 2013)).	58
4.4	Embedded steel FE model.	63
4.5	Slipping rebar model.	64

4.6	Input data for rebar geometry definition.	67
4.7	Relative position of rebar macro-element and concrete FE: (a) Segment enters and exits FE, (b) Segment enters but does not exit FE, (c) Segment embedded in FE, (d) Segment is external to FE.	69
4.8	Relative position of spatial segment and polygon by using Plücker coordinates: (a) Rebar goes through FE face, (b) Rebar intersects with one FE edge, (c) Rebar trajectory is outside the FE face, (d) Rebar is parallel to the FE face.	70
4.9	Discretisation of curved spatial rebar.	72
4.10	Geometry and reinforcement details of beam specimens with spiral reinforcement (from Karayannis and Chalioris (2013)) . .	73
4.11	Discretisation of spiral rebar in beam SP80.	74
4.12	Discretisation of spiral rebar in beam SPA80.	74
4.13	Experimental and FE load-deflection curves for beams with spiral stirrups.	75
4.14	Steel stress profile along spiral stirrup.	76
4.15	FE plot of concrete principal compressive stress directions for beam SPA80.	76
5.1	Coordinates mapping for quadrilateral element.	83
5.2	Determination of equivalent nodal forces of a distributed load. .	84
5.3	Static condensation of loading substructure.	86
5.4	Automatic generation of auxiliary FEs to consider circular pile.	91
5.5	FE mesh for pile cap BPC-30-30-1. Column omitted.	93
5.6	FE mesh for pile cap BPC-30-30-1. Column included.	93

5.7	FE vertical stress field at loading area. Column effect not included: (a) uniform square load with parallel FE mesh, (b) uniform square load with arbitrary orientation, (c) uniform circular load with regular mesh, (d) uniform circular load with distorted mesh.	95
5.8	FE vertical stress field at loading area. Column effect included.	96
5.9	FE vertical stress field at support areas: (a) Fixed supports, (b) Uniform-stress supports (c) Flexible supports (steel plates), (d) Flexible supports (concrete piles).	97
5.10	FE load-deflection curves for pile cap BPC-30-30-1 obtained under different load and support assumptions. $f_{ct} = 0$	99
6.1	Geometry of specimens tested by Suzuki, Otsuki, and Tsubata (1998).	105
6.2	FE meshes for Suzuki's specimens.	109
6.3	Experimental and FE load-displacement curves.	111
6.4	Experimental and FE load-displacement curves with constrained horizontal displacements at top of the column.	112
6.5	FE principal compressive directions for specimen BP-20-30-2 in analysis case 1. $P = 450$ kN	113
6.6	FE principal compressive directions for specimen BPC-30-30-2 in analysis case 1. $P = 900$ kN	113
6.7	FE rebar stresses at maximum load.	114
6.8	FE principal compressive directions for specimen BP-20-30-2 in analysis case 2. $P = 247$ kN.	115
6.9	FE principal compressive directions for specimen BPC-30-30-2 in analysis case 2. $P = 646$ kN.	115
6.10	FE principal compressive directions for specimen BP-20-30-2 in analysis case 3. $P = 336$ kN.	116
6.11	FE principal compressive directions for specimen BPC-30-30-2 in analysis case 3. $P = 879$ kN.	117

6.12	FE rebar stresses at maximum load.	117
6.13	FE principal compressive directions for specimen BP-20-30-2 in analysis case 4. $P = 336$ kN	118
6.14	FE principal compressive directions for specimen BPC-30-30-2 in analysis case 4. $P = 855$ kN	119
6.15	Geometry of specimens tested by Blévo \acute{t} and Frémy (1967). . .	122
6.16	FE load-displacements curves for Blévo \acute{t} and Frémy specimens.	125
6.17	FE compressive stress directions for Blévo \acute{t} and Frémy specimens at maximum load. In black, yielded rebars.	125
6.18	FE results for specimen 4N2bis at maximum load on the diagonal plane.	126
6.19	FE results for specimen 4N3bis at maximum load on the diagonal plane.	127
6.20	FE results for specimen 4N1 at maximum load on the diagonal plane.	128
7.1	Test view (Gutiérrez Vela 2015).	133
7.2	Proposed base strut-and-tie models: (a) Model 1, (b) Model 2, (c) Model 3. (Gutiérrez Vela 2015)	133
7.3	FE model for socket base column-to-foundation connections. . .	135
7.4	Linear FE results for socket base column-to-foundations connection specimens.	137
7.5	Elastic stress fields for socket base column-to-foundation connection X2.	138
7.6	FE results and STM model for specimen X2.	140
7.7	FE results and STM model for specimen X3.	141
7.8	FE results and STM model for specimen X7.	142

8.1	Description of anchorage block and strut-and-tie model (after Bajo and Pérez-Fadón 2002).	147
8.2	Details of simplified FE model	149
8.3	Reinforcement arrangement for simplified FE model.	150
8.4	FE principal compressive stress directions and reactions obtained from the simplified model.	153
8.5	FE steel stresses obtained from the simplified model.	154
8.6	Evolution of the three-dimensional compressive stress field throughout the iteration process.	156
8.7	Details of refined FE model.	158
8.8	FE principal compressive stress directions for anchorage block obtained from refined FE model at the design load	160
8.9	FE compressive stress field for anchorage block obtained from refined FE model at design load.	161
9.1	Strut-and-tie model for four-pile cap without shear reinforcement: (a) 2D model; (b) 3D model.	169
9.2	Proposed strut-and-tie model: (a) truss 3D view; (b) truss 2D side view; (c) 3D view of strut and tie details; (d) strut projection onto cap diagonal plane and (e) plan view of strut and tie details.	175
9.3	Limit functions P_{nt} , $P_{ns,1}$ and $P_{ns,2}$ and yielding function P_{yt} to predict pile cap strength.	182
9.4	Ratio of test-to-predicted strengths P_{test}/P_{pred} for 162 specimens by the proposed method.	185

9.5	FE results for four-pile cap BP-30-30-2: (a) comparison of measured/predicted load-deflection curve; at the diagonal cap plane, superimposed to the strut-and-tie geometry obtained from the proposed method ($\theta_s^{3d} = 48.54^\circ$); (b) FE contour plot of compressive stress field and principal compressive directions at maximum load; (c) FE contour plot of compressive stress field and principal compressive directions after failure; (d) FE contour plot of concrete softening coefficient ξ_c at maximum load; (e) contour plot of concrete softening coefficient ξ_c after failure. . .	187
9.6	Ratio P_{test}/P_{pred} for 162 specimens obtained from the considered methods.	190
9.7	Fixed strut angle θ_0^{3d} adopted by other truss models vs. predicted strut angle at failure θ_{pred}^{3d} by the proposed model for 162 specimens.	192

List of Tables

6.1	Summary of specimens of Suzuki, Otsuki, and Tsubata (1998).	106
6.2	Summary of FE predicted strengths for Suzuki's specimens. . .	110
6.3	Summary of Blévoet and Frémy (1967).	122
6.4	FE predictions for Blévoet and Frémy's specimens.	124
7.1	Column forces at failure (after (Gutiérrez Vela 2015))	134
8.1	Calculated rebar areas based on FE and STM results	152
9.1	Experimental data and obtained predictions for the considered specimens.	194